Low Reflectivity Facet Realization in GaAs-Based Optoelectronic Devices Using Self-Aligned Stripe Process

Omar Mobasher Salih Ghazal

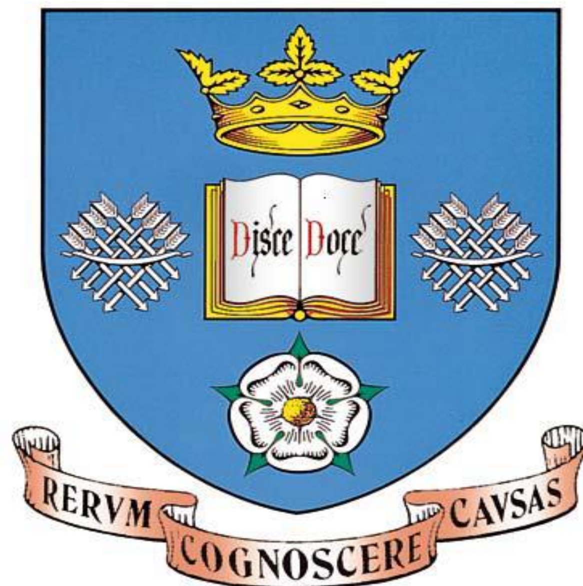

Department of Electronic and Electrical Engineering

Thesis submitted to the University of Sheffield to fulfil the requirement of Philosophy Doctorate Degree

February 2016

Abstract

This thesis explores the realization of low facet reflectivity using self-aligned stripe buried waveguide configuration and its implementation in optoelectronic devices such as superluminescent diodes (SLDs) and semiconductor optical amplifiers (SOAs).

I explored the development of the buried waveguide in AlGaAs/GaAs material system ,since its first presentation in 1974 by Tsukada, in order to identify the problems associated with this technology.

A novel window-faceted structure is demonstrated. The experimental measurements demonstrated effective reflectivity $<10^{-14}$ as a result of both divergence and absorption within these window-like regions (i.e. not transparent). Its implementation to suppress lasing in tilted and normal-to-facet waveguide SLDs was thoroughly investigated in chapters 3 and 4. In the tilted devices, ~40mW output power with spectral modulation depth < 2% is demonstrated. In the latter types of SLDs, up to 16mW output power with <5% spectral modulation depth was recorded, which is the highest power demonstrated for such configurations. The performance of the two types of devices was measured without the application of anti-reflective coatings on the rear facet, which makes them inherently broadband.

By incorporating a windowed facet at each end of a waveguide I could realize an SOA with window structured facet. Promising results were demonstrated in this configuration including 33dB gain and <6dB noise figure, which are comparable to the state-of-the-art.

A trial was held to extend the concept of absorptive rear window to visible wavelengths available in the GaInP/AlGaInP material system. Problems associated with such devices were explored briefly and two solutions are suggested. Simulations were performed to realize design of an optimized device. Unfortunately, the experimental implementation of the design was not successful but suggestions for strategies to overcome these problems are discussed

Acknowledgement

It has been a quite long 4 years for me pursuing the goal of myself, my late father and all of my family. I would like to thank my mother, brothers, and my lovely wife samara for their unlimited support they showed during my study time starting from 2011.

I would like to thank the epitaxial growers working in the EPSRC who helped to provide the material required in my work, I would like to specify Dr. Benjamin J. Stevens who grew my first set of devices and Dr. Andrey Krysa for growing the visible ARROW structure lasers. I would like also to thank the technical staff in the device fabrication clean room who helped during the use of the clean room.

The research group headed by Prof. Richard Hogg made the PhD period a worthy to remember time in my life. I have to show my appreciation to Dr. David T Childs for his technical support that helped me to do the experimental measurements as accurate as possible and also for the nice memories he left during the group nights out. Thanks to Dr. Nasser Babazadeh for the tips and tricks he taught me when I was messing some of the samples and drove me back to the right path. Thanks to all my friends in the III-V centre in the north campus for the moral support they offered and the memories they shared, I hope you all good luck and success in you carriers hopefully to meet sooner than later in some conference around the globe. With a final big thanks to the head of the group Prof. Richard Hogg for the scientific, technical, and moral support he provided.

Finally, I would like to thank my supervisor Dr. Kristian Groom for his support and guidance during my study and I hope I was not a student to forget in the future.

Table of Contents

Chapter one: Introduction and background

1.1 Introduction: 1
1.2 Project motivation: 1
1.3 Optical Coherence Tomography 4
  1.3.1 TD-OCT 5
  1.3.2 SD-OCT 5
  1.3.3 Impact of light source on the OCT operation 7
1.4 Superluminescent diodes: 7
  1.4.1 Device Emission: 8
1.5 Semiconductor Optical Amplifier 9
  1.5.1 Operation principle: 10
1.6 Buried Heterostructure Lasers: 12
1.7 Self-aligned stripe background: 39
1.8: Thesis outlines: 48
  1.8.1 Chapter two 48
  1.8.2 Chapter three 48
  1.8.3 Chapter four 49
  1.8.4 Chapter five 49
  1.8.5 Chapter six 50
1.9 References 50

Chapter Two: Methodology

2.1 Introduction. 59
2.2 Growth and fabrication: 59
  2.2.1 Growth, stripe formation and regrowth: 59
  2.2.2 Post growth process: 64
    1- P-ohmic contact metallization 64
    2- Electrical isolation trenches 64
    3- SiN deposition and Bond-Pads windows 65

4- Wafer thinning and n-contact 66
5- Cleaving and packaging 67
2.3 Measurement setups: 67
2.3.1 light-current characteristics: 67
2.3.2 Low resolution electroluminescence (EL) setup: 68
2.3.3 High resolution EL setup: 69
2.3.4 Photocurrent setup: 70
2.3.5 Farfield setup: 71
2.3.6 SOA characterization setup 72
2.4 Photocurrent Spectroscopy: 74
2.4.1 Sample Preparations 75
2.4.2 Measurement and Results 76
2.5 Length dependant measurement: 77
2.6 Summary and Conclusions: 81
2.7 Future Work 83
2.8 References 83

Chapter Three: Tilted Self-Aligned Stripe Superluminescent Diodes with Low Facet Reflectivity

3.1 Introduction: 85
3.2 Background: 85
3.2.1 Single Pass Amplification 86
3.2.2 Common structures 87
3.2.3 Spectral Modulation Depth 89
3.2.4 Output Power 90
3.2.5 Research fields 90
3.4 Techniques used to achieve low facet reflectivity: 91
3.4.1 Anti-Reflective (AR) Coating: 91
3.4.2 Tilted Optical Cavity: 92
3.4.3 Transparent Window: 93
3.5 GaAs-Based Buried Facets (Window Facets): 94
3.5.1The proposed window-like structure 97

3.5.2 Estimation of the buried-facet reflectivity......97
3.5.2 Facet effective reflectivity:......99
3.5.4 Experimental measurements:......100
3.6 Expected Spectral Modulation Depth......103
3.7 Output Power Characterization:......107
3.7.1 Geometry effect on the output power......108
3.7.2Temperature Effect:......110
3.8 Spectral Characterization:......111
3.8.1 Low resolution spectral characterization......112
3.8.2 High resolution spectral characterization......113
3.9 Excess heat avoidance:......116
3.9.1 Epi-side down configuration:......117
3.9.2 Pulsed Operation......122
3.9.3 Window absorption band control using on-chip resistor:......123
3.10 Summary and conclusion:......127
3.11 Future Work......130
3.12 References......130

Chapter Four: Normal-to-Facet Superluminescent Diodes

4.1 Introduction:......135
4.2 Device preparation:......137
4.3 Results......139
4.4 Further Development......141
4.4.1 Widths variation effect:......142
4.4.2 1mm Stripe Spectral Modulation Depth......143
4.4.3 Length variation effect:......145
4.4.4 Stripe width effect in > 1mm devices:......147
4.5 Heat Effect Reduction:......150
4.5.1 Shorter Than 1mm Device......151
4.5.2 Longer Than 1mm Device......152
4.6 Summary and Conclusions:......153
4.7 Future Work......154
4.8 References......155

Chapter Five: Self-Aligned Stripe Semiconductor Optical Amplifier

5.1 Introduction: 157
5.2 SOA Background 157
5.2.1 Operation principle: 158
5.2.2 The four parameters: 159
5.2.3 Structures used 161
5.3 Sample Preparation: 163
5.4 SOA Characterization: 164
5.4.1 Initial Screening 165
5.5 Results 166
5.5.1 Amplification bandwidth 167
5.5.2 Small signal gain and saturation output power 168
5.5.3 Noise figure 173
5.6 Discussion. 176
5.6 Summary and Conclusions: 180
5.7 Future Work: 181
5.8 References 181

Chapter Six: Index-Guided Buried Waveguide in the Visible Range in the GaAs-Based Material System

6.1 Introduction 185
6.2 Red Laser Background 186
6.3 Problems in Red material 189
6.3.1 Problems in Total Internal Reflection 190
6.3.2 ARROW structure 190
6.3.3 The shallow bandgap step in $(Al_xGa_{x-1})_yIn_{y-1}P$ material system and the multiquantum barrier MQB. 194
6.4 The Proposed Red ARROW Laser: 197
6.4.1 The multiquantum barrier active design: 198

6.4.2 Anti-Resonance Reflecting Optical Waveguide Design: 203
6.5 Experimental Implementation of the Simulated Device. 209
6.5.1 The full clad structure:...209
6.5.2 The ARROW buried structure...211
6.6 Device Characterization 212
6.6.1 The LI characteristics of the reference laser structure: 212
6.6.2 MQB laser characterisation: 215
6.6.3 Arrow structure observations: 216
6.7 Future Work 217
6.8 References 219

Chapter Seven: Summaries and Conclusion

7.1 Summaries:...225
7.1.1 Chapter two summary: 225
7.1.2 Chapter three conclusions: 225
7.1.3 Chapter four conclusions:...227
7.1.4 Chapter five conclusions: 228
7.1.5 Chapter six summary:..229
7.2 Conclusion: 230

List of Publications

Related papers:

1. Omar M.S. Ghazal, Nasser Babazadeh, David T. D. Childs, Benjamin J. Stevens, Richard A. Hogg, and Kristian M. Groom, *“GaAs-based superluminescent diodes with window-like facet structure for low spectral modulation at high output powers”,* Semiconductor Science and Technology, 31(3), 2016.
2. Omar M.S. Ghazal, Nasser Babazadeh, David T. D. Childs, Benjamin J. Stevens, Richard A. Hogg, and Kristian M. Groom, “GaAs-Based Self-Aligned Stripe Superluminescent Diodes Processed Normal to the Cleaved Facets”, SPIE Photonic West Proceedings, 13-18 February 2016, San Francisco, California, USA.
3. Omar M.S. Ghazal, Nasser Babazadeh, David T. D. Childs, Benjamin J. Stevens, Richard A. Hogg, and Kristian M. Groom, “Self-aligned Stripe Semiconductor Optical Amplifiers with Buried Facets”, Electronic Letters, 2016. (Rejected and now in the process to resubmit following the required corrections,).

Related oral talks and posters presented in conferences:

1. Omar M.S. Ghazal, Kristian M. Groom, Nasser Babazadeh, David T. D. Childs, Benjamin J. Stevens, and Richard A. Hogg, “*High-power GaAs-based Superluminescent Diodes with Low Spectral Modulation*”, UK Semiconductor 2014, July-2014, Sheffield, United Kingdom.
2. Omar M. S. Ghazal, Kristian M. Groom, Benjamin. J. Stevens, Nasser Babazadeh, David T. D. Childs and Richard A. Hogg, "GaAs Based Superluminescent Diodes Employing Window Facets in a Self-Aligned Stripe," *2014 International Semiconductor Laser Conference*, Palma de Mallorca, 2014, pp. 175-176.
3. Omar M.S. Ghazal, Kristian M. Groom, Nasser Babazadeh, David T. D. Childs, Benjamin J. Stevens, and Richard A. Hogg, *“GaAs Self-Aligned Stripe Superluminescent Diodes Processed Normal to the Cleaved Facets”*, Semiconductor and Integrated Optoelectronics SIOE’15 Conference, 31st March-2nd April 2015, Cardiff, Wales.
4. Omar M.S. Ghazal, Kristian M. Groom, Nasser Babazadeh, David T. D. Childs, Benjamin J. Stevens, and Richard A. Hogg, *“High-Power GaAs-based Superluminescent Diodes Employing Window-like Facets for Low Spectral Modulation”,* Conference of Laser and Electro-Optics (CLEO) Europe- European Quantum Electronics Conference, 21-25 June 2015, Munich, Germany

Chapter one: Introduction and background

1.1 Introduction:

This thesis describes the implementation of a recently developed Gallium Arsenide based (GaAs-based) self-aligned stripe (SAS) technology incorporating Gallium Indium Phosphide (GaInP) layer, which was born out of attempts to realize GaAs buried heterostructure, in realization of extremely low effective facet reflectivity. The low reflectivity facet was used to present high performance superluminescent diodes (SLDs) and semiconductor optical amplifiers (SOAs) for use in enhanced optical coherence tomography (OCT). Since the whole thesis is based on cutting edge buried waveguide technology, in this chapter I review the literature on buried heterostructure laser designs with more particular focus on self-aligned stripes at the end of the review. At the end of the chapter, I briefly outlined the contents of the thesis and the main findings for each of the four experimental chapters which followed the experimental methods described in chapter two.

1.2 Project motivation:

SLDs and SOAs have been used as optical broadband emitters in OCT since its presentation in 1991 by Huang *et.al.* [1]. SLDs are used alone usually relying on their ability to provide more than 50nm spectral bandwidth in spectral-domain OCT (SD-OCT). On the other hand, SOAs are usually accompanied with a narrow linewidth tunable light source (e.g. tunable semiconductor laser or external cavity laser) in order to provide high brightness light source in swept-source OCT (SS-OCT). 1.3µm wavelength was the main interest for plenty of efforts since OCT presentation in order to enhance the imaging quality. Most of this development was focused on the Indium Phosphide based (InP-based) devices which can offer wavelengths in the 1250-1600nm

by the Indium Gallium Arsenide Phosphide/ Indium Phosphide (InGaAsP/InP) material system.

The recent interests of OCT development are the retina, choroid, and vitreous imaging for diagnosis/therapy [2], [3]. The main obstacle faces such wavelengths in the case of living tissues is the high absorption of such wavelength in the biological fluids such as water, haemoglobin, and oxidized haemoglobin as reported by Huang and shown in Figure 1-1 [4].

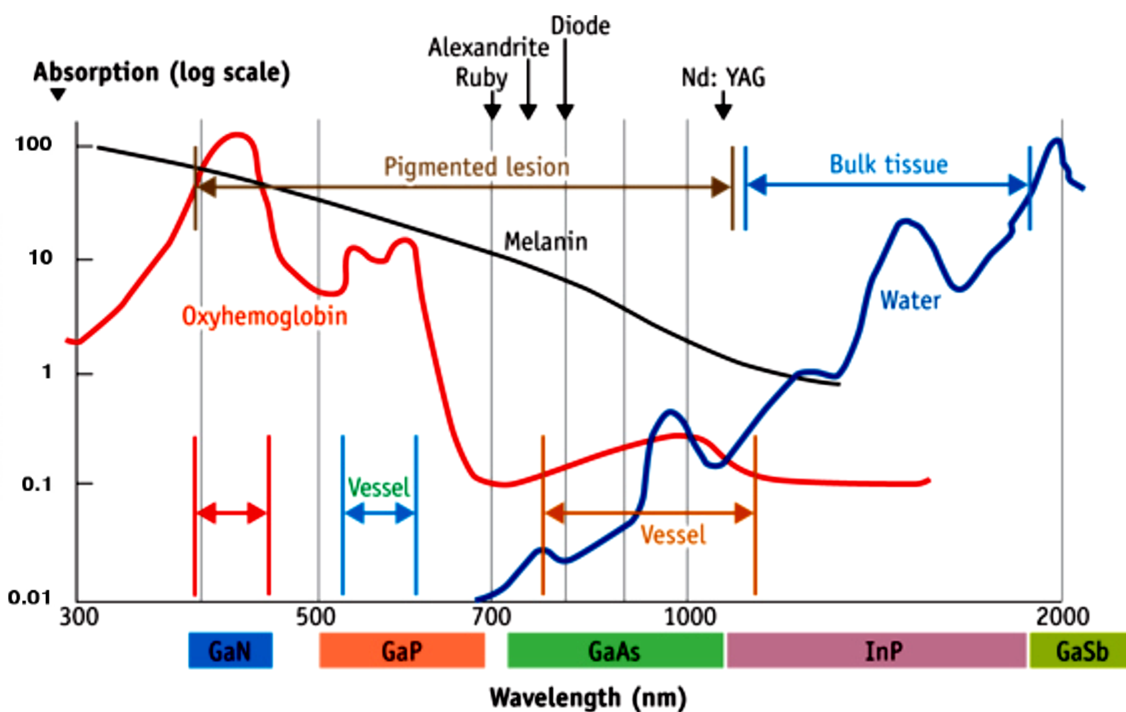

Figure 1-1: A re-print of the biological window graph published by Huang in their paper [4].

Figure 1-1 shows absorption minima in the spectral region that can be offered by GaAs-based devices. This fact increased the interest in developing GaAs-based SLDs and SOAs which emit in such wavelengths and can be used as OCT broadband sources as can be seen in Figure 1-2 which plots the bandgap as a function of the lattice constant for a range of III-V semiconductor material. It was proven that the quality of the resultant image of an OCT system is in direct relation to the emitted light quality which is governed by the quality of the source.

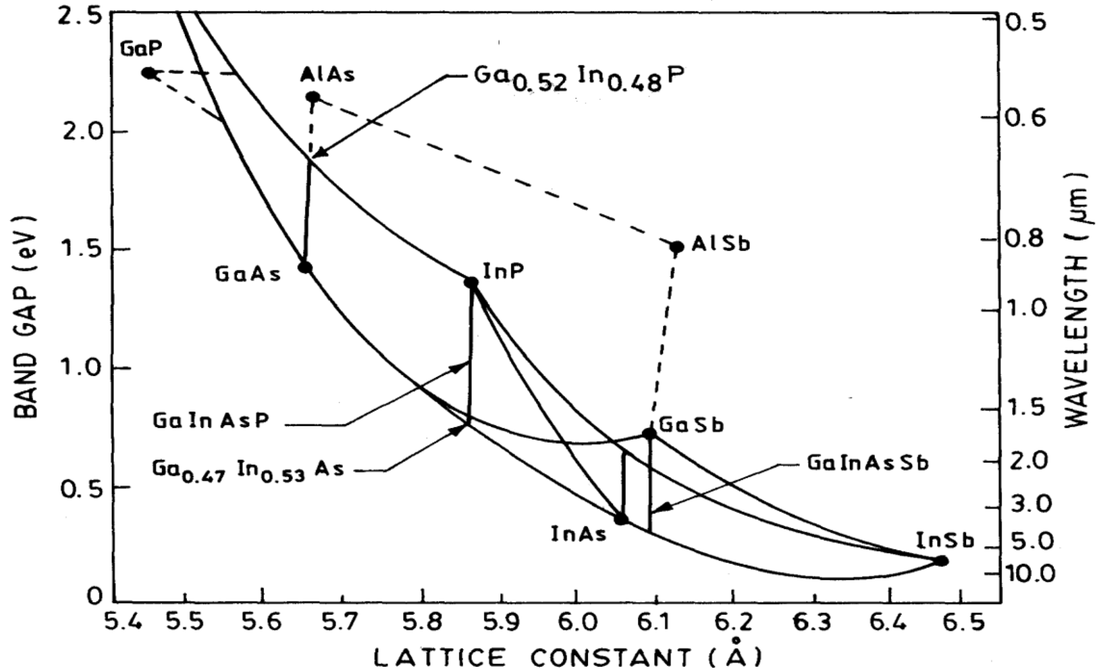

Figure 1-2: A Figure 1-showing the bandgap and the operating wavelength as a function of the lattice constant of the III-V semiconductor material. Examination of the figure can show that InGaAsP/InP operates mainly in the 1.1-2µm while the GaAs/AlGaAs system can operate from ~0.6-1.1µm in case no strain was applied. In case of strained quantum structures, operating wavelength of GaAs-based material can be extended up to 1600nm.

A number of methods were used to transform the diode laser into SLD/SOA which will be reviewed briefly in chapters 3 and 5. One of these methods is windowed (buried) facet structure. Such facet is usually achieved by a process includes etching and overgrowth. This process was developed in the InP platform to create windowed SLDs [5]and windowed SOAs[6]. The problem associated with such structures in the GaAs-based devices is that Aluminium Gallium Arsenide (AlGaAs) is key element in any structure and exposure of Al-containing layer during the etching process results in poor quality overgrowth. This problem was solved by incorporating GaInP protecting layer as suggested by B.J. Stevens [7]. In this thesis I used this method to present broadband devices with high performance which are suitable for biomedical OCT imaging in chapters 3, 4, and 5. In addition to that, I suggested in chapter 6 GaAs-based devices emit at the very edge of the GaAs-based spectral range. These devices can be realized

via a similar method to those presented in chapters 3-5 with one key factor difference in their optical confinement method.

1.3 Optical Coherence Tomography

Optical coherence tomography is a high resolution imaging technique first presented by Huang *et.al.*[1], this method enables measurement of the thickness layers that comprise the scanned tissues with no need of further processing or specific preparation for the tissue [8]. In any imaging system the key features to be considered is the axial resolution and penetration depth. While the classical imaging technologies such as ultrasound provide very deep imaging the resolution is limited to larger than 10µm, ultrahigh resolution <1µm can be achieved by confocal microscopy but the imaging penetration is limited to less than 1mm. The essential properties that can be offered by OCT compared to other imaging techniques is that the axial resolution from 10-2µm can be achieved for a relatively deep imaging, which plays a key role in tissue diagnosis and imaging. Fujimoto located OCT with respect to the other imaging techniques as shown in Figure 1-3 below in his book [8].

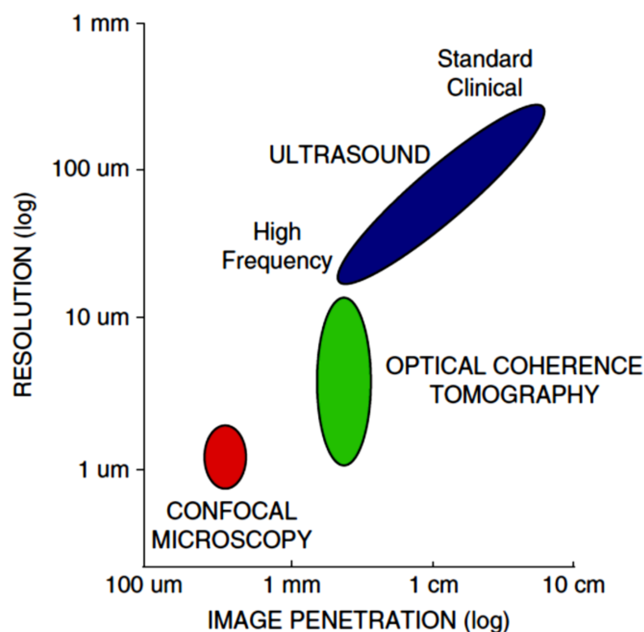

Figure 1-3: The conventional imaging techniques used for biomedical imaging from clinical to laboratory based systems as reported by Fujimoto in [8].

OCT operated in two domains, time-domain OCT (TD-OCT) in which OCT was presented for the first time and Fourier- or spectral-domain OCT (FD-OCT or SD-OCT) which replaced the old approach nowadays.

1.3.1 TD-OCT

The technique presented for the first time by Huang *et.al.* [1] was based on a non-coherent light source (SLD) emits a light which is split by a 50:50 beam splitter to a form a reference and information signals. By detecting the interference between them based on the time difference, the tomography of the specimen is detected. This type of OCT is called time-domain OCT. Figure 1-3 below shows a simplified diagram of the operation.

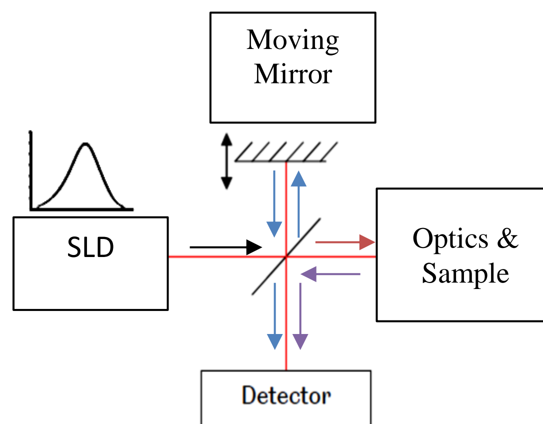

Figure 1-4: simplified schematic of time-domain optical coherence tomography [1].

TD-OCT had a limited sensitivity and a signal-to-noise-ratio that is lower than the one provided by SD-OCT.

1.3.2 SD-OCT

The SD-OCT differs from the TD-OCT by considering the frequency of the information (or the wavelength) in order to extract the thickness of the tissue layers. Instead of using a moving mirror and compare white optical powers of the information and the reference signals in terms of the time variation which results in a phase shift between the two signals as occurs in TD-OCT, SD-OCT compares the reflected optical

intensity across a range of wavelengths, since each wavelength results in a constructive interference[9]. This is performed by either changing the detected wavelength using a spectrometer or a line-detector as happens in the case where SLD is used (as shown in Figure 1-5 below), or by using a fixed detector and alter the injected wavelength.

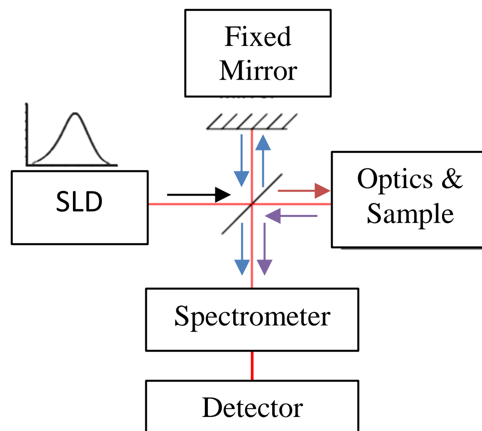

Figure 1-5: a simplified schematic of a spectral-domain OCT utilizing broadband emitter

In the latter case, a tunable laser is commonly used as the initial light source and it is usually combined with an SOA to amplify the signal to the desired level. The OCT operation is called a Swept-Source OCT (SS-OCT) which a simplified diagram of its configuration is shown in Figure 1-6 below.

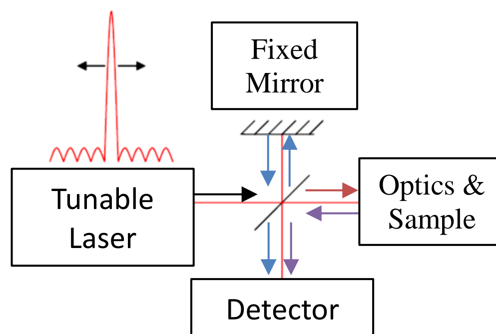

Figure 1-6: Simplified schematic of swept-source OCT.

1.3.3 Impact of light source on the OCT operation

The light source used in the OCT apparatus is the most essential part of the setup. The properties of the source govern the image quality. The equation that governs the axial resolution, Δz, of the OCT system is shown in equation (1-1) below such that

$$\Delta z = \frac{2\ln 2}{\pi}\frac{\lambda^2}{\Delta\lambda} \qquad \text{……(1-1)}$$

where λ is the light source wavelength and Δλ is the bandwidth of the source. Examining equation (1-1) reveals that the axial resolution is directly proportional to the squared value of the source and inversely proportional to the bandwidth of the source. This means that in order have a better resolution the light source bandwidth should be increased at the same wavelength or decrease the operating wavelength.

While the broadband emitters are not the main interest in this thesis, I presented a study on realization of buried semiconductor laser device operate at 650nm in chapter 6. This can be developed into a broadband emitter operating in that wavelength using the same concepts I presented.

The other feature that can affect the OCT operation is the output power of the light source, which directly related to the setup sensitivity [9]and the signal-to-noise-ratio [10] of the system.

In chapter 3 of this thesis I presented a tilted SLD that can operate with output power up to 38mW with no observable noise if it was run under pulsed operation. Also I demonstrated a very high gain and low signal-to-noise-ratio SOA which can benefit if it was used for SS-OCT.

1.4 Superluminescent diodes:

Superluminescent diodes are widely used essential opto-electronic elements in a broad range of applications such as optical-communication [11], [12], fibre-optic

gyroscopes [13], sensing [14], [15], and optical coherence tomography both industrial [16] and biomedical [15].

1.4.1 Device Emission:

SLDs make use of Amplified Spontaneous Emission (ASE), provides relatively broadband emission with relatively high brightness. In a laser diode the ASE is found as a transitional state between the broadband low brightness spontaneous emission of the laser below threshold (essentially act as light emitting diodes (LED)), and the very narrow band very high brightness amplified stimulated emission above lasing threshold where lasing occurs. This process is demonstrated in Figure 1-7 which plots the three emissions in three different colours with their related emission in the in-set. Amplified spontaneous emission is the spontaneous emission that undergoes amplification through stimulated emission as it travels through an optical cavity under population inversion. Generally the SLD emission can be described as a broadband high brightness emission. While the bandwidth of the LED can be as wide as 300nm or more, a bandwidth of ~ 30-50nm is typical for the SLD [8]. ASE (the superluminescence) occurs in all of the laser devices for a small range of injection current prior to lasing threshold, when feedback of coherent photons with a specific band of wavelengths start to stimulate the excited carriers to make the transitions at that band. Figure 1-7 shows the common LI of the any laser device with the spectral transitions from spontaneous emission to amplified stimulated emission.

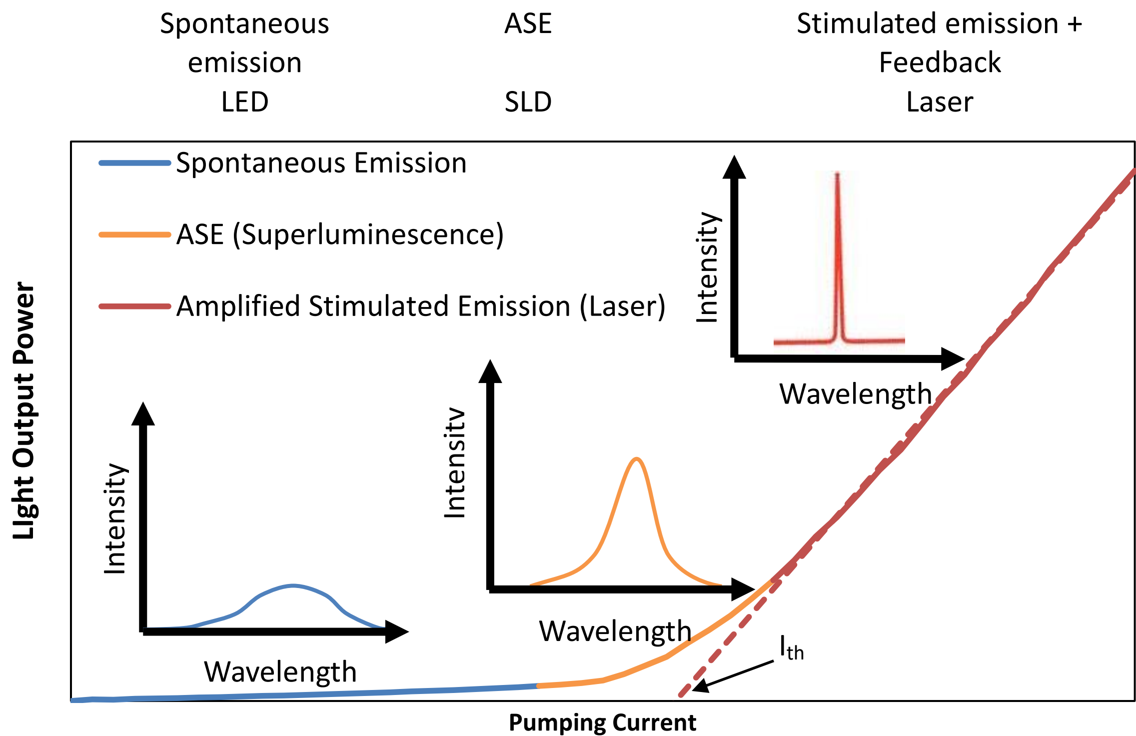

Figure 1-7: The Common Light-vs-Current Characteristic curve of any semiconductor laser. In this process three types of emission is emitted from the same device according to the pumping level 1) The spontaneous emission (the blue line) it is low brightness wide spectrum, this emission results from almost random transitions along the device spectral band, 2) the amplified stimulated emission (the red line) which is a very narrow band as shown in the related inset with very high brightness and this is because the transitions are now more driven by the wavelengths already active in the device cavity, 3) the transition in between is the Amplified Spontaneous Emission which has a high brightness (sometimes compared to the laser) and wide band, the ASE results from a driven transition from multiple wavelengths rather than just one as in laser.

An SLD exploits this by suppressing the optical feedback through reduction of reflectivity provided by the optical facets to effectively extend lasing threshold to such a point that it will not be reached. More comprehensive study regarding the applications and the used techniques to achieve low facet reflectivity is presented in chapter 3.

1.5 Semiconductor Optical Amplifier

Semiconductor Optical Amplifiers (SOA) are key devices used in wide variety of applications since their presentation by Crowe and Craig Jr. from IBM in 1964 [17]. Applications like optical communications [18] [18], OCT [19], high power lasers [20],

optical signal processing [21] and optical logic gates [22], and wavelength conversion [23] are all covered by SOAs.

Since optical communications and optical fibre applications were the main fields of interest for a very long time, the main bandwidths that SOA were developed in was 1550 [18], 1300 [19], [24], and 850 [25]. As the erbium doped fibre amplifier EDFA technology grew bigger and the presentation of the optical coherence tomography the need for amplifier to enhance these devices performance increased. The 980nm amplifiers and 1050nm amplifiers were presented by implementing InGaAs strained quantum wells in the GaAs/AlGaAs material systems [20]. Emissions at 1550 and 1300nm were usually achieved by implementing InGaAsP/InP material systems, while the 850n was achieved by the GaAs actives. Recently, reports on 1550nm band using different material systems such as AlGaInAs [26] and GaInNAsSb[27] in order to enhance the SOA performance (e.g. noise reduction, temperature performance enhancement) in the 1550nm. The 1300nm band also reported with diluted nitride (GaInNAs) [28].

As most of the semiconductor devices privileged over their counterparts, SOA size and volume production cost are considered their main advantages. Integratability with other semiconductor components as lasers, LEDs, or SLDs is opening a new field of applications especially when the coupling losses are minimized when the SOA is integrated monolithically.

1.5.1 Operation principle:

The simplest description for the SOA is that the input light signal stimulates the free injected carriers to recombine and emit photons coherent to the injected optical signal. Figure 1-8 explains the operation schematically.

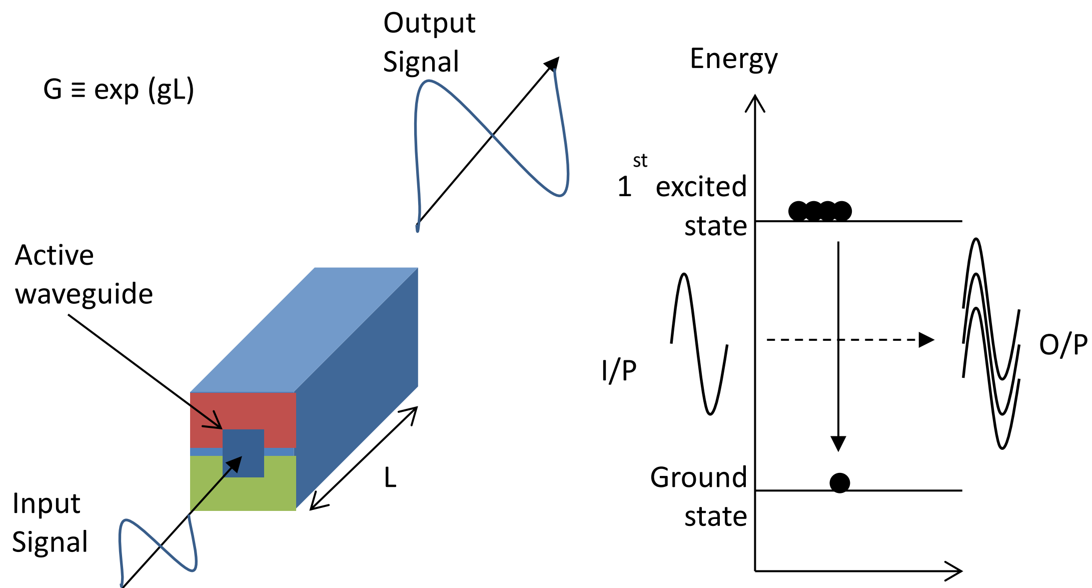

Figure 1-8: The simplest schematic diagram of the SOA showing a buried waveguide within a p-i-n junction (shaded red-blue-green) in which the input signal with intensity I_{in} enters the active waveguide and get amplified to the I_{out} output signal. The SOA gain, G, is the ratio of I_{out} to I_{in}. The device gain is related to the material gain, g, where ($G \propto gL$) such that L is the active cavity length. The right figure on the other hand is the two-level energy system showing that the amplification of the I/P signal to O/P is due to the transition of the excited carriers from the upper level to the lower level. Maintaining the population of the excited carriers defines the devices performance.

The gain relates directly to the device ability to produce spontaneous emission/amplified spontaneous emission which is the spontaneous emission rate R_{spont}. As the pumping current increases the gain at specific input power increases as we can see in all gain measurement done by developers [25], [29]–[33]. What happens when the input power increases is the thing that governs the modal limit of the device. The increase in the photon density (more optical power) of the input signal results in an increase in the free-carriers recombination according to the R_{spont} of the device, this increase will reach a point that the free carriers' population cannot maintain this rate so this rate will decrease and eventually reduce the gain provided. When the gain is decreased by 3dB from the maximum value it is called the saturation gain and the associated output power is donated as the saturation output power. Further discussion regarding the reflectivity reduction and device evaluation is presented in chapter 5.

1.6 Buried Heterostructure Lasers:

Isolating the medium carrying transmitted signals is a concept first developed in 1960 when International Telephone and Telegraph (ITT) Corp. developed what they called a cylindrical and flexible waveguide to be used in transmission of television, radio and telephone signals during heavy traffic periods [34]. This development enabled operation of a long distance service with a decreased number of repeaters. In spite of the fact that the whole technology is quite different from the semiconductor laser technology yet it was the first developed technology with a waveguide that is isolated from the surrounding environment.

Optical waveguides in the semiconductors capture light in a small cavity made of a semiconductor material of refractive index n_1 surrounded by a semiconductor material that has a refractive index n_2 such that $n_1>n_2$ (See Figure 1-9). This difference in the refractive index causes limited expansion of the optical mode outside the core by total internal reflection.

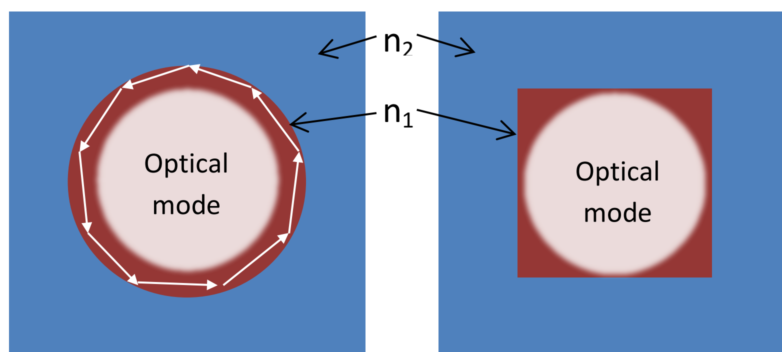

Figure 1-9: simplest Buried Heterostructure schematic diagram showing the two materials with different refractive indices and the optical mode confined

The semiconductor laser in the first 12 year of its development did not have a waveguide that is buried within the structure but they mostly tended to have a mesa (ridge) structure that operates by the difference in the refractive indices between the air (n=1) and the active semiconductor material (n> 1, n=f(λ)) [35][36]. The development of a buried stripe was delayed until the maturity of the heterostructure junction in

GaAs/AlGaAs material system. In 1974 Tsukada submitted a paper [37] demonstrating the first buried structure which was a GaAs filament in an n- and p- AlGaAs cladding. The fabrication process was very simple where grooves where etched chemically on the n-AlGaAs grown surface followed by growth of a few microns thick GaAs active layer and ending the structure with p-AlGaAs layer using liquid phase epitaxy (LPE). In the buried structure the optical confinement is realized through the step-index change between the core material (guiding) and the surrounding material and carrier confinement is realized through the n-p-n-p (i.e. a reverse biased) structure that effectively cancels the electric field at either sides of the active core. Tsukada described how the small lateral sizes gave rise to smaller current densities compared to the ridge devices presented at that time. With the help of Y. Shima, Tsukada presented a thermal characterization and compared it to an epi-side up mesa (ridge) waveguide laser [38]. Their study demonstrated superior characteristics of the buried structure and less sensitivity to change in temperature. Figure 1-10 shows a schematic representation of the structure Tsukada presented in [37] The structure was a simple pn junction of AlGaAs material with a GaAs filament in the middle which has a smaller bandgap, the operating wavelength of the device was 817nm.

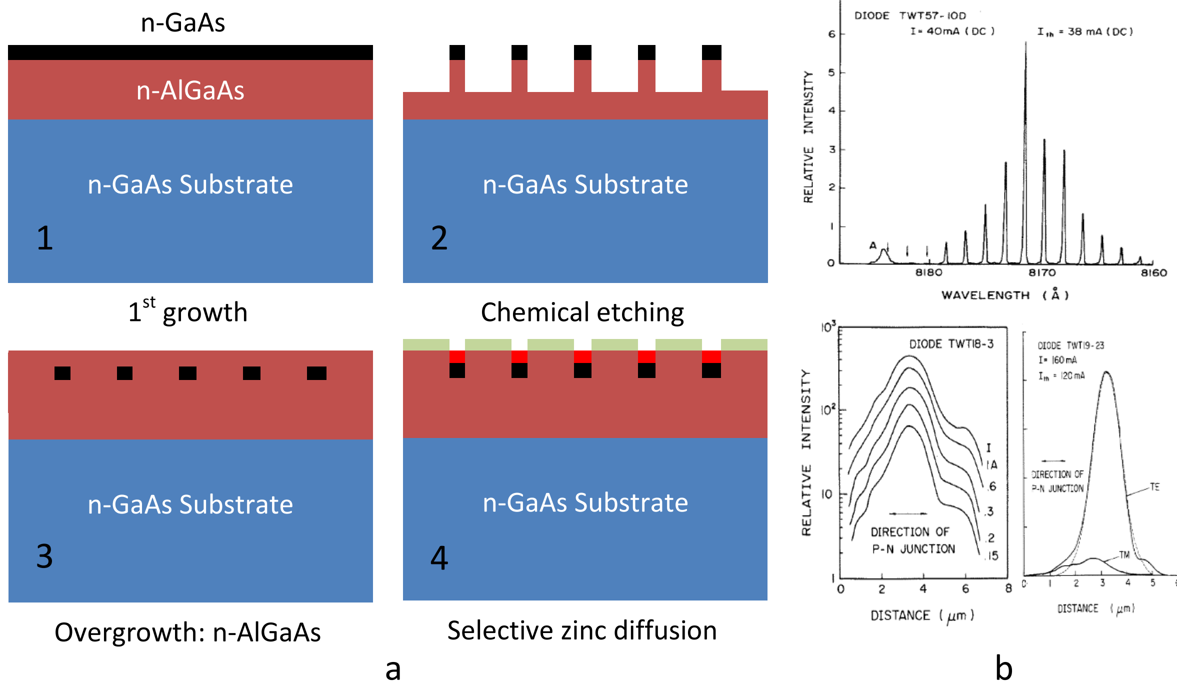

Figure 1-10: The processing of Tsukada's device (a) and the electroluminescence (EL) spectrum shows lasing (top (b)) and the farfield pattern which proved the single spatial mode operation [37].

The advantages of the buried heterostructure encouraged development of more complicated structures such as DFB laser by adding a grating to the structure to allow wavelength selectivity. Examples of such structures are described by Nakamura [39] and Burnham [40] in 1975 and 1976, respectively. The latter one was identical to Tsukada's structure but with the addition of a distributed feedback (DFB) corrugated layer closer to the p-side of the structure as shown in Figure 1-11a[40]. Buried heterostructure lasers were also realized with DBR mirrors at each end, as the one presented by Tsang and Wang in 1976 [41]. Successful wavelength selection was presented in this study which device structure is shown in Figure 1-11b.

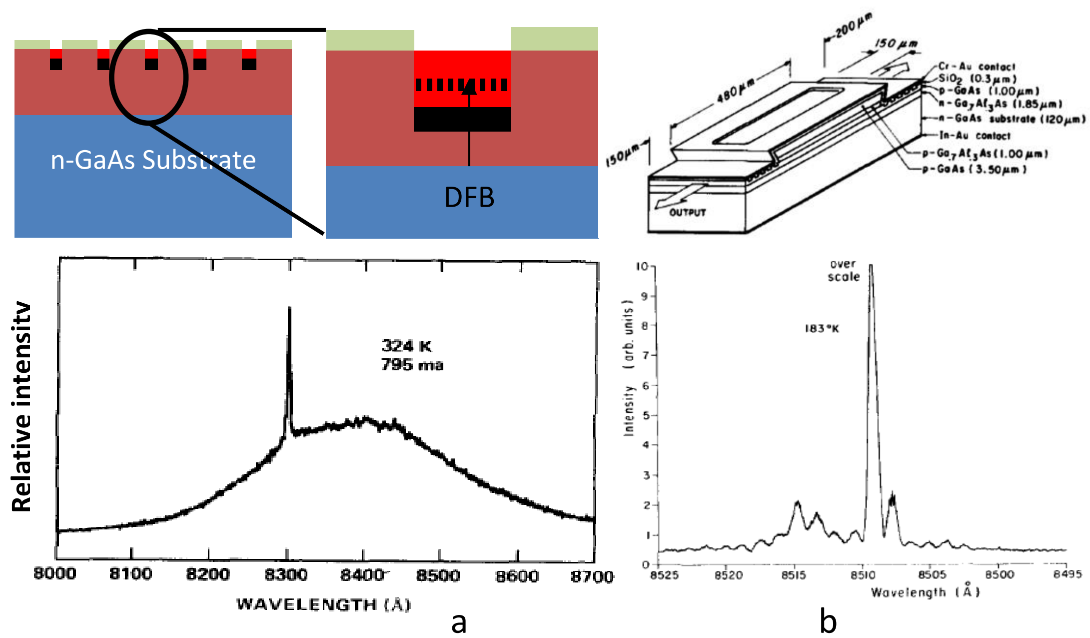

Figure 1-11: The same device presented by Tsukada [37] *earlier with integrated gratings. (a) Schematic diagram of the device presented by Burnham* [40] *and the EL below the diagram shows the wavelength selection and (b) is the device presented by Tsang and Wang with integrated DBR at each facet with the EL showing the wavelength singularity.*

A theoretical analysis of implementing the buried structure side-to-side with double heterostructure configuration suggested greater reduction in the threshold current density (J_{th}) [42]. Following that, Kirkby presented a simpler technique to process the buried heterostructure [43]. In this technique channels were etched in the substrate prior the growth of the whole laser structure, which enabled stripe formation without the need of growth interception. A simplified procedure can be explained in Figure 1-12a, first the n^+-GaAs substrate was etched down first to provide grooves with specific widths which would be the active stripe widths. Following chemical etching, (n-AlGaAs, p-GaAs, p-AlGaAs, and p^+-GaAs contact layer) were grown successively by LPE. As a result of the substrate etching, the active p-GaAs will be surrounded by n-AlGaAs from 3 directions and topped with p-AlGaAs (see Figure 1-12 b), limiting the recombination to the stripe area.

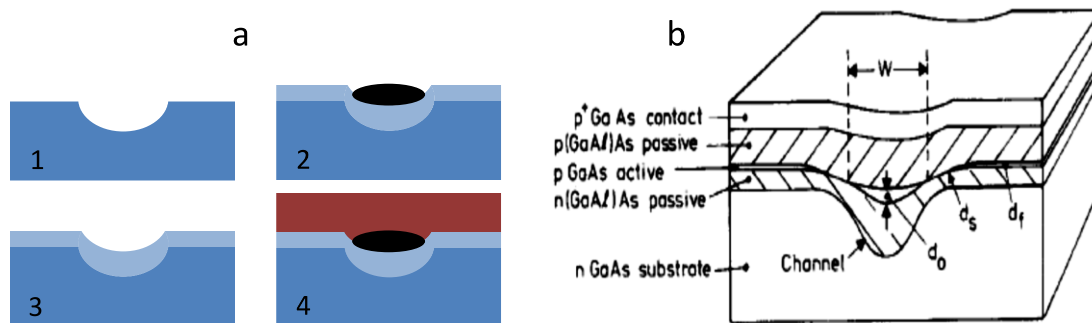

Figure 1-12: A schematic diagram of the channelled substrate buried laser presented by Kirkby and Thompson [9] where (a) is the growth process starting with chemical etching (1) then depositing the n-AlGaAs layer (2), later depending on the substrate tomography the p-GaAs active is grown (3) and finaly the top p-AlGaAs. (b) showing the schematic diagram of the grown devices.

A number of articles described the superiority of buried stripes over other laser structures, such as that by Takahashi *et.al.* [44], which directly compared between buried structure and the stripe lasers, and the more comprehensive reviews provided by Panish [45] and Tsukada *et.al.* [46]. This study opened a new field of interest around the buried heterostructure laser different structures, growth methods, and operating conditions where demonstrated over the next 10-15 years. Buried heterostructure technology was first demonstrated in the InP-based system by Hsieh and Shen in 1977 [47], who compared the “new” technology with oxide and proton bombardment defined stripes that were common at the time. The new platform enabled the device to work at the wavelengths offering the minimum absorption/dispersion in the glass fibres and development of buried heterostructure in these wavelengths had much of attention in the telecoms developments over the subsequent decades. The buried structures showed a decrease in the threshold current density to half the value required for the oxide defined geometry, with a differential quantum efficiency of 10%.

Efforts were made to enhance the buried structure by adding more elements to improve the optoelectronic confinement in both vertical and parallel directions. One of the earliest reports by Tsang and Logan [48] demonstrated a buried structure incorporating a reverse biased pn-junction at either sides of the stripe to provide

electrical confinement. The new methods used in this design is that the two reverse biased pn-junctions in order to limit the current spread along the whole from top to bottom as shown in Figure 1-13 below.

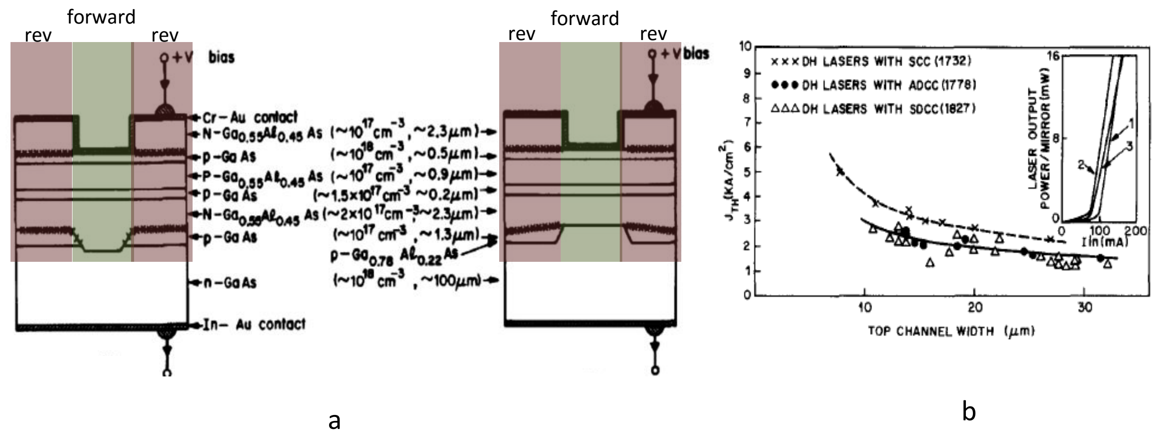

Figure 1-13: Tsang and Logan device showing the biased area, where red shaded areas were reversed biased and the green ones were forward biased. (b) shows the threshold current density as a function of the channel width with the inset showing LI curves of the devices as published in [48].

They presented two configurations to achieve current confinement via the two pn junctions. The authors proved that the precise alignment of the two junctions (or the two stripe regions) did not have a significant effect on the device performance. This was proven by making a shift of 10μm between the top and bottom stripes in a group of the devices, Figure 1-14 b shows that the two groups of lasers were identical.

M.J. Adams [49] presented an analytical study of the optical waveguiding in both vertical and parallel directions, which can enable the single mode operation of the laser system if the structure was tuned properly. This became the main method goal to be achieved by the following enhancement presented to the buried heterostructure in the AlGaAs material system. In addition to that the fact that a small refractive index step could benefit toward a single mode operation more than the high step by releasing the higher order modes to the material outside the stripe rather than capturing them into the active stripe. Since then different methods were developed to achieve this sort of optoelectronic confinement in the system. The main method used is to change the

effective refractive index of a number of layers rather than relying on the actual refractive index between two materials as in Tsukada's design. The effective refractive index of a material was found to be affected by the thickness of the material; this concept was implemented by Ito [50], they presented a laser structure that contained only AlGaAs material with different AlAs mole fraction. In this structure the inner layers were made of $Al_xGa_{1-x}As$ layer (x=~0.25) and the cladding layers were made of an $Al_xGa_{1-x}As$ with an x value of ~0.4 while the active was $Al_xGa_{1-x}As$ of x=0.1 to produce a laser that can operate in the ~850 nm. The measured LI curve was recorded with no kinks up to $2\times J_{th}$ which was the maximum achieved until that time.

Another method to achieve single mode operation was by absorbing the higher order modes. An example of this was presented by Aiki *et.al.* [51]. In this structure GaAs/AlGaAs structure was grown on a grooved n^+-GaAs substrate but, unlike the channelled substrate laser (CSL) mentioned earlier, the layers were planarized rather than transferring the depth variation to the upper layers. This resulted in a similar expansion of the optical modes along the active layer. Because of the difference in the GaAs substrate between the in-stripe and out-of-stripe areas, the optical mode was absorbed in the areas outside the stripe as shown in Figure 1-14. This is because the GaAs was actually absorptive to the lasing wavelength produced here (~850nm). This configuration achieved single mode operation and stable LI with no kinks up to $2J_{th}$.

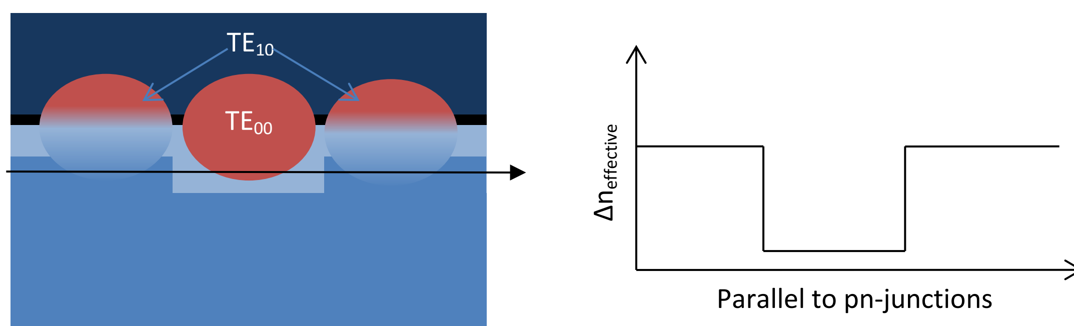

Figure 1-14: Schematic diagram of the laser structure published in [51], *the elimination of the higher order mode was done by absorption of the higher order modes since they would be located where the GaAs substrate was closer to the GaAs active.*

Wang and Figueroa presented a structure that could achieve optoelectronic confinements via a structure referred to as an Inverted Ridge Waveguide IRW [52]. This structure was tested with two sets of dimensions with 8×30μm^2 and 3.5×6μm^2 (d×w). The structure was grown in two steps LPE, first, p- and n-GaAs layers were deposited on the n$^+$-GaAs substrate, then, the wafer was patterned and etched to the required widths, the etching was performed from the n-GaAs grown layer to the n$^+$-GaAs substrate. Following the etching, n- and p-$Al_{0.7}$GaAs guiding layers, sandwiching the GaAs active layer, were grown and the structure is finished by adding the contact p$^+$-GaAs layer. The final structure is shown in Figure 1-15 below with the p-n-p-n layer is highlighted on the sides of the IRW.

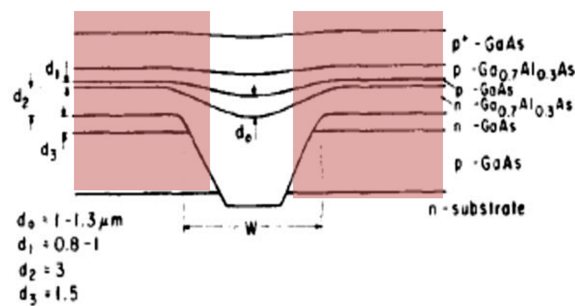

Figure 1-15: Schematic diagram of the device presented by Wang and Figueroa [52]. *The red highlighted regions are the regions where current blocking is performed by p-n-p-n junction.*

The structure provided a good optoelectronic confinement, however, high threshold current densities were exhibited compared with the other reports as a result of using bulk actives where the active GaAs layer thickness varied between 1-1.3μm.

One of the early examples of the use of different materials in the GaAs-platform to grow semiconductor laser structures was the incorporation of a small concentration (~1%) of phosphorous in the GaAs alloy to produce a high resistance polycrystalline GaAsP layer for carrier confinement. This was the main point presented by Itoh [53] in which they showed that creating a layer of $GaAs_{1-x}P_x$ ($0 \leq x \leq 0.01$) under a specific pressure conditions resulted in an increase in the layer resistance to 3 orders of

magnitude compared to that of a pure GaAs layer. They found that setting the arsine (AsH_3) pressure to 11.4 times the trimethyl-gallium (TMG) pressure results in a series resistance of the GaAsP layer of 5×10^3. This 1% of phosphorous does not cause a large lattice mismatch to GaAs and so did not affect the crystallography of the whole structure for the chosen layer thicknesses. The whole laser structure of GaAs/AlGaAs containing the required optical confinement layers were grown first, then a ridge mesa was etched chemically and the $GaAsP_{0.01}$ layer was overgrown to planarize the structure, as shown in Figure 1-16 a, using MOVPE. Following this the contact p^+-GaAs layer was grown to complete the structure. This configuration was one of the first high linearity, low threshold current examples where the threshold current density was four times lower than a reference dielectric-defined stripe laser of the same material, as shown in 16 b. Linear LI was exhibited up to several multiples of threshold current density.

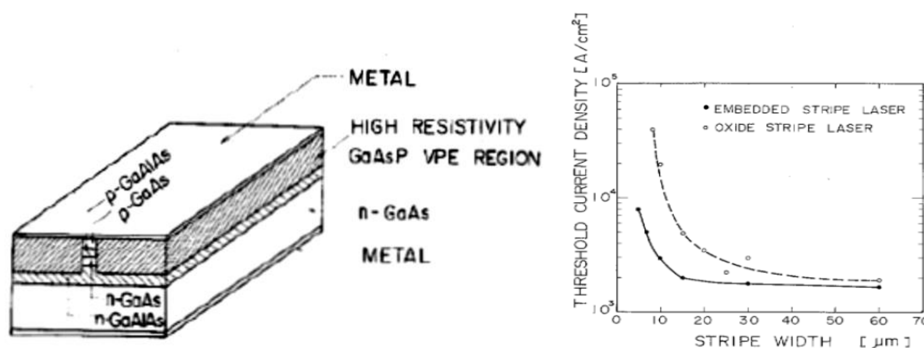

Figure 1-16: Embedded-stripe laser structure as published by Itoh [53] *and the comparison in the threshold current reduction between the embedded-stripe laser and the oxide-stripe laser as a function of active stripe width.*

The easiest way to achieve electronic confinement only is to rely on different types of doping in the same crystal. A study was presented by Lee *et.al.* in 1978 [54] concerning the zinc diffusion speed with respect to the aluminium composition in AlGaAs alloy and compared it to GaAs as a reference. It was found that by changing the Al composition from 0 in GaAs to 0.7 in $Al_{0.7}GaAs$ the diffusion depth was changed

from 1.5μm to 5-6μm under the same conditions. The study showed large uncertainty for Al-compositions > 0.5 yet two trends could be expected from the study. For moderate temperature the diffusion depth started to level-up and even decrease, whilst at higher temperatures case with a short contact time or a low temperature with long contact time the diffusion tended to expand even more and can be expected to reach ~8μm.

Changing the shape of the channel etched in the substrate, and consequently the active stripe, can improve the beam quality of the output laser due to the enhancement of the optical confinement. This was proved by Wang and Figueroa in their paper presented in 1978 [55] when they used different etchant to form their IRL structure. This caused the resulted channel to have a curved shape rather than a squared shape. This improved the confinement since the circular beam shape can fit better in the circular channel. This increased the confinement factor to a point where ~90% of the beam overlapped the active region, where losses were minimized for the operating wavelength. Farfield and spectral measurements proved the single-mode behaviour of the device both in horizontal and vertical directions with respect to the growth axis. Again, the electronic confinement in this IRL structure was provided by the p-n-p-n junction at either side of the stripe.

The challenges at that time that faced the buried heterostructure in GaAs/AlGaAs system was the low power since the output power is proportional to the active stripe width, which were typically ~1μm to maintain single mode operation. Tsang presented a laser structure that benefited from a moderate Al composition between the active GaAs and the burying high refractive index material, where the Al-composition was $0<x\leq1$[56]. Figure 1-17 a shows a schematic diagram of the laser structure presented

and highlighting the new guiding layer added and the LI curves for a group of identical devices are shown in Figure 1-17 b.

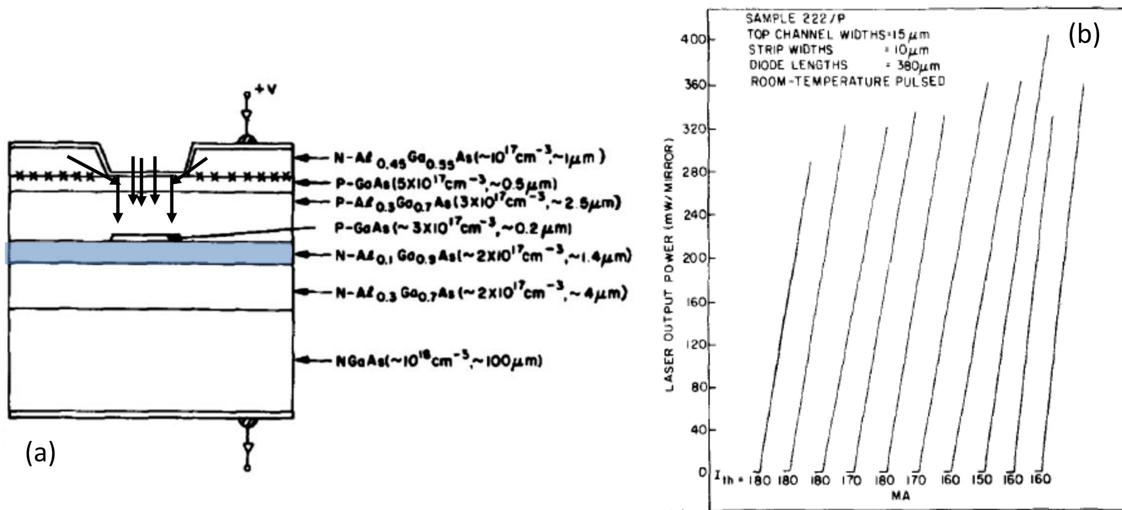

Figure 1-17: the laser structure presented by Tsang in [56] *(a) and the LI curves of identical devices had an active stripe of 10×380μm² (b). A record output power of 260mW with single longitudinal and transvers modes.*

This separate confinement heterostructure laser operated in the fundamental mode over a wide range of pumping current and this led to the demonstration of the first “high power” buried laser as shown in Figure 1-17 b. A Pulsed output power as high as 260mW was recorded from devices with 10μm wide buried stripe with a single mode operation in both transverse and longitudinal directions. To provide the electronic confinement for the device an n-AlGaAs was grown and a stripe etched on the top of the device before the metallization.

Aiki *et.al.* presented a more comprehensive study of buried heterostructure lasers with channelled substrates in [57], in which theoretical calculations proved the relationship between the active thickness and width with both the effective refractive index and the internal losses for buried heterostructure laser operating at 830nm.

The main limit to the output power in GaAs/AlGaAs laser was the COD due to oxidation of aluminium containing layers that were exposed at the facets and/or the dislocation that occurred in the crystal structure due to the increase in the junction

temperature up to the melting points as a result of the very high optical flux intensity at the facets. Various solutions to overcome this problem were presented. One of the earliest was the buried facet structure presented by Takahashi *et.al.* when they presented a standard stripe geometry configuration laser structure with actives terminated prior to the facet [58]. The structure was simple, with no optical or electronic confinement applied. The devices were grown in common two-step LPE method in which portions of the active p-GaAs were etched down to the n^+-GaAs substrate prior to regrowth as shown in Figure 1-18. The resulted wafer had lines of active p-GaAs separated by 150µm window regions in which no GaAs was grown. Three different structures were evaluated 1) a standard stripe laser device with no unpumped windows at the facets, 2) a device that had an unpumped window at one of the facets, and 3) a device that had unpumped windows at each end. The results plotted in Figure 1-18 showed improvements in lasers with buried facets, which were not affected by the environment, as the standard lasers (Type 1) were. Lasers with no buried facets or one buried facet experienced increase in the threshold current after being boiled in DI water, while the buried facet devices showed a constant threshold current throughout the experiment [58].

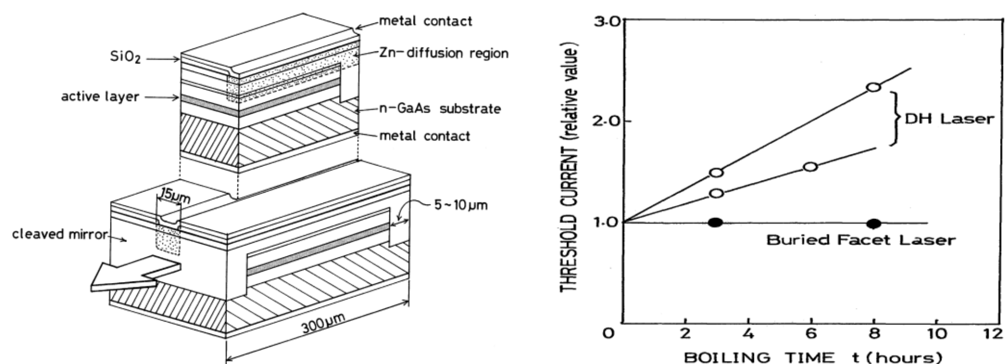

Figure 1-18: the structure of buried facet laser device presented by Takahashi [58] (left) and a simulation of facet damage by boiling the device in deionized water (right). The figure showed protection of the device facet by burying them.

Kano *et.al.* demonstrated a laser in the 1.3-1.6µm wavelength region where the fibre loss is minimized [59]. The device comprised an InGaAsP active with InP burying layer

which provided the current confinement. The demonstrated structure could operate via CW operation at room temperature with 60mA I_{th} (equivalent to 4kA/cm^2) with 9mW output power at 120mA and differential efficiency of 14%.

Single mode operation was achieved not only by the index-guided structures but also by using gain guiding. An example of this was demonstrated by Bar-Chaim *et.al.* [60], in which they used ion implantation (Beryllium was used as doping ion) to confine carriers to specific areas in which was limited to. Outside of this, absorption by unpumped active material resulted in loss, confining the optical mode to the gain region. By comparing different Be-doped Al-compositions with different annealing temperatures and junction depths, parameters for achieving minimum surface resistivity were determined. A 3.5×125µm^2 device had a low threshold current of 21mA (pulsed) and output power of 10mW with differential efficiency of 45%. A 2.3µm FWHM spot size was obtained for 3.5µm stripe width.

R. Lang suggested [61] that the three main mechanisms for mode instability were spatial hole burning, negative dependence of refractive-index on the carrier density, and lack of the perfect symmetry in the laser structures due to the poor growth control in LPE compared to Metal Organic Vapor Phase Epitaxy (MOVPE) and Molecular Beam Epitaxy (MBE), and the presence of >100µm thick GaAs substrate on the n-side of the device. Since the development of (MOVPE) as a crystal growth offering superior control on layer thickness and doping concentration compared to LPE, improved device characteristics could be demonstrated.

Zinc diffusion was commonly used to produce buried double heterostructure lasers. Studies showed controllable diffusion under dielectric masks. In such cases only a single epitaxial growth was required to complete the growth and diffusion is used to produce the pn junction in the structure. A number of publications studied the effect of

diffusion on the refractive index of the device such as that discussed by Ueno and Yonezu [62] who formed a pn-junction stripe in a planar of a structure with all n-doped layers except the contact layer which was p^+-GaAs. Following the growth, p-doping was provided by zinc diffusion through a mask of SiO_2. By increasing the doping levels in the layers a step-index was formed between the n- and p-doping. This step provided the optical confinement required for single mode operation, with fundamental mode operation measured using nearfield, farfield, and EL measurements. When the device was doped selectively to p-type in the middle and n-type at either side, a gain-guided type buried stripe was formed similar to the devices demonstrated by Bouley *et.al.* [63] and Thompson *et.al.* [64]. In the first one, the gain guiding was not achieved by zinc diffusion only but by using the proton implantation applied to the areas around the stripe to increase the resistance and decrease the leakage current. This configuration resulted in a laser with I_{th}=35mA for a 12×150μm^2 device. However, the optical confinement was insufficient to result in single mode operation to high power levels.

To overcome the problem of COD, a window structure was used in a similar manner to that presented by Takahashi [58] but here using selective zinc diffusion to define the active stripe. Yonezu *et.al.* [65] demonstrated devices with 5 or 10μm active width and 250μm length in addition to a 100μm separation between the devices in the processed wafer which formed the window used to protect the facet. The key factor in this study was the use of gain control via the doping level. The high doping level in the active region resulted in high differential quantum efficiency and a very high pulsed output power (1.5-1.8 W).The reduced difference in the doping concentration lowered the COD threshold of the device to 700mW of the same device configuration. Figure 1-19 shows the main results achieved. The pulsed power was measured up to a maximum of 1.5W. Darklines defects appears in the SEM images resulted from the dislocations in

the crystal structure caused by the sudden increase in the optical power density (localized heating).

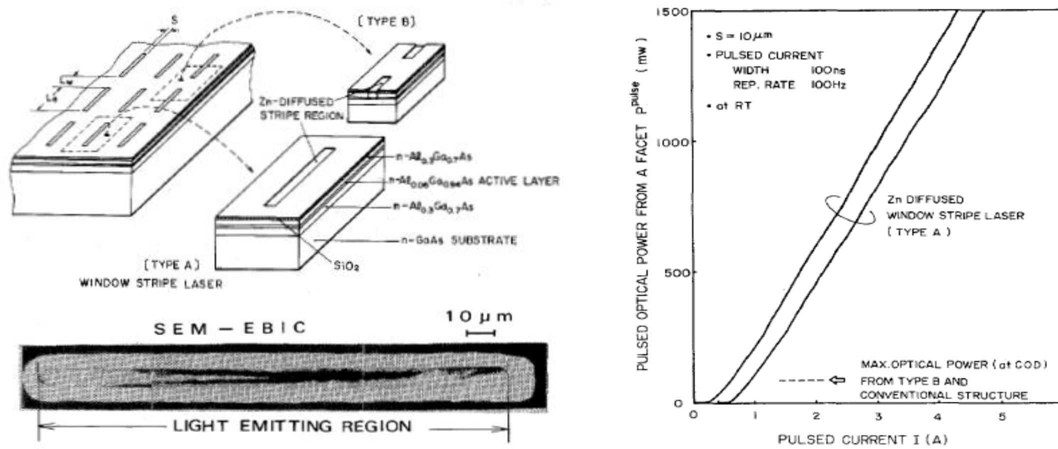

Figure 1-19: The window structure laser presented by Yonezu [65] where stripes are opened and different configuration can be achieved. The SEM image shows the dark line defects in the low doped light emitting region (~1E18 cm^{-2}) device. The LI curve is the one recorded for the highly doped (1E18 cm^{-2}) in which an output power of 1.8W was achieved.

In the late 1970s, the main motivation for buried heterostructure laser was associated with application of semiconductor lasers in optical communications. The fact that buried heterostructure (buried stripe) lasers provide the best geometry for optical fibre coupling. Nakamura's and Hakki's papers are good examples of theoretical studies into operation stability. Nakamura focused on the design aspects and available geometries that could present stable single mode operation, and the pulse response of the devices [66]. Hakki presented a theoretical study on the factors that cause mode instability in the buried stripe lasers [67]. Gain saturation in the active medium was found to affect the mode stability directly, where devices with unsaturated gain worked more stable than devices with saturated gain as the internal feedback loop can be affected by gain saturation.

Kano and Sugiyama presented an InGaAsP/InP buried stripe laser emitting at 1.3µm [68]. The process used to achieve the buried structure included two LPE growths interrupted by etching to define the optical waveguide. Low threshold current ~60mA

was recorded in both pulsed and CW operation at room temperature, which increased to ~120 and 160mA for the pulsed and CW operation, respectively, for ambient temperature of 85°C. The maximum CW output power recorded was 40mW with differential quantum efficiency up to 24% per facet.

Tsang *et.al.* [69] developed an enhanced melt-back overgrowth technique to achieve an improved interface between the grown layers. This resulted in a threshold current decrease to 70mA from the 180mA I_{th} reported in an earlier version. This enhancement enabled the authors to integrate DFB gratings on both sides of the active stripe to limit the higher order modes which otherwise appeared in high power operation. The structure provided the transverse optical confinement of the buried heterostructure, as well as a longitudinal mode selection through the DFB grating [70]. Single longitudinal and transverse mode lasers were demonstrated up to $3\times I_{th}$, and wavelength tunability over the temperature range between 0 to 35°C. In early 1980 Tsang and Logan applied the newly developed (MBE) technology to produce buried heterostructure lasers by a hybrid growth method [71], as shown in Figure 1-20. The initial double heterostructure was grown using MBE then, after the mesas were defined, LPE was used under enhanced conditions developed earlier to produce high quality interfaces between the MBE and the LPE grown layers. This resulted in very low threshold currents compared to the earlier versions of this structure, with 15mA and 26mA I_{th} and 68% differential efficiency recorded for 250 and 360µm long lasers both with 5µm wide active stripes, as shown in Figure 1-20. The uniformity of the heterostructure layers, through use of MBE, played a major role in this reduction.

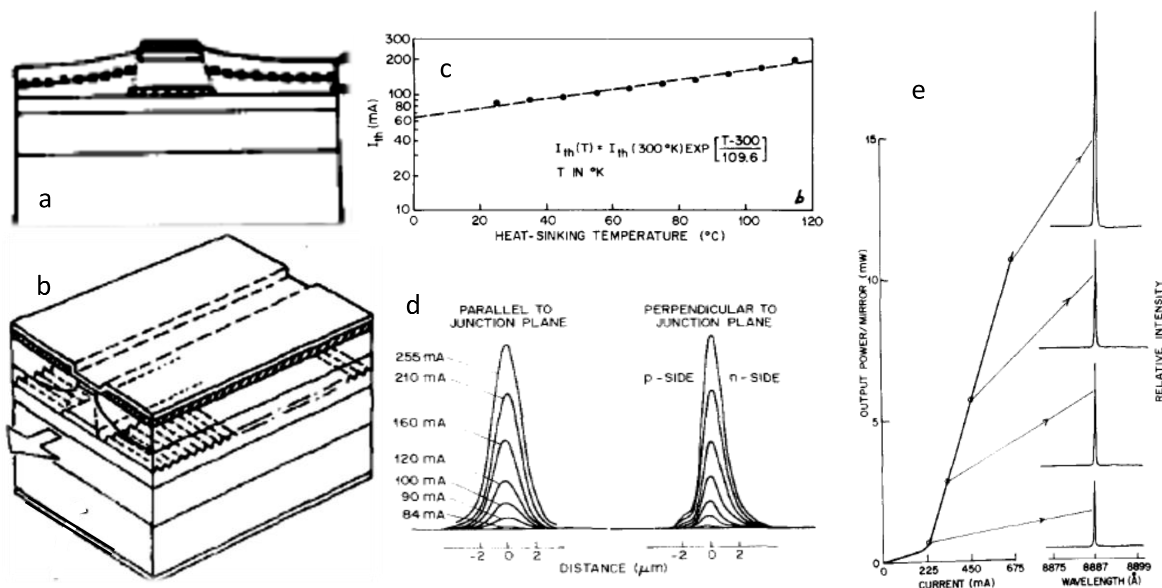

Figure 1-20: The buried structure that was grown by the melt-back method developed by Tsang where (a) is the standard buried stripe and (b) is the one with integrated DFB gratings. (c) is the threshold current as a function of ambient temperature for the buried device in (a) while (c) and (d) are the nearfield pattern and the LI and EL measurements for the DFB integrating devices, respectively.

The strip-buried heterostructure was the most common buried laser device configuration used at that time to produce single mode lasers in optical communications systems and optical disc read/write. The stripe-buried heterostructure design was presented by Nelson *et.al.* [72] grew an InGaAsP/InP junction upon an InP substrate. Through use of a Si_3N_4 mask, a mesa was chemically etched before layers of n- and p-InP were grown by LPE melt-back to bury the stripe and provide enough optoelectronic confinement. In spite of the fact that the threshold current was still relatively high ~120mA for a 5×120 μm^2 active area, a single-mode output power up to 100mW and 500mW maximum output power before thermal roll over were recorded.

Most of the stripe laser structures presented includes dielectric mask deposition. This mask needs to be removed completely and leave clean semiconductor material in order to obtain very low series resistance when the p-contact is processed. In fact, this process always has a possibility of leaving some contamination on the device surface, which will affect the electrical features of the device and might result in a relatively high series

resistance. Self-aligned stripe are commonly processed through two-step growth process interrupted by etching process without the need for any post growth dielectric deposition. Figure 1-21 shows a simplified version of a self-aligned stripe laser showing the upper and lower cladding separated by the current confinement layer.

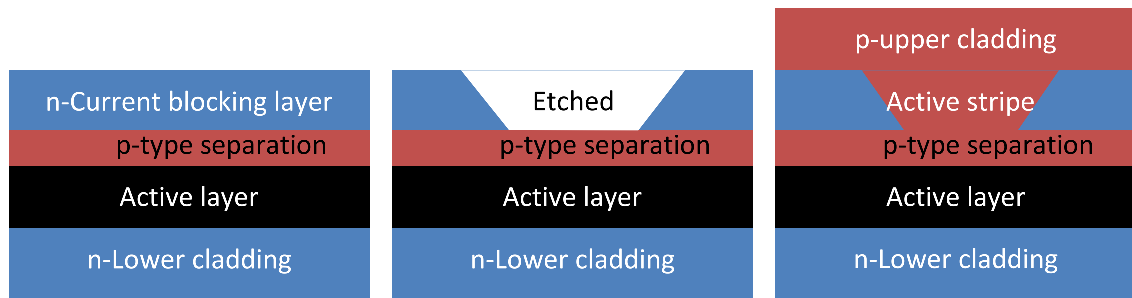

Figure 1-21: simplified schematic diagram of self-aligned stripe buried waveguide. (a) 1st growth stopping at the current blocking layer. (b) etching through the current blocking layer. (c) the overgrowth of the upper cladding.

An early example of the self-aligned stripe devices is the one demonstrated by Coleman and Dapkus [73] which they presented it in the AlGaAs/GaAs material system. The wafer was grown by a two-step MOCVD method. An undopped GaAs active of 70nm was grown between upper and lower cladding, followed by etching and regrowth to complete the structure. The threshold current was 75 and 90mA for pulsed and CW operations, respectively, of a 450µm.

The main problem associated the use of two-step epitaxy methods for realization of buried waveguides in GaAs is the oxidation of the Al-containing layers when exposure to atmosphere following the etching and prior to the overgrowth. Solutions like the one suggested by Yariv *et.al.* when a single LPE growth was developed to overcome the oxidation problem [74]. This process started by depositing and etching Si_3N_4 slabs for selective area growth. The selectivity caused the structure to have pyramid-like shape with a flat top to enable the contact. The elimination of any oxidation resulted in a better interface, which led to low I_{th} ~9mA for150µm and high characteristics temperature up

to 175°C, and a differential quantum efficiency of 45%. Single mode operation was observed up to 12mW/facet.

Chinone *et.al.* presented a buried heterostructure laser that is very similar to the separate confinement heterostructure (SCH) laser [75] in which additional layers were inserted, sandwiching the active layer, the proposed structure is shown in Figure 1-22 a. These additional layers had a larger refractive index than the index of the cladding layers and smaller than that of the active region in causing Δn to be decreased from ~0.4 to ~0.1 for the operating wavelength of 850nm. The threshold current for this device was ~25mA for a 2.5×300μm^2 device and a highest differential quantum efficiency of 85% was recorded as shown in Figure 1-22 c.

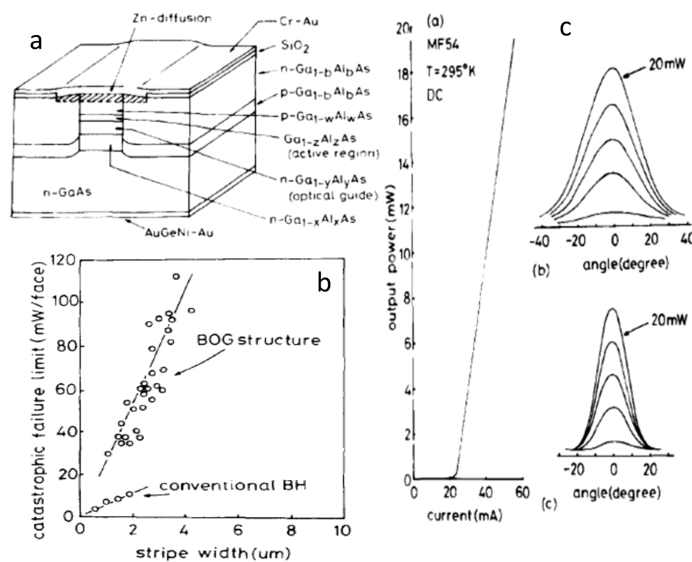

Figure 1-22: A schematic diagram of the buried optical guide laser presented by Chinone [75] *(a), a COD comparison between the conventional buried heterostructure and the presented lasers, and (c) the primary results showing the LI of the device and the vertical/horizontal farfield of the device which proved single-mode operation.*

This technique was also used by Saito and Ito with a thinner active layer [76]. Their structure, shown in Figure 1-23 a, was more similar to the SCH used today. With fine-tuning of the layers the device could operate with threshold current as low as 5mA with an increase in the COD up to 120mW/facet due to the accompanying increase in spot size and the corresponding decrease in the optical density at the facets. The devices

presented in [76] showed single-mode lateral power scalability with stripe width. Figure 1-23 shows the structure presented both in Chinone [75] and Saito & Ito [76]with some related performance Figures.

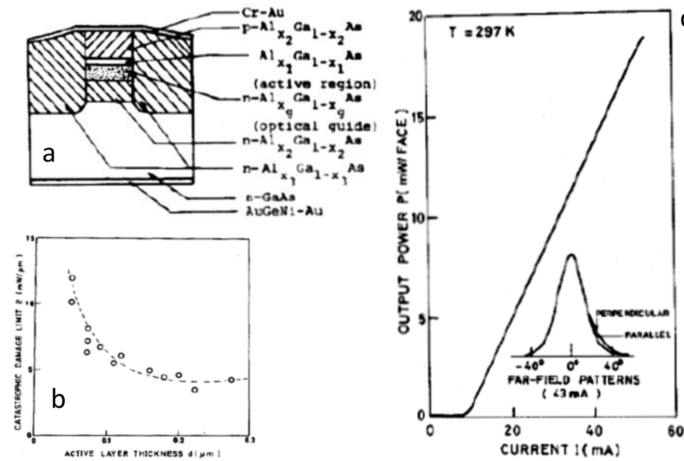

Figure 1-23: The BOG device presented Saito & Ito [76] *is shown in a, the increase of the COD threshold power can be seen in b and fundamental mode operation was achieved as can be seen in c.*

Ishikawa *et.al.* [77] presented an enhanced waveguide called the separate multi-clad layer (SML) stripe geometry laser in the GaAs/AlGaAs system. Wave guiding in this structure was based on the step refractive index (effective refractive index) in the layered material to divert the light to the stripe rather than absorbing the higher order modes, in order to achieve single mode operation. The authors compared this configuration to the self-aligned stripe laser. The SML structure enabled the device to work with a fundamental mode + leaky modes. The improved waveguiding enabled the device to work in single mode up to 20mW with a threshold current of 60mA for a device measuring 200µm long and 5µm wide. These devices presented by Chinone *et.al.* [75], Saito and Ito [76], and finally Ishikawa *et.al.*[77] all employed the Separated confinement Heterostructure SCH.

Following the implementation of a guiding layer offering refractive index between the high index of the active and the low one of the cladding layer as the lasers shown by Ishikawa *et.al.*[77] and Saito & Ito [76] which gave more stability to the optical mode,

Tsang and Logan added a graded index layer and used it as a separate confinement layer [78] by putting an AlGaAs layer with gradual increase (or decrease) in the Al-composition. Figure 1-24 shows the difference between the step index SCH and the graded index SCH. Using the graded index SCH, A threshold current as low as 2.5mA was achieved. The growth method was a hybrid technique between MBE growth of the planar wafer and LPE used to overgrow the burying layer. MBE provided the required control for grading the SCH composition and thickness, as well as the better surface uniformity for the laser structure, while LPE provided the route to create the n-p-n blocking layer. A differential quantum efficiency of 80% was demonstrated.

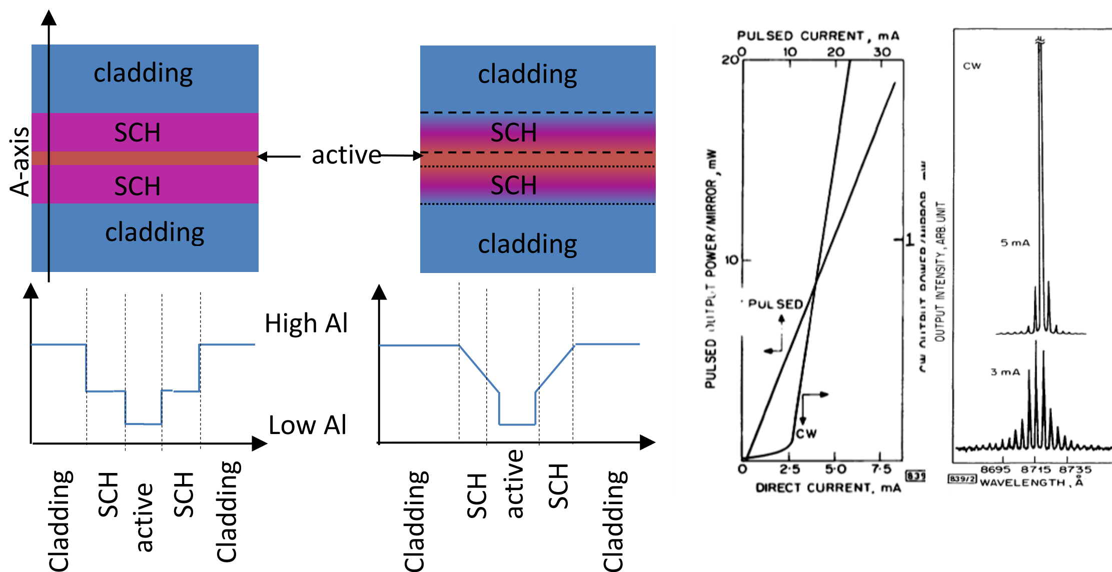

Figure 1-24: A schematic diagram showing the difference between the step-index SCH and the graded index SCH structures (left) and on the right are the LI (pulsed and CW) and the EL measurements of the low threshold current buried heterostructure laser presented by Tsang [78].

Tsang, Logan and Ditzenburger demonstrated in 1982 a buried structure that could emit multiple wavelengths, which could be of use in WDM [79]. The multimode operation could be achieved by tilting the active waveguide by θ° in order to decrease the effective reflectivity of the facets and cause the radiative transitions to result be from multiple energy levels rather than one. They used similar structure reviewed earlier [71]. Tilting the active stripe by 5° with respect to the normal to the facet was sufficient to

destroy the optimum coherence normal to the facet and allow competing spectral modes oscillating in the cavity to be amplified. The proposed device and he associated results including LI curves, EL spectra, and the farfield patterns are all shown in Figure 1-25. Single spatial mode operation was maintained in this device since the active stripe was a few microns as can be seen in 26 b. The differential efficiency was improved by inclining the active stripe by 2.5° and 5°, as shown in 26 c, due to the marginal decrease in the facet reflectivity, this reduction allowed more optical energy to escape the device. A successful multimode operation was observed via the EL measurement as shown in 25 d

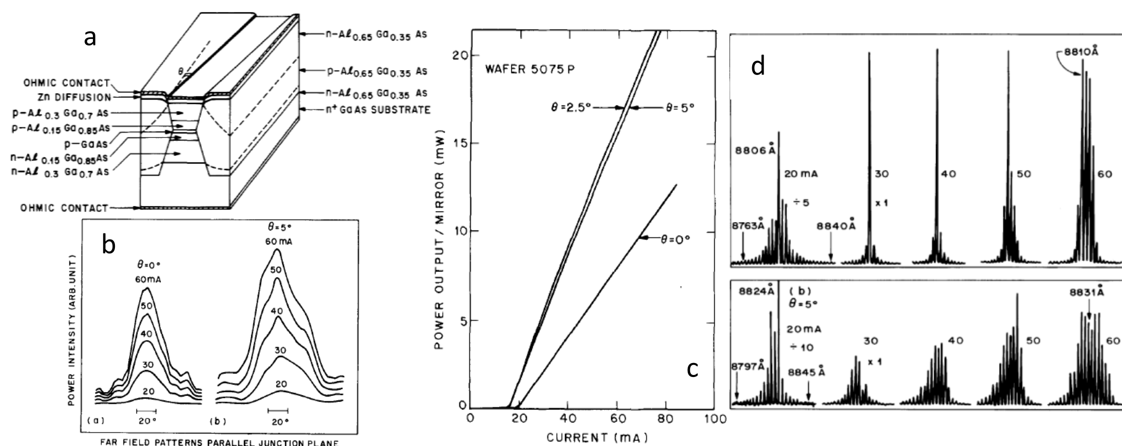

Figure 1-25: The tilted cavity buried laser configuration is shown in (a) with single mode operation is shown by the farfield pattern shown in (b), a comparison between devices with cavities tilted 0°, 2.5°, and 5° with respect to the cleaved facets (c). The EL spectra measured at a range of pumping currents (d) shows the benefit of tilting the cavity to achieve multi spectral mode.

With the advent of improved uniformity, interference quality, and control of MOVPE and MBE compared to LPE. Performing a structure fully grown by MOVPE or MBE became a priority. An early example was that demonstrated by Milano *et.al.* [80], who used metalorganic chemical vapour deposition (MOCVD) twice to grow a buried heterostructure laser. Enhancement of the surface morphology and the growth interface between the two growth steps enabled leakage current to be minimized and the optical quality of the structure to be improved, leading to threshold currents of 9mA for

6×250μm^2 sized laser (compared to 45mA of a similar structure and dimensions grown using a hybrid or just LPE). Another example of buried structures grown by the newer technology was the twin-channel structure presented by Ackley and Hom [81] which was grown using MOVPE. This was a simple structure of P-I-N diode laser grown on an n$^+$-GaAs channelled substrate. The channels were v-grooves obtained by selective etching in the <111> plane. Similar to the earlier examples, the optical confinement was achieved using very low refractive index material (air) adjacent to side of the active stripe, forming cladding layers , which is in addition to the high Al-composition layer above and below the optical mode in the centre of the waveguide. Ion implantation outside the grooves limited the current injection to the central area, as shown in Figure 1-27. The device exhibited single mode operation. The uniform and controllable growth using MOVPE enabled active layer thickness as thin as 50nm (one of the thinnest available at that time) which allowed the threshold current to be decreased down to 40mA for a 2×300μm^2 sized device. Application of asymmetric AR-coating of Al_2O_3 increased the COD threshold power up to 80mW/ facet (47mW/μm).

Tsang *et.al.* reduced active layer thickness down to 25-30nm [78] essentially using a quantum well (QW). The main benefits of this were the low threshold current which was <5mA and high differential efficiency, which resulted from the high electrical-optical conversion. Thornton *et.al.* realized buried heterostructure lasers incorporating multiple QWs [82]. In this structure the electrical confinement was achieved through use of impurity diffusion method in which Si was diffused to a specific area around the active stripe and by raising the diffusion temperature to ~850°C for 7 hours the 5QW active area was disordered and its resistivity increased.

Another example of the single step epitaxy trials similar to Yariv's device described earlier [74] using LPE growth is the device presented by Yoshikawa *et.al.* [83]. In this

device MOCVD was used to benefit from the mass transport phenomenon to grow the device upon the ridge-etched substrate. The first step was to form the undercut ridge profile by chemical etching. Following this, the wafer was entered the MOCVD reactor and the growth was completed by growing a buffer n^+-GaAs layer, then the GaAs/AlGaAs P-I-N structure of an active between two cladding layers. Figure 1-26 shows an SEM image of the grown device and some of the related results including LI, Farfield, and the threshold current as a function of temperature. If the growth was stopped at this point it would be easy to notice that two regions were created 1) on the ridge which formed the active stripe in the final structure and 2) the exact same structure adjacent to the ridge which was electrically isolated by the n-AlGaAs burying layer. To achieve this, the ridge height should be > the thickness of the cladding/core/cladding structure. An n-AlGaAs burying layer covered the structure and the growth was completed with an n-GaAs layer to protect the whole structure from oxidation. Selective Zn diffusion above the formed stripe p-doped this area and provided the current confinement required. The presented structure operated via the fundamental mode with ~30mA threshold current for $2\times250\mu m^2$. The characteristic temperature, T_o, was 190°C, indicative of excellent crystal growth using this method.

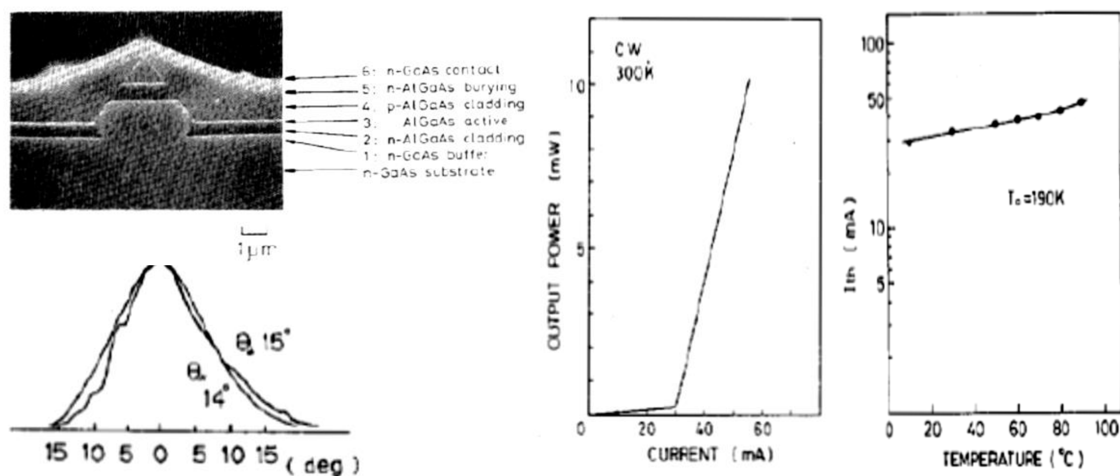

Figure 1-26: The single growth device developed by Yoshikawa [83] *is shown in the SEM image. The LI curve at room temperature and the I_{th} as a function of the temperature is also shown showing a characteristic temperature of ~190K, the Farfield pattern shown is a proof of the fundamental mode operation.*

An early method to design a semiconductor laser with a strained active layer buried in the GaAs/AlGaAs system was reported by York [84]. The device had a single InGaAs/GaAs quantum well active that contained $In_{0.23}Ga_{0.77}As$ layers sandwiching the $In_{0.41}Ga_{0.59}As$ layer to relax the strain between the QW and the surrounding GaAs layer, this laser structure operated at ~1074nm wavelength. $Al_{0.2}Ga_{0.8}As$ layer formed the p- and n-cladding layers to finish the structure. The final structure did not exhibit any dislocation or polycrystalline growth due to the use of a SiO_2 layer between the two growth steps to define the ridge for etching before the regrowth of the burying AlGaAs layer. COD threshold power was increased since the burying layers were all transparent to the operating wavelength. High power up to 130mW/facet could be obtained with high linearity up to 30 times the threshold current. The differential efficiency and the threshold current measured were 61% and 7-9mA for a device with 3.5μm wide and 405μm long.

Another early example of an InGaAs SQW active device on the GaAs-based system with operating wavelength in the 900-1000nm (designed for Er-doped fibre application as pumping sources) region is the device presented by Major *et.al.* [85]. Active stripe

were defined using impurity induced definition. A thin GaAs layer of 69nm thickness sandwiched a 15nm InGaAs quantum well which was confined by $Al_{0.8}Ga_{0.2}As$ confining layer and topped with a 150nm p^+-GaAs contact layer. The first GaAs layer was etched chemically through a Si_3N_4 mask and another layer of SiO_2 was used as the impurity source. After cleaning of photoresist and SiN layer from the unwanted areas, the wafer was annealed in a furnace for 7 hours at 850°C. The diffusion of Si caused the layers underneath it to disorder and destroy the pn-junction in the areas outside the active stripe. A 2µm wide stripe could operate with 7mA threshold current and up to 20mW output power was achieved before nonlinearity took-place as a result of self-heating.

A shift in the operational wavelength could also be achieved through disordering the bandgap structure of the system to select a range of wavelengths shorter than the originally given wavelengths in both GaAs and InP [92][93].

To improve the device performance from that of Major *et.al.* design low threshold current GRINSCH structures were integrated with the strained quantum well InGaAs/GaAs. Offsey *et.al.* [88] demonstrated threshold current ~12mA for a device with 3µm wide and 400µm long active stripe with an operating wavelength of 1030nm.

Chen *et.al.* used the MBE-LPE hybrid epitaxy method to present a SQW semiconductor laser operating at 980nm for application in pumping Er-doped fibre amplifier [89]. The first growth by MBE involved growing a single InGaAs quantum well, sandwiched by a GRINSCH AlGaAs layer. Following this, mesa etching and subsequent overgrowth of p- and n-AlGaAs burying layers was performed using LPE. As-cleaved devices showed maximum efficiency of 90% with single mode operation. When the rear and front facets were coated with High-Reflective/Anti-Reflective (HR/AR) coating of 90% and 5%, respectively, the output power from the AR-coated

was increased to 330mW. Thermal roll-over limited the power at this level due to high injection current density. No COD was observed over the measured range, as a result of AlGaAs and GaAs materials being transparent to the 980nm wavelength. According to the report COD threshold power was more than 100mW/μm. LPE overgrowth was replaced by MOVPE overgrowth for this material system as shown by Liou *et.al.* [90] where they presented a structure similar to the design of Chen *et.al.* grown using a two-step MOVPE. The structure had similar differential quantum efficiency with threshold current decreased to only 8mA for a $4\times400\mu m^2$ and 3mA for a $2.5\times400\mu m^2$ devices. Comparison the pulsed to the CW operation revealed the LI to be identical up to $10\times I_{th}$, attributed to improved thermal characteristics resulting from improved surface and interface quality.

Oxidation was the main problem facing any buried structure AlGaAs/GaAs system during device processing. Vail *et.al.* presented a replacement of the AlGaAs/GaAs system by incorporating InGaAsP layer to create the separate confinement heterostructure instead of AlGaAs [91]. Following the growth of the GRINSCH InGaAsP sandwiching a single InGaAs quantum well in an InGaP guiding layers a mesa was etched and the AlGaAs optoelectronic confinement layers were grown to finish the structure.

Shima *et.al.* presented a buried ridge heterostructure (BRH) laser by selectively growing an AlGaAs burying layer utilizing chloride during the MOCVD process[92]. The authors grew two structures which operated at two wavelengths 780nm for CD drivers and 980nm for fibre amplifier pumping. The targeted Δn was 5×10^{-3} to achieve strong index guiding at high powers. This index step was achieved by fixing the Al-composition to 0.7 in the confinement layer, with the cladding layers being comprised of $Al_{0.4}GaAs$. By tuning the chloride flow rate, growth selectivity could be achieved and

laser diodes were realized operating at 780nm and 980 with good operating parameters (high power, low threshold, and linear (single mode) operation). The narrow stripes width used enabled high coupling efficiency.

Reviewing the presented buried waveguide structures shows that most of the techniques used to realize buried structures included etching through the active layer and exposing it and the Al-containing layer to the atmosphere. Although both processing and growth techniques were developed to overcome this problem, it had to be executed to perfection and also it might not be so commercially applicable. For that reason the self-aligned stripe is explored in the following section in which the active is left intact.

1.7 Self-aligned stripe background:

The term stripe comes from the fact that the final wafer has a planar top. The realization of buried stripe configuration includes deposition of dielectric for selective etching, growth, doping, or oxidization. This process has to be followed by a thorough etching and cleaning and sometimes even a successive overgrowth process. This is a source of a potential contamination which may cause an increase in the series resistance for the associated contacts. Self-aligned stripe (SAS), is a process that enable realization of stripe geometry without the need of dielectric deposition. Instead an etch process in a current blocking layer followed by an overgrowth is used to achieve the stripe geometry. Depending on the material crystallography and the direction of the growth of such material the stripe is formed and the material is self-aligned in the designated location within the epitaxial structure. This technique provides protection to the active layer of the structure since the SAS realization process is limited to the current blocking layer which is usually located at a distance above the active layer.

Nishi *et.al.* [93] presented this technique for the first time in the InGaAsP/InP material system which operated in the 1.3µm. The device shown in Figure 1-27 was realized in a slightly different process included deposition of SiO_2 and opening windows in them to define the stripes, recently the stripes are defined using basic photolithography patterning followed by selective chemical etching. The device was grown by two growth LPE process. Single mode operation was achieved in a laser of 8µm wide and 310µm long. This device had threshold current of ~120mA with differential quantum efficiency of 0.17/facet.

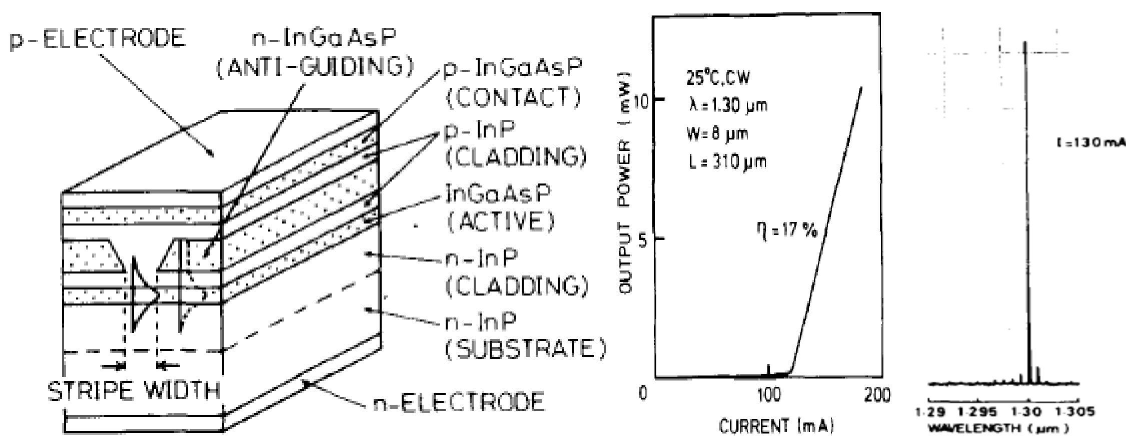

Figure 1-27: The self-aligned stripe laser presented by Nishi [93]. *In addition to the schematic diagram of the structure, the LI curve and the EL spectrum is shown.*

In 1985, Watanabe *et.al.* [94] developed a processing method including etching, growth, etch-back, and overgrowth of a GaAs/AlGaAs system to realize a self-aligned stripe structure, as shown in Figure 1-28. The process started by growing the lower n-cladding and the confinement layers in addition to the active GaAs and topping it with an n-GaAs layer which form the seed of the electrical confinement layer. Half the n-GaAs layer was etched following an overgrowth of the other part of the n-current confinement layer finishing the current confinement. Using the left n-GaAs material on the top which was melted and removed and an overgrowth of the p-AlGaAs layer and the p+-GaAs capping layer finished the whole structure.

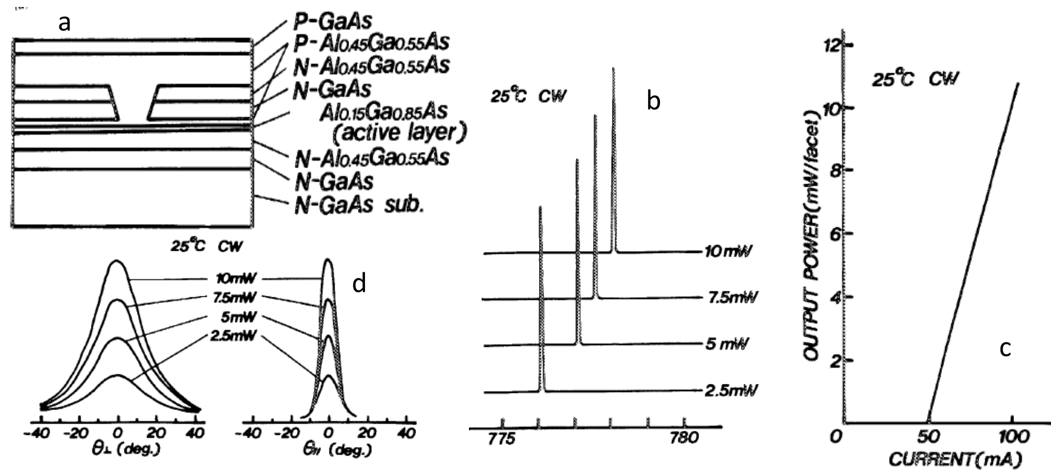

Figure 1-28: The self-aligned stripe device developed by Watanabe [94] *is shown in (a) with the performance measurements EL, LI, and farfield proving the mode singularity is shown in (b), (c), and (d).*

Yamada *et.al.* [95] presented a structure that was grown on a grooved p-GaAs substrate and exploited the effective refractive index change caused by thickness variation in the layer grown upon this corrugated surface to achieve optical confinement. Electrical confinement was achieved by growing a shallow n-GaAs layer, grown selectively via a SiN mask which was initially used to form the grooves. Despite the differences in the methodologies used to realize the two structures above, they both operated with almost the same threshold current and fundamental mode confinement.

A process developed by Nido *et.al.* [96] was used to fabricate a self-aligned stripe device by MOVPE growth only [96]. This device had features in common with the two devices above and it avoided exposure of the Al-containing layers to air by performing the stripe etching and overgrowth inside vacuumed chamber in the MOVPE reactor. The process method can be described using Figure 1-29. The GaAs layers sandwiching the AlGaAs layer were selectively etched utilising the difference in the etching rates between the GaAs (fast) and the $Al_{0.45}GaAs$ (slow). The first growth comprised of a 70nm AlGaAs active layer with separate confinement structure and lower cladding layer, while the final three layers were the n-GaAs current blocking layer, an AlGaAs etch stop layer, and a GaAs layer protecting the AlGaAs layer. The wafer was patterned

using standard photolithography to form the stipes followed by chemical etching to the lower GaAs layer through the etch stop layer. By maintaining the flow rate of HCl and AsH3 to 5cc/min and 50cc/min, respectively, and the ambient temperature to 850°C, the n-GaAs current blocking layer could be etched and stopped just before the $Al_{0.45}GaAs$ cladding layer. Following this process cleaning and overgrowth was held without the need to remove the wafer from the reactor which ensured both cleanliness and protection against oxidation. Figure 1-29 shows a schematic diagram of the process steps and some results that were published.

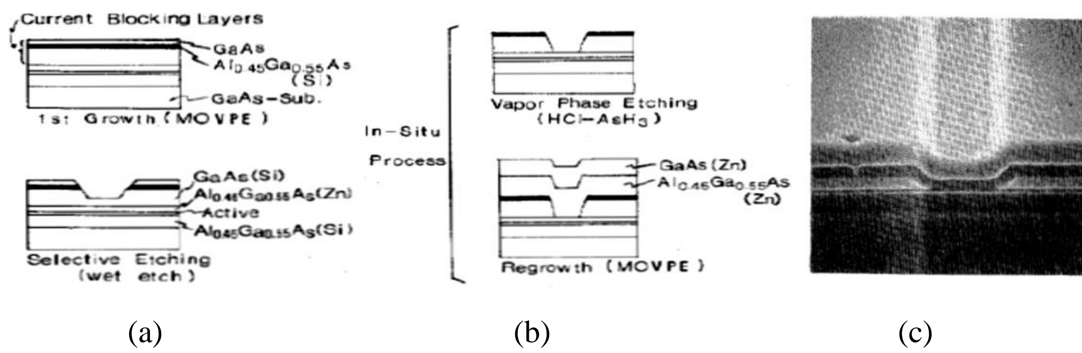

(a) (b) (c)

Figure 1-29: The in-situ process developed by Nido [96] is shown in (a-b) while an SEM image of the final device is shown in (c) showing high quality surface.

A number of alternative approaches were employed to provide electrical and optical confinement. One example that utilized impurity induced disorder to achieve vertical electrical confinement. In such processes the impurity was selectively diffused at the sides of what became later an active stripe in order to modify the optoelectronic properties of the material adjacent to the stripe. An example of this was presented by Zou *et.al.* [97] who grew the full separate confinement heterostructure laser structure comprised strained InGaAs quantum wells active layer. Following the growth, a dielectric layer was deposited and a mask formed by opening windows in the dielectric layer. Si-diffusion was applied through the opened windows and, because the Si is more uniformly diffuse in the GaAs/AlGaAs system than the zinc, the diffusion occurred only in the areas underneath the opened windows [97]. The diffusion caused disorder in the

band structure of the structure at the sides of the stripe which changed both the electrical and optical features of the stripe, enabling the formation of a buried stripe in the structure. A fundamental mode operation was achieved.

Another method was to use selective oxidation in an oxidization furnace such that the oxidized layer provides resistive path. This method, developed by Kish *et.al.* [98], was prepared by first growing the whole structure up to the capping p+-GaAs layer. The capping layer was then removed by wet etching from the area around the active stripe and the $Al_{0.8}Ga_{0.2}As$ layer was exposed. The wafer was then inserted in a furnace with a steady rate of nitrogen gas bubbled in water at 450°C in order to oxidize the upper AlGaAs cladding layer. SEM and TEM images proved a steady and controlled process where the oxide did not expand to the area under the p^+-GaAs capping layer. The native-oxide provided excellent electrical confinement due to the very high resistance in the area outside the stripe and also the optical confinement was achieved as the measured refractive index of the native oxide was found to be ~1.6 providing a 3.1-1.6 index step [98]. The device operated in a fundamental mode over the measured range of power and current.

Although the native-oxide and the IID structures showed good output features, they did not match the performance of the analogous multi-step-growth devices in term of mode stability, efficiency and thermal properties. The researchers tended to develop different methods to achieve the self-aligned stripe structure by changing the processing conditions or changing the material systems, but the main goal was to keep the Al-containing layer away from the atmosphere to eliminate any probability for oxidation.

Ishikawa *et.al.* presented a more comprehensive study on wavelength tuning in the spectral range between 980-1020nm by changing the quantum well composition $In_xGa_{1-x}As$ and the separate confinement layer $Al_yGa_{1-y}As$ [99]. Broad area laser structures,

showed low current density, stable and high differential and internal efficiency, high characterisation temperature, and low internal loss. Following this study, the broad area laser structure was integrated with an $In_{0.5}Ga_{0.5}P$-GaAs confinement layer, as shown in Figure 1-30, to provide the electrical confinement by use if a p-n-p-n structure and the optical confinement by the real index step (i.e. buried heterostructure). The integration of an InGaP layer increased the design flexibility of the device where the step-index can be changed from 1×10^{-2} down to 2×10^{-3} by changing the InGaP layer thickness over the whole range of the Al-composition studied in this paper. This range of index provided enough confinement to operate in a stable fundamental mode. The processed devices were HR/AR coated on the rear and front facets of the device, respectively, before testing in pulsed operation. The low thermal resistance of the InGaP layer resulted in high internal efficiencies up to 85% and high output power where powers ~550mW were achieved for the 980nm devices and output power up to 415mW was achieved for the devices that operate at 1020nm. Despite comprising a structure based on overgrowth up on exposed AlGaAs, the device operated for ~2400 hours at an output power level greater than 100mW with no obvious degradation. The LI measured from an AR/HR coated devices, 550mW maximum power to the measured range was measured from the 980nm and while 415mW maximum power was measured from 1020nm operating device. The figure also shows farfield for the two devices at 100mW output power which showed single-mode operation at least up to this level. Differential efficiency of ~0.49W/A was expected for the two devices.

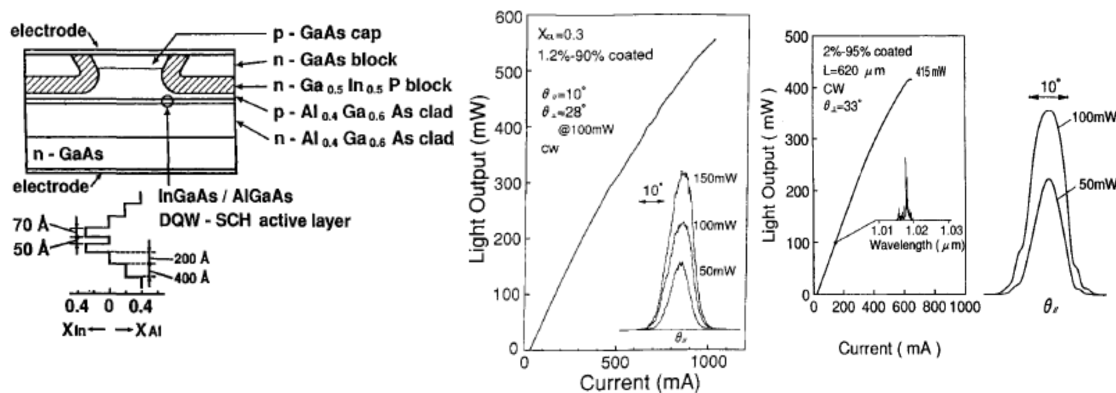

Figure 1-30: The InGaAs DQW device developed by Ishikawa [99] *is shown in (a) the ability to operate from 980nm to 1020nm with modified facet reflectivities is shown by the LI curves with the farfield inset.*

An alternative approach was to exclude the aluminium from the material system used to grow the devices in a way similar to the device presented by Sin *et.al.* [100], in which they used InGaP cladding layers instead of AlGaAs. InGaP lattice matched to GaAs for indium compositions ~0.5 and has E_g=~1.9e.V. Such material is transparent to wavelengths >700nm, and this can benefit in using them as optical confinement due to the smaller refractive index than GaAs or InGaAs. In this structure a standard buried ridge configuration was used where two layers of n- and p-InGaP layers sandwiching the GaAs-InGaAs single quantum well active were grown and topped with a p^+-GaAs contact layer. Following the first growth a ridge was created by etching the layers down to the lower n-InGaP layer. Finally, the two layers of p-InGaP and n-InGaP were grown to form the p-n-p-n current blocking structure outside the active stripe. The device performed well with low threshold currents down to <5mA for a 350μm long laser with the ability to perform at high power as the maximum power measured was ~95mW at 190mA, and high temperature operation as the device operated at 100°C with <13mA threshold current and 23mW output power.

Whilst replacement of AlGaAs with InGaP cladding can provide sufficient ΔE_g and optical confinement it does not offer the flexibility of $Al_xGa_{1-x}As$, which is lattice matched to GaAs for all compositions of Al_x, therefore lacks the design flexibility of the

AlGaAs, which by changing the Al_x can tailor the optical mode. To this point, aluminium oxidation was the main problem facing the development of buried waveguide in the AlGaAs/GaAs material system. A number of methods were used to avoid oxidation of Al-containing layers. Solutions varied from the melt-back method used in the LPE growth (which is not being used recently), to the single growth processes as the one shown by a number of examples shown earlier or performing in-situ growth/etching/overgrowth process developed by others, and ending with the solution of changing the cladding material from AlGaAs to Al-free cladding. Despite the improved performance of the previous examples in this section and section 1.6, the improvement targeted a specific wavelength or material system.

Stevens *et.al.* [7] suggested an alternative process to benefit from the flexibility of $Al_xGa_{1-x}As$ and the fact that GaInP does not suffer oxidization when exposed to atmosphere. They introduced a structure that incorporates $GaAs/Ga_{0.5}In_{0.5}P/GaAs$ optoelectronic confinement layer, lattice matched to GaAs, to realize a self-aligned stripe laser structure [7]. This layer enabled formation of the stripe by wet selective etching easily without exposure of rich Al-containing cladding layer to oxygen. Figure 1-31 shows a simplified schematic of the process followed in realization of this structure. The structure was grown by two-step growth process which both ends at Al-free containing layer, namely upper GaAs etch stopping layer for the first growth and the p^+-GaAs contact layer for the latter overgrowth. The first growth started with growth of lower cladding, the active layer, a 300nm p-clad as a separation between the active and the optoelectronic confinement layer. Following the first growth, the wafer was taken outside the reactor and selective etching to define the stripes was performed. The etchant used was highly selective to GaAs. This resulted in a smooth and clean GaAs surface when the GaInP layer is removed. Following a thorough cleaning of the wafer,

it was returned to the reactor to perform the overgrowth of the upper cladding and p^+-contact layer.

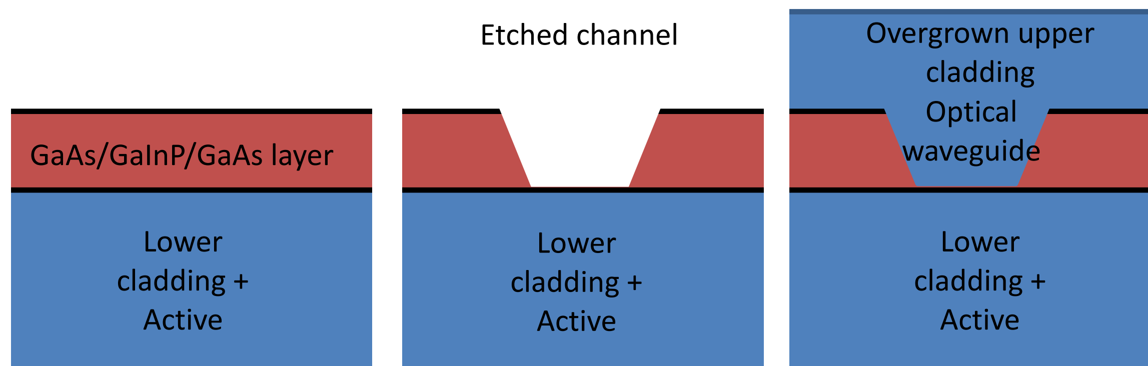

Figure 1-31: A simplified schematic showing the process followed by Stevens [7] to realize self-aligned stripe laser with GaInP layer.

The published data demonstrated lasing in the fundamental optical mode for stripes < 5μm wide and output powers of ~100mW were recorded from 3μm wide stripe and an external quantum differential efficiency was ~50%. The recorded characteristic temperature was ~80 K.

In addition to the QW active region, QD active layer operating at ~1250nm was implemented in this structure to test the structure durability for delicate active layer. The measured data showed no shift in the emitted wavelength compared to the photoluminescence (PL) measurement performed for the unprocessed material. This proved that, in addition to the protection from oxidization offered by the GaInP layer, the optoelectronic confinement layer protect the active layer during the fabrication process which included two annealing processes and SiN deposition at high temperature.

It was found that the self-aligned stripe process can present, in addition to the protection of Al-containing layer, an extra protection to the active layer during the post regrowth step. Since the scope of the thesis is to implement buried facets, which will be defined and explained in chapter 3, whose realization process include termination of the

buried waveguide prior to the cleaved facet to use it to achieve ultralow reflectivity, it was decided to use the self-aligned stripe process presented by Stevens et.al. to realize these facets.

The structure developed by Stevens *et.al.* is discussed in more details in chapter 2 and its implementation to realize low reflectivity facets is discussed in chapters 3-5 where it was used as SLDs and SOAs.

1.8: Thesis outlines:

An abstract overviews of the experimental chapters presented in this thesis are outlined below.

1.8.1 Chapter two

To avoid replication of the growth and fabrication processes to realize the devices presented in chapters 3-5 the common information is discussed in this chapter. The epitaxial structure and growth, the fabrication process, and the experimental setups are described in the first three sections in this chapter, followed by a spectral and gain characterization of the DQW material to be used. The wafer provided devices with tilted and normal-to-facet waveguides which are used in the subsequent three chapters in different configurations.

1.8.2 Chapter three

In the third chapter I characterized the devices with tilted cavities with a window at one end as superluminescent diodes (SLDs). Starting by explaining the differences between the SLD and the semiconductor laser device, the methods commonly used to convert one to the other are outlined. In my devices I employed the rear unpumped window configuration to achieve low facet reflectivity in addition to tilting the active stripe with respect to the crystal axis. Before characterizing the tilted device, I characterized the proposed window as a feedback suppression element by measuring the

reflectivity of straight cavity devices. Since the spectral modulation depth (SMD) is a key factor in evaluating the SLD performance, I first determined the SMD power dependence of the structure by use of a simplified theoretical model based on the measured reflectivity and comparing with actual SMD measured from devices with different cavity geometries. Results demonstrated a significant thermal effect on the device performance and so different cavity configurations were explored in order to optimize the device performance. First the structure was mounted epi-side down to increase the heat sinking, second this epi-side down mounted device was tested under pulsed conditions, and third a resistor was integrated at the unpumped window region of the device to control absorption of the window.

1.8.3 Chapter four

The outcomes of the third chapter increased my interest in such device performance in SLDs with waveguides processed normal-to-facet since the low R_{eff} is suggestive of the potential to use this more desirable configuration. In chapter four such devices are processed and characterized thoroughly with different geometries. A number of design parameter limitations are discussed in this chapter such as the active cavity dimensions, and the propagated beam divergence angle.

1.8.4 Chapter five

Following on the footsteps of a number of researchers in the InP world I presented a study on windowed SOAs, using the same GaAs-based material combination as the previous two chapters but which had a window region at each end of a waveguide. This chapter describes the experimental design and the measurement of the four main parameters used to evaluate an optical amplifiers performance which revealed excellent performance in number of aspects. Based on this characterization the device showed contrasting performance points associated mainly with the material used as an active layer. The recorded small signal gain of the device was >33dB which is considered in

the high range of quantum well amplifiers. The bandwidth of the device was limited due to the limited bandwidth of the structure. The saturation output power, P_{sat}, was <10dBm which is considered low compared with the common P_{sat} reported in the literature, this low value is expected to be resulted from the low pumping current density which was <2kA.cm^{-2}.

1.8.5 Chapter six

The GaAs-based material system enables emission across the spectral region 600-1600nm however due to absorption by GaAs at wavelengths shorter than 700nm, it is not possible to simply extend the SAS scheme studied in chapters 3-5 to such regions. In this chapter, I use the AlGaInP/GaInP system to design a buried structure that could operate at ~645nm wavelength. As an introduction to this chapter, a review of the development of the red laser is first presented. Next, the problems associated with this spectral range are outlined. These two problems being the shallow energy barrier and the high refractive index of the material used when Al-free containing layers are used. The first problem was addressed by placing a multiquantum barrier (MQB) layer in the active portion, and the second problem was addressed by changing the principle of operation used to confine the light to an anti-resonance reflecting optical waveguide (ARROW). Simulations were made to optimize the design. However, reliance on aluminium-containing layers could not be overcome, and an (Al0.3Ga07)0.5In0.5P needed to be etched down and exposed to air. The chapter concluded with suggestions of how this could be overcome in future iteration.

1.9 References

[1] D. Huang, E. A. Swanson, C. P. Lin, J. S. Schuman, W. G. Stinson, W. Chang, M. R. Hee, T. Flotire, K. Gregory, C. a Puliafito, and J. G. Fujimoto, "Optical Coherence Tomography," *Science*, vol. 254, no. 5035,pp. 1178–1181, 1991.

[2] L. Charters, "Swept-source OCT affords greater detailing in vitreous imaging," Ophthalmology Times 2015, [online], Available: http://ophthalmologytimes.modernmedicine.com/ophthalmologytimes/news/swep

t-source-oct-affords-greater-detailing-vitreous-imaging,. [last Accessed :4th of May 2016].

[3] Michalewska Z., J. Michalewski, and J. Nawrocki, “Swept-source OCT: Wide-field simultaneous choroid, retina, and vitreous visualization,” *Retina Today*, 2013. [Online]. Available: http://retinatoday.com/pdfs/0913RT_F2_Michalewska.pdf. [Accessed: 20-Feb-2016].

[4] Y.Y. Huang, “Low-level laser therapy: an emerging clinical paradigm,” *SPIE Newsroom*, pp. 2–4, 2009.

[5] Y. Kashima, A. Matoba, and H. Takano, “Performance and Reliability of InGaAsP Superluminescent Diode,” *Journal of Lightwave Technology*, vol. 10, no. 11, pp. 1644–1649, 1992.

[6] I. Cha, M. Kitamura, H. Honmou, and I. Mito, “1.5um Band Travelling-Wave Semiconductor Optical Amplifiers With Window Facet Structure,” *Elecronics Letters*, vol. 25, no. 18, pp. 1241–1242, 1989.

[7] K. M. Groom, B. J. Stevens, P. J. Assamoi, J. S. Roberts, M. Hugues, D. T. D. Childs, R. R. Alexander, M. Hopkinson, A. S. Helmy, and R. A. Hogg, “Quantum Well and Dot Self-Aligned Stripe Lasers Utilizing an InGaP Optoelectornic Confinement Layer,” *IEEE Journal of Selected of Topics in Quantum Electronics*, vol. 15, no. 3, pp. 819–827, 2009.

[8] W. Drexler and J. G. Fujimoto, *Optical Coherence Tomography: Technology and Applications*, 2nd edition, Springer International Publication: Switzerland, 2015.

[9] R. Leitgeb, C. Hitzenberger, and A. Fercher, “Performance of Fourier Domain vs Time Domain Optical Coherence Tomography,” *Optics Express*, vol. 11, no. 8, p. 889, 2003.

[10] M. Choma, M. Sarunic, C. Yang, and J. Izatt, “Sensitivity Advantage of Swept Source and Fourier Domain Optical Coherence Tomography.,” *Optics Express*, vol. 11, no. 18, pp. 2183–2189, 2003.

[11] C.-W. Tsai, “Extremely Broadband Superluminescent Diodes/Semiconductor Optical Amplifiers in Optical Communication Band,” *Proceedings of SPIE*, vol. 4989, no. 2, pp. 69–77, 2003.

[12] S. S. Wagner and T. E. Chapuran, “Broadband High-Density WDM Transmission Using Superluminescent Diodes,” *Elecronics Letters*, vol. 26, no. 11, pp. 696–697, 1990.

[13] O. Çelikel and S. E. San, “Establishment Of All Digital Closed-Loop Interferometric Fiber-Optic Gyroscope and Scale Factor Comparison For Open-Loop and All Digital Closed-Loop Configurations,” *IEEE Sensors Journal*, vol. 9, no. 2, pp. 176–186, 2009.

[14] H. S. Djie and C. E. Dimas, “Semiconductor Quantum-Dot Based Wideband Emitter for Optical Sensors,” *IEEE Sensors Journal, 2005.*, vol. 1, pp. 932–934, 2005.

[15] H. S. Djie, C. E. Dimas, D. Wang, B. Ooi, S. Member, J. C. M. Hwang, G. T.

Dang, and W. H. Chang, "InGaAs / GaAs Quantum-Dot Superluminescent Diode for Optical Sensor and Imaging," *IEEE Sensors Journal*, vol. 7, no. 2, pp. 251–257, 2007.

[16] B. Heise, S. E. Schausberger, S. Häuser, B. Plank, D. Salaberger, E. Leiss-Holzinger, and D. Stifter, "Full-Field Optical Coherence Microscopy With a Sub-Nanosecond Supercontinuum Light Source for Material Research," *Optical Fiber Technology*, vol. 18, no. 5, pp. 403–410, 2012.

[17] J. W. Crowe and R. M. Craig, "Small-Signal Amplification In GaAs Lasers," *Applied Physics Letters*, vol. 4, no. 3, p. 57, 1964.

[18] M. J. O'Mahony, "Semiconductor Laser Optical Amplifiers For Use In Future Fiber Systems," *Journal of Lightwave Technology*, vol. 6, no. 4, pp. 531–544, 1988.

[19] Y. X. Mao, C. Flueraru, S. D. Chang, D. P. Popescu, and M. G. Sowa, "High-Quality Tissue Imaging Using a Catheter-Based Swept-Source Optical Coherence Tomography Systems With an Integrated Semiconductor Optical Amplifier," *IEEE Transactions on Instrumentation and Measurement*, vol. 60, no. 10, pp. 3376–3383, 2011.

[20] K. Sakai, N. Shimada, K. Shibata, Y. Hanamaki, and A. D. Structure, "High-Power 1.06μm Near-Diffraction-Limited Planar Tapered Amplifier Injected With Seed Light Through a Fiber Biconical Microlens", Journal of *Lightwave Technology*, vol. 26, no. 6, pp. 710–719, 2008.

[21] G. Contestabile, "All optical processing in QD-SOAs," *Optical Fiber Communications Conference*, p. W4F.6, 2014.

[22] P. Li, D. Huang, and X. Zhang, "SOA-Based Ultrafast Multifunctional All-Optical Logic Gates With PolSK Modulated Signals," *IEEE Journal of Quantum Electronics*, vol. 45, no. 12, pp. 1542–1550, 2009.

[23] T. Simoyama, H. Kuwatsuka, B. E. Little, M. Matsuda, Y. Kotaki, and H. Ishikawa, "High-efficiency wavelength conversion using FWM in an SOA integrated DFB laser," *IEEE Photonics Technology Letters*, vol. 12, no. 1, pp. 31–33, 2000.

[24] E. Dietrich, B. Enning, G. Grosskopf, L. Kuller, R. Ludwig, R. Molt, E. Patzak, and H. G. Weber, "Semiconductor-Laser Optical Amplifiers for Multichannel Coherent Optical-Transmission," *Journal of Lightwave Technology*, vol. 7, no. 12, pp. 1941–1955, 1989.

[25] C. Tombling, T. Saito, Y. Suzuki, and H. Tanaka, "Experimental Gain and Saturation Performance of GaAs/AlGaAs SCH Quantum Well Travelling Wave Optical Amplifier," *Electronics Letters*, vol. 27, no. 15, 1991.

[26] P. M. Stolarz, V. Pusino, J. Akbar, L. Hou, A. C. Coleman, J. H. Marsh, A. E. Kelly, and M. Sorel, "High-Power and Low-Noise Mode-Locking Operation of Al-Quaternary Laser Diodes," *IEEE Journal of Selected Topics in Quantum Electronics*, vol. 21, no. 6, 2015.

[27] G. Giannoulis, V. M. Korpijärvi, N. Iliadis, J. Mäkelä, J. Viheriälä, D.

Apostolopoulos, and M. Guina, "Dilute Nitride SOAs for High - Speed Data Processing in Variable Temperature Conditions," in *Optical Fiber Communication Conference*, 2015, vol. 6, pp. 6–8.

[28] J. Hashimoto, K. Koyama, T. Katsuyama, Y. Iguchi, T. Yamada, S. Takagishi, M. Ito, and A. Ishida, "1.3 µm Traveling-Wave GaInNAs Semiconductor Optical Amplifier," *Japanese Journal of Applied Physics*, vol. 43, no. 6A, pp. 3419–3423, 2004.

[29] M. Anagnosti, C. Caillaud, G. Glastre, J.-F. Paret, D. Lanteri, and M. Achouche, "High performance monolithically integrated SOA-UTC photoreceiver for 100Gbit/s applications," *26th International Conference on Indium Phosphide and Related Material*, no. 2, pp. 1–2, 2014.

[30] K. Magari, S. Kondo, H. Yakasha, Y. Noguchi, To. Kataoka, and O. Mikami, "A High Gain GRIN-SCH MQB Optical Semiconductor Laser Amplifier," *IEEE Photonics Technology Letters*, vol. 2, no. 11, pp. 792–793, 1990.

[31] T. Mukai and Y. Yamamoto, "Gain, frequency bandwidth, and saturation output power of AlGaAs DH laser amplifiers," *IEEE Journal of Quantum Electronics*, vol. 17, no. 6, pp. 1028–1034, 1981.

[32] G. Sherlock, C. P. Seltzer, D. J. Elton, S. D. Perrin, M. J. Robertson, and D. M. Cooper, "1.3um MQW Semiconductor Optical Amplifiers with High Gain and Output Power," *Electronics Letters*, vol. 27, no. 2, pp. 165–166, 1991.

[33] P. Brosson, B. Fernier, and J. Benoit, "Design and Realisation of High-Gain 1.5µm Semiconductor TW Optical Amplifiers," *Elecronics Letters*, vol. 23, no. 6, pp. 254–256, 1987.

[34] "Microwave Transmission Through Buried Waveguide," *Electrical Engineering*, vol. 79, no. 3, pp. 257–258, 1960.

[35] M. I. Nathan, W. P. Dumke, G. Burns, F. H. Dill, and G. Lasher, "Stimulated Emission of Radiation From GaAs pn-Junctions," *Applied Physics Letters*, vol. 1, no. 3, pp. 62–64, 1962.

[36] H. Nelson, H. Kressel, "Improved Red and Infrared Light Emitting $Al_xGa_{1-x}As$ Laser Diodes Using The Close-Confinement Structure," *Applied Physics Letters*, vol. 15, no. 1, p. 7, 1969.

[37] T. Tsukada, "$GaAs/Ga_{1-x}Al_xAs$ Buried-Heterostructure Injection Lasers," *Journal of Applied Physcis*, vol. 45, no. 11, p. 4899, 1974.

[38] T. Tsukada and Y. Shima, "Thermal Characteristics of Buried-Heterostructure Injection Lasers," *IEEE Journal of Quantum Electronics*, vol. 11, no. 7, pp. 494–498, 1975.

[39] M. Nakamura, K. Aiki, J. Umeda, and A. Yariv, "CW Operation of Distributed-Feedback GaAs-GaAlAs Diode Lasers at Temperatures Up to 300°K," *Applied Physics Letters*, vol. 27, no. 7, pp. 403–405, 1975.

[40] R. D. Burnham, D. R. Scifres, and W. Streifer, "Distributed Feedback Buried Heterostructure Diode Laser," *Applied Physics Letters*, vol. 29, no. 5, pp. 287–289, 1976.

[41] W.-T. Tsang and S. Wang, "GaAs-$Ga_{1-x}Al_xAs$ Double-Heterostructure Injection Lasers With Distributed Bragg Reflectors," *Applied Physics Letters*, vol. 28, no. 10, p. 596, 1976.

[42] T. Tsukada, K. Saito, N. Shige, and Y. Shima, "Reduction of Threshold Current of Buried-Heterostructure Injection Lasers," in *Proceedings of the 7th Conference on Solid State Devices*, 1975, vol. 15, pp. 289–292.

[43] P. a. Kirkby and G. H. B. Thompson, "Channeled Substrate Buried Heterostructure GaAs-(GaAl)As Injection Lasers," *Journal of Applied Physics*, vol. 47, no. 10, p. 4578, 1976.

[44] S. Takahashi, T. Kobayashi, and Y. Furukawa, "Dependence of Net Gain of Buried Laser on Mirror Loss," *Japanese Journal of Applied Physics*, vol. 15, no. 2, pp. 395–396, 1976.

[45] M. B. Panish, "Heterostructure Injection Lasers," *Proceedings of IEEE*, vol. 64, no. 10, pp. 1512–1540, 1976.

[46] T. Tsukada, K. Saito, N. Shige, S. Kajimura, K. Aiki, and R. Ito, "Buried-Heterostructure Injection Lasers (Invited)," *Device Research Conference*, 1976, p. 1255.

[47] J. J. Hsieh and C. C. Shen, "Room-Temperature CW Operation of Buried-Stripe Double- Heterostructure GaInAsP / InP Diode Lasers ," *Applied Physics Letters*, vol. 30, no. 8, pp. 429–431, 1977.

[48] W. T. Tsang and R. A. Logan, "Lateral Current Confinement by Reverse-Biased Junctions in GaAs-$Al_xGa_{1-x}As$ DH Lasers," *Applied physics Letters*, vol. 30, no. 10, p. 538, 1977.

[49] M. J. Adams, "The Cladded Parabolic-Index Profile Waveguide: Analysis and Application to Stripe-Geometry Lasers," *Optical and Quantum Electronics*, vol. 10, no. 1, pp. 17–29, 1978.

[50] T. Kajimura, K. Saito, N. Shige, and R. Ito, "Leaky-Mode Buried-Heterostructure AlGaAs Injection Lasers," *Applied Physics Letters*, vol. 30, no. 11, p. 590, 1977.

[51] K. Aiki, M. Nakamura, T. Kuroda, and J. Umeda, "Channeled-Substrate Planar Structure (AlGa)As Injection Lasers," *Applied Physics Letters*, vol. 30, no. 12, p. 649, 1977.

[52] L. Figueroa and S. Wang, "Inverted-Ridge-Waveguide Double-Heterostructure Injection Laser With Current And Lateral Optical Confinement," *Applied Physics Letters*, vol. 31, no. 1, p. 45, 1977.

[53] K. Itoh, K. Asahi, M. Inoue, and I. Teramoto, "Embedded-Stripe GaAs-GaAlAs Double- Heterostructure Lasers with Polycrystalline GaAsP Layers-I: Lasers with Cleaved Mirrors," *IEEE Journal of Quantum Electronics*, vol. QE-13, no. 8, pp. 623–627, 1977.

[54] C. P. Lee, S. Margalit, and A. Yariv, "Dependence of Zn Diffusion on The Al Content In $Ga_{1-x}Al_xAs$," *Solid State Electronics*, vol. 21, pp. 905–907, 1977.

[55] L. Figueroa and S. Wang, "Curved Junction Stabilized Filament (CJSF) Double-

Heterostructure Injection Laser," *Applied Physics Letters*, vol. 32, no. 1, p. 55, 1978.

[56] W. T. Tsang, R. A. Logan, and M. Ilegems, "High-Power Fundamental-Transverse-Mode Strip Buried Heterostructure Lasers With Linear Light-Current Characteristics," *Applied Physics Letters*, vol. 32, no. 5, p. 311, 1978.

[57] K. Aiki, M. Nakamura, T. Kuroda, J. Umeda, R. Ito, N. Chinone, and M. Maeda, "Transverse Mode Stabilized $Al_xGa_{1-x}As$ Injecition Lasers with Channeled-Substrate-Planar Strcuture," *IEEE Journal of Quantum Electronics*, vol. QE-14, no. 2, pp. 89–94, 1978.

[58] S. Takahashi, T. Kobayashi, H. Saito, and Y. Furukawa, "GaAs – AlGaAs DH Lasers with Buried Facet," *Japanese Journal of Applied Physics*, vol. 17, no. 5, pp. 865–870, 1978.

[59] H. Kano, K. Oe, S. Ando, and K. Suiyama, "Buried Stripe GaInAsP / InP DH Laser Prepared by Using Meltback Method," *Japanese Journal of Applied Physics*, vol. 17, no. 10, pp. 1887–1888, 1978.

[60] N. Bar-Chaim, M. Lanir, S. Margalit, I. Ury, D. Wilt, M. Yust, and A. Yariv, "Be-Implanted (GaAl)As Stripe Geometry Lasers," *Applied Physics Letters*, vol. 36, no. 4, p. 233, 1980.

[61] R. Lang, "Lateral Transverse Mode Instability and Its Stabilization In Stripe Geometry Injection Lasers," *IEEE Journal of Quantum Electronics*, vol. 15, no. 8, 1979.

[62] M. Ueno and H. Yonezu, "Stable Transverse Mode Oscillation in Planar Stripe Laser with Deep Zn Diffusion," *IEEE Journal of Quantum Electronics*, vol. QE-15, no. 10, pp. 1189–1196, 1979.

[63] J. C. Bouley, J. Landreau, P. Delpech, and P. Ged, "A Stabilized Zinc Diffused-Proton Bombarded (GaAl)As Laser," *IEEE Journal of Quantum Electronics,* vol. QE-15, no. 8, pp. 767–771, 1979.

[64] G. H. B. Thompson, D. F. Lovelace, and S. E. H. Turley, "Deep Zn-Diffused (GaAl)As Heterostructure Stripe Laser with Twin Transverse Junctions for Low Threshold Current and Kink-Free Light Characteristics," *IEEE Journal of Quantum Electronics*, vol. QE-15, no. 8, pp. 18–21, 1979.

[65] H. O. Yonezu, M. Ueno, T. Kamejima, and I. Hayashi, "An AlGaAs Window Structure Laser," *IEEE Journal of Quantum Electronics*, vol. QE-15, no. 8, pp. 775–781, 1979.

[66] M. Nakamura, "Single Mode Operation of Semiconductor Injection Lasers," *IEEE Transactions on Circuits and System*, vol. Cas-26, no. 12, pp. 1055–1065, 1979.

[67] B. W. Hakki, "Instabilities in Output of Injection Lasers," *Journal of Applied Physics*, vol. 50, no. 9, p. 5630, 1979.

[68] H. Kano and K. Sugiyama, "Operation Characteristics of Buried-Stripe GaInAsP/InP DH Lasers Made by Melt-Back Method," *Journal of Applied Physics*, vol. 50, no. 12, p. 7934, 1979.

[69] W. T. Tsang, R. A. Logan, and J. P. van der Ziel, "Low-Current-Threshold Strip-Buried-Heterostructure Lasers With Self-Aligned Current Injection Stripes," *Applied Physics Letters*, vol. 34, no. 10, p. 644, 1979.

[70] W. T. Tsang, R. a. Logan, and L. F. Johnson, "GaAs-$Al_xGa_{1-x}As$ Strip-Buried-Heterostructure Lasers With Lateral-Evanescent-Field Distributed Feedback," *Applied Physics Letters*, vol. 34, no. 11, pp. 752–755, 1979.

[71] W. T. Tsang and R. A. Logan, "GaAs-$Al_xGa_{1-x}As$ Buried-Heterostructure Lasers Grown by Molecular Beam Epitaxy With $Al_{0.65}Ga_{0.35}As$ (Ge-Doped) Liquid Phase Epitaxy Overgrown Layer for Current Injection Confinement," *Applied Physics Letters*, vol. 36, no. 9, p. 730, 1980.

[72] R. J. Nelson, P. D. Wright, P. A. Barnes, R. L. Brown, T. Cella, and R. G. Sobers, "High-Output Power InGaAsP (λ=1.3 μm) Strip-Buried Heterostructure Lasers," *Applied Physics Letters*, vol. 36, no. 5, p. 358, 1980.

[73] J. J. Coleman and P. D. Dapkus, "Single-Longitudinal-Mode Metalorganic Chemical-Vapor-Deposition Self-Aligned GaAlAs-GaAs Double-Heterostructure Lasers," *Applied Physics Letters*, vol. 37, no. 3, p. 262, 1980.

[74] J. Katz, S. Margalit, D. Wilt, P. C. Chen, and A. Yariv, "Single-Growth Embedded Epitaxy Algaas Injection Lasers with Extremely Low Threshold Currents," *Applied Physics Letters*, vol. 37, no. 11, p. 987, 1980.

[75] N. Chinone, K. Saito, R. Ito, K. Aiki, and N. Shige, "Highly efficient (GaAl)As Buried-Heterostructure Lasers With Buried Optical Guide," *Applied Physics Letters*, vol. 35, no. 7, p. 513, 1979.

[76] K. Saito and R. Ito, "Buried-Heterostructure AlGaAs Lasers," *IEEE Journal of Quantum Electronics*, vol. QE-16, no. 2, pp. 205–215, 1980.

[77] H. Ishikawa, I. Hanamitsu, N. Takagi, T. Fujiwara, and M. Takusagawa, "Separated Multiclad-Layer Stripe-Geometry GaAlAs DH Laser," *IEEE Journal of Quantum Electronics*, vol. QE-17, no. 7, pp. 1226–1234, 1981.

[78] W. T. Tsang, R. A. Logan, and J. A. Ditzenberger, "Ultra-Low Threshold, Graded Index Waveguide, Separate Confinement, CW Buried-Heterostructure Lasers," *Electronics Letters*, vol. 18, no. 19, pp. 845–847, 1982.

[79] W. T. Tsang, R. A. Logan, and J. A. Ditzenberger, "Multilongitudinal Mode Operation in Angled Stripe Buried Heterostructure Lasers," *Journal of Applied Physics*, vol. 54, no. 2, p. 1137, 1983.

[80] C. S. Hong, D. Kasemset, M. E. Kim, and R. A. Milano, "GaAlAs Buried-Heterostructure Lasers Grown by a Two-Step MOCVD Process," *Electronics Letters*, vol. 19, no. 19, p. 759, 1983.

[81] D. E. Ackley, "Twin-Channel Substrate-Mesa-Guide Injection Lasers Fabricated by Organometallic Vapor Phase Epitaxy," *Applied Physics Letters*, vol. 42, no. 8, p. 653, 1983.

[82] R. L. Thornton, R. D. Burnham, T. L. Paoli, N. Holonyak, and D. G. Deppe, "Low Threshold Planar Buried Heterostructure Lasers Fabricated by Impurity-Induced Disordering," *Applied Physics Letters*, vol. 47, no. 12, p. 1239, 1985.

[83] A. Yoshikawa, A. Yamamoto, M. Hirose, T. Sugino, G. Kano, and I. Teramoto, “A Novel Technology for Formation of a Narrow Active Layer in Buried Heterostructure Lasers by Single-Step MOCVD,” *IEEE Journal of Quantum Electronics*, vol. 23, no. 6, pp. 725–729, 1987.

[84] P. K. York, K. J. Beernink, G. E. Fernández, and J. J. Coleman, “InGaAs-GaAs Strained-Layer Quantum Well Buried Heterostructure Lasers (λ>1 μm) by Metalorganic Chemical Vapor Deposition,” *Applied Physics Letters*, vol. 54, no. 6, p. 499, 1989.

[85] J. S. Major, L. J. Guido, K. C. Hsieh, N. Holonyak, W. Stutius, P. Gavrilovic, and J. E. Williams, “Low-threshold disorder-defined buried heterostructure strained-layer $Al_yGa_{1-y}As$-GaAs-$In_xGa_{1-x}As$ quantum well lasers (λ~910 nm),” *Applied Physics Letters*, vol. 54, no. 10, p. 913, 1989.

[86] M. D. Camras, J. M. Brown, N. Holonyak, M. A. Nixon, R. W. Kaliski, M. J. Ludowise, W. T. Dietze, and C. R. Lewis, “Stimulated emission in strained-layer quantum-well heterostructures,” *Journal of Applied Physics*, vol. 54, no. 11, p. 6183, 1983.

[87] M. J. Ludowise, W. T. Dietze, and C. R. Lewis, “Continuous 300°K Laser Operation of Strained Superlattices,” *Applied Physics Letters*, vol. 42, no. 1983, p. 487, 1983.

[88] S. D. Offsey, W. J. Schaff, P. J. Tasker, H. Ennen, and L. F. Eastman, “Strained-layer InGaAs-GaAs-AlGaAs Graded-Index Separate Confinement Heterostructure Single Quantum Well Lasers Grown By Molecular Beam Epitaxy,” *Applied Physics Letters*, vol. 54, no. 25, p. 2527, 1989.

[89] T. R. Chen, L. E. Eng, Y. H. Zhuang, Y. J. Xu, H. Zaren, and A. Yariv, “High-Power Operation of Buried-Heterostructure Strained-Layer InGaAs/GaAs Single Quantum Well Lasers,” *Applied Physics Letters*, vol. 57, no. 26, p. 2762, 1990.

[90] D. C. Liou, W. H. Chiang, C. P. Lee, K. H. Chang, D. G. Liu, J. S. Wu, and Y. K. Tu, “A Novel Technique for Low-Threshold and High-Power InGaAs/GaAs Strained-Layer 0.98-μm Buried Heterostructure Laser Fabrication,” *Journal of Applied Physics*, vol. 71, no. 3, p. 1525, 1992.

[91] E. C. Vail, S. F. Lim, Y. A. Wu, D. A. Francis, C. J. Chang-Hasnain, R. Bhat, and C. Caneau, “Buried Heterostructure 0.98 μm InGaAs/InGaAsP/InGaP Lasers,” *Applied Physics Letters*, vol. 63, no. 16, p. 2183, 1993.

[92] A. Shima, H. Kizuki, A. Takemoto, S. Karakida, M. Miyashita, Y. Nagai, T. Kamizato, and K. Shigihara, “0.78- and 0.98um Ridge-Waveguide Lasers Buried with AlGaAs Confinement Layer Selectively Grown by Chloride-Assisted MOCVD,” *IEEE Journal of Selected Topics in Quantum Electronics*, vol. I, no. 2, pp. 102–109, 1995.

[93] H. Nishi, M. Yano, Y. Nishitani, Y. Akita, and M. Takusagawa, “Self-aligned structure InGaAsP/InP DH lasers,” *Applied Physics Letters*, vol. 35, no. 3, p. 232, Aug. 1979.

[94] A. Watanabe, T. Yamada, K. Imanaka, H. Horikawa, Y. Kawai, and M. Sakuta, “AlGaAs/GaAs Melt-Etched Inner Stripe Laser Diode With Self-Aligned Structure,” *Applied Physics Letters*, vol. 46, no. 11, p. 1023, 1985.

[95] T. Yamada, T. Yuasa, K. Kamon, M. Shimazu, and M. Ishii, “PAIR-GROOVE-SUBSTRATE GaAs / AIGaAs Multiquantum-Well Lasers with a Self-Aligned Stripe Geometry,” *Electronics Letters*, vol. 22, no. 22, pp. 1164–1166, 1986.

[96] M. Nido, I. Komazaki, K. Kobayashi, M. Ueno, T. Kamejima, and T. Suzuki, “AlGaAs/GaAs Self-Aligned LD's Fabricated by the Process Containing Vapor Phase Etching and Subsequent MOVPE Regrowth”, vol. QE-23, no. 6, pp. 720–724, 1987.

[97] W. X. Zou, J. L. Merz, R. J. Fu, and C. S. Hong, “Very-Low-Threshold, Strained InyGa1-yAs/GaAs Quantum-Well Lasers Defined by Impurity-Induced Disordering,” *IEEE Photonics Technology Letters*, vol. 3, no. 5, pp. 400–402, 1991.

[98] F. A. Kish, S. J. Caracci, N. Holonyak, J. M. Dallesasse, K. C. Hsieh, and M. J. Ries, “Planar Native-Oxide Index-Guided $Al_xGa_{1-x}As$-GaAs Quantum Well Heterostructure Lasers,” *Applied Physics Letters*, vol. 59, no. 14, p. 1755, 1991.

[99] S. Ishikawa, K. Fukagai, H. Chida, T. Miyazaki, H. Fujii, and K. Endo, “0.98-1.02 µm Strained InGaAs/AlGaAs Double Quantum-Well High-Power Lasers with GaInP Buried Waveguides,” IEEE Journal of Quantum Electronics, vol. 29, no. 6, pp. 936–942, 1993.

[100] Y. K. Sin, H. Horikawa, and T. Kamijoh, “High Power InGaAs-GaAs-InGaP Buried Heterostructure Strained Quantum Well Lasers Grown by Two Step MOVPE,” *Electronics Letters*, vol. 29, no. 2, pp. 240–242, 1993.

Chapter two: Methodology.

2.1 Introduction.

This chapter focuses on the materials grown and the methods used to fabricate the devices explored in later chapters. The wafer structure and its subsequent processing steps are described at the beginning of this chapter, followed by a description of the setups used to characterize the processed devices.

2.2 Growth and fabrication:

The material described in this chapter was used in the investigations detailed in chapters 3, 4 and 5. In order to avoid repetition of the same information regarding the growth, processing, and sample preparation, I describe the whole process used in the following sections. Minor deviation from this regarding specific devices will be mentioned whenever occurred.

2.2.1 Growth, stripe formation and regrowth:

The superluminescent diodes (SLDs) studied in this thesis employ self-aligned stripe (SAS) optical waveguides. The realization of these SLDs is achieved via two-step growth method previously utilized for realization SAS laser [1]. The active layer consists of two 7.6nm $In_{0.17}GaAs$ quantum wells (QWs) separated by 20nm GaAs and sandwiched by a 100nm GaAs confinement layer. The structure emits at central wavelength ~980nm.

The wafers used in chapters 3-5 were all grown and overgrown using Thomas Swan horizontal MOVPE reactor. The growth process starts by depositing an n-GaAs buffer layer and a 1.5µm n-$Al_{0.41}GaAs$ cladding layer on an n^+-GaAs substrate. Following the AlGaAs deposition, the active region described above is grown and topped with 300nm p-$Al_{0.41}GaAs$ separation layer, prior to growth of a 600nm thick GaInP (lattice matched

to GaAs) current blocking layer, which will provide both optical and electronic confinements. This layer is sandwiched in between two 10nm layers of GaAs in order to use the lower GaAs layer as an etch stopper and to protect the lower Al-containing layers from exposure to atmosphere. The growth temperatures were set to 715°C to grow AlGaAs, 703°C for QW growth, and 715°C for GaInP growth. Figure 2-1a shows the schematic diagram of the grown structure to this point and Figure 2-1 b shows wavelength as a function of lattice constant for the GaAs and InP systems.

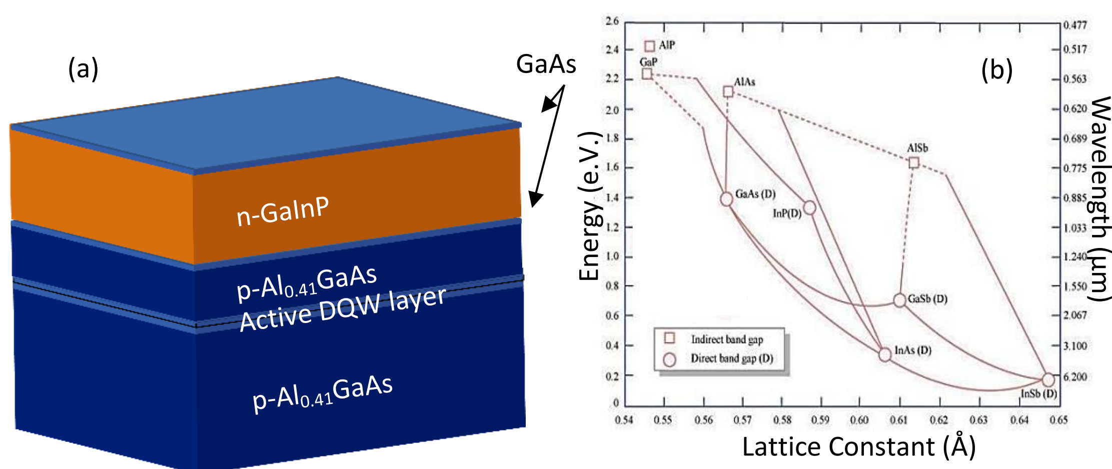

Figure 2-1: (a) schematic diagram of the grown structure ending at the second GaAs layer works as etch stopping layer (the GaAs substrate was excluded in this figure). (b) Energy Gap and Wavelength as a function of lattice constant for common III-V material [2],

Stripes are formed in this wafer by etching down regions through the n-GaInP layer and filling the gaps created with p-AlGaAs upper cladding. First the wafer was patterned using standard vacuum photolithography utilizing SPR350 photoresist. This specific photoresist is originally chosen due to its resolution, potentially able to resolve 600nm features, so, widths down to 1μm are available using this combination. The sample patterning starts with spinning SPR350 at 4000RPM leaving 1μm thick photoresist coating the wafer. After UV exposure through UV300 optics of an MJB-3 mask aligner, the wafer is developed using MF26A and finished with O_2 asher cleaning to remove any residue from the stripes. Following the patterning, the wafer is dry etched

using inductive coupled plasma (ICP) etcher, using $SiCl_4$/Ar to remove the upper 10nm GaAs and penetrate into the GaInP. Then the wafer is etched chemically using $C_6H_8O_7$/HCl (1:1) selective etchant to totally remove the GaInP and abruptly stop at the lower GaAs protecting layer which cannot be etched by this solution. The photoresist is then removed to re-grow the upper cladding and contact layers. The resist removal is done by dipping the wafer into a warm EKC830 photoresist stripper and then rinsing it in isopropyl acetate (IPA) before 1min O_2 plasma ash. The final step before reloading the wafer into the MOVPE reactor is to wash the sample in 1% buffer HF for 30sec and rinse in D.I. water.

The mask used to pattern this wafer has periods of stripes each with 5000μm length grouped in to sets of five elements. Two configurations can be taken from this wafer, the first one is the full active devices in which the active stripe is extended from end to end, the second configuration is the configuration in which the active stripes are stopped prior to the cleaved facet. Also, the wafer is divided into two regions. The first has stripes aligned along the <010> direction which can form SAS lasers (used later in the length dependant gain measurement) and devices that have normal-to-facet stripes and window regions will be used in estimation of the effective reflectivity of the window section (see section 3.5 for more details). The second has the same configuration but stripes tilted 10° w.r.t the <010> plane.

The designated target for this work is to present SLDs with window structures, which could easily coupled to standard single mode fibres. For that reason, the mask included 3 and 4μm width and 5000μm long stripes to allow or more geometrical selection flexibility. Figure 2-2a shows a schematic diagram of the etched planner wafer with the stripe formed. It also shows cross-section TEM images of test stripes in Figure 2-2b.

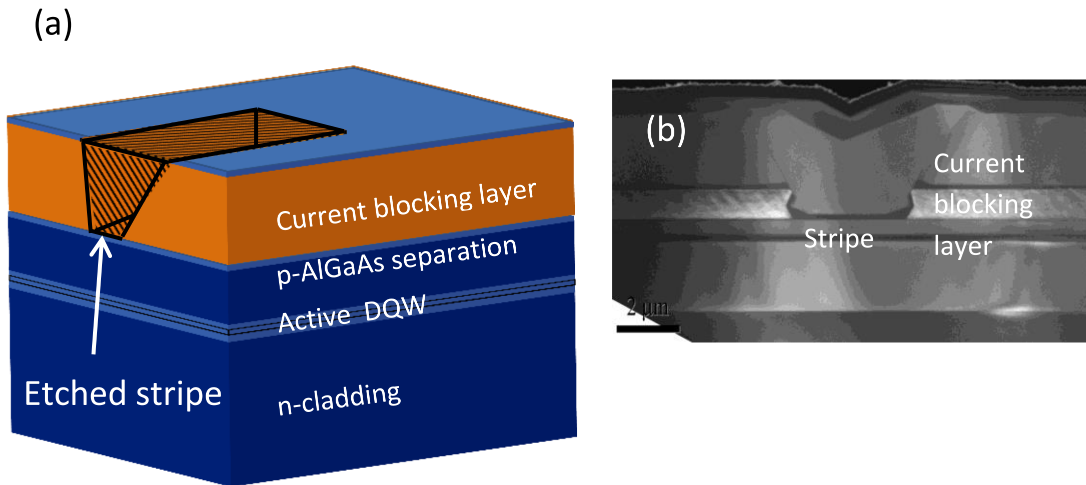

Figure 2-2: (a) a schematic diagram showing the etched planner wafer, (b) a TEM image of a cross-section of a test stripe showing the long side wall , and (c) a section taken in the longitudinal direction (along the stripe) showing the ends of the stripe.

Following formation of the stripes, a 100nm of undoped GaAs was first deposited, followed by 1.5µm p-$Al_{0.42}$GaAs, which was grown to form the p-cladding layer. The structure was finished with 300nm of p^+-GaAs capping layer. The doping density was set to $5\times10^{17}cm^{-2}$ in the n-GaInP and the p-AlGaAs separation layers, while the doping concentration of the cladding layers were stepped so that the 750µm closer to the active was maintained at $5\times10^{17}cm^{-2}$ while the 750µm farther from the active region was selected to have slightly higher doping of $1\times10^{18}cm^{-2}$. The contact layer was doped to $2\times10^{19}cm^{-2}$ and the active region containing the quantum wells, the GaAs barrier, and the GaAs guiding layers are left undopped.

The <111> cut caused a slight aluminium variation above the angled edges, which is typical for overgrowth of AlGaAs on non-planar surfaces, and has previously been used for growing quantum wire [3].

Figure 2-3a shows a schematic diagram of the final grown SAS structure, while the PL spectrum is recorded from unprocessed planar wafer at room temperature is shown in Figure 2-3b.

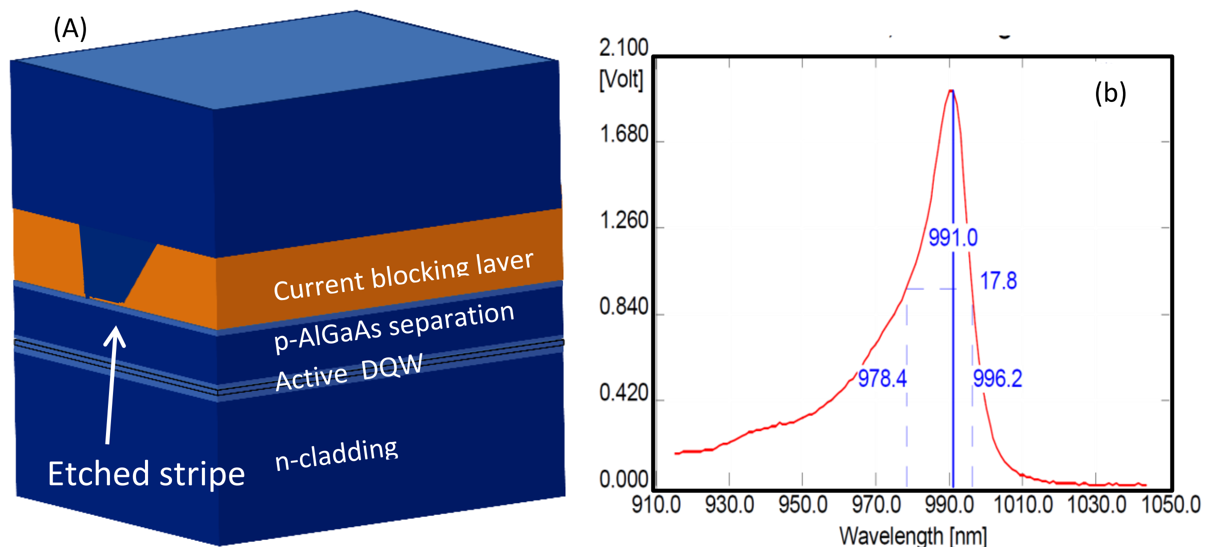

Figure 2-3: (a) A schematic diagram of the fully grown wafer with a self-aligned stripe etched and refilled. (b) the photoluminescence spectrum of the fully grown sample at room temperature.

Photoluminescence emission recorded from planar wafer at room temperature shows a peak at 990nm and a FWHM bandwidth of 18nm. Such a narrow bandwidth is expected for a material designed originally as a laser device active medium with identical quantum wells. This type of active is unusual for SLD devices which usually employ broadening techniques (e.g. QW chirping) to achieve a broader emission. The intention of my work was not to present broadband SLDs but to present a technique that can provide ultra-low facet reflectivity used to suppress the parasitic Fabry-Pérot resonance within the SLD. For this reason I used an active that provides high gain with narrow bandwidth to make lasing suppression more difficult and in this way I can investigate the maximum limits of the proposed low reflectivity facet. Suppressing the lasing in broadband actives is expected to be easier bearing in mind that the gain is smeared over a broad range of wavelengths and the peak gain is correspondingly low.

The wafer was processed with both straight waveguides (i.e. normal to cleaved facets) and 10° tilted waveguides using the same mask. The only penalty in this mask

design is that the adjacent devices in the same group have some difference in the active and passive parts length. For each pair of adjacent devices, the length uncertainty is ~70.5µm. This penalty will be apparent if we compared two devices at each end of a cleaved chip.

2.2.2 Post growth process:

Laser and SLD devices were processed from the overgrown material described earlier by the following process flow shown below.

1- P-ohmic contact metallization

The wafer is first patterned with PMGI and SPR 350 to provide a better lift-off photoresist profile. A 1 minute cleaning in the O_2 asher is used after the patterning, then, 20µm wide Au/Zn/Au 20/10/250nm thick layer is deposited above the active SAS stripes regions. The deposition is done using the thermal evaporator under low pressure (~10^{-5} mbar).

Following the deposition, lift-off is performed using acetone and the sample was annealed for 3 seconds at 360°C to minimize the contact series resistance.

2- Electrical isolation trenches

To isolate the adjacent devices trenches are etched. We stop the etching at n-GaInP layer since it already has high series resistance between the adjacent devices. As done with the metallization, the etching is started with patterning the wafer to protect the metal coated areas (the ohmic contacts) of the device. Trenches were etched down using HBr:$C_2H_4O_2$:K_2Cr_2O 1:1:1 wet chemical etching. Later, the photoresist was removed using EKC830 photoresist stripper and a three step solvent cleaning was performed to prepare the etched wafer for the next step. Figure 2-4 shows the etched wafer with the ohmic contact stripes on it and demonstrates the effect of the trenches on the carrier flow highlighted by the arrows in the figure 2 (*i.e.* isolation trenches provided individually separated devices but

they are sufficiently far from the stripes so as not to interfere with the operation of the SAS.

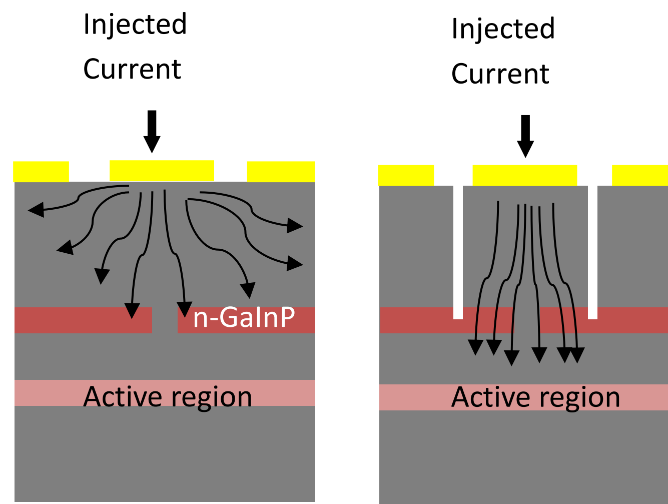

Figure 2-4: A comparison between the (a)non-etched, and (b) etched. The carriers flow without etching will spread to the adjacent devices in the first case will the carriers will be driven to the device underneath the pumping area only.

3- SiN deposition and Bond-Pads windows

The ohmic contact is only 20µm wide, which is not wide enough to bond the individual devices for electrical connection using the gold wire ultrasound bonder. A dielectric layer (namely SiN) is deposited to enhance the electrical isolation between the adjacent devices. By the plasma enhanced chemical vapour deposition (PECVD), 500nm of SiN was deposited on the wafer surface.

The deposition of SiN required a window opening to connect the devices. To do this the surface was patterned using SPR350 and the patterned wafer was loaded in the Reactive Ion Etching (RIE) for dry-etching. O_2/CHF_3 gas mixture was used in the process to etch away 500nm of the SiN from the areas covered with metal to open up the contact.

Following a thorough cleaning to remove any photoresist residue, the wafer was patterned by the same photolithography method used earlier. The patterned wafer was loaded to the thermal evaporator and Ti-Au layers of 20 and 300nm

thicknesses were deposited and Lift-off was performed. Figure 2-5 shows the processed device to this stage.

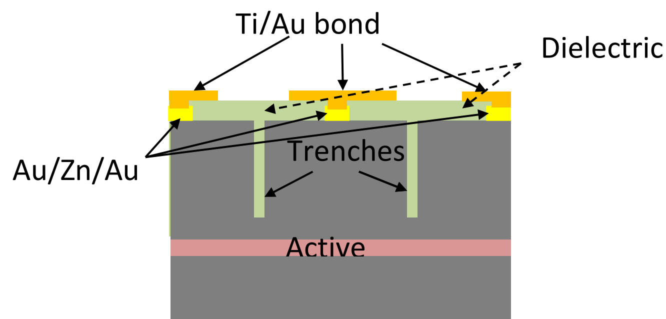

Figure 2-5: Device structure after depositing SiN, windows etching and bond pads deposition.

4- Wafer thinning and n-contact

To improve heat sinking and allowing cleaving, the wafer was thinned down to <120µm.

The final step in the device processing before dicing the wafer into individual devices was to create the back contact. An InGe/Au (20/300nm) alloy was deposited on the backside of the thinned wafer and annealed at 340°C in an RTA. Figure 2-6 shows the final processed device.

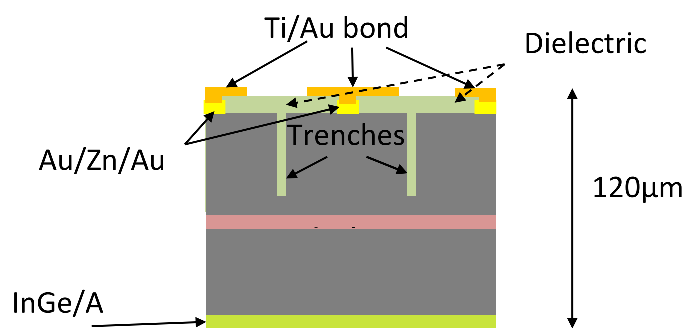

Figure 2-6: the final grown structure

5- Cleaving and packaging

Although the wafer was cleaved in different manners according to the device (section) required, the mechanism is the same. Cleaving was performed in a Loomis LSD-100 scribe and break system. Chips were mounted on a range of sub-mounts using InPbAg coating paste.

Goldwireball bonder, at a rate of two bonds per 250µm, was performed to connect the SLDs to the lead-out of the submount.

2.3 Measurement setups:

The measurement setups used in the experiments included in the thesis are described briefly in the following sections

2.3.1 light-current characteristics:

The setup shown schematically in Figure 2-7 is used as a mean to measure the emitted optical power from the characterized device as a function of the injected current. This setup implemented an InGaAs NIR photodetector connected to a Hewllet Packard (HP) 1810 power meter. The current was supplied from a CW current source integrated with a temperature controller in a laser diode modular controller ILX LDC 3900. The whole set of equipment was connected to a desktop PC controller running Labview that enables both manual and automatic control.

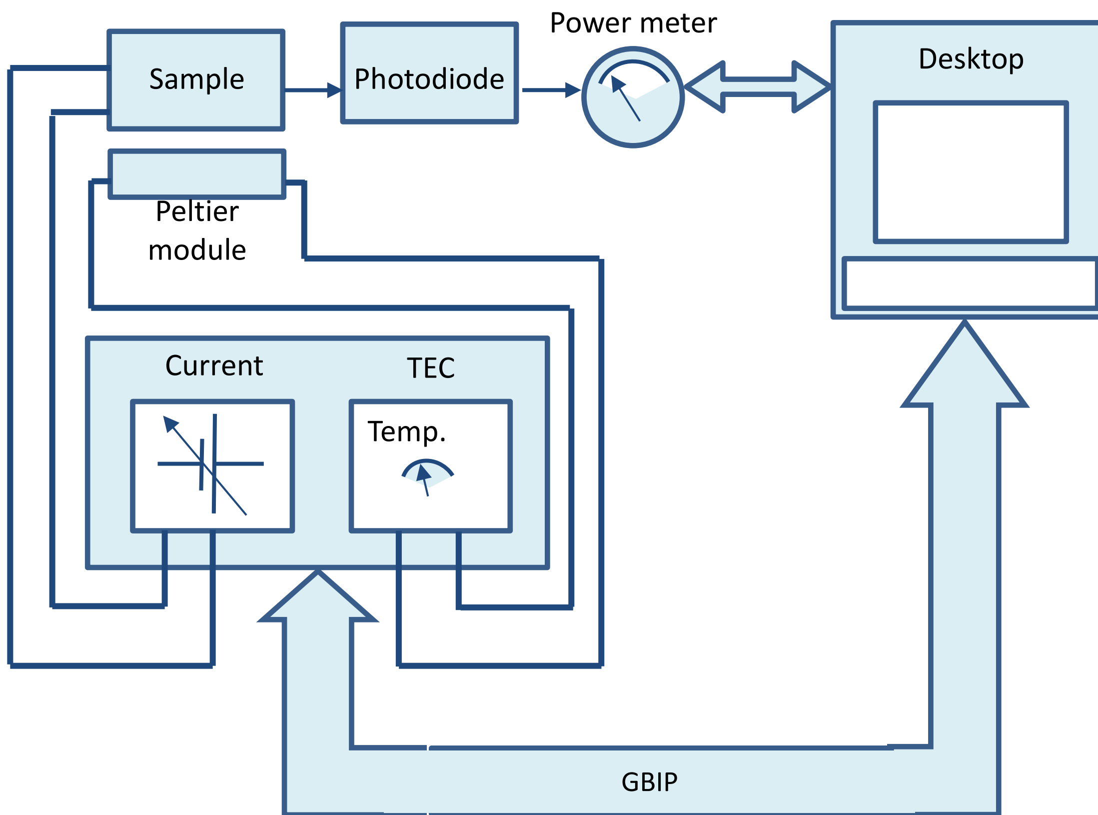

Figure 2-7: Light-Current Characteristic setup

2.3.2 Low resolution electroluminescence (EL) setup:

This setup was used to measure the EL spectrum of the tested device with a resolution range between 10 nm to 0.1nm. Usually, this setup is used as initial screening of the devices, in order to determine whether the devices exhibits lasing or not. The setup consists of current sources (pulsed and CW) for current injection into the devices under test, which are situated on a temperature controlled stage. The emitted light is collected by a multimode fibre fixed on an X-Y-Z translation stage, and the collected light in the fibre is delivered to an HP 70004A optical spectrum analyser (OSA). Again, the whole setup is driven by a desktop computer, enabling automatic or manual data collection. The spectral range, maximum resolution, and number of samples per scan is governed by the limits available in the OSA, which are 600-1700nm, 0.1nm, and 2048 sample points respectively. The setup is shown schematically in Figure 2-8 with all its parts highlighted.

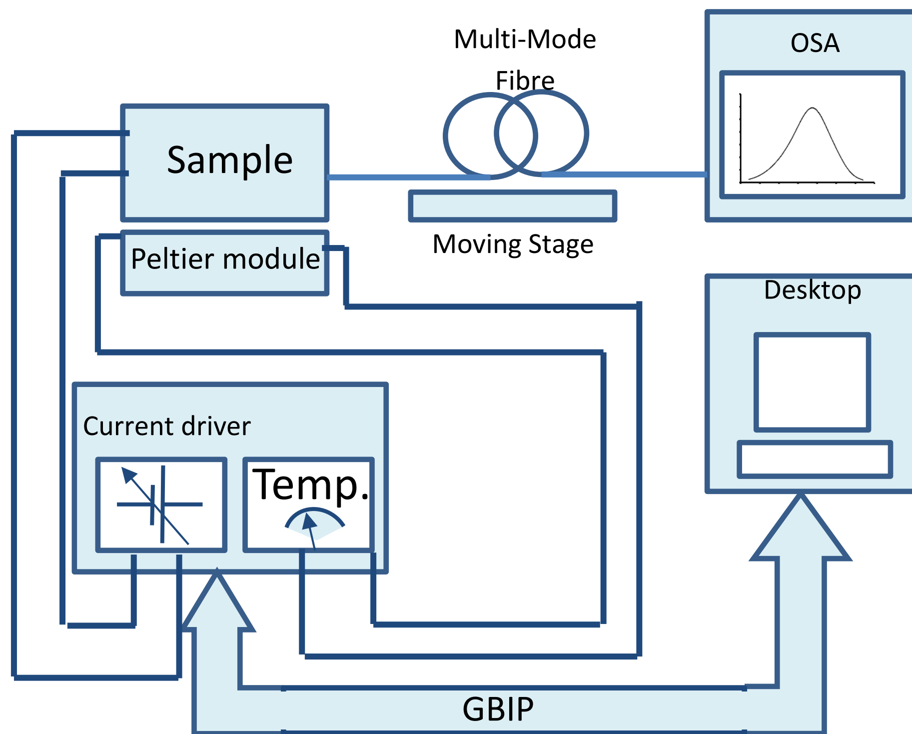

Figure 2-8 Low resolution EL measurement setup.

2.3.3 High resolution EL setup:

The high resolution EL setup, shown schematically in Figure 2-9 is very similar to the low resolution counterpart, but replaces the multimode (MM) fibre with a single mode fibre.

Positioning of the single fibre is much less tolerant to mis-alignment compared to the MM case. For this reason, the XYZ stage is now attached to an adaptive positioner that enables the position of the lensed fibre tip to be automatically controlled to sub-µm alignment precision, which will enable high and consistent coupling efficiency and more accurate data collection The OSA used in this setup is the Q3804 Advantest optical spectrum analyser. The resolution range is now expanded from 0.5nm to 0.01nm while the number of sample points is almost increased to five folds to reach 10001 sample points over the same wavelength range. The rest of the apparatus is the

same as that shown for the low resolution EL setup. This setup is used to inspect the Fabry-Pérot modes of the device as it can resolve them easily.

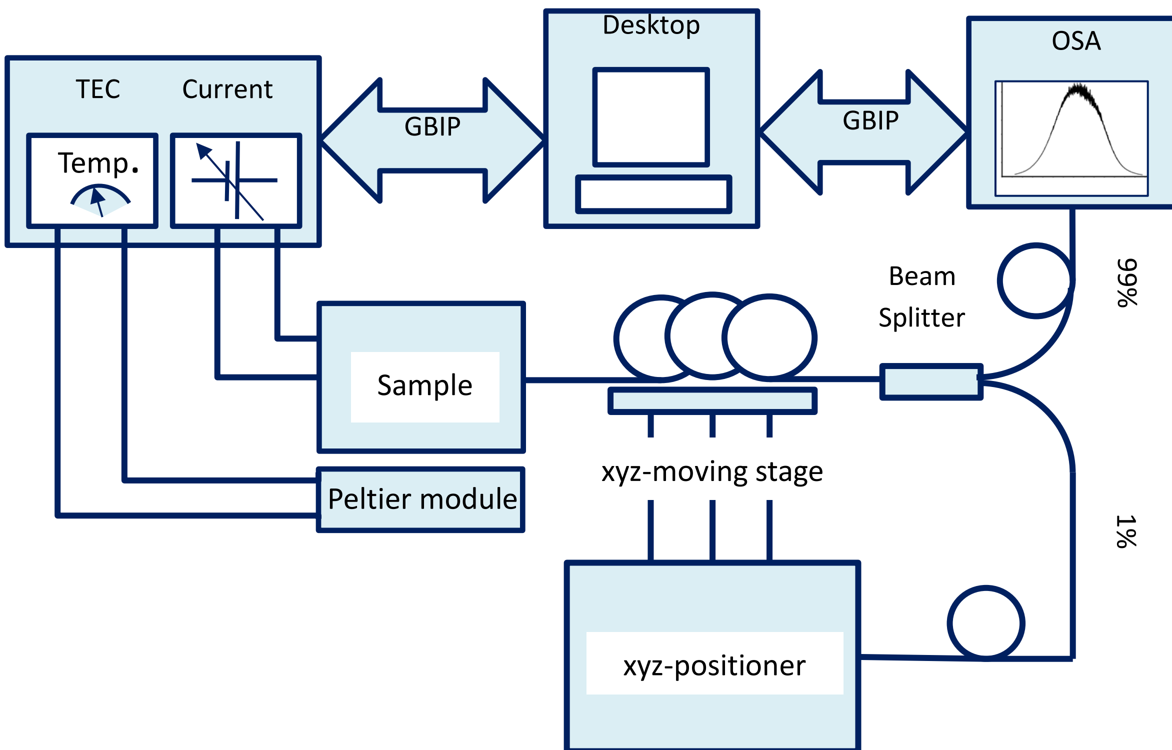

Figure 2-9: Setup used for the high resolution EL measurements

2.3.4 Photocurrent setup:

The photocurrent setup, shown in Figure 2-10 below, is used in this thesis to identify the absorption peaks of the unpumped material which corresponded to emission peaks if forward bias is applied to the structure. When optical excitation is applied to a semiconductor structure, e^- and h^+ pairs are excited through interband absorption. If the charge carriers are able to escape before they have the chance to recombine, then a photocurrent (PC) signal results. The PC signal provides a quantative representation of the absorption spectrum of the sample (where $I_{pc} \propto \alpha L$). Excitation light is modulated by a mechanical optical chopper, enabling the small PC signal (usually in nA range) to be extracted from the background using lock-in amplifier. The spectrometer of the setup is synchronised with the lock-in amplifier through a desktop PC.

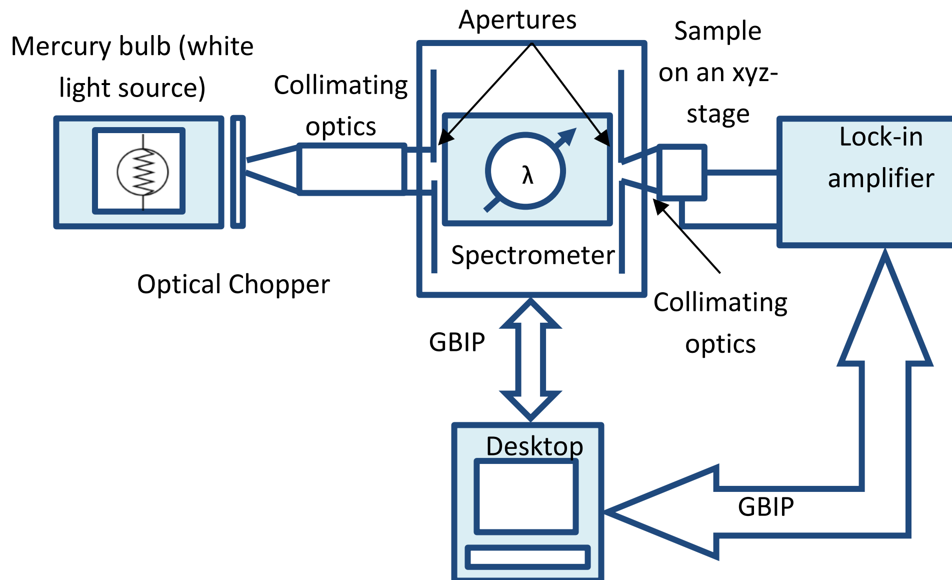

Figure 2-10: Setup used for photocurrent measurement.

2.3.5 Farfield setup:

The farfield setup used for the measurements described in the thesis is simply an XY plane detector covered with a swinging slit, and intensity data to produce even the farfield in the x (horizontal) direction or Y (vertical) direction and 3-dimensional measurement. The swinging slit is positioned at a specific distance from the output facet of the device, this distance need to be accurately inserted to the running program since it will be the reference point to be used in the measurement. The divergence angle is calculated by the program from comparing the exposed length in the slit and the distance between the slit and the output facet. The running device is operated under conditions controlled as in the previous measurements.

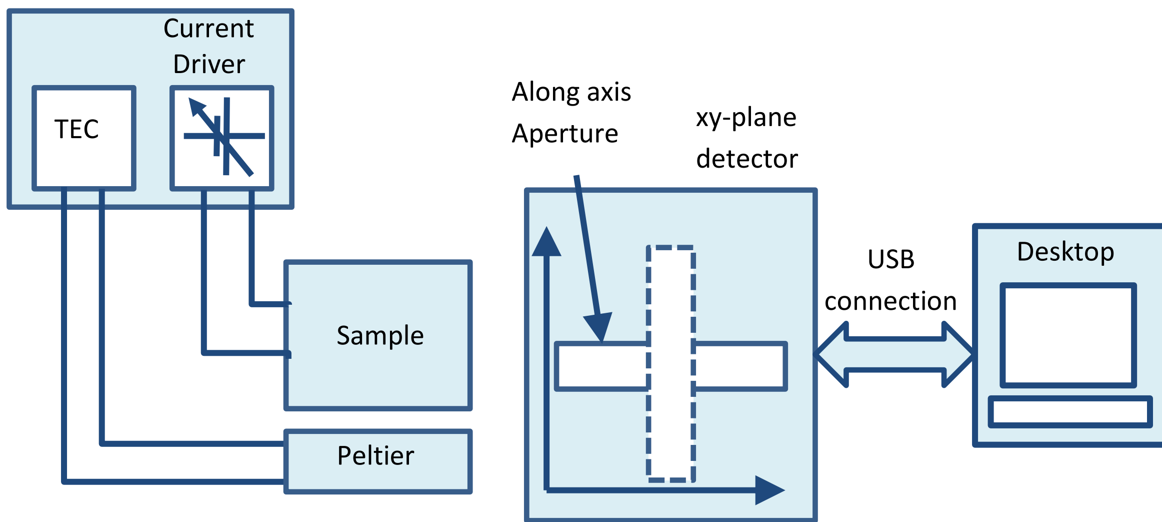

Figure 2-11: The setup used for farfield measurement.

2.3.6 SOA characterization setup

In order to characterize the SAS waveguides as semiconductor optical amplifiers, a setup was assembled based around a Thorlabs TLK1050 tunable laser with a maximum power of 16mW and a central wavelength around 1050nm. This laser was used as an input signal while the output is observed on an HP 70004 optical spectral analyser. The tunable laser is centred at 1050nm±40nm; unfortunately this is some distance away from the central wavelength of the grown material which was at 993nm. However, a 3dB intensity of ASE of the two devices can meet at ~997nm as can be seen in Figure 2-12.

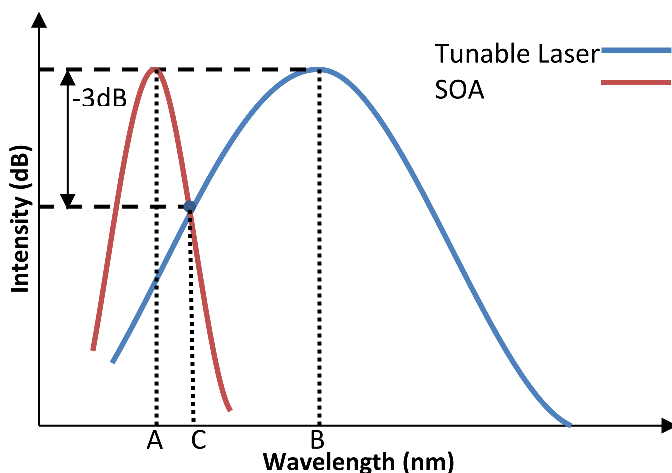

Figure 2-12: the relative spectra of the SOA (red line) and the tunable laser (blue line). The central wavelength of the SOA is at 993nm (represented by point A) while the central wavelength of the tunable laser is around point B (1050nm). The spectra of the two devices meet point C which is around 997nm; at this point the two devices can provide an output power within the 3dB bandwidth of the device.

The assembly is shown in Figure 2-13. A variable attenuator is fitted at the output of the tunable laser in order to control the intensity of the injected light. Also, since the SOA can have any polarization (a typical property of the edge emitting device) a polarizer was inserted between the attenuator and the input facet of the SOA to tailor the tunable laser polarization to the polarization of the SOA. The polarization effect can be sensed as an intensity of the amplified signal on the OSA, when the two devices have the same polarization the maximum intensity will be observed while the intensity drops once the polarization differs. The light was driven in the setup using a single mode lensed fibre to achieve the best coupling efficiency. The lasing peak was tuned using a thermo-electrical controller (TEC) integrated with a CW current source feeding the tunable laser. The SOA was pumped using a separate CW current source.

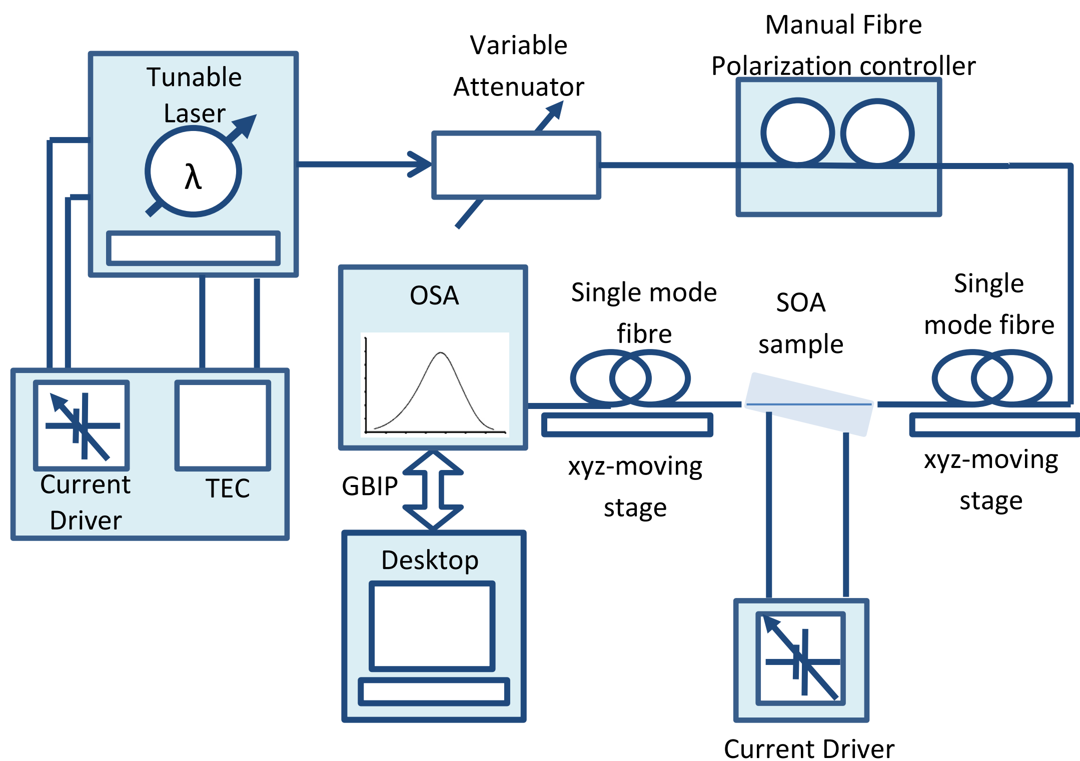

Figure 2-13: The assembly used to characterize the material as a semiconductor optical amplifier.

2.4 Photocurrent Spectroscopy:

Photocurrent is one of the spectroscopy techniques used to investigate the behaviour of the semiconductor structure. Presented for the first time by Tarricone et.al. in 1992 [4]. If an optical signal with specific energy (E) is applied to a specific quantum structure (QW or QD), the carriers within these structures will be excited accordingly. If this energy a greater than or equals the bandgap (Eg) of this structure the excited carriers will possibly escape the bond of the structure and become free charge carriers. If a complete circuit is connected to this structure, the charge carriers appear in the form of dark current.

This technique is considered the opposite of the other two techniques presented before it (the electroluminescence [5][6], and photoluminescence [7]) where in the latter two the optical emission from the excited structure is collected at a range of wavelengths to identify the emission peaks. Figure 2-14 shows a simplified schematic of the latter two spectroscopy methods.

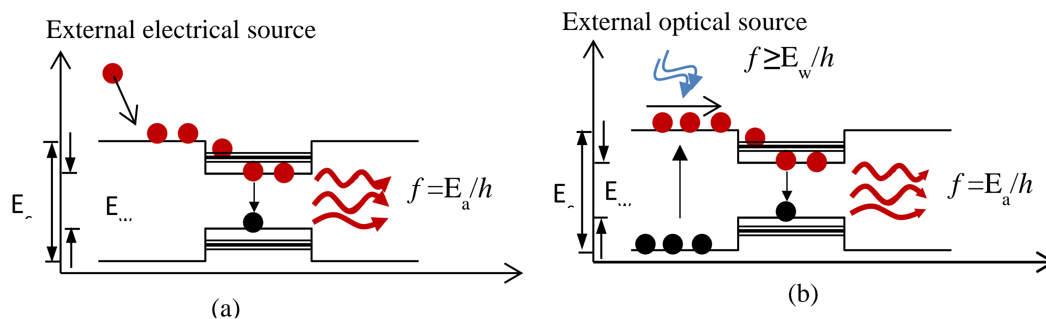

Figure 2-14: The Electroluminescence (a) and Photoluminescence (b) mechanisms in simple two level system with active and cladding region having Ea and Ew, respectively. In (a) an external source pump the structure with excited electrons which undergoes transitions in the active region and emit light with a specific bandwidth corresponding to the available sub-bands in the active. On the other hand, the external optical source with energy >E_w in the PL spectroscopy excites the electrons from the valance band in the cladding layers, these excited electrons relax to the lower energy levels available in the active layer and do the transition which results in light emitted associated with the emission peaks available.

To detect the higher energy emission in EL and PL spectroscopies requires filling the quantum states with enough energy to move to shorter wavelength (higher energy). On

the other hand, since the photocurrent is resulted from the free carriers created from any transition, higher order emission does not require any state filling as long as an emission with enough energy is applied. For that reason, the photocurrent spectroscopy method is superior over EL and PL methods in detecting all the available absorption peaks in the case of unbiased structure.

These peaks are the emission peaks in the cases of active (forward biased) devices. Figure 2-15 shows a schematic of the photocurrent spectroscopy mechanism and a PC spectrum measured by Polland et.al. [8] for a GaAs/$Al_{0.4}Ga_{0.6}As$ structure.

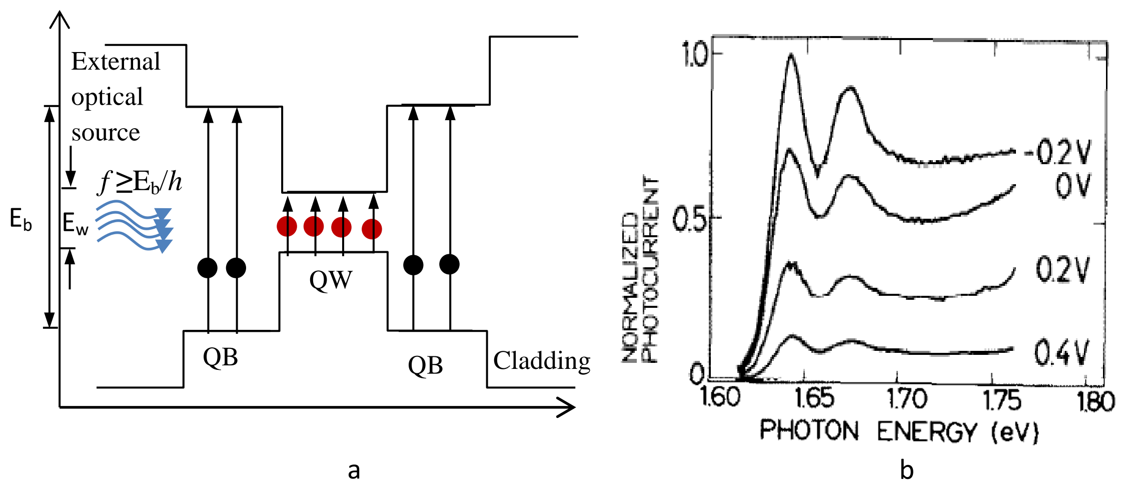

Figure 2-15: a simple schematic of QW/QB system showing the concept of photocurrent (a) and the PC spectrum published by Polland et.al. [8] (b). The incident optical energy excites the electron in the undopped region these excited carriers can be collected in form of dark current, the intensity of the current collected is related directly to the absorption capability of the device at the associated wavelengths. Polland et.al presented devices that could absorb light with photon energy around 1.65eV which correspond to GaAs and $Al_{0.4}GaAs$.

2.4.1 Sample Preparations

Measuring the photocurrent requires a sample to be prepared with optical access mesa and annular top contact. Such mesa diodes are prepared with diameter equal to 100µm in design with top contacts (Au/Zn/Au) that was 100µm outer diameter and 80µm inner diameter. The required mesas were processed at the same time as the stripes were done in some areas in the mask, these mesas also had the current blocking layer

etched away to create a p-i-n junction. Figure 2-16 shows the mesa diode used to characterise the material using the photocurrent technique.

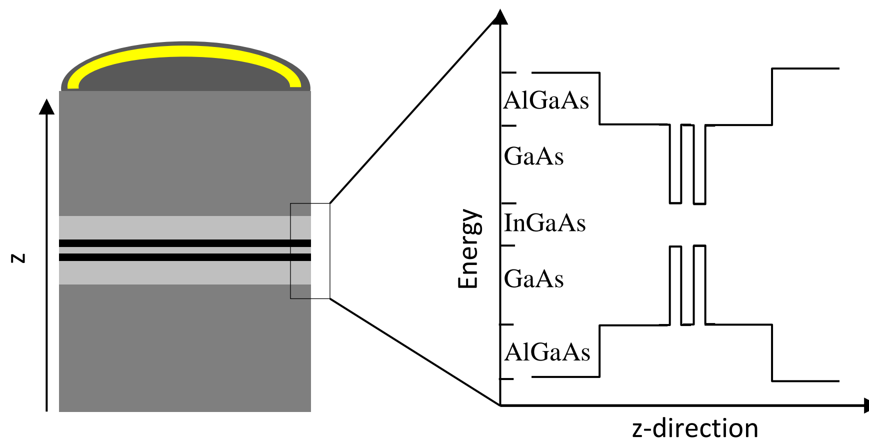

Figure 2-16: A simplified schematic diagram showing the epitaxial structure with the band structure of the active layer and the surrounding area. The energy diagram shows the material that can provide a radiative recombination if the photocurrent technique is used.

2.4.2 Measurement and Results

The sample was set on the photocurrent setup described in 2.3.4. The measurement was conducted with no applied bias on the structure and no temperature control. The output in this case will show the natural absorption peaks of the grown material. Such absorption would be expected in the unpumped regions of window structure devices, where the active region remains intact below the current blocking layer. The light source used is a broadband mercury lamp which provides light signal from the UV wavelengths up to the near IR. The wavelength was swept using the monochromator from 750nm up to 1050.

Figure 2-17 shows the absorption spectrum measured from this mesa diode. Six peaks are observed in the spectrum, taking into account that the $Al_{0.4}GaAs$ absorption peak is located ~620nm it can be assumed that the six peaks appeared are the absorption peaks of the $In_{0.17}GaAs$ (990, 960, and 915nm) quantum wells and GaAs (855, 813, and 776nm) quantum barrier and guiding layers. The thick GaAs layers results in higher absorption compared to the thin InGaAs quantum wells. The GaAs 776nm is expected

to be e_1-lh_1 of the strained GaAs barrier between the two quantum wells while the 810nm is the e_1-hh_1 transition. The 850nm is the common absorption/emission central wavelength of the relaxed GaAs material, such material is available in the guiding layer sandwiching the active DQW layer.

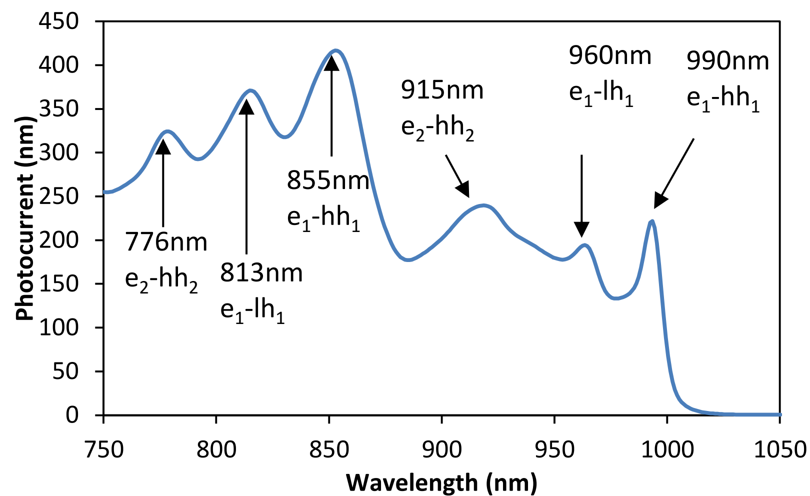

Figure 2-17: The photocurrent spectra showing the absorption peak available.

The three peaks that appear between 910nm and 993nm correspond to the absorption maxima related to the strained $In_{0.17}GaAs$ QWs. The maximum absorption is at the QW basic e_1-hh_1 transition at 990nm which appears usually at the pumping levels used in most of the devices presented in the thesis. The higher order transitions, second and third peaks, require high pumping levels to fill the states in between the ground state and the higher ones. The second and third absorption peaks cannot be observed usually by pumping the related device electrically at room temperature especially the shortest, the ~960nm absorption/emission peak can be observed in the EL spectrum at room temperature if the pumping level was high enough to fill in the quantum states in the first transitions to move to the next one (the 960nm).

2.5 Length dependant measurement:

A number of techniques are available to accurately characterise the optical gain, such as segmented-contact method [9], or Hakki-Pauli method [10]. However, perhaps the

simplest and the quickest method is the length dependant method shown in this section. Devices with different cavity lengths are processed from the same material used. All the devices will have the same internal properties and differ only in their cavity lengths. By measuring the slope efficiency as a function of cavity length, both the optical gain and the internal losses can be extracted. By tracing the variation of the threshold modal gain as the threshold current density changed, a gain vs threshold current curve can be constructed relating the modal gain G_o to the transparency threshold current density (J_o), the relationships are described thoroughly by Coldren and Corzine in [2].

Devices with straight waveguides were used as SAS lasers to measure the gain of the grown material. Multiple laser cavity lengths were selected and a particular focus was made on devices shorter than 1000µm in order to achieve high threshold current density. The reason of that is to ensure accuracy of the fit to the experimental data at high current densities employed in the SLD devices. The gain measurement procedure can be summarized by measuring the LI of the devices to ~1kA.cm^{-2} after the threshold. Then by extracting the internal losses combined with the mirror losses, the material gain G_o can be estimated.

The devices were first cleaved to obtain devices with 250, 350, 400, 500, 600, 700, 750, 1000, and 1500 microns. The devices were operated to maximum a current of 25mA for the shortest devices up to 70mA for the 1500µm devices. These values are equivalent to 3.333kA.cm^{-2} and ~1kA.cm^{-2}, for the 250µm devices, respectively. The threshold current density for each device was found and set in groups according to their cavity lengths. The threshold current densities are plotted in Figure 2-18 as a function of the reciprocal cavity length (1/L) in order to find the transparency current density J_o, which is the threshold current density for an infinitely long device. The measurement showed J_o to be 560kA.cm^{-2}.

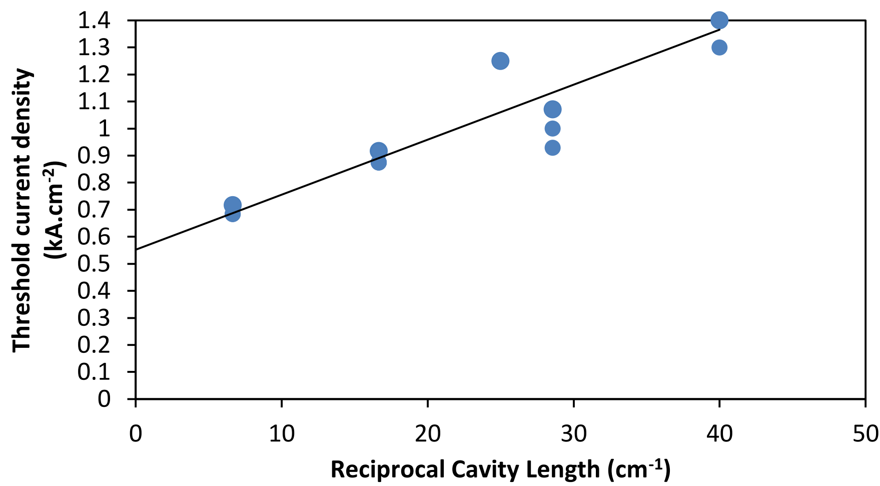

Figure 2-18: shows the threshold current density curve as a function of the reciprocal cavity length.

From the examination of the LI curve of every device beyond the threshold the slope efficiency (dP/dI) was extracted, representing the ratio of the collected output power to the injected current. From this ratio the differential efficiency can be found by:

$$\eta_d = \frac{q.\lambda}{h\ c} \cdot \frac{\Delta P}{\Delta I} \qquad \text{...... eq. (2-1)}$$

While q is the elementary charge, λ is the central wavelength of the emitted light (990nm), h is Plank's constant and c is the light speed in the vacuum. The differential efficiency is the number photons leaving the laser to the number of electrons injected in it, including the losses inside the laser cavity and the light reflected back into the laser cavity due to the facet reflectivity. If the inverse value of the differential quantum efficiency is calculated for each cavity length, then the value of the 0µm long device is the internal quantum efficiency since in this case the other parameters are not presented. Figure 2-19 shows the differential quantum efficiency as a function of cavity lengths.

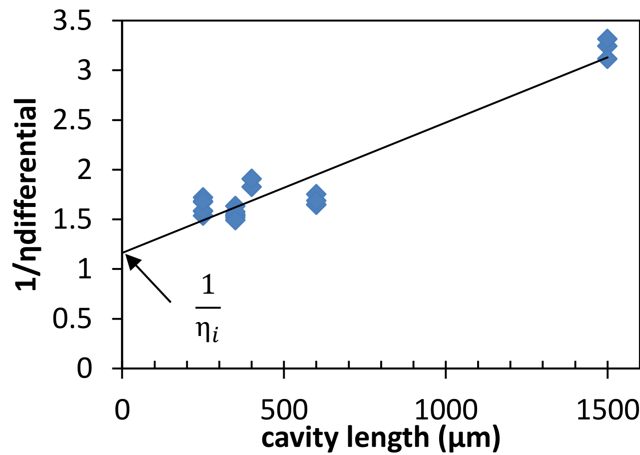

Figure 2-19: Reciprocal $\eta_{differential}$ as a function of cavity length.

From the relationship between η_i and η_d the internal losses can be extracted where:

$$\frac{1}{\eta_d} = \frac{1}{\eta_i}.\left[1 + \frac{\alpha_i}{\ln(\frac{1}{R})}.L\right] \qquad \text{...... eq. (2-2)}$$

where α_i is the internal losses, L is the cavity length and R is the reflectivity of the facets. Rearrangement of eq. 2-2 allows the internal losses to be calculated:

$$\alpha_i = \frac{\ln(\frac{1}{R}).\left[\frac{\eta_i}{\eta_d} - 1\right]}{L} \qquad \text{...... eq. (2-3)}$$

To achieve lasing, the gain should be greater than the combined losses of the device (α_i+α_m). The threshold gain is the value of gain for that specific device where the gain of the material is exactly equal to the losses. For simplicity, the losses were limited to mirror losses and internal losses.

Internal losses can be extracted following the procedure described above while the mirror losses depend on both the reflectivity of the facets, and the active cavity length. Since both of them are constant for a specific device, each device will have a constant mirror losses added to the internal losses. This will result in a specific threshold gain G_{th} for each device. By putting the resulted G_{th} as a function of the relating threshold current

density J_{th} , the resulted curve has a logarithmic behaviour which can be fit to the equation relates the four parameters G_o, G_{th}, J_{th}, and J_o:

$$G_{th} = G_o \,.\ln\frac{J_{th}}{J_o} \qquad \text{...... eq. (2-4)}$$

If J_o is fixed to the value extracted from the measured data, the calculated G_{th} can fit the measured data if the material gain G_o is between 80 and 85cm^{-1}. The final GJ figure shows that three curves can be fitted for the three widths in the mask used.

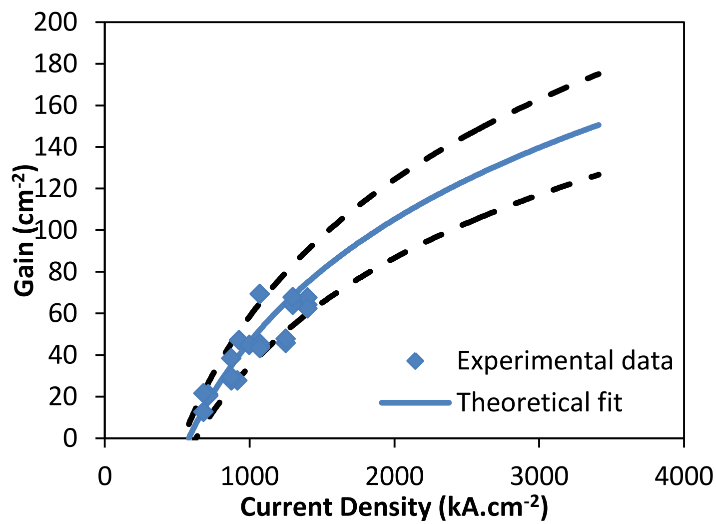

Figure 2-19: The Modal Gain as a function of Current density, square dots are the threshold gain estimated at the measured current density.

2.6 Summary and Conclusions:

In this chapter two main subjects were highlighted, the first one was the measurement setups used in this thesis to characterize the devices and the material used in this study.

Measurement setups are explained briefly combined with schematics that show how they are connected and how they operate. 5 systems are demonstrated, the Light-current characteristics setup which can be used to measure the emitted power from the device in free-space. Additional information such as the efficiency of the device and the heating effect can be extracted from such measurements using this setup. This setup specifically helped measuring the modal gain of the developed structure by the length dependant

gain measurement method. The second and the third setups are very similar in function in which they both measure the electroluminescence of the developed material. The low resolution setup is used mainly to confirm the spectral range of the devices presented in the thesis, the high resolution setup on the other hand is used in the characterization of the superluminescent diodes that will be presented in the third and fourth chapter of the thesis. The maximum resolutions of these systems are 0.1nm for the low resolution setup and 0.01nm for the high resolution one. The fourth setup presented in this chapter the photocurrent setup is used to identify the absorption peaks of the grown material as detailed in section 2.4. The fifth setup shown in 2.3.5 is the farfield setup which is used to define the farfield pattern of the light/laser emitting devices studied in this thesis. Finally the sixth setup is the one used to characterize the semiconductor optical amplifier as will be detailed in chapter five.

The second part of this chapter is the one related to the material grown and used in 3 of the next 4 chapters of the thesis where first started with detailed growth and processing methods used to achieve the self-aligned stripe devices (SAS). The final wafer included sections that included windowed and non-windowed areas with tilted and straight waveguides. The tilted waveguides are studied thoroughly in the upcoming chapters where the straight waveguides are characterized as laser devices with different cavity geometries to measure the modal gain of the grown structure. The gain was estimated by setting a curve showing the threshold current density as a function of the threshold gain of the devices, the modal gain G_o was found to be fluctuating between the 90 and 75 cm^{-1}.

Since the absorption (or in the suitable conditions emission) peaks play an important role in the device performance, the photocurrent of the device was measured at a range of wavelengths. The main peaks detected by this measurement was the ground state

peak at 992nm, the first excited state peak at 960nm and the second excited state at 915nm. Extra peaks related to the cladding layers of GaAs and AlGaAs is detected too in the short wavelength part of the spectrum shown in Figure 2-(4). The photocurrent measurement was done on the mesa diodes that were available on the same grown wafer.

2.7 Future Work

Further investigation can be done on the material gain where two other methods are available which are Hakki-Paoli [1], and the segmented contact methods[2]. These two methods are done in the pre-lasing range of pumping.

2.8 References

[1] K. M. Groom, B. J. Stevens, P. J. Assamoi, J. S. Roberts, M. Hugues, D. T. D. Childs, R. R. Alexander, M. Hopkinson, A. S. Helmy, and R. A. Hogg, "Quantum Well and Dot Self-Aligned Stripe Lasers Utilizing an InGaP Optoelectornic Confinement Layer," *IEEE Journal of Selected Topcis in Quantum Electronics*, vol. 15, no. 3, pp. 819–827, 2009.

[2] L. A. Coldren and S. W. Corzine, *Diode Lasers and Photonic Integrated Circuits*, First Edit. New York, USA: John Whiley and Sonds Inc., 1997.

[3] M. Walther, E. Kapon, J. Christen, D. M. Hwang, and R. Bhat, "Carrier Capture and Quantum Confinement in GaAs/AlGaAs Quantum Wire Lasers Grown on V-Grooved Substrates," *Applied Physics Letters*, vol. 60, no. 5, p. 521, Feb. 1992.

[4] L. Tarricone, C. Arena, A. Parisini, and F. Genova, "Photovoltage and Photocurrent Spectroscopy of p^+-i-n^+ GaAs/AlGaAs Quantum Well heterostructures," *Journal of Applied Physics*, vol. 72, no. 8, p. 3578, 1992.

[5] T. L. Larsen, "The Effect of Cu Impurities on Infrared Electroluminescence in GaAs p-n Junctions," *Applied Physics Letters*, vol. 3, no. 7, p. 113, 1963.

[6] S. Ku and J. F. Black, "Injection Electroluminescence in GaAs-GaP Diode," *Solid State Electronics*, vol. 6, no. 7, pp. 505–509, 1963.

[7] R. Cingolani and K. Ploog, "Frequency and Density Dependent Radiative Recombination Processes in III-V Semiconductor Quantum-Wells and Superlattices," *Advanced Physics*, vol. 40, no. 5, pp. 535–623, 1991.

[8] H. J. Polland, Y. Horikoshi, E. O. Gobel, J. Kuhl, and K. Ploog, "Photocurrent and Picosecond Photoluminescence Spectroscopy In GaAs/AlGaAs Quantum Wells," *Surface Sciences*, vol. 174, pp. 278–282, 1986.

[9] A. Sobiesierski, I. C. Sandall, P. M. Smowton, P. Blood, A. B. Krysa, M. R.

Brown, K. S. Teng, and S. P. Wilks, "AlGaInP Laser Diodes Incorporating a 3λ/4 Multiple Quantum Barrier," *Applied Physics Letters*, vol. 86, no. 2, p. 021102, 2005.

[10] B. W. Hakki and T. L. Paoli, "Gain Spectra in GaAs Double-Heterostructure Injection Lasers," *Journal Applied Physics*, vol. 46, no. 3, pp. 1299–1306, 1975.

Chapter 3: Tilted Self-Aligned Stripe SLDs with Low Facet Reflectivity.

3.1 Introduction:

In this chapter I describe the design and characterisation of window-structured self-aligned stripe SLDs based on the structure described in 2.2. Analysis of the spectral modulation depth (SMD) and its dependence on the device geometry and the pumping levels revealed a high output power could be attained with low spectral modulation depth, which was not achievable before without the additional application of AR-coating.

The presence of the active medium in a “window-like” region at the back facet enhances feedback suppression compared to the transparent window counterparts. The SLDs were able to suppress lasing to very high pumping levels, despite being manufactured from a material based on an active medium designed for low threshold current lasers. With improved heatsinking, I was able to present SLDs that are competitive with commercially available devices. SLD output with spectral modulation depth of 1-2% and output power up to 38mW was achieved under pulsed operation and 5.5% SMD at 30mW output power in CW operation. A relationship between the emission band in the active stripe and the absorption band in the window region is revealed and suggestions for potential improvements are discussed at the end of the chapter.

3.2 Background:

SLDs played essential role in the development of applications such as optical-communication [1], [2], fibre-optic gyroscopes [3], sensing [4], [5], and both industrial [6]and biomedical [5] optical coherence tomography.

As mentioned earlier, ASE is described as high brightness broadband emission. This type of emission combines the benefits of the low brightness broadband emission of the spontaneous emission, and the very high brightness narrow bandwidth stimulated emission. Figure 1-7 showed a common LI curve of a semiconductor laser highlighting the transitions take place during the operation from the linear increase in spontaneous emission at low pumping current, then the exponential increase which represent the amplified spontaneous emission, and ending with the linear increase in intensity of the amplified stimulated emission.

The common bandwidth of SLDs ~30-50nm [7] which is narrower than the common bandwidth of LEDs which can exceed 400nm. However, recent reports demonstrated SLDs with bandwidth up to 150nm for improved application of OCT [8]. As mentioned above, ASE appears when the spontaneous emission undergoes amplification in a gain medium with population inversion before reaching the threshold gain. The feedback provided by the device facets enable stimulation of excited carriers to emit light coherent to the propagated light. In order to stop turning ASE into amplified stimulated emission, feedback should be suppressed. Feedback suppression can be achieved by reduction of facet reflectivity to effectively extend lasing threshold to such a point that it will not be reached.

3.2.1 Single Pass Amplification

Single pass amplification can be described using Figure 3-2. This type of emission results from amplification of incoherent light generated at point x=0 propagating in an optical cavity of length L. To keep this emission broadband the reflectivity of the device facets/mirrors should ideally be zero in order to suppress feedback and permit light to pass through the cavity only once, where it subject to amplification according to the gain provided by the material, G. Figure 3-1 shows a simplified version of a two-level energy system in a semiconductor device in which spontaneous emission is taking

place. If we assume that the spontaneous emission generated at facet number 1 (at x=0) of an edge emitting SLD traveses the optical cavity to x=L, the generated photon population at x=L (facet 2) is proportional to exp(GL).

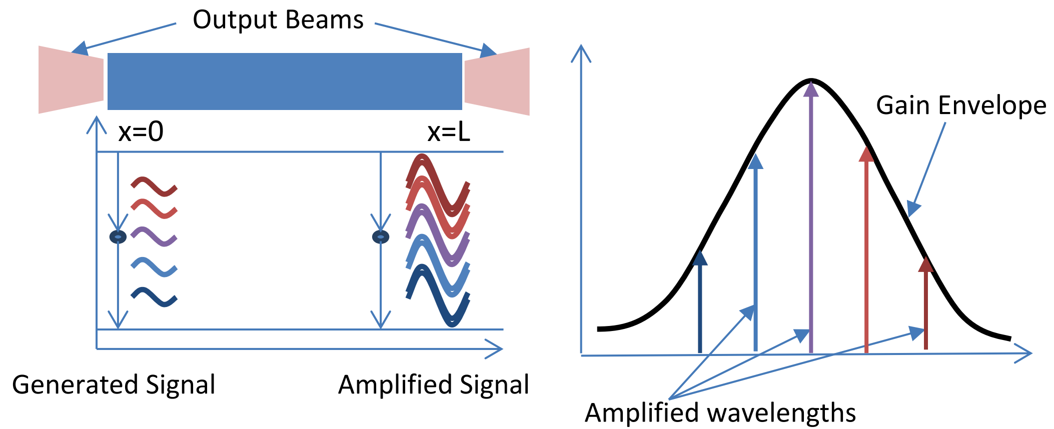

Figure 3-1: A simple two-level energy system showing that the light generation and its amplification depend on the transitions from the excited to ground levels. Both of them start as non-coherence, while the light travels along the active that have a gain profile shown in the right-hand side-figure with an exponential rate. In SLDs the reflectivity should be zero to disable any amplification for the amplified wavelengths.

The gain envelope shown in Figure 3-1 represents a probability of the transitions to occur in the system. With the presence of feedback the probability of having more transitions at the central wavelength and though more amplification, this results in faster accumulation of optical density in the related wavelength and eventually lasing. The effect of feedback suppression is mainly to keep the probability of all the transitions to remain the same as they are and so no mode is preferable to be amplified than the others.

3.2.2 Common structures

The basic form of an SLD is very similar to that of an edge emitting laser but with an essential difference in the reflectivity of the facets. Facet reflectivity should ideally be zero in order to achieve the single pass amplification. Reduction of facet reflectivity to zero remains a significant challenge, one which has been discussed widely during a number of attempts to reduce facet reflectivity using a variety of methods which I will

outline in the next section. If facet reflectivity cannot be reduced to zero there will exist some residual reflectivity which results in an unwanted feedback loop in the active waveguide. This feedback allows formation of Fabry-Pérot mode from the standing wave set up within the cavity. These parasitic Fabry-Pérot modes appear as ripples, or spectral modulation, in the electroluminescence spectrum of the SLD. With sufficient electrical pumping these modes could eventually reach threshold and lase. The period of the spectral modulation therefore corresponds to the Fabry-Pérot spacing which can be calculated from the cavity length between the two facets, L, the propagated wavelengths, λ, and the related refractive index, n:

$$\Delta\lambda = \frac{\lambda^2}{2nL} \qquad \text{...... eq. (3-1)}$$

This ripple is considered as a noise superimposed upon the SLD performance and its existence has a negative effect in all intended applications. In communications applications it can affect the coding of the transmitted signal, for example in wavelength division multiplexing, WDM. To understand the effect of ripple on such events, assume two signals sent in two close-by wavelengths, one of them is 0 (with low intensity) and 1 (with high intensity). The modulation can alter the values of the two signals. In optical coherence tomography (OCT) applications the ripple affects the operation in two aspects. The first one is that the ripples amplitude appear as ghost images accompanied by the original image, whilst they also decrease the resolution of the whole system since the resolution is directly related to the squared value of the device bandwidth [9]. Figure 3-2 below shows the Fourier transform of a practical SLD with some spectral modulation on the top of the electroluminescence spectrum.

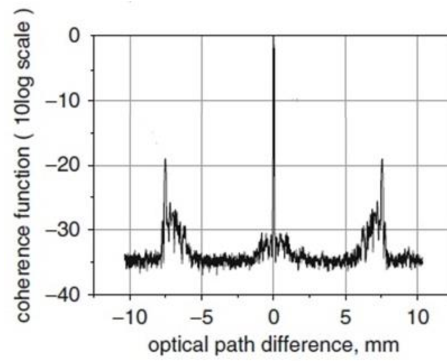

Figure 3-2: The fast fourier transform of a signal with high SMD values showing the components that appear as ghost images in the final image. Image taken from[7].

3.2.3 Spectral Modulation Depth

The noise added to the electroluminescence spectrum of the device can be quantified as the ratio between peaks and valleys formed. This ratio is called the spectral modulation depth and will be briefly described below [10]. Figure 3-3 shows a typical SLD EL spectrum with the associated ripple. Around the peak intensity of the spectrum the ripple can be observed as a region of noise atop of the broad SLD emission. The inset plots the ripple over a reduced range showing three periods. The spectral modulation depth is the peak-to-valley difference ratio to their sum as in eq. (3-2) which returns a unit-less quantity.

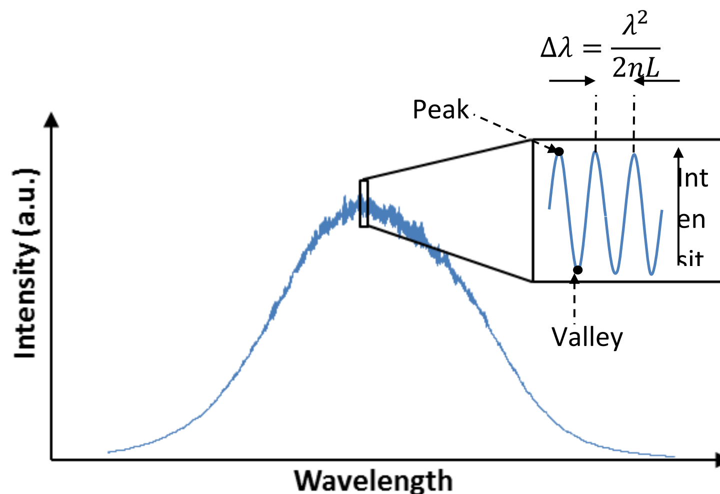

Figure 3-3: A common electroluminescence spectrum of a practical SLD (facet reflectivities ≠0) measured by a spectrum analyser with resolution high enough to detect the optical modes. The mode spacing of the EL is highlighted in the zoomed in wave of the top part of the spectrum. The peak and valley intensities are spotted in the inset. Those intensities are used to determine the spectral modulation depth of the SLD.

Spectral modulation depth,

$$SMD = \frac{I_{peak} - I_{valley}}{I_{peak} + I_{valley}} \qquad \text{...... eq. (3-2)}$$

where I_{peak} and I_{valley}, are peak and valley intensities, respectively.

Examination of eq. (3-2) reveals that SMD values are in the range 0 to 1 (or 0% to 100%), with the SMD of the device that has ideal/very-good performance tending to zero.

Shidlovski quantified the accepted range of ripples in SLDs [7], with devices exhibiting 1% spectral modulation depth considered noise free and treated as ideal. With particular attention of applications of SLD as the light source for OCT, he suggested the 5% SMD as a suitable maximum limit for the OCT application. Commercial suppliers like Superlume and Thorlabs offer their SLDs with 1%-6% spectral modulation depth depending on the output power and the operating wavelength.

3.2.4 Output Power

Output powers greater than 10mW are typically required for most of SLD applications. However, power in SLD is usually accompanied by large spectral modulation depths. This is because SMD and the output power are both related to gain as we will see in section 3.6. Therefore an increase in the gain to increase the output power results in an increase in SMD. In applications where high power must be accompanied with low SMD, further pressure exists on reduction of facet reflectivity, R.

3.2.5 Research fields

Many articles discussed design criteria and device performance of SLD whether describing a method for higher power [10]–[24],broader output spectra [1], [12], [13], [22], ripple level [11], [17]–[19], [21], [25], [26], or other performance features [10], [27]–[29] they all aimed to deliver an SLD that can provide the highest power with the

widest spectrum without the penalty of high ripples. Other reports were more concerned about the ripple development with the increase of the output power. Reports such as the one of Kwong *et.al.* [23] and Alphonse *et.al.* [17], [18], and [25] suggested that ripples do not develop randomly with increasing the power but they follow a specific trends regarding the amplitude increase and the mode spacing variation. Finally some reports were more interested in investigating other methods for low effective reflectivity.

3.4 Techniques used to achieve low facet reflectivity:

A number of methods have been used to reduce the facet reflectivity in SLDs, including AR-coating, tilted facets, and windows, and variety of combinations of these. These methods seek to reduce the reflectivity, R, directly or reduce the effective facet reflectivity, R_{eff}, and are outlined below.

3.4.1 Anti-Reflective (AR) Coating:

This method is considered one of the oldest used to suppress the facet reflectivity. Anti-reflective coatings have long been used since their presentation by Bauer G. as a mean to decrease the reflectivity of the optical surfaces (e.g. mirrors, lenses, etc.) [30]. Decreasing the reflectivity in this method is done by depositing a specific thickness of the related transparent optical material. For a simple single layer AR-coating, depending on the wavelength emitted by the device (λ) and the refractive index of the coating material at that wavelength (n), a coating layer is required whose thickness, d, is

$$d = \frac{\lambda}{4n} \qquad \text{...... eq. (3-3)}$$

Figure 3-4 shows a simplified schematic of two devices with and without AR-coating. This method has been used widely in the fabrication of optoelectronic components such as SLDs, SOAs, solar cells, and DFB lasers.

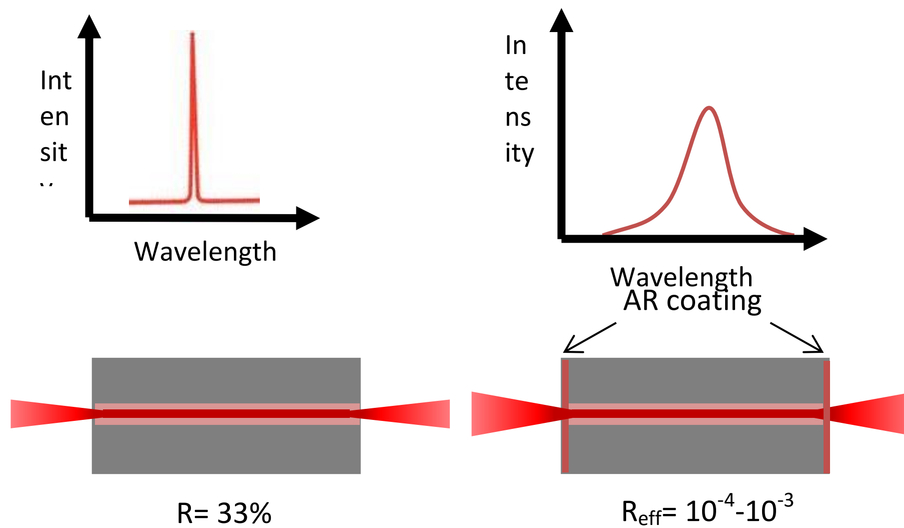

Figure 3-4: Simplified schematic showing two devices, one with AR-coating on both facets (SLD) and one without (laser). The main difference between them is the facet reflectivity to be 0.33 in the laser device and 10^{-4}-10^{-3} in the SLD.

Since the layer thickness which controls the facet reflectivity is governed by the refractive index of the deposited material at a specific wavelength, the bandwidth of the AR-coating is usually limited compared with other methods, especially if the coating comprised a single layer. A multilayer coating has been used to achieve reflectivity as low as 10^{-4} -10^{-5} for broadband devices [31], [32]. Furthermore, R is limited by the quality of the facet coating. Although $<10^{-5}$ reflectivity is theoretically available using AR-coating, thickness control to 20Å is required as suggested by Alphonse et.al. [19].

3.4.2 Tilted Optical Cavity:

This method was first presented by Tsang *et.al.* in 1983 [33] for multimode laser and it has been developed to realize broadband emission. It is based on deflection of light outside the waveguide by mis-orienting the SLD waveguide with respect to the crystal-axis by an angle ~5-10°. This simple method of reducing R_{eff} is naturally broadband (compared to AR-coating) and has been used to enable R_{eff} ~10^{-4} [19], [27].

Feedback suppression is via deflection of the reflected light from the facet to the cladding layers as shown in Figure 3-5. According to the material used and operating wavelength the tilting angle can be selected accordingly but generally angles between 6

and 10° are chosen to process SLDs. Angles greater than 10° cause extensive deformation of the output beam that cause increase in the coupling losses.

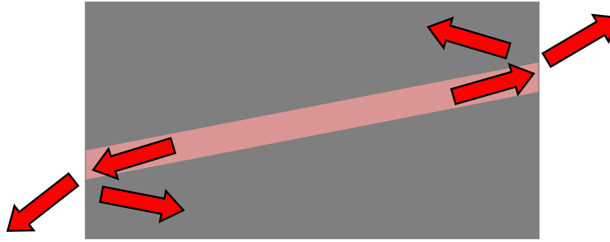

Figure 3-5: A simplified schematic of a tilted cavity SLD. The optical mode reflects to the cladding layer (grey) rather than the active waveguide which reduce the constructive feedback of the resonating signal. Reflectivity down to 10^{-4} is achieved and lowered to 10^{-6} when AR-coating is added.

The advantage of this method over the previous method is that it is less wavelength-dependent which makes it more flexible, especially given the recent push towards broader active materials such as these using QDs or hybrid QD/QW material. The tilted cavity configuration is able to achieve facet reflectivity down to 10^{-6} when combined with AR coating[34].

An example of such devices was reported by Alphonse *et.al.* [19] in which the tilted cavity is combined with the AR-coating to achieve low reflectivity facets of 10^{-6}. The disadvantage of this method is the excess material used and the quality of the output beam and the corresponding coupling efficiency and packaging complicity (further discussion will be given in chapter 4).

3.4.3 Transparent Window:

Another method commonly used to achieve low effective reflectivity, R_{eff}, is to terminate the active waveguide before achieving the rear facet. This method was the first method used to fabricate SLDs when Miller *et.al.* included a transparent window at the rear facet to provide the required loss to push the threshold current to a sufficient high level to enable the device to provide amplified spontaneous emission [35] to a higher power before the onset of lasing.

The feedback suppression in this method comes from spreading out of the optical beam in the transparent, unguided, window region in such a way that light which travelled all the way to the rear facet will have spread out laterally and after reflecting back only a small percentage will be coupled back into the active waveguide. This can be seen in Figure 3-6 below which shows a simple schematic of the transparent window structure SLD. The divergence angle of the propagated beam, which eventually governs the resultant effective reflectivity, is determined by the index step, the interface shape, and also the waveguide widths.

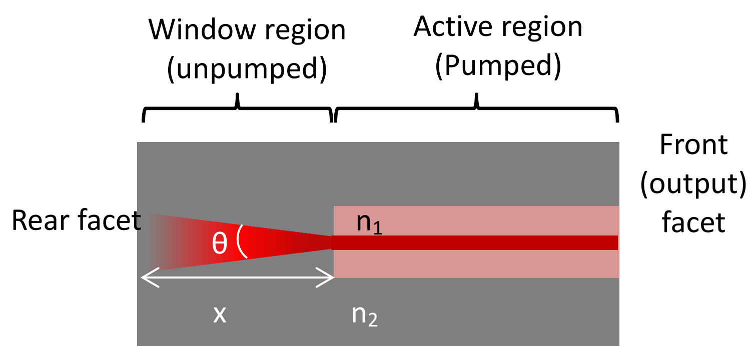

Figure 3-6: A schematic of an SLD with a windowed rear facet. The optical waveguide, which is the pumped part of the device, is terminated at a distance x from the rear facet, which is usually unpumped. The optical mode propagates from the active waveguide to the unguided window. According to the index step between, n_1, and, n_2, of the core and cladding, respectively, the optical beam divert at divergence angle, θ.

This chapter focuses on characterization of an SLD device with a rear window combined with the tilted cavity configuration to achieve very low effective facet reflectivity.

3.5 GaAs-Based Buried Facets (Window Facets):

The catastrophic optical damage (COD) that limited operation in high power laser diodes resulted from two reasons. The first one, which has the larger effect and the quicker to notice, is the fast damage due to localized heating due to high optical densities nearby or at the facet. Such high density can result from light generation (due to radiative recombination), reflection from the facet, and local heating generated by the non-radiative recombination. The other reason that causes COD is the facet erosion due

to the surrounding atmosphere (oxygen, water vapour *etc.*), yet, the facet degradation due to this takes long running time (multiple thousands of running hours) to be noticed[36].

A method to prevent COD is to implement a short transparent window at each facet. By comparative study, Takahashi proved that adding ~15μm window to the facet can minimize the erosion [37]. The transparent window is also used to stop the facet degradation due to the localized heat, which is caused by the high optical density. Leaving an unpumped section prior to the facet was sufficient enough to decrease the optical density, and eventually decrease the facet degradation [36][38].

The dimensions used for COD threshold increase were limited to few tens of microns. Figure 3-7 demonstrate a windowed device having two regions, an active core of Al_xGaAs with refractive index of 3.5 and a window section of Al_yGaAs with refractive index of 3.3. The device is presented in two cases in Figure 3-7. The first one, shown in figure 3-7a, is the one used for the increase of the threshold power of COD where only a very short window is used. The other case is the windowed SLD where the window length is now hundreds of microns as shown in Figure 3-7b. The short window used for COD will not change the threshold current of the device dramatically. However, increasing the length of the unpumped region allows the light to expand more and by duplicating the length for a full loop only a small percentage of the original signal is feedback into the active waveguide.

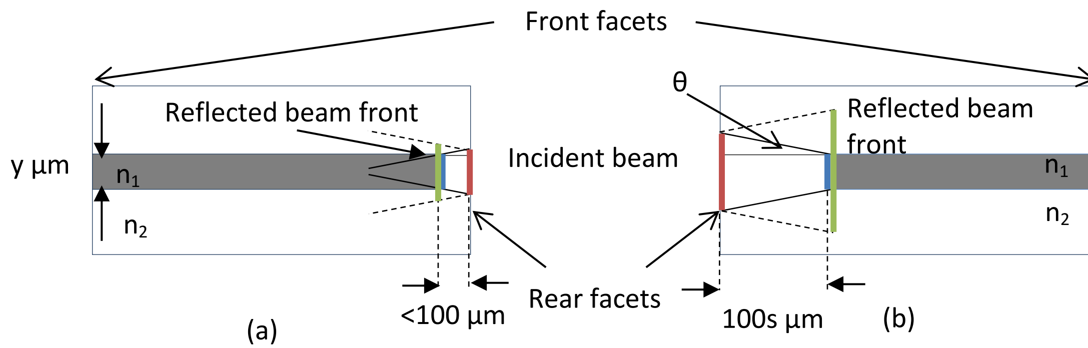

Figure 3-7: shows a comparison between devices with the same features except the window length where (a) device with short window of 4 a.u. length and (b) of 140a.u. length

The device configuration shown in Figure 3-7 has two materials active (grey) with high refractive index for the operating wavelength and passive (white) with lower refractive index. A step index change, Δn, is considered between the active and the passive materials. At the interface the propagated light beam will undergo divergence which alters the beam size. Since the materials and the active geometry are identical in the two devices, the propagated beam size is only governed by the separation between the termination of the active stripe and the rear facet. For material system with a specific Δn, the light beam will diverge by θ° and the beam size is increased by x.tan(θ) where x is the window length. Assuming that the window length of the device in Figure 3-8b is 10 times the one which is in Figure 3-7a, this means that beam size of the first is increased 20 times than that of the second. This increase will cause the effective reflectivity of the case in Figure 3-7b to reduce much less than the one in Figure 3-7a.

Based on this idea, Tien-Pei Lee presented the first SLDs with rear window section and also the first ever presentation of SLDs [35]. Such configuration is usually combined with anti-reflective coating and/or tilting the active waveguide.

In chapter two I showed that the pattern of the processed wafer can provide devices with unpumped rear section and since the active section is left intact the section is not only unpumped but also absorptive to the central emission wavelength of the processed

devices. In the following sections the proposed window-like SLD devices are discussed and analysed starting with the facet reflectivity and followed by the device performance.

3.5.1The proposed window-like structure

The window structure studied here is also based on the beam expansion in an unpumped laterally unguided region. However, in this structure the active region remains intact below the optoelectronic confinement layer. The presence of the active region in the unpumped window section increases its ability to decrease the effective reflectivity through absorption of light by the unpumped active medium, in the case of the presented devices, by the virtually limitless absorption provided by the QWs. This is in contrast to traditional window facets in which the window is formed by etching through the active region. Therefore, light propagating through the window will be absorbed, meaning that only a very small portion of the light will be coupled back to the active waveguide. Figure 3-8 shows the effect of the absorption in the rear part of the device.

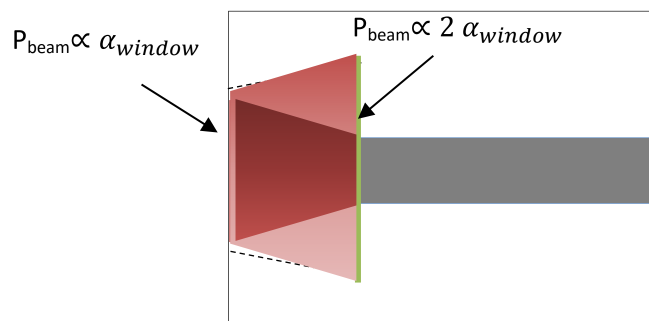

Figure 3-8: a simplified schematic of a window structure with an absorption factor α_{window} combines all the losses caused by the window whether it's a material loss or due to geometry.

Although the buried facet structure described here is not transparent, I will continue to refer it as window throughout the thesis

3.5.2 Estimation of the buried-facet reflectivity

The mask used to process the devices could provide SLDs with both electrically pumped active and unpumped (and therefore absorbing) sections. When the device is

processed normal-to-the facet with no AR-coating on either facet, the effect of the presence of the window can be determined from measuring the effective reflectivity. To measure the effect of the unpumped window region on the structure, devices with a 1mm active stripe were fabricated with a range of window lengths and compared to a 1mm long laser (i.e. without a window section).

Figure 3-9 shows the device used in this experiment, and traces the modal gain, g-α, added to an optical signal generated at the front facet and took a round trip to the rear facet.

In a Fabry-Pérot laser device with facets reflectivity R_f (front) and R_r (rear), a material gain g, losses α, and cavity length L, the modal gain, G, of a round trip starting from the front facet can be calculated by:

$$G = G_{th} R_f R_r e^{2(g-\alpha)L} \qquad \text{...... eq. (3-4)}$$

where G_{th} is the threshold gain required to overcome internal losses.

An identical device but with an additional window section at the rear facet can be described in a similar manner. Two factors need to be added which are the window length, L_w, and the losses contributed by the window, α_w. This loss term combines both the absorption in the active DQW region and the losses due to the geometry (e.g. beam expansion) as the schematic shown in Figure 3-9 b. The modal gain for a round trip through this structure can be estimated as.

$$G = G_{th} R_f R_r e^{2(g-\alpha_a)L-2(\alpha_w L_w)} \qquad \text{...... eq. (3-5)}$$

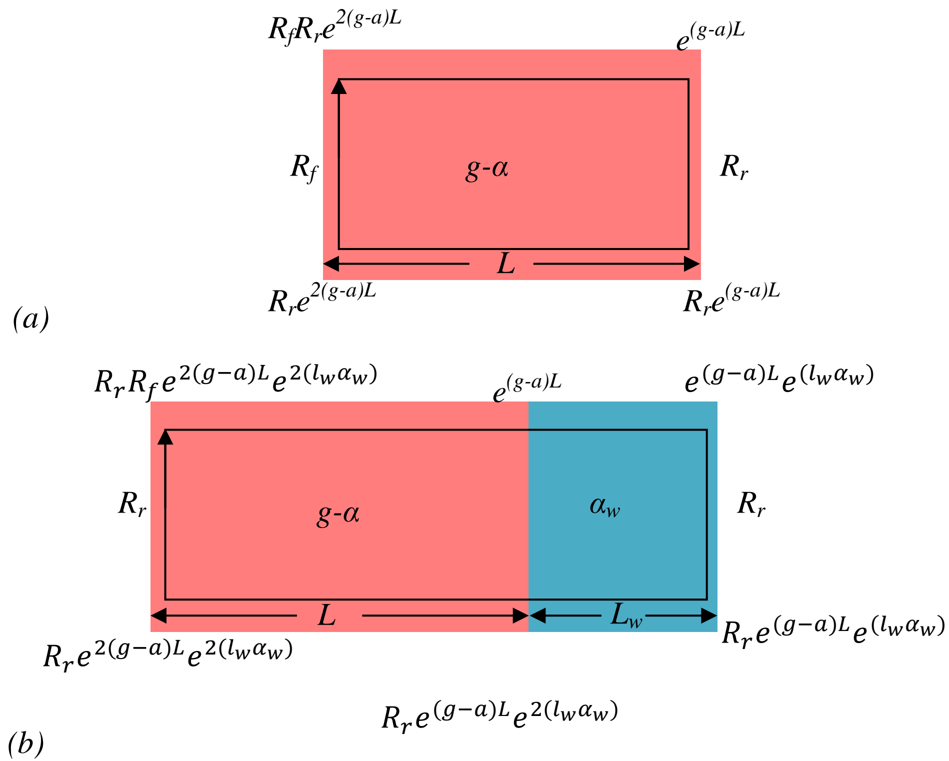

Figure 3-9: A schematic tracing the gain of the laser device (a) and the SLD device (b).

3.5.2 Facet effective reflectivity:

The effective facet reflectivity can be calculated from comparison of the threshold gain (the gain required to start lasing) of the device with window of length= L_w to the standard Fabry-Pérot laser (L_w=0). The difference in the G_{th} between the two devices comes from the excess loss associated with the presence of the rear window section.

In the case of a laser at threshold, modal gain G is Gth, so substituting in (3-4):

$$R_f R_r e^{2(g-\alpha_a)L} = 1 \qquad \text{...... eq. (3-6)}$$

Similarly for the device with rear window section, equation (3-5) becomes:

$$R_f R_r e^{2(g-\alpha_a)L-2(\alpha_w L_w)} = 1 \qquad \text{...... eq. (3-7)}$$

Since the two equations (3-6) and (3-7) are equalities of 1, they can be combined into:

$$R_f R_r e^{2(g-\alpha_a)L-2(\alpha_w L_w)} = R_f R_r e^{2(g-\alpha_a)L} \qquad \text{...... eq. (3-8)}$$

Assuming that $(g - \alpha_a)$ is the amount of gain required to reach lasing threshold G_{th} for the laser device and the other device with the absorber, rearranging eq. (3-8) into:

$$2(G_{th\,SLD})L_{SLD} - 2(\alpha_w L_w) = 2(G_{th\,Laser})L_{laser} \quad \text{...... eq. (3-9)}$$

By reformulating (3-9) the integrated window losses α_w can be calculated as

$$\alpha_w = \frac{G_{th\,SLD}L_{a\,SLD} - G_{th\,laser}\,L_{laser}}{L_w} \quad \text{...... eq. (3-10)}$$

Back to the original equations (3-4) and (3-5), they are exactly the same accept the part added to represent the rear window. Comparing the two equations gives a formula that can predict the effective reflectivity of a device with rear absorber structure. Where

$$G = G_{th}R_f R_r e^{2(g-\alpha)L} \quad \text{...... eq. (3-4)}$$

$$G = G_{th}R_f R_r e^{-2(\alpha_w L_w)} e^{2(g-\alpha_a)L} \quad \text{...... eq. (3-5)}$$

$$R_{eff} = R_r e^{-2(\alpha_w L_w)} \quad \text{...... eq. (3-11)}$$

3.5.4 Experimental measurements:

To characterise the effective reflectivity of the rear window structure, normal-to-facet SLDs were fabricated. The SLDs have 1mm active stripe and different window lengths varied from 250µm to 2250µm with an increment of 250µm. The output power from the SLDs is measured as a function of current and the threshold current was recorded. From the transparency threshold current, J_o, and the material gain, G_o, the threshold gain, G_{th}, of the SLD can be estimated by

$$G_{th} = G_o . ln\frac{J_{th}}{J_o} \quad \text{...... eq. (3-12)}$$

Fixing the active stripe of the SLD to 1mm enabled comparison with a 1mm laser (without a window), where eq. (3-10) can be applied to estimate the excess losses

provided by the window. The effective reflectivity, R_{eff}, of the window facet can then be determined using equation (3-11), and taking into account that R_r is the reflectivity for an as-cleaved uncoated facet (0.33). Figure 3-10 shows threshold current density, and threshold gain plotted as a function of window length. The Figure 3-shows an increase in threshold current, as a result of increase in the threshold gain, as the window length increases. Recalling the length dependent measurement described in section 2.5, the threshold current density, J_{th}, for a 1mm laser device was around 740 $A.cm^{-2}$ (in the case of the measured device it was 725 $A.cm^{-2}$) which represented a threshold gain, G_{th}, of ~24cm^{-1} (23.5 cm^{-1} in the case of the measured device). J_{th} was increased about 6 times from 725 to 4250$A.cm^{-2}$ when the window length was changed from 0 in the laser up to 2250µm in the SLD. By comparing the threshold current density, J_{th}, to the transparency current density, J_o, and taking into account modal gain, G_o, the threshold current of the SLD device with 2250µm is increased up to 173.8cm^{-1}.

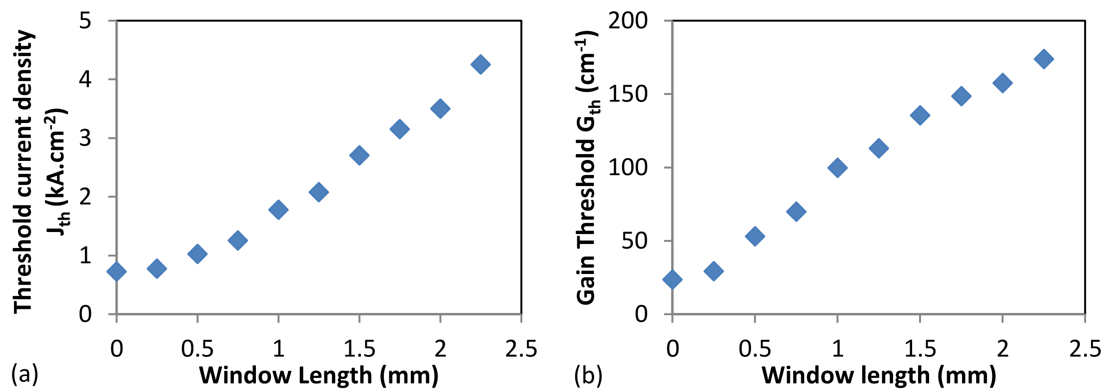

Figure 3-10: the threshold current density, J_{th}, (a) and the gain threshold, G_{th}, (b). An increase in J_{th} from 0.725 to >4.25kA.cm^{-2} resulted from an increase in G_{th} from just off 23cm^{-1} up to > 170cm^{-1}.

Figure 3-11 shows the excess losses (a) and the effective reflectivity (b) measured as a function of window lengths for an SLD with 4µm wide and 1mm long active stripe.

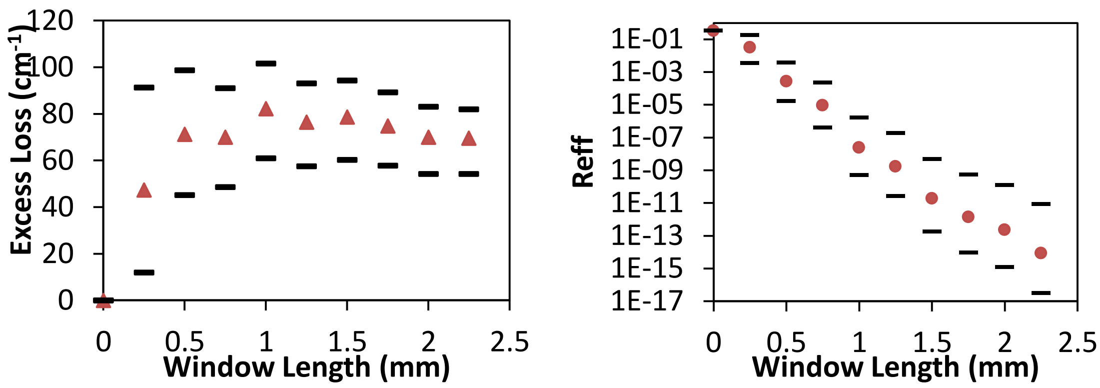

Figure 3-11: The window excess loss (a) and the effective reflectivity measured for different window lengths.

The excess losses increased dramatically as can be seen in Figure 3-11a, starting from 0cm^{-1} in the laser device (with no window) up to 82cm^{-1} when the window length is 1mm. The excess loss starts to level up following this value with a slight decrease to ~70cm^{-1} in the longer window lengths. This saturation is expected to result when the propagated beam size is already 100µm, the same as the separation between the trenches. Following that point the expanded light will reflect at the trenches and no more expansion will take place, so the losses will be mainly related to the material absorption.

On the other hand, the effective reflectivity of the rear facet is found to be related to both the length of the window, l_w, and the excess losses, α_w, as can be concluded from equation 10. For that reason the effective reflectivity did not saturate as the excess losses did, but decreased throughout the range of window lengths. The minimum reflectivity recorded for 4µm wide stripes in this experiment was 8.4×10^{-15}.

The mask used in device fabrication gave 3 different stripe widths 3, 4 and 5µm. When the length dependant gain measurements done as described in section 2.5 the 4µm wide stripes was considered the central and the main trend while the trends related to 3 and 5µm are considered as the limits of the values as shown in Figure 3-19 in chapter two. In order to estimate the windowed-facet reflectivity as accurate as

possible the modal gain resulted from the 3 and 5µm wide stripes was used to find the excess losses and the effective reflectivities based on the measurements done for 4µm wide stripe.

3.6 Expected Spectral Modulation Depth.

In any Fabry-Pérot resonator with an active medium in between the mirrors, Fabry-Pérot modes are developed which will lase once threshold has been reached. In the case of SLDs, the low facet reflectivity should ideally suppress the internal feedback permitting only single pass amplification. However, it is practically impossible to obtain zero (R_{eff}) and therefore there is always a residual feedback that causes these modes to develop. Residual Fabry-Pérot oscillation can be observed in the EL spectrum as a spectral modulation, typically at the peak of the emission. As a result of the long cavities used in SLDs, the resolution of the OSA must be high enough to resolve the individual closely spaced modes. Figure 3-12 shows the difference between the EL spectrum of the same device measured once with OSA that has resolution lower than required (a) and other with resolution high enough to resolve the individual modes (b).

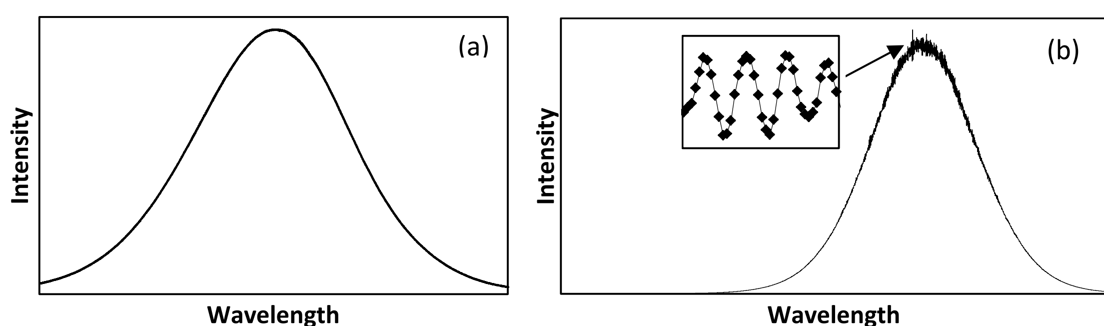

Figure 3-12: The EL of the same SLD (a) when the resolution of the OSA is less than required and (b) when the OSA resolution is high enough to resolve the Fabry-Pérot modes. The inset in (b) is a portion cut from the top of the spectrum showing the individual modes. Note in the inset that many points can be recorded for one period which ensures the detection of the peak and the valley.

SLDs with different cavity lengths are assumed to simulate the development of the spectral modulation depth as a function of the output power from each device.

The output power of an ideal SLD (0% facet reflectivity and no self-heating) can be calculated by considering the spontaneous emission rate in the cross-sectional area at the central wavelength of the output emission; this rate is amplified along the active cavity of length, *L,* by the modal gain, *G*. The amplified spontaneous emission, *P,* is calculated as [39]:

$$P = \frac{(h * A_{beam} * \lambda)}{R_{spont}} \times \frac{(e^{GL} - 1)}{G} \qquad \text{.... (3-12)}$$

Where h is Plank's Constant, A_{beam} is the beam cross-sectional area, λ is the central wavelength, R_{spont} is the spontaneous emission rate, G is the modal gain, and L is the active length. R_{spont} is the rate of light that is generated spontaneously within the active volume (area (s) × thickness (d)) with quantum efficiency η_{sp} when current I is injected [39]

$$R_{spont} = \frac{\eta_{sp} * I}{s * d * q} \qquad \text{.... (3-13)}$$

q is the elementary charge. For simplicity the injected current is fixed, which will give a fixed spontaneous emission rate. A plot of the output power as a function of modal gain can be generated, which takes an exponential path towards higher gain. This is plotted in Figure 3-13 for active stripe lengths 1, 2, and 3mm. In the case of non-ideal facets (i.e. reflectivity ≠ 0%) emissivity (1-R) is still ~1, and has negligible effect on the output. Self-heating due to current density injection is also assumed to be zero which would otherwise results in gain reduction and/or a shift in the central wavelength.

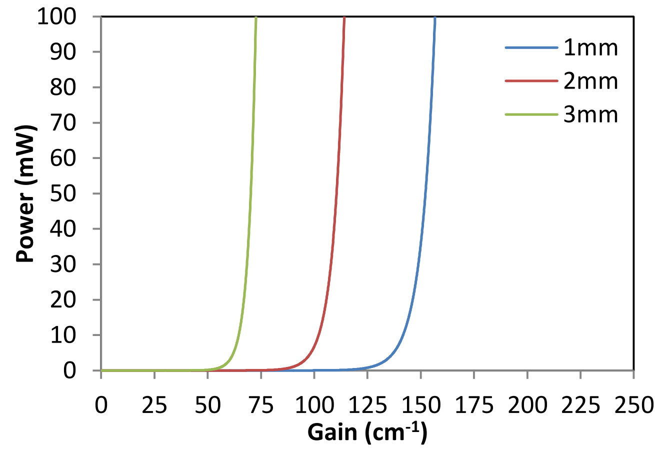

Figure 3-13: The simulated output power from an ideal SLD as a function of Gain. Reflectivities are zeros for front and rear facets

The modal gain of a semiconductor laser can be determined from the Fabry-Pérot modulation depth as described by Hakki and Paoli [40]. For a given cavity length, L, and effective reflectivity for both rear and front facets, R_r and R_f, respectively, the modal gain, G, can be extracted using the measured peak-to-valley ratio, M, across the electroluminescence (EL) spectrum using:

$$G = -\frac{1}{L}\left(\ln\frac{\sqrt{M}+1}{\sqrt{M}-1} + \ln\sqrt{R_r R_f}\right) \qquad \text{.... (3-14)}$$

M can be defined as a function of the modal gain G by rearranging (3-14) such that

$$M = \left(\frac{e^{-GL}+R}{e^{-GL}-R}\right)^2 \qquad \text{.... (3-15)}$$

where $R = \sqrt{R_r R_f}$.

If the valley is considered as the basic intensity I while the peak is the basic intensity in addition to the increase in the intensity due to the gain I+ΔI, M can be defined as

$$M = \frac{I+\Delta I}{I} \qquad \text{.... (3-16)}$$

The spectral modulation depth (SMD) of an SLD is defined by equation (3-2) as the ratio of the difference to the summation of the peak (I_{max}) and valley (I_{min}) of each spectral mode.

$$\mathrm{SMD} = \frac{I_{max} - I_{min}}{I_{max} + I_{min}}$$

$$\mathrm{SMD} = \frac{(I + \Delta I) - I}{(I + \Delta I) + I} = \frac{M - 1}{M + 1} \qquad \text{.... (3-17)}$$

Substituting equation (3-15) in equation (3-17), the spectral modulation depth can be related to the Gain as shown in the following equation.

$$SMD = \frac{\left(\frac{e^{-GL} + R}{e^{-GL} - R}\right)^2 - 1}{\left(\frac{e^{-GL} + R}{e^{-GL} - R}\right)^2 + 1} \qquad \text{.... (3-18)}$$

SMD is plotted as a function of gain in Figure 3-14 for SLDs stripe lengths 1, 2, and 3mm, the reflectivities are considered constant for the three devices. We observe that SMD also takes an exponential path until it reaches 100%.

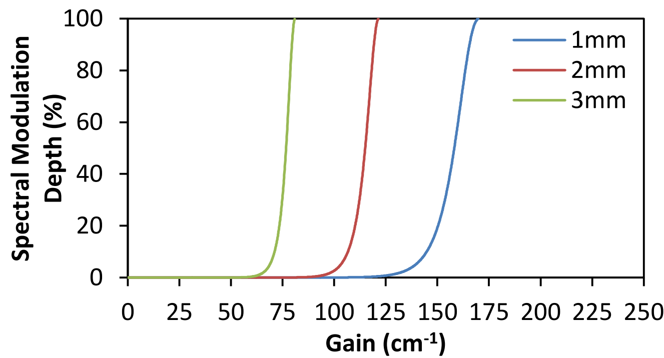

Figure 3-14: The Spectral Modulation Depth (SMD) as a function to gain.

Since the output power and the SMD are both functions of the modal Gain, a plot of SMD *versus* power can be constructed. This is shown in Figure 3-15 for a reflectivity provided by a tilted device with 2mm window and for stripe lengths 1, 2, and 3mm. The resultant curves are in agreement with Kwang *et.al.* [23], in the regime of low R_{eff}, who

made similar studies on SLDs using AR coating and a grounded internal absorber. In Figure 3-15, the SMD is observed to increase with an increase in the output power. The gradient of the curves is observed to reduce with increasing cavity length, implying that the SMD/power condition can be optimised through choice of active stripe length (lower SMD at higher powers for longer active stripe lengths).

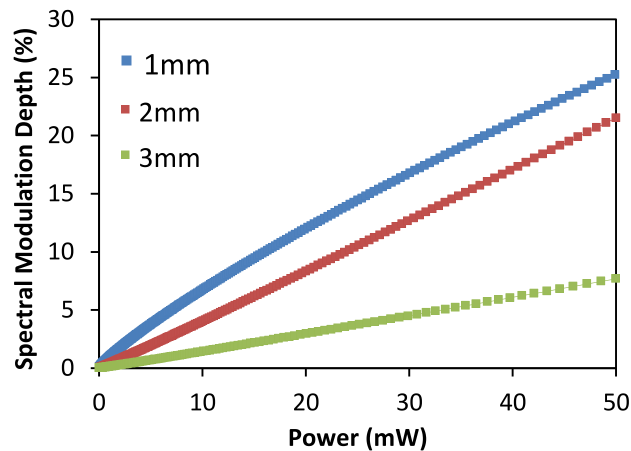

Figure 3-15: The spectral modulation depth as a function to the output power for different cavity lengths. The lowest SMD calculated was obtained from the wider devices as shown (the green line is 3mm long active) while the shortest exhibited the highest SMD (blue line, 1mm long stripe).

3.7 Output Power Characterization:

Window-structured SLDs were grown following the process described in section 2.2, where 3 and 4µm wide self-aligned stripes were formed in a 2-step growth process. SLDs were cleaved and characterized with a range of active stripe and window lengths.

SLDs were characterized using the LI characterization setup described in 2.3.1 to obtain parameters such as maximum output power, slope efficiency, and the temperature dependence.

Devices with 1, 1.5, 2, 2.5, and 3 mm long active stripes were cleaved. These SLD had varying windows length due to the mask design issue mentioned in 2.2.2. The LI curves recorded from these SLDs demonstrated typical superluminescence and eventually rolled over at current densities greater than $4kA.cm^{-2}$. The lack of laser

threshold or kinks in the LI curve suggested that the SLDs did not experience any lasing throughout the current range operated in. this was later confirmed by the low and high resolution EL spectra collected from the devices but this will be discussed in more details in later section. Figure 3-16 shows the LI curves of devices with 1.7, 2.1 and 3mm active stripes and 1, 1, and 2mm windows, respectively. The fractions in the devices lengths came from the way the mask was designed; I put the numbers this way just seeking data accuracy. The slope efficiency was extracted for each of the devices from the LI curves in Figure 3-16. Slope efficiency of 1.7 was ~10%, 14 % for the 2.1mm and ~16% for 3mm.

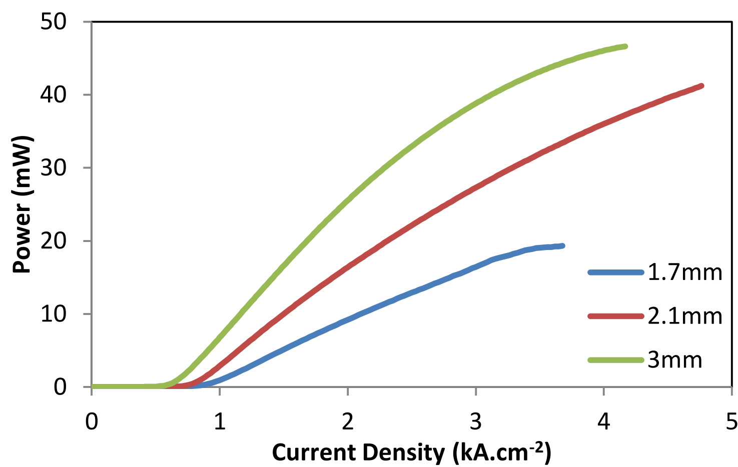

Figure 3-16: LI curves of the epi-side-up SLD devices. As expected the longest device has the maximum differential efficiency.

3.7.1 Geometry effect on the output power.

In order to ascertain the effect of the device geometry on the performance of the SLD, a set of SLD were tested and compared to each other. All measurements were conducted using pulsed injection for a bare chip unmounted SLDs using the LI characterisation setup described in 2.3.1.

First, fixed active length was chosen (1800µm) with three different window lengths 77µm, 2500µm and 3600µm at the rear facet. They were tested at room temperature under pulsed conditions (10µsec pulse width, 1% repetition). Figure 3-17a plots the LI

curves for the three devices. The performance of the three devices was very similar, with output power >25mW achievable in all SLDs. In fact, although there appears to exist a trend of increasing power with increased window length the difference is very small, and the three devices in Figure 3-17a were, within experimental uncertainty, identical. Therefore I believe that the window length has a negligible effect on performance for window length > 77μm.

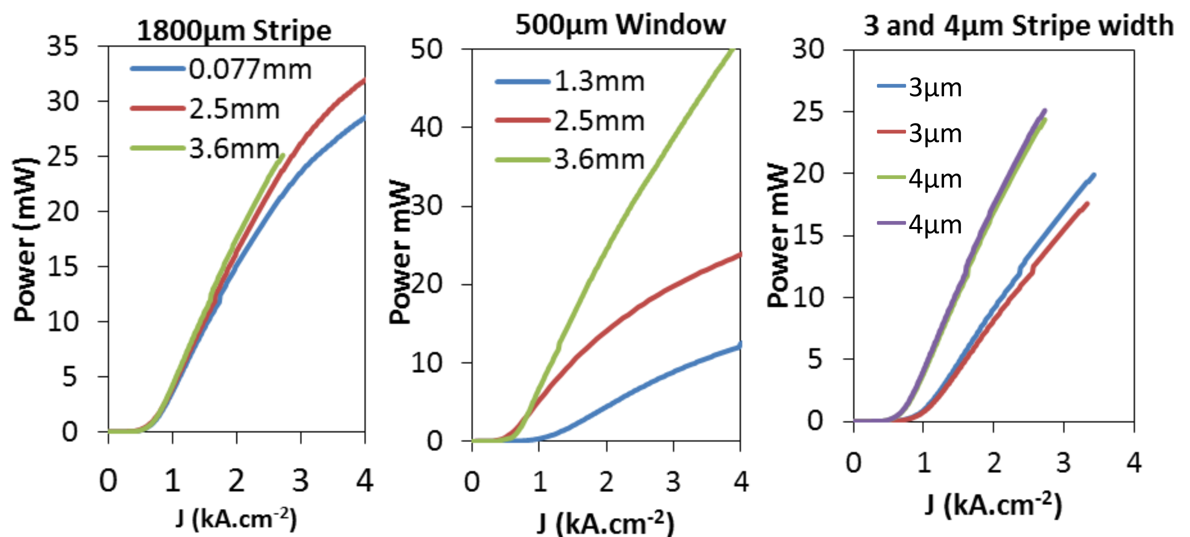

Figure 3-17: The results of the experiment that revealed the device geometry on the device performance. (a) The stripe geometry is fixed to 1800×4μm with different window lengths. (b) The window length and the stripe widths are fixed to 500μm and 4μm while the stripe length is changed according to the number shown in the figure, and (c) the stripe and window lengths are fixed to 1800 and 2500μm while the stripe widths were 3 and 4.

Comparison of Figure 3-17 and Figure 3-16 suggests that the main contributor to the difference observed in Figure 3-16 is from the increase in active stripe length. This was confirmed from the next set of devices in which devices with a fixed window length and three different stripe lengths were tested. Figure 3-17b compares 3 SLDs with 500μm long window and active stripe lengths 1300, 2500, and 3600μm. Output power is observed to increase with increasing stripe length, with output power 50mW for the device with 3600μm long active stripe compared to <12mW for the 1300μm at the same current density.

Up until now, I have concentrated on SLDs with 4µm stripe width. Our mask design allowed for two stripe widths 3 and 4µm. Figure 3-17c compares SLDs with these two widths. The slope efficiency of 3 and 4µm wide stripe SLDs can be grouped according to the width, with ×2 increase in power for 4µm compared to the 3µm width SLDs.

3.7.2Temperature Effect:

The temperature dependence of the devices was explored by testing a device with 2.1mm active stripe and 1mm window and another device with 3mm active stripe and 2mm long window. The two devices were mounted epi-side up on gold coated c-mount and operate in CW over a temperature range from 10 to 70°C. The pumping current was limited to 250mA which is equivalent to 2.98kA.cm^{-2} and ~2.1kA.cm^{-2} current densities for 2.1 and 3mm long stripes, respectively. These are the currents at which self-heating is minimized using the c-mounts used. I focused on these two lengths since they have shown better performance than the one with 1.7mm long stripe. The LI curves of the two tested devices are shown in Figure 3-18 over the temperature range mentioned above. The results show the expected reduction in the slope efficiency with increasing the temperature. By sweeping the temperature from 10-70°C the slope efficiency decreased from 15% to 8% in the 2.1mm devices while in 3mm device the efficiency dropped more to be ~3.6% in the 3mm device. Although the current density is lower in the 3mm device leading to less heat being generated in the junction through Joule heating, the reduction in the output power with increasing the temperature is greater in the 3mm long stripe SLD than the 2mm SLD.

A possible reason for this behaviour could be due to the amount of heat stored in the device and the ability of the window section to maintain the temperature. The amount of unpumped semiconductor material surrounding the buried stripe and the material of the rear window play an important role in distributing the heat across the structure. With stabilized thermal control the junction temperature can be maintained. Another reason

that can affect the device performance this way is the heat dissipation, generated in the intrinsic region, provided by the rear window. Move of the heat generated in the shorter stripe can dissipate, reducing the temperature of the junction, compared to the longer stripe which may suffer a thermal gradient along the stripe with the heat generated toward the front facet unable to dissipate through the window.

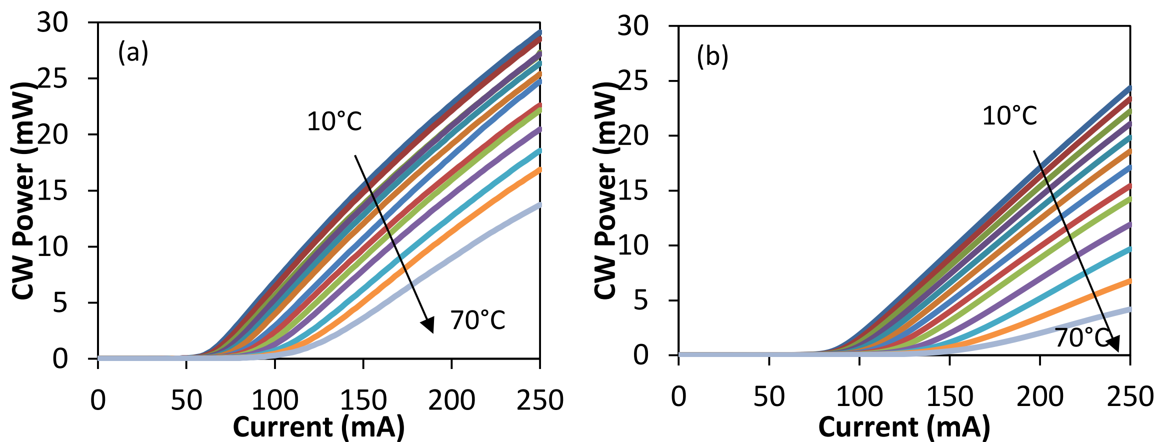

Figure 3-18: LI curve at different heat-sink temperature. (a) for 2.1mm active stripe devices, and (b) for 3mm active stripes. The arrows show the lowest to highest temperature as set on the heat-sink.

This evidence supports the idea that the unpumped window region at the rear facet can provide an extra route for heat sinking for the active stripe to the surrounding semiconductor, since the heat transfer at the semiconductor/semiconductor interface is higher than the one at the semiconductor/air or semiconductor/metal.

3.8 Spectral Characterization:

Spectral characterization of the SLD emission was performed using two different setups which are the low resolution EL and the high resolution EL. These apparatus are described in sections 2.3.2 and 2.3.3, respectively. Low resolution EL was used to confirm no-lasing in the range of pumping current at which the device was tested. The other important piece of data extracted by the low resolution EL was central wavelength, the red-shift which provides an indication of junction temperature. High resolution EL was used to investigate spectral modulation depth of the ripple that

appears in the EL spectrum at various power levels. All spectral measurements were taken at room temperature unless it is stated differently.

3.8.1 Low resolution spectral characterization

Low resolution EL spectra were examined at the maximum power of SLDs with 1.7, 2.1 and 3mm active stripes and 1, 1, and 2mm windows. The devices were mounted on gold coated c-mounts and tested under CW current at room temperature. Lasing was not spotted in the three devices throughout the measurement range.

All devices exhibited red-shift in central wavelength, example of such shift is shown in Figure 3-19a below, which plots the EL spectra for SLD with 3mm active stripe and 2mm long window and Figure 3-19b shows the shift occurred in the peak wavelength in more currents that was not added to Figure 3-19a seeking figure clarity.

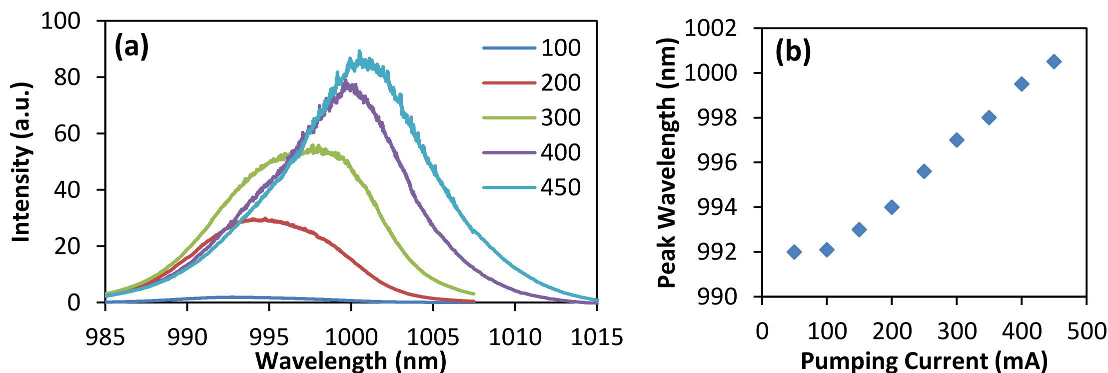

Figure 3-19: EL spectra of the SLD that has 3mm long active stripe and 2mm window at different pumping currents (a) and the peak red-shift (b).

The spectra obtained at the maximum power for the three devices under test are plotted in Figure 3-20 for current densities 3.5, 4.5 and 4kA.cm-2 for 1.7, 2.1, and 3mm devices, respectively. By comparing the central wavelength shift of each device with the central wavelength which was indicated by the photoluminescence measured at room temperature with optical pumping “no self-heating” (Figure 2-3b), we can notice that the peak wavelength was shifted from 990nm, up to 1010, 1005, and 1001nm for the 1.7, 2.1 and 3mm device, respectively. This shift can attribute to Joule’s heating of the active junction by ~50°C assuming a shift of ~0.4nm/°k for GaAs [41]. The reason of

this contrast in the shift between the three devices is the active area of the stripe, bearing in mind they are all 4μm wide stripes.

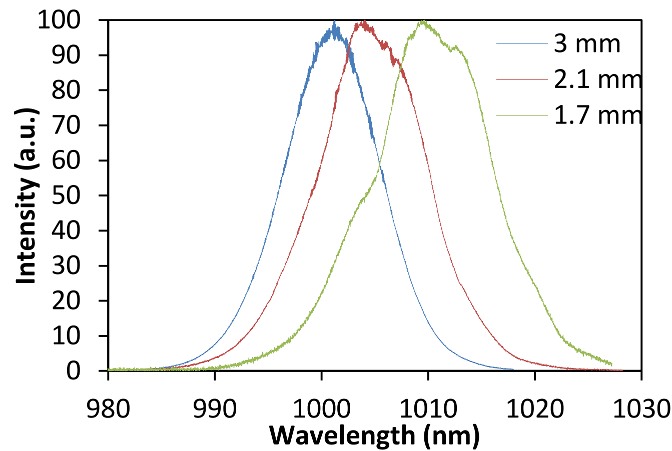

Figure 3-20: The Low resolution EL spectra of the 1.7, 2.1 and 3mm device at the maximum power of each device. A red-shift in the central wavelength is noticed in all devices with different values and the no-lasing state is confirmed to the maximum power

3.8.2 High resolution spectral characterization

Following the confirmation that the SLDs are not lasing over a reasonable range of current injection, devices were characterized using high resolution EL setup described in 2.3.3 in order to measure the spectral modulation depth of each device at various output powers.

In order to fully detect the modulation on the top of the EL spectra of the devices the resolution of the OSA should be smaller than the Fabry-Pérot mode spacing of the device. Inspection of mode spacing of spectral modulation around the central wavelength revealed mode spacing commensurate with the standing wave between the front facet and the stripe/window interface and not between the two end facets. Since the OSA in the high resolution setup has a minimum resolution of 0.01nm, the lengths of the measured devices were limited to these that can provide at least five sample points within a full wave of the ripple (i.e. the spectral length that shows two successive peaks). This is demonstrated in the schematic in Figure 3-21.

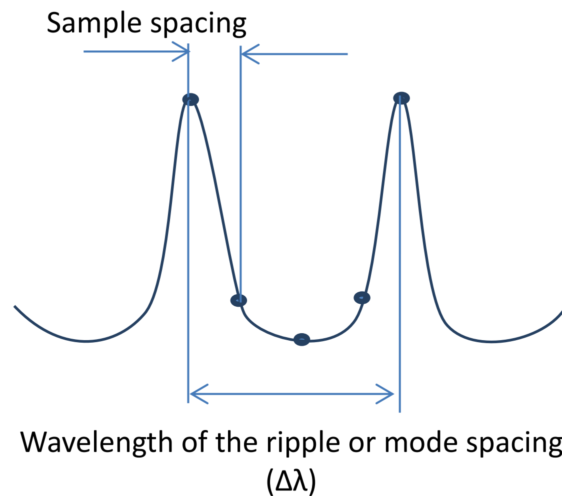

Figure 3-21: A single wave period highlighting the required number points to detect the peak and valley in a single period. The minimum sample spacing in the used spectrum analyser is 0.01for that reason 0.05nm mode spacing is needed.

Therefore, considering minimum mode spacing of 0.05nm to unsure at least 5 sample points, at a central wavelength of 990nm, the maximum cavity length is 6.125mm. The total lengths of the measured devices were 1.7+1, 2.1+1, and 3+2mm stripe + window, so, even if the reflection was from the two end mirror, they are in the allowable range of lengths.

The high resolution EL spectra of the three devices were measured, and the SMD associated with each device over a range of output powers was extracted as plotted in Figure 3-22. The three devices showed the trend expected in the simulation done in section 3.6. In three devices, SMD is increased by increasing the output power (corresponds to an increase in the pumping current). The maximum SMD recorded for these three devices were 19.7% at 17mW, 34.6% at 41.2mW, and 17.3% at 43mW for SLDs with active stripes of 1.7, 2.1, and 3mm, respectively. Figure 3-22 also shows that for each device, the rate of SMD increase as the power increase changes at some point I called this point, point-A. Point-A for each device was 12mW, 31.5mW, and ~40mW for devices that have active stripes of 1.7, 2.1, and 3mm, respectively.

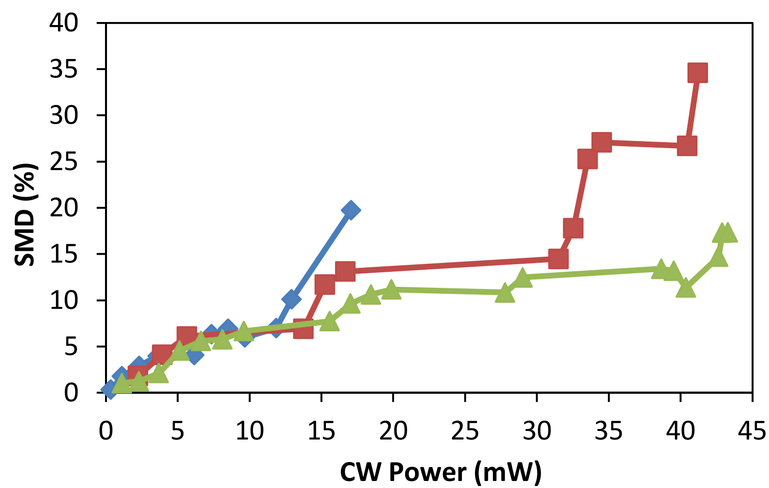

Figure 3-22: The spectral modulation depth value for devices with three active lengths (1.7mm (blue), 2.1mm (red), and 3mm (green) active stripes).

This difference in the SMD rate before and after point-A resulted because of a sudden change in the effective reflectivity of the rear facet. This change is associated with the red-shift in the central wavelength of the emission band due to Joule's heating. At low powers, the absorption band of the window in coherent to the emission band of the active stripe. This way, most of the light spread in the unpumped region will be absorbed by the window. In the second section of the SMD *vs* output power after point-A, the pumping current will be high which results in higher red-shift in the emission band. This results in a reduction in the overlap between the two bands and eventually a decrease in the effective reflectivity. The shift in the emission band is plotted in Figure 3-23 in two cases, high and low output powers, for the device that has 2.1mm active stripe as an example of the three devices. The selection of this length was because of the obvious step between the two sides around point-A.

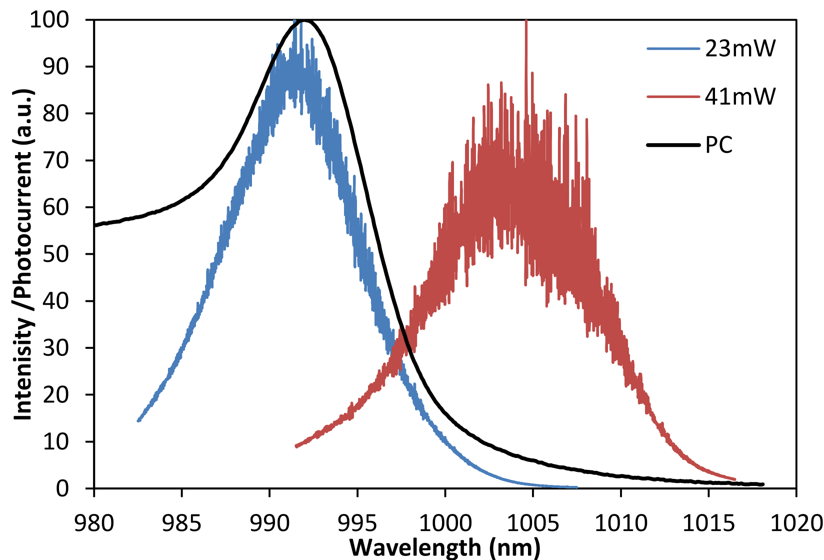

Figure 3-23: The high resolution EL spectra of the same device at two output power levels 23mW (blue) and 41mW (red). The figure shows the shift of the central wavelength in the high power with respect to the photocurrent (black).

The acceptable value for SMD in most of SLD applications should be at most 5%, this means that the SMD values measured from the discussed devices is about 3-4 times the acceptable range in the best case. On one hand, the measured data is taken from devices with no AR-coating, which suggests further reduction can be achieved from the very same devices after applying the AR-coating. On the other hand, the outcomes of the latest experiment suggest that devices with improved heat dissipation can perform better. The excess un-thinned GaAs substrate (about 150µm) is the main reason of this insufficient cooling to this system, regarding that the device is mounted on a c-mount placed on a cooled surface to room temperature.

3.9 Excess heat avoidance:

In order to develop a set of design criteria for window structured SLD and investigate the main parameters governing their behaviour it is necessary to separate the effects of self-heating from SLD operation. Joule heating was responsible for the poor operation of the devices presented in section 3.8, with devices mounted on gold coated c-mounts epi-side up and subjected to high current densities ~4kA.cm^{-2}. Therefore,

improvement in heatsinking was required before detailed investigation could be carried out.

3.9.1 Epi-side down configuration:

Under electrical pumping, it is the top side of the device that gets hot. Therefore, if the device is mounted epi-side down, this should bring the active (hot) layer closer to the cooled heatsink surface, as opposite to the previous case where heat involved have to be extracted via the GaAs substrate.

Two devices with comparable dimensions 1.7 and 3mm long active stripes both 4µm wide stripes were mounted epi-side down so that the excess substrate does not contribute in the cooling process, this should improve the heat sinking and fixing the central wavelength to a value closer to the absorption band in the window region. The devices had undergone the basic LI and the low resolution EL tests to identify the power level and confirm the no-lasing state first. Figure 3- 24shows the CW EL spectra for devices with 1.7mm long stripe (a) and 3mm long stripe (b).

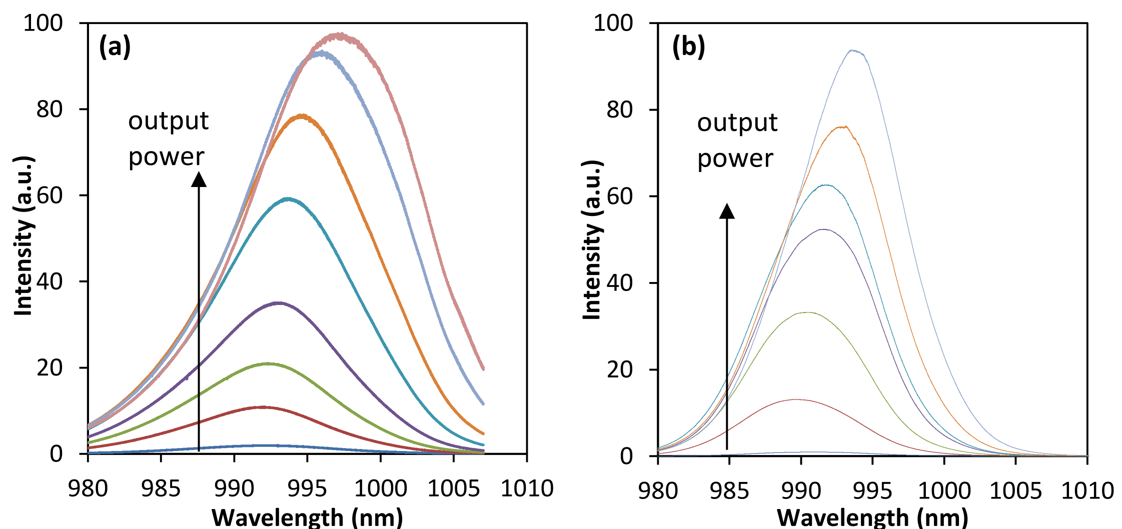

Figure 3-24: Low resolution spectra for SLDs mounted epi-side down, (a) for the device with 1.7mm stripe and 1mm window, and (b) for device 3mm active stripe and 2mm window. The shift detected in the 3mm active stripe was ~5nm from 990 to 995nm while the shorter active device showed a shift of ~7nm from 991nm to 998nm.

Later on, the SMD of the two devices were investigated using the high resolution EL. The maximum power of the 1.7mm device almost doubled this time where a 32.5mW power was collected while a power of 31mW was collected from the 3mm device at 400mA pumping level. The SMD *vs* output power curve was extracted from the measured data using the same technique. Significant improvement in the SMD level was observed, in the 1.7mm Device, SMD of 19% was recorded at 32.5mW while an SMD of only 8% at 20mW which is the A-point in this device. The performance of the 3mm Device is improved as well to the measured power level. The spectral modulation depth was found to be only 5.5% at 30mW, which is less than half the previously measured value (~12.5% at 29mW). Again all the values were recorded without the application of AR-coating to the tested devices, which can result in even better performance when 10^{-3} or 10^{-4} effective reflectivity is added to the already available by the rear section and the tilted waveguide. Figure 3-2 5below shows a comparison in the SMD development of the two devices to those of the epi-side up configurations.

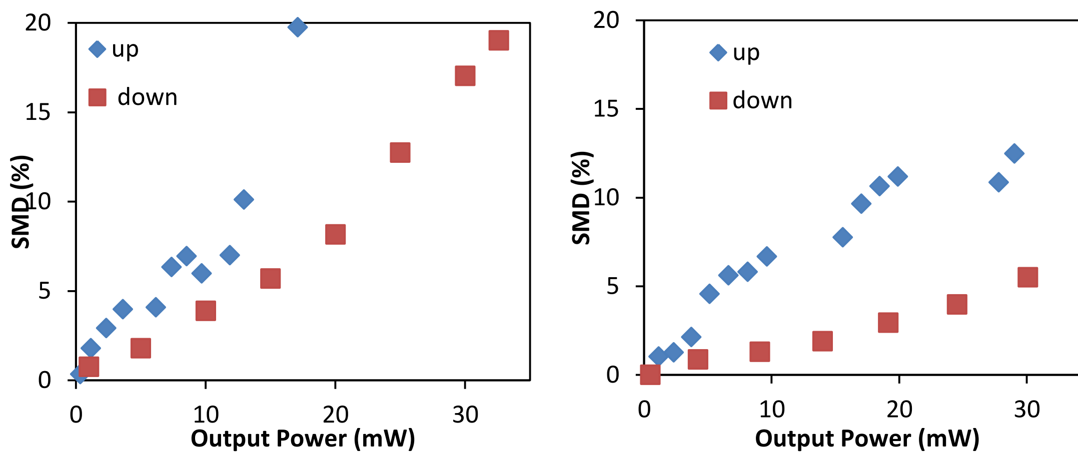

Figure 3-25: SMD comparison for the device with 1.7mm (a) and 3mm (b) active stripes. The blue rhombus marks are associated with the epi-side up devices while the red squares are the SMD of the epi-side down devices. Comparing the two cases shows a significant improvement in both cases due to the red-shift reduction in the epi-side down devices.

The simulation done previously in section 3.6 is repeated for the epi-side down devices to confirm the trends. For each device, the effective reflectivity of the facets

was selected such that the front facet is considered 10^{-4} since it is a tilted facet [27], and the rear facet reflectivity was selected by multiplying the reflectivity provided by the associated window length by the 10^{-4} reflectivity of the tilted facet. The effective reflectivity of the window section is selected from the measured data in 3.5 while the 10^{-4} reflectivity was selected since it is the most repeated number in GaAs broadband structure, a study presented Alphonse suggested this number for example [20].

Examining the simulation done to the device with 3mm long active stripe showed a very good coherence to experimental value in which a linear increase in the spectral modulation depth is obvious as the output power increases to values larger than 1mW. In contrast to this case, the 1.7mm showed a kink at 20mW power level at which the slope of the SMD increase became steeper. As discussed earlier in 3.8, this increase in the slope was because of the decrease in the rear facet reflectivity.

By examining the central wavelength shift in the low resolution EL spectra of the device that had 1.7mm active stripe, the EL spectrum at the maximum power is shifted ~8nm to 998nm. Recalling the photocurrent spectrum measured in 2.5, the relative photocurrent at 998nm is ~55%. If we assumed linear relationship between the effective reflectivity of the window and the absorption (which is commensurate to the photocurrent measured at this wavelength), the reflectivity can be assumed to be half the value estimated under no red-shift conditions. Based on this assumption, simulation is held of the exact same parameters except that the reflectivity is doubled. The coherence between the experimental and simulation work is resumed. Figure 3-26 shows the simulations held for the two devices.

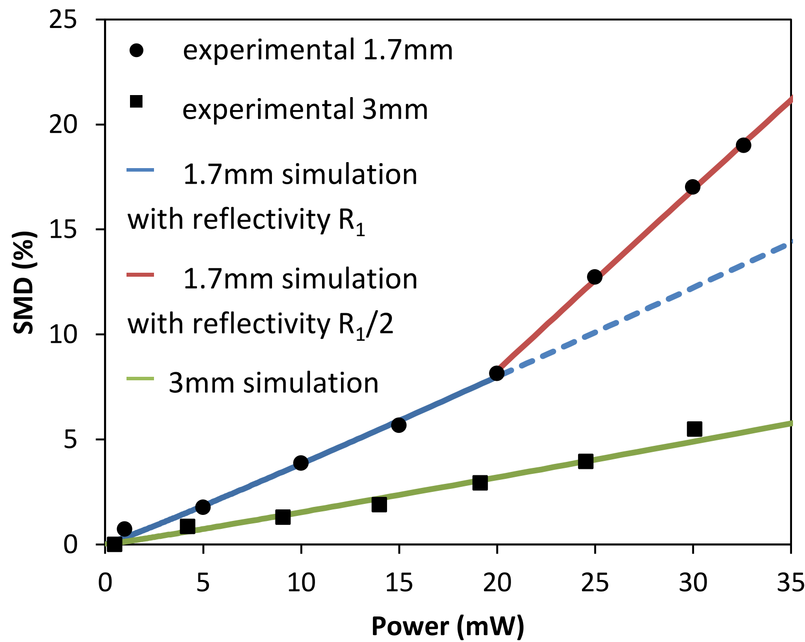

Figure 3-26: Comparison between the experimental SMD measured from the epi-side-down devices and the outcomes of the simulation held for the same devices.

An SLD of 1mm active stripe and 1mm active window is mounted epi-side down to study the window. The device initial screening showed an output power up to ~20mW. The development of the SMD as a function of output power and the LI curve of the measured device is shown in Figure 3-27 below. SMD had the same behaviour of the one shown in the device of 1.7mm stripe.

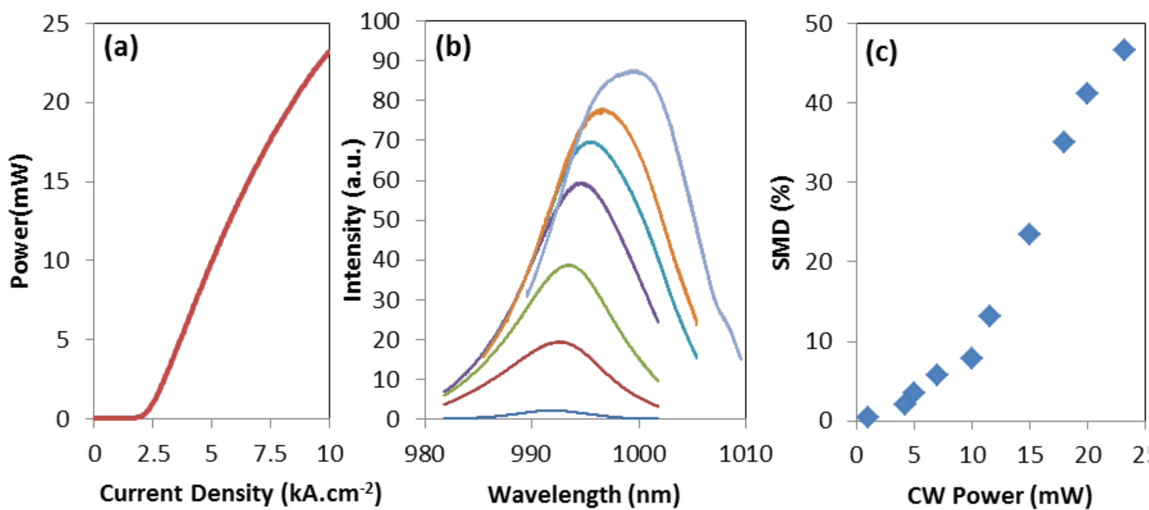

Figure 3-27: The initial screening of a device with 1mm stripe and 1mm window showing the LI curve (a) and the low resolution spectra with peak red-shift to 1001nm (b). SMD as a function of output power for this device is shown in (c). Beyond 10mW the modulation developed very quickly to achieve ~50%.

Figure 3-28 shows the high resolution EL spectra at the maximum output power. In this power the central wavelength of the emission envelope is located at 1µm. The spectrum is actually split around the central wavelength to two areas, the first one where the absorption of the window is in the >50% region at shorter than 1µm wavelengths, the SMD in that region is very low. On the other hand, the range of wavelengths longer than 1µm showed high SMD levels since the relative absorption decreased to less than 10% at wavelength ≥ 1005nm. This is confirmed by determining SMD throughout the wavelength range as shown in Figure 3-28. We can notice SMD as low as 5% at the central wavelength and the short range of the wavelengths while this SMD increases up to 35% on the longer wavelength side.

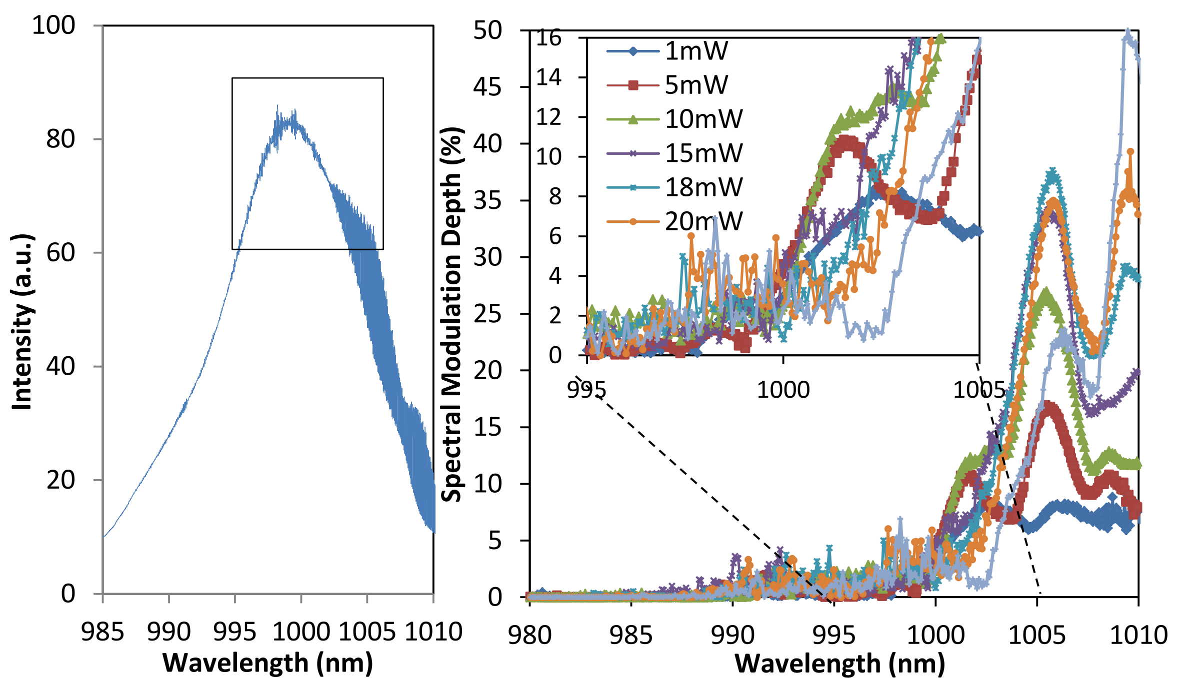

Figure 3-28: a comparison between the left and right side of the peak wavelength in the full EL spectrum (a) taken at maximum power, and the SMD measured (b). The SMD in the longer wavelength region (lower absorption) is always higher than the short wavelength region.

The window transform from the absorptive window at low output powers to the transparent window based on the wavelength shift can be proved by examining the fabry-pérot mode spacing along the wavelength range. Increasing the optical cavity

length results in decrease of the Fabry-Pérot mode spacing as eq. (3-1) suggests. Figure 3-29 shows the measured mode spacing as a function of wavelength for a device with 1mm long stripe and 1mm long window. The mode spacing decreases from 0.075nm, at 993nm, to 0.052 at 1010nm.

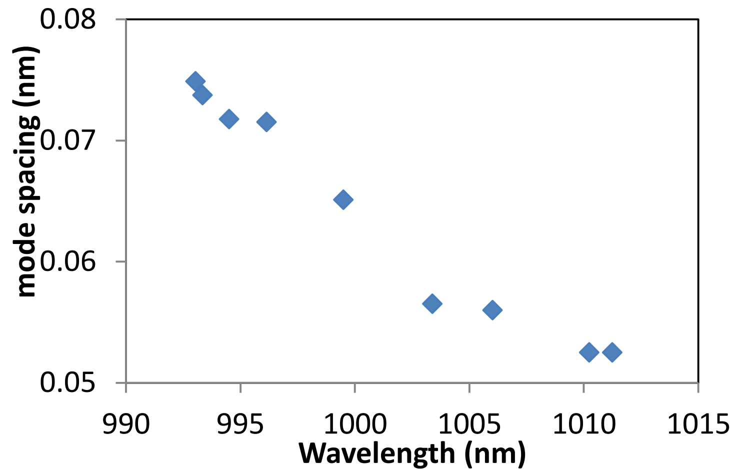

Figure 3-29: The mode spacing of the 1mm active stripe and 1mm window device along the measured spectrum. The mode spacing decreased from 0.075nm to 0.052nm due to optical cavity lengthening from stripe only to stripe + window length.

3.9.2 Pulsed Operation

Since the higher SMD was observed at longer wavelength as a result of emission red-shifting with respect to the absorption peak in the window region, one might expect to suppress this effect if Joules heating in the stripe can be minimized. To reduce the effect of self-heating and test the "ideal" case of the proposed structure (i.e. when not limited by our device fabrication process and the packaging series resistance), the device that was mounted epi-side down with 1.7mm active stripe was tested under pulsed operation at room temperature. A pulse train of 10µsec pulse width and 1msec pulse duration (1% duty cycle) was applied to the device with variable amplitude. Figure 3-30 shows the device performance under pulsed conditions. The pulsed LI (Figure 3-30a) showed an increase of about 20% output power as the output power recorded was 38mW compared to 32.5mW recorded for the continuous wave operation at the same injected current (300mA). Perhaps a more significant difference is the reduction of the red-shift from

~6nm in CW to <1nm in the pulse operation, this difference is also recorded at the same pumping currents (300mA in both cases). The low resolution EL spectra recorded at power levels from 5-35mW in a step of 5mW and at the maximum power recorded in this pumping range is plotted in Figure 3-30b. Two insets are included in this Figure 3- the first one shows the high resolution EL spectrum at the maximum power and a magnified portion of the high resolution EL which demonstrate the mode spacing. This wavelength stability resulted in an SMD at the highest power (38mW) of only 1-2% which is considered the ideal SLD operation reported in the literature [7], the tolerable range for applications like OCT and fibre optic gyroscope FOG.

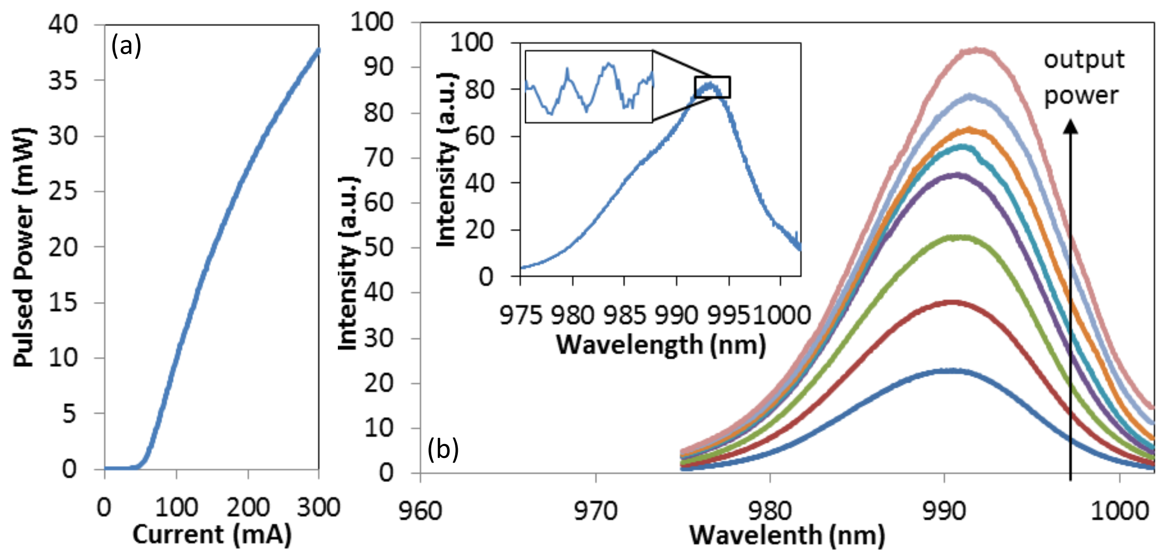

Figure 3-30: The basic characterization of the 1.7mm epi-side-down device where the LI is shown in (a), the low resolution is shown in (b), and the high resolution at the maximum power measured is shown in the inset. Due to the negligible red-shift in the central wavelength the device worked with 1-2% SMD at 38mW compared to ~20% at 32mW in CW operation.

3.9.3 Window absorption band control using on-chip resistor:

CW operation of the SLD results in red-shift of the emission until it is no longer resonant with the absorption available in the window section, and lasing suppression is only contributed to the divergence of light in the window section. Section 3.9.2 described how the absence of self-heating can delay the onset of large SMD, however, this is not always practical. Here I suggest an alternative approach based on control of

absorption in the window section via use of a resistor placed above it. When a voltage is applied across the resistor, the heat generated will red-shift the absorption spectrum.

Figure 3-23 showed the effect of red-shift with respect to the absorption band. Poor heatsinking in the device studied earlier could be attributed to resistive electrical contact and/or poor packaging when the device is mounted epi-side up with thick (~120μm) GaAs substrate.

The first modification to the standard configuration was to flip the device and mount it epi-side down to improve the heat sinking at the p-side of the device instead of the n-side. This improvement is a result of bringing the heat-generating part of the chip into contact with the heat sink rather than heat needing to conduct via the more resistive GaAs substrate. Figure 3-25 showed the differences in performance of identical devices and how the development of the Fabry-Pérot modes has been suppressed to a certain level in the case of the epi-side down device.

Another method to spectrally control the device is to red-shift the absorption band in the window region and tunes it to the central wavelength emitted by the active stripe. The easiest way to tune the wavelength of a semiconductor structure is to heat the structure up or cool it down. In the case of red-shift it needs to be heated up. Heating up the whole structure was not a viable option as the energy structure of the chip will also shift. Also, heating the window section through the substrate was not so practical as the spatial temperature control was not precise enough to control window temperature alone. Therefore, my suggestion to use a heating source, such as an on-chip-resistor, which can be placed at a specific location on the surface of the chip immediately above the window region and its temperature controlled in order to locally modify the absorption properties of the material. At the onset of Joule heating in the self-aligned stripe which manifest itself as a red-shift of the SLD emission, the voltage across the

resistor can be increased to realize a commensurate red-shift of the absorption spectrum in the window region, bringing the two into resonance again, where the window can absorb the light propagating through it.

Whilst integration of a thin film heating element with the fabrication process for the SLD would present the most effective methodology (as will be describe later), the simplest method to trial the concept is to integrate a film type resistor on the rear window section of the device. Figure 3-31 shows this configuration. The SLD used has a 3mm long active stripe and 2mm window. The reason for choosing this long window was mainly for assurance that the heat generated will be as localized as possible, bearing in mind that the surface is covered with 500nm of SiN as part of the fabrication process. A film resistor of 8.5Ω was fixed on the surface using thermal glue. Although it is not the perfect way to create an on-chip heat source, the presence of this low value resistor can provide enough control of the thermal energy provided, whilst the use of the thermal glue will aid better heat distribution along the window rather than just a point.

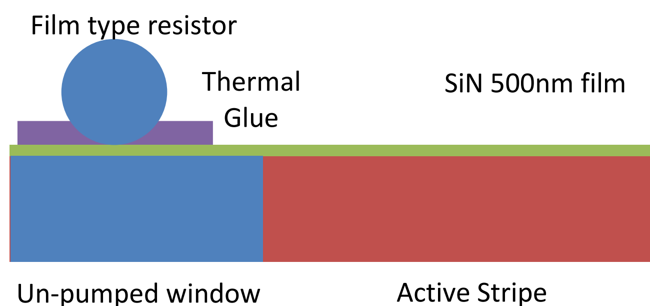

Figure 3-31: configuration used to heat up the rear window.

The resistor was driven by an external DC voltage source. Knowing the voltage provided combined with the resistor value, the output thermal power can estimated to be:

$$P = \frac{V^2}{R} \qquad \text{.... (3-19)}$$

where P is the thermal power in watts, V is the potential difference in volts, and R the resistance of the mounted resistor.

The applied voltage across the resistor was changed between 0 and 6.5V with a step of 0.5V. At each step, the high resolution EL was measured with resolution of 0.01nm. The output power was fixed during the measurements. After measuring the EL spectrum, the spectral modulation depth was calculated at each step by the same formula shown in eq. (3-2). Figure 3-32 below shows the SMD as a function of the applied power. The level of the spectral modulation depth decreased gradually as the applied power increased beyond 2.5W.

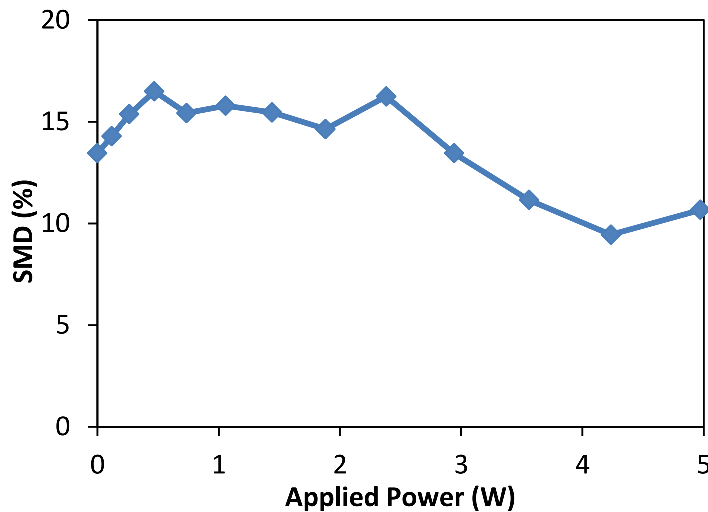

Figure 3-32: The spectral modulation depth measured in the CW EL as a function of the applied power.

Although the results prove the concept, a better configuration can provide improved spectral control. The main problem associated with these measurements was the offset of using the SiN layer deposited for electrical isolation of the SLD. The 500nm thick insulating SiN deposited on the semiconductor prevented sufficient heat transfer from the resistor to the semiconductor, limiting even distribution and control of the actual amount of thermal energy required. Also a measurement of the actual temperature of the semiconductor material was not available in the configuration used. An on-chip thermistor can be added to measure the temperature of the window section.

A modification to the design is required to include a metallic alloy filament directly on the GaAs surface so that minimum is dissipated in the dielectric covering the device, since the thermal conductivity of the dielectric is lower than the one of the semiconductor the thermal "current" prefers to expand to the semiconductor part, and since it is made from the same material the heat flow will be isotropic under the contact point. The thickness need to be achieved is ~2.2µm, 300nm contact GaAs, 1.5µm AlGaAs 900nm, n-InGaP and AlGaAs. This means that a 5µm resistive contact will be more than enough. Figure 3-33 shows the concept and the design suggested for spectral control by on-chip-resistor.

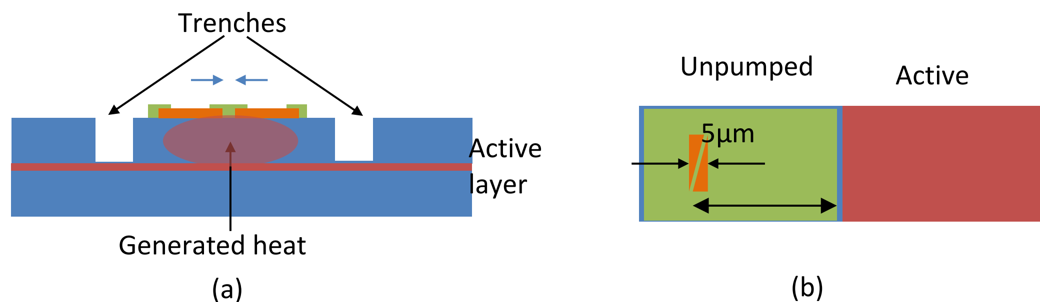

Figure 3-33: The concept and simplified design for an on-chip-heater for window spectral control. The orange portions are the alloy surfaces to be used as a resistor with a small separation (pointed by the small blue arrows in (a)) defines the resistance used. As shown in (b) the integrated heater should be located on a distance enough to isolate the two sections thermally.

3.10 Summary and conclusion:

In this chapter tilted windowed SAS superluminescent diodes (SLDs) fabricated from 980 nm emitting DQW material were investigated. The methods to achieve superluminescence from laser were briefly introduced followed by a thorough study of the mechanism behind operation of the window structure. From the characterization of devices processed normal-to-facets the effective reflectivity (R_{eff}) of the rear window was determined. The experimental measurement showed a reflectivity as low as 10^{-14} when a 2250µm window was integrated with the active device. This is resulted from a combination of the mode spreading out in the laterally unguided area of the device (in

the window), and the absorption taking place in the unpumped window region, in which the active layer was not intact during the fabrication process.

Based on the effective reflectivity estimation in section 3.5 a simple simulation was designated to estimate the behaviour of the spectral modulation depth (SMD) for the operating devices. It was found that in addition to the window effect, the active stripe geometry has a significant effect on the spectral modulation depth of the output emission.

The experimental characterization of the windowed tilted SLD showed output power in the level of +40mW for devices with active stripes longer than 2mm. The window existence did not affect the slope efficiency of the devices with specific active stripe geometry, in contrast the active stripe geometry showed a significant effect on the output power. The LI curves at various temperature values a role for the rear window in temperature distribution and maintenance during the CW operation.

The spectral screening of the devices confirmed that the devices did not lase throughout the operation range. The spectral modulation depth of the devices were measured and showed similar behaviours in the three tested devices. The SMD trend, suggested by the simulation held, with increasing the output power was confirmed experimentally. Though, the devices did not show the level of SMD expected by the simulation. The device with the best performance in this category was the one that had an active stripe of $3000\times4\mu m^2$. The measured SMD at 43mW was ~17%. Although this value is more than 3 times higher than the value that Shidlovsky stated as the acceptable value for applications such as OCT, it gave an indication that the window used was capable to suppress the lasing in an active material that was designed originally for low threshold laser operation.

All of the tested devices experienced different levels of Joule's heating which resulted in a red-shift in the emission peak. This shift results in detuning of the emission peak with respect to the absorption peak in the window region. This causes the window to change gradually from absorptive to transparent window, in the latter case only mode spreading and the cavity tilt contribute in lasing suppression. This was the reason of high SMD determined from those devices.

Three methods were used to bring back the emission and absorption peaks, in the active and window regions, respectively, into resonance. The first one was to mount the devices' hot layer closer to temperature-controlled-surface of the heatsink. The second option used to minimize the self-heating was to pump the structure under pulsed operation. The third and last option was an attempt to control the spectral properties of the absorbing window region by integrating a heating element on the unpumped window region.

The epi-side down showed a significant improvement in heat-sinking appeared as smaller red-shift in the central peak. The experimental results showed better correlation with the simulation results. An epi-side down device with 3mm long and 4µm wide active stripe with 2mm unpumped window emitted 30mW of ASE output power with only 5.5% SMD. This enhancement in the SMD was a result of minimized red-shifting down to 3nm as shown in the low resolution EL.

The pulsed operation enabled testing the device under its ideal circumstances at which the series resistance of the ohmic contacts and the imperfect fabrication process was minimized. Less than 1nm shift was detected by the low resolution EL and SMD of only 1-2% was recorded at 38mW output power. The pulsed operation proved that the presented window can suppress the back reflections to extremely low levels that results in an ideal SLD in case the required heat sinking is used.

The last experiment done was a more realistic method to tune the device performance to the optimum operation conditions. Integrating a resistor to the rear section of the device is proved to enable absorption band tailoring to the requirement of the emission bandwidth. An epi-side up mounted device is prepared to test the resistor effect on the SMD behaviour. At the same output power this device showed a reduction of SMD level from ~15% to below 10% when the power applied by the resistor exceeded 4W.

3.11 Future Work

1- Further investigation of the new window ability and its effect on the device performance. Parameters such as the effect of the active layer gain, and the effective refractive index step between the active stripe and the unpumped window region need to be investigated for future development.

2- Integration of the rear window to an active that is designed for wide spectrum operation. This can decrease the problem results from the peak shift by increasing the relative overlap between the active and window parts.

3- Design of a proper spectral controller for the rear section, a start point is to integrate an on-wafer resistor with the suitable metal alloy. The main point is to get rid of the 500nm thick SiN layer that prevents adequate thermal pumping of the window.

4- A study of the refractive index change due to the variables changed during the operation in both active and window, and how will this affect the final operation. Changes like the one caused by the carrier injection, or the heat rise.

3.12 References

[1] C.-W. Tsai, "Extremely broadband superluminescent diodes/semiconductor optical amplifiers in optical communication band," *Proceedings of Conference on Laser and Electro-Optics CLEO/Pacific Rim 2003,* pp. 54, 15-19 December 2003, Taipei:Taiwan.

[2] S. S. Wagner and T. E. Chapuran, "Broadband High-Density WDM Transmission Using Superluminescent Diodes," *Elecronics Letters*, vol. 26, no. 11, pp. 696–697, 1990.

[3] O. Çelikel and S. E. San, "Establishment of all digital closed-loop interferometric fiber-optic gyroscope and scale factor comparison for open-loop and all digital closed-loop configurations," *IEEE Sensors Journal*, vol. 9, no. 2, pp. 176–186, 2009.

[4] H. S. Djie and C. E. Dimas, "Semiconductor Quantum-Dot Based Wideband Emitter for Optical Sensors," *IEEE Sensors Journal,* vol. 1, pp. 932–934, 2005.

[5] H. S. Djie, C. E. Dimas, D. Wang, B. Ooi, S. Member, J. C. M. Hwang, G. T. Dang, and W. H. Chang, "InGaAs / GaAs Quantum-Dot Superluminescent Diode for Optical Sensor and Imaging," *IEEE Sensors Journal*, vol. 7, no. 2, pp. 251–257, 2007.

[6] B. Heise, S. E. Schausberger, S. Häuser, B. Plank, D. Salaberger, E. Leiss-Holzinger, and D. Stifter, "Full-field optical coherence microscopy with a sub-nanosecond supercontinuum light source for material research," *Optical Fiber Technology*, vol. 18, no. 5, pp. 403–410, 2012.

[7] W. Drexler and J. G. Fujimoto, *Optical Coherence Tomography: Technology and Applications*. 2008.

[8] N. Ozaki, T. Yasuda, S. Ohkouchi, E. Watanabe, N. Ikeda, Y. Sugimoto, and R. A. Hogg, "Near-infrared superluminescent diode using stacked self-assembled InAs quantum dots with controlled emission wavelengths," *Japanese Journal of Applied Physics*, vol. 53, no. 04EG10, pp. 1–4, 2014.

[9] a F. Fercher, W. Drexler, C. K. Hitzenberger, and T. Lasser, "Optical Coherence Tomography — Principles and Applications," *Reports on Progress in Physics*, vol. 66, pp. 239–303, 2003.

[10] Y. Kashima, A. Matoba, and H. Takano, "Performance and Reliability of Ingaasp Superluminescent Diode," *Journal of Lightwave Technology*, vol. 10, no. 11, pp. 1644–1649, 1992.

[11] L. Burrow, F. Causa, and J. Sarma, "1.3-W Ripple-Free Superluminescent Diode," *IEEE Photonics Technology Letters*, vol. 17, no. 10, pp. 2035–2037, 2005.

[12] X. Li, P. Jin, Q. An, Z. Z. Wang, X. Lv, H. Wei, and J. J. Wu, "A high-performance quantum dot superluminescent diode with a two-section structure", *Nanoscale Research Letters*, vol. 6, p. 625, 2011.

[13] Q. Jiang, Z. Y. Zhang, M. Hopkinson, and R. a. Hogg, "High performance intermixed p-doped quantum dot superluminescent diodes at 1.2µm," *Electronics Letters,* vol. 46, no. 4, p. 295, 2010.

[14] Z. Y. Zhang, Z. G. Wang, B. Xu, P. Jin, Z. Z. Sun, and F. Q. Liu, "High-Performance Quantum-Dot Superluminescent Diodes," *IEEE Photonics Technology Letters*, vol. 16, no. 1, pp. 27–29, 2004.

[15] M. Matsumoto, K. Sasaki, M. Kondo, T. Ishizumi, T. Takeoka, H. Nakatsu, M. Watanabe, O. Yamamoto, and S. Yamamoto, "High-Power 780 nm AlGaAs Narrow-Stripe Window Structure Lasers with Window Grown on Facets," *Japanese Journal of Applied Physics*, vol. 32, no. 5A, pp. 665–667, 1993.

[16] H. Nagai, Y. Noguchi, and S. Sudo, “High-power, high-efficiency 1.3 μm superluminescent diode with a buried bent absorbing guide structure,” *Applied Physics Letters*, vol. 54, no. 18, p. 1719, 1989.

[17] G. a. Alphonse, “Design of High-Power Superluminescent Diodes with Low Spectral Modulation,” *SPIE Proceedings in Test and Measuerments Applications of Optoelectronic Devices*, san jose: California: USA, 18 January 2002.

[18] P. A. Lobintsov, D. S. Mamedov, Va. V Prokhorov, A. T. Semenov, and S. D. YAkubov, “High-Power Superluminescent Diodes With Non-Injection Output Sections,” *Quantum Electronics (aka Kvantovaya Elektron.*, vol. 34, no. 3, p. 209, 2004.

[19] G. A. Alphonse, J. C. Connolly, N. A. Dinkel, S. L. Palfrey, and D. B. Gilbert, “Low spectral modulation highpower output from a new AlGaAs superluminescent diode / optical amplifier structure,” *Applied Physics Letters*, vol. 55, no. 22, pp. 2289–2291, 1989.

[20] G. a. Alphonse, D. B. Gilbert, M. G. Harvey, and M. Ettenberg, “High-power superluminescent diodes,” *IEEE Journal of Quantum Electronics*, vol. 24, no. 12, pp. 2454–2457, 1988.

[21] L. Fu, H. Schweizer, Y. Zhang, L. Li, A. M. Baechle, S. Jochum, G. C. Bernatz, and S. Hansmann, “Design and realization of high-power ripple-free superluminescent diodes at 1300 nm,” *IEEE Journal of Quantum Electronics*, vol. 40, no. 9, pp. 1270–1274, 2004.

[22] D. S. Mamedov, V. V Prokhorov, and S. D. YAkubov, “Superbroadband high-power superluminescent diode emitting at 920 nm,” *Quantum Electronics (aka Kvantovaya Elektron.*, vol. 33, no. 6, pp. 471–473, 2003.

[23] N. S. K. Kwong, K. Y. Lau, and N. Bar-Chaim, “High-power high-efficiency GaAlAs superluminescent diodes with an internal absorber for lasing suppression,” *IEEE Journal of Quantum Electronics*, vol. 25, no. 4, pp. 696–704, 1989.

[24] K. Tateoka, H. Naito, M. Yuri, M. Kume, K. Hamada, H. Shimizu, M. Kazumura, and I. Teramoto, “A high-power GaAlAs superluminescent diode with an antireflective window structure,” *IEEE Journal of Quantum Electronics*, vol. 27, no. 6, pp. 1568–1573, 1991.

[25] A. T. Semenov, V. R. Shidlovski, S. A. Safin, V. P. Konyaev, and M. V Zverkov, “Superluminescent Diodes for Visible (670nm) Spectral Range Based On AlGaInP/GaInP Hetersostructures with Tapered Grounded Absorber,” *Elecronics Letters*, vol. 29, no. 6, pp. 530–532, 1993.

[26] F. Causa and L. Burrow, “Ripple-Free High-Power Super-Luminescent Diode Arrays,” *IEEE Journal of Quantum Electronics*, vol. 43, no. 11, pp. 1055–1059, 2007.

[27] G. A. Alphonse and M. Toda, “Mode coupling in angled facet semiconductor optical amplifiers and superluminescent diodes,” *Journal of Lightwave Technology*, vol. 10, no. 2, pp. 215–219, 1992.

[28] L. H. Duan, L. Fang, J. Zhang, Y. Zhou, H. Guo, Q. C. Luo, and S. F. Zhang,

"Fabrication and characteristics of high speed InGaAs/GaAs quantum-wells superluminescent diode emitting at 1053 nm," *Semiconductor Science and Technology*, vol. 29, no. 5, p. 055004, 2014.

[29] K. Hamamoto, T. Ohgoh, and H. Asano, "Reliability Improvement of superluminescent diodes emitting at 1.0 µm band using InGaAsP barrier structure," *Electronics Letters*, vol. 49, no. 6, pp. 409–410, 2013.

[30] G. Bauer, "Absolutwerte der optischen Absorptionskonstanten von Alkalihalogenidkristallen im Gebiet ihrer ultravioletten Eigenfrequenzen," *Annual Physics*, vol. 411, no. 4, pp. 434 – 464, 1934.

[31] J. Lee, T. Tanaka, S. Sasaki, S. Uchiyama, M. Tsuchiya, and T. Kamiya, "Novel Design Procedure of Broad-Band Multilayer Antireflection Coatings for Optical and Optoelectronic Devicesg," *Journal Lightwave Technology*, vol. 16, no. 5, p. 884–, 1998.

[32] I. C. Stevenson, "High performance antireflection coatings for telecommunications," in *Optical Science and Technology, the SPIE 49th Annual Meeting*, 2004, pp. 79–92.

[33] W. T. Tsang, R. A. Logan, and J. A. Ditzenberger, "Multilongitudinal mode operation in angled stripe buried heterostructure lasers," *Journal of Applied Physics*, vol. 54, no. 2, p. 1137, 1983.

[34] Z. Y. Zhang, I. J. Luxmoore, C. Y. Jin, H. Y. Liu, Q. Jiang, K. M. Groom, D. T. Childs, M. Hopkinson, A. G. Cullis, and R. A. Hogg, "Effect of facet angle on effective facet reflectivity and operating characteristics of quantum dot edge emitting lasers and superluminescent light-emitting diodes," *Applied Physics Letters*, vol. 91, no. 8, p. 081112, Aug. 2007.

[35] T. Lee, C. A. Burrus, and B. I. Miller, "A Stripe-Geometry Double-Heterostructure Amplified-Spontaneous-Emission (Superluminescent) diode," *IEEE Journal of Quantum Electronics*, vol. QE-9, no. 8, pp. 820–828, 1973.

[36] M. Ettenberg and H. Kressel, "The Reliability of (AlGa)As CW Laser Diodes," *IEEE Journal of Quantum Electronics*, vol. QE-16, no. 2, pp. 186–196, 1980.

[37] S. Takahashi, T. Kobayashi, H. Saito, and Y. Furukawa, "GaAs – AlGaAs DH Lasers with Buried Facet," *Japanese Journal of Applied Physics*, vol. 17, no. 5, pp. 865–870, 1978.

[38] H. O. Yonezu, M. Ueno, T. Kamejima, and I. Hayashi, "An AlGaAs Window Structure Laser," *IEEE Journal of Quantum Electronics*, vol. QE-15, no. 8, pp. 775–781, 1979.

[39] T. Suhara, *Semiconductor Laser Fundamentals*. CRC Press, 2004.

[40] B. W. Hakki and T. L. Paoli, "Gain spectra in GaAs double-heterostructure injection lasers," *Journal of Applied Physics*, vol. 46, no. 3, pp. 1299–1306, 1975.

[41] S. Adachi, *Properties of Aluminium Gallium Arsenide*. London, United Kingdom: INSPEC, The Institution of ELectrical Engineers, 1993.

Chapter 4: Normal-to-Facet Superluminescent diodes

4.1 Introduction:

The early reports of Superluminescent diodes described structures in which the optical cavity was aligned normal to the cleaved facets. Such devices relied upon the well matured AR-coating method to suppress optical feedback from the cavity end mirrors. Whether AR-coating alone or used together with an integrated transparent window at one end, these were the most preferred method used for SLD fabrication. In 1983 Tsang *et.al.* presented a laser structure which had an optical waveguide tilted with respect to the (010) axis with facets cleaved along the (100) plane. They proved experimentally that this structure can decrease the device spectral coherence and operate in multimode [1]. This was the first step that developers took toward presenting SLDs with tilted facets to decrease the optical feedback, relying on the simplicity of the device fabrication. Usually this technique is combined with AR-coating for low facet reflectivities.

Utilizing the window structure presented in this thesis, SLDs with normal facets are discussed in Chapter three with the measurement held to estimate the effective reflectivity of the window facet. Such devices are expected to have a reflectivity $\sim 10^{-11}$ with sufficiently long window sections ($\geq$1.5mm).

This very low effective reflectivity should allow suppression of lasing threshold to very high currents. In fact, in chapter three normal-to-facet devices with 1mm long active stripe exhibited a shift of threshold current from <30mA in the 1mm laser (normal facet device with no window) to 170mA for a normal facet device that has 1mm long active stripe and 2.25mm rear window section. This suppression of threshold, together with the very low effective reflectivity determined from my experiment

supported the idea of studying the performance of SLD devices with their waveguides processed normal to the cleave facets. In the straight waveguides the additional contributions to the reduction of the effective reflectivity that comes from tilting the waveguide (which is commonly ~10^{-4}-10^{-3}) will be sacrificed, however two important advantages will be enabled. The first one is that the beam shape will overcome the distortion problem associated with the tilt. The beam shape of two devices, one with its optical waveguide aligned to the (010) axis (a laser) and other with a tilted waveguide with respect to the (010) axis (e.g. SLD) is compared when projected on the (100) plane. Since the divergence angle in the two devices is considered the same it all comes to the difference in the optical paths (1_1 and l_2). We can see that the paths are equal in the case of the normal to facet devices (Figure 4-1 a) when projected on the (001) plane while $l_1<l_2$ due to the tilt in the second device (Figure 4-1 b). This difference is transferred into the farfield pattern shown in (Figure 4-1 c and d) where the first one has an elliptical shape while the other one has a crescent shape which will decrease the coupling efficiency in the tilted devices when used with a standard couplers and connections in the networks.

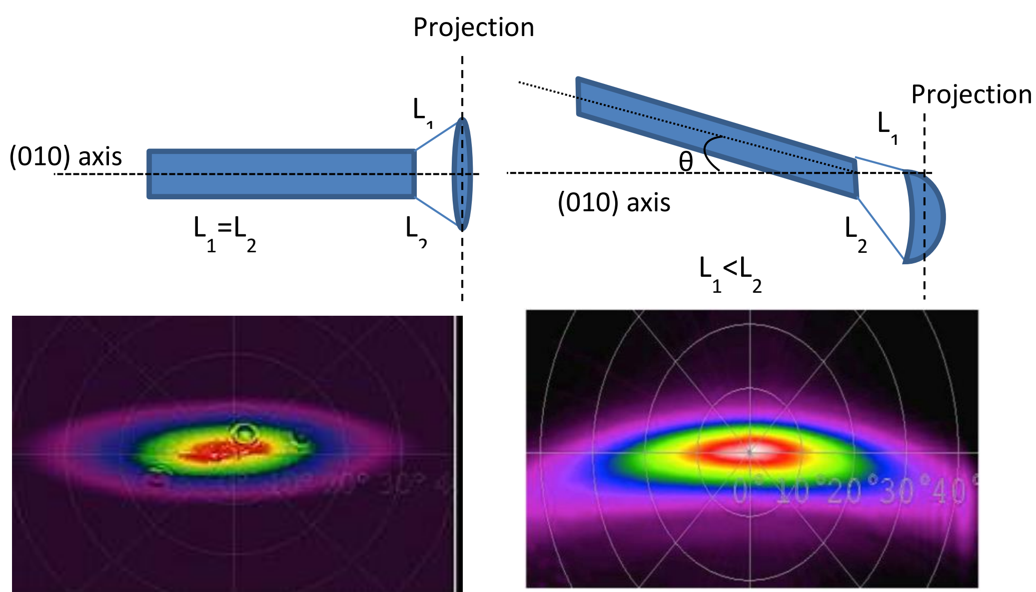

Figure 4-1: The farfield patterns of a straight cavity (e.g. diode laser) and tilted cavity (e.g. SLD). The crescent shape is obvious in the SLD farfield pattern.

Another advantage of processing the SLD with normal to facet waveguides is the semiconductor material saving in cleaving individual chips, which has a significant impact on cost savings in volume production. The excess material lost on both sides of the devices can be visualized using Figure 4-2. The chip size is bound by the dotted lines, with the extra area shaded in grey being the chip that will be wasted in cleaving.

Whilst the width of chip for the normal to facet devices is only limited by the substrate thickness (as the device width should be at least three times the thickness to have successful cleave), the width of the tilted chip is governed by the device total length L and the angle of the alignment (θ) where the width of a successful cleave will be $\geq L.sin(\theta)$.

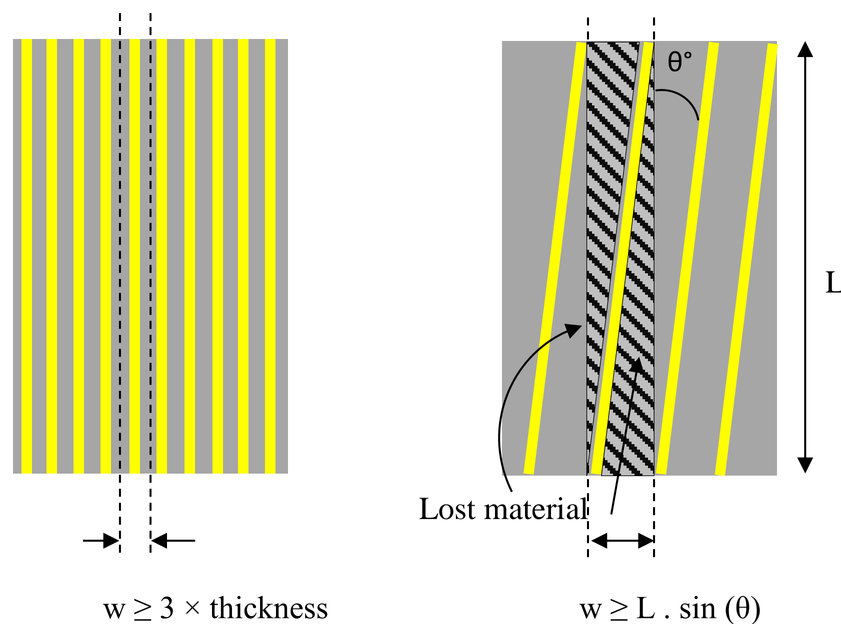

Figure 4-2: Visual comparison between two pieces of semiconductor which is required to be cleaved into individual devices. The only parameter that limits the width of the straight SLD is the chip thickness. On the other hand the piece with tilted SLD should be cleaved into chips that have width governed by the total length and the device tilting angle.

4.2 Device preparation:

Normal-to-facet SLDs were fabricated from the same material as that described in chapters 2 and 3. The dimensions of devices studied in this chapter were based on the outcomes of chapter 3. The study conducted regarding the device length suggested that

the longer the device the better performance so initially a 2mm long stripe was selected as the active part of the device. The active stripe was 3μm wide and 2mm long stripe as shown in Figure 4-3.

To achieve amplified spontaneous emission (ASE) operation, the resultant effective reflectivity of the two facets of the device has to be close to 10^{-10} as suggested by V.R. Shidlovski [2]. Since the front facet is not tilted in this case it will have a rather high reflectivity compared to the tilted SLD in chapter three, for this reason extra attention has to be paid to the selection of the rear window length. According to Snell's law, the as-cleaved facet will have a reflectivity ~33% due to the semiconductor/air interface unless an AR-coating is applied, in which case reflectivity < 0.1% is achievable. The effective reflectivity experiment I described in section 3.5 suggests that effective reflectivity of the rear facets for devices that has 1.5mm long window section is about 1.65×10^{-11}. Therefore, to guarantee a rear facet with low effective reflectivity, a window with 2mm long was selected to be integrated. This length should provide an effective reflectivity of $\sim2.287\times10^{-13}$.

To compensate for the 10^{-4} contribution to the effective reflectivity provided by tilting the front facet, this facet was coated by Helia Photonics Ltd in order to provide reflectivity down to 10^{-4}. I decided to coat the front facet as a consequence of the initial measurements performed on a 1mm long devices earlier in which the as-cleaved facet has an order of magnitude lower output power compared to their tilted counterparts. The reason of this low power is that a large portion of the light bounces back into the active stripe and develops to a stimulated emission on the opposite direction (towards the rear facet). The feedback results also in carrier depletion which decreases the population of the free carriers and the recombination rate which is directly related to the ASE output power as analysed by Suhara [3].

Taking these factors into consideration, the initially designed normal-to-facet SLD, which is shown schematically in Figure 4-3, comprised a 2mm active stripe with a 2mm rear window section. The front facet was coated with a single layer AR-coating designed to provide a reflectivity of 10^{-4}. The rear facet should provide a reflectivity down to 2.28×10^{-13} which suggests a resultant theoretical reflectivity of the two facets ($R1 * R2 \sim 2.28\times10^{-17}$). To enhance the heat sinking of the device, the chip was mounted epi-side down on a gold coated c-mount.

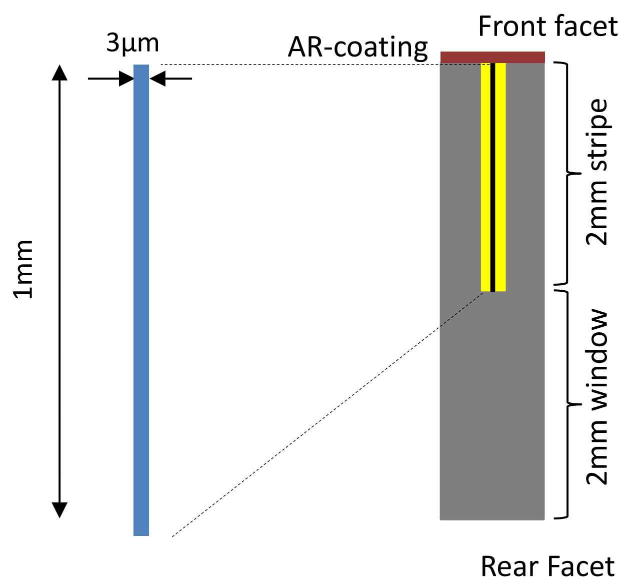

Figure 4-3: The normal-to-facet device dimensions. The figure highlights the AR-coating (dark red) on the front face.

4.3 Results

The performance of the device was first investigated using the LI setup described in chapter two (2.3.1). Output power was recorded up to 6.5mW in CW operation at 20°C from pumping the device up to 450mA (7.5kA.cm-2) before it starts lasing at 500mA and output power closer to 7.8mW as shown in Figure 4-4a below. Low resolution EL spectra were recorded as described in chapter 2 (2.3.2) at (150, 200, 250, 400, 450, and 500mA), the EL spectra are shown in Figure 4-4b. In the current range (0-450mA), no lasing was observed. However, beyond ~450mA a lasing peak started to develop at a wavelength ~1010nm. As was the case for the tilted SLDs discussed in chapter three the

lasing is occurring outside the absorption band provided in the window region due to Joule heating within the active stripe.

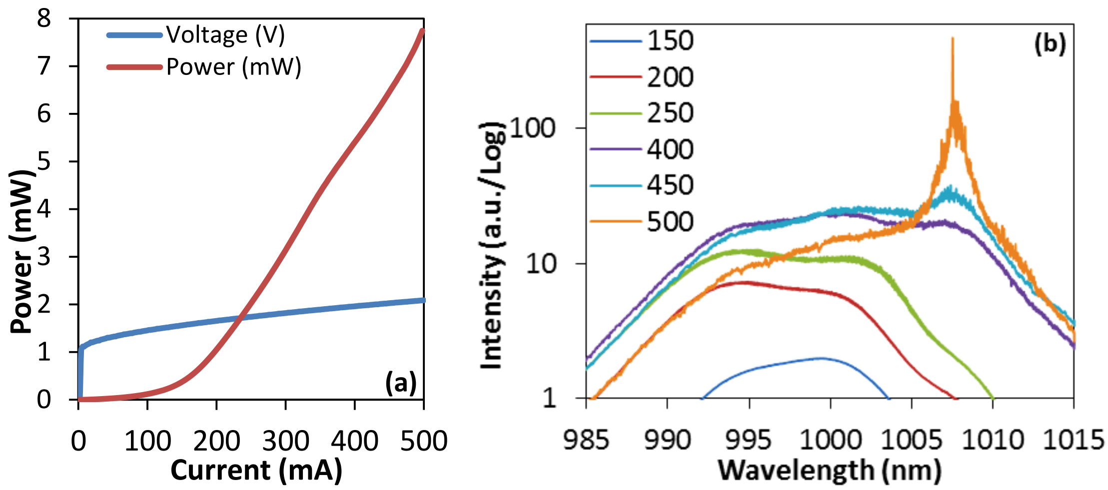

Figure 4-4: the LI curve (a) and the EL spectra at different current levels (b). The lasing peak occurred outside the power level shown in the LI curve.

The farfield pattern of the device was measured for the maximum ASE current (350mA) using the Farfield setup described in 2.3.5, the current level selected is the one comparable to the maximum current of the 1.7mm tilted SLD characterized earlier in chapter three. The measurements reveal an elliptical output beam instead of the crescent-shaped profile recorded from the tilted device. Figure 4-5 shows the farfield profile of the two devices.

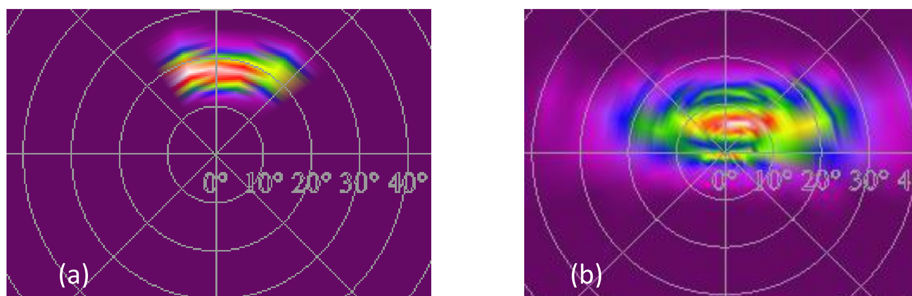

Figure 4-5: A comparison between the farfield patterns of the tilted cavity SLD (a) and the developed normal-to-facet cavity SLDs (b). The elliptical shape was maintained in the second configuration.

So, by applying the conclusions drawn from the third chapter to the case of the normal-to-facet SLD, we see that a device with an active stripe of 2mm long × 4µm width and 2mm rear window has successfully emitted amplified stimulated emission,

with the lasing threshold was suppressed to a current level as high as 450mA (compared to only 40mA in the corresponding laser cavity (i.e. no window)). The output power collected from the device was +6mW, which is considered a low level of output power compared with its tilted stripe counter parts from the same wafer discussed in chapter three. The reasons for this low power can be 1) the front facet reflectivity is still high compared with the tilted SLDs, and 2) the quality of the semiconductor structure of the SLDs presented in this chapter is worse than the one presented in chapter three because these devices are taken from a piece of the semiconductor closer to the edge of the processed wafer. Also, in spite of the fact that the 4µ provided output powers more than 30mW in the case of tilted devices, it looks like wider stripes are required in order to increase the spontaneous emission initially generated in the stripe before the amplification took place.

4.4 Further Development

In a bid to improve normal-to-facet SLD performance and to further investigate the design criteria associated with this device scheme, another batch of normal-to-facet SLDs were fabricated. For this batch, an identical planar starting wafer was used; however, another overgrowth was required. Therefore the active media are identical, yet, the completed structure may have undergone run-to-run variation according to the reproducibility of the stripe etch and the regrowth process. Furthermore, for this batch of devices the stripe widths were also changed from (3 and 4µm) to (5, 7, and 10µm). The new widths are less compatible with fibre coupling, yet, it should provide more ASE power. Devices were cleaved with various active stripe lengths and a fixed window length. The stripe lengths were chosen to be 0.5, 0.75, 1, 2, and 3mm while the window length was fixed to 1mm. According to section 3.3 the 1mm window should provide an effective facet reflectivity of ~2.35×10^{-8}. As before, a single layer of 125nm thick SiN was deposited in order to decrease the reflectivity of the front facet below 5%.

4.4.1 Widths variation effect:

Using a device that has 1mm active stripe, the effect of varying the cavity width was investigated by changing the stripes width. The ASE output power was measured as a function of the injected current using the light-current measurement setup described in section 2.3.1. A few tens of milliwatts output power was recorded as shown in Figure 4-6a, which plots the output from 1mm long active stripes with 5, 7, and 10µm stripe widths. The output power can be described as a combination of the spontaneous emission which was amplified by increasing the spontaneous emission rate and stimulated emission which results from the feedback within the active waveguide. At some point along the LI curve, the dominating emission will turn from amplified spontaneous emission into lasing. This process is investigated by monitoring the spectral modulation development in the high resolution EL spectrum measured from the devices. Examples of such emission are shown in Figure 4-6b, where the high resolution EL spectra were recorded for 5, 7, and 10µm wide stripes at 16mW. If we examine the spectral modulation depth of the three devices in Figure 4-6b we can notice that they are working in a similar manner to that discussed for the tilted devices, where the device that has a 5µm wide stripe experiencing an SMD of more than 10% for this current level, while the 10µm while device emitted EL with SMD <5%. The 7µm device exhibited SMD in between these two values. At the same time, we can observe the EL expansion sides of the central peak, especially in the 5µm wide stripes. This expansion is expected to the right hand side is expected since the pumping level was at 4.4kA.cm^{-2} at 16mW by which Joule heating took place and caused red-shift, while the expansion on the short-wavelength side was not observed in the previous batch or in the tilted devices. Usually the peak development to the shorter wavelength side is a result of transition from a higher order excited state when the ground state is saturated. It is worth mentioning that in spite of the peaks that were developed on either sides of the

central peak in the 5µm device, they are still outside the central absorption band in which the devices experienced the lowest SMD.

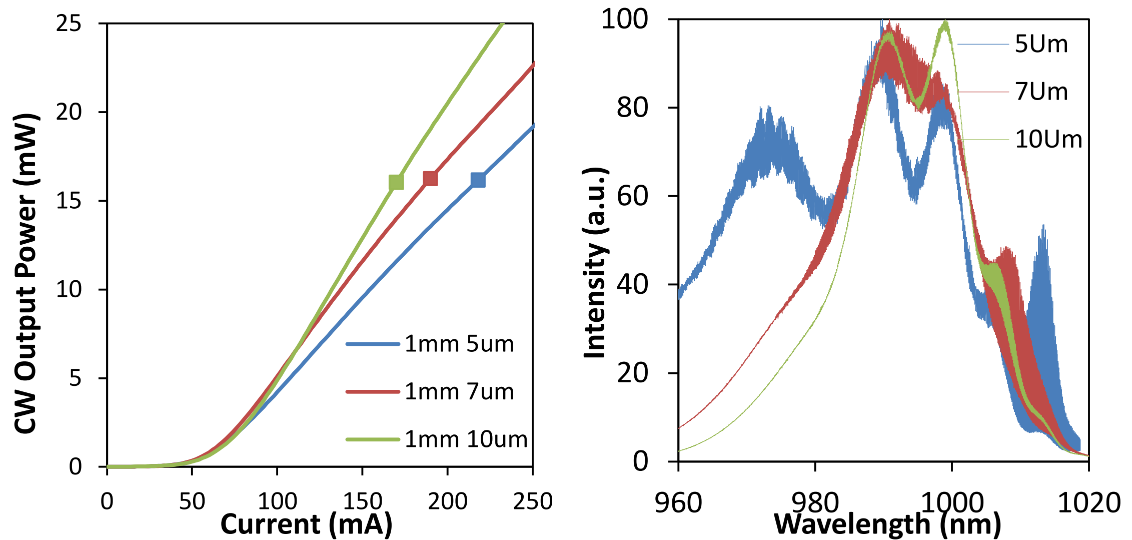

Figure 4-6: The output power as a function of current for the 1mm long normal-to-facet devices of three widths (5, 7, and 10µm) wide stripes. Output powers ≥ 20mW is recorded in which amplified spontaneous emission and amplified stimulated emission undergo competition to dominate. These dominations are more apparent in the high resolution EL spectra shown in (b) at 15mW power level. At this level, the domination of a specific emission type depends on the device stripe width where we can find mostly ASE in the 10µm and very small stimulated emission on the long wavelength side, and on the other hand very high stimulated emission spread all over the 5µm device spectrum.

4.4.2 1mm Stripe Spectral Modulation Depth

The spectral modulation depth is a Figure of merit usually used to assess an SLD performance, as described earlier. The normal to facet devices are no exceptions to this. The high resolution EL spectra of the three devices was recorded using the high resolution EL setup detailed in 2.3.3 from 2mW output power up to the lasing power which varied in the three devices from 14mW in the 5µm wide device up to 32mW in the 10µm wide device. Figure 4-7 shows the SMD development as the output power increases in the three devices.

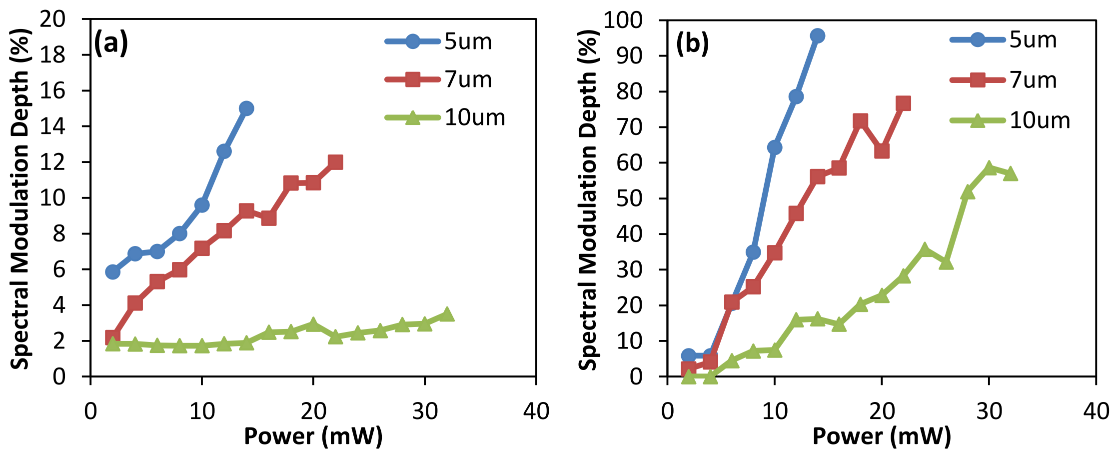

Figure 4-7: The spectral modulation depth of 1mm long devices with 5, 7, and 10µm wide stripes. The device emitted two peaks because of the heat distribution (the carrier injected heavily at one side of the stripe and almost none on the other side of the stripe due to device front facet coating. The ripple development at the two peaks is recorded in this figure. (a) is the peak at 990nm or the original peak, the ripples were developed fairly low compared to the other peak, the maximum SMD was 16% for the device with 5µm wide stripe and the minimum was <4%. (b), on the other hand, is the long wavelength peak where the device experienced very high SMD due to window transparency in this range of wavelengths. The maximum was 95% for the 5µm and the least SMD was also for the 10µm wide active with ~56%.

As shown in Figure 4-6 as an example of the EL spectra for the three devices, the devices generally had two peaks, one developed at ~990nm which is the original peak observed in the tilted devices, and the other one is the one developed at the longer wavelength side of the spectrum due to Joule heating. Figure 4-7 shows the development of the SMD for the two peaks in the three devices.

Two behaviours were observed, the first one is a rather slow development in the magnitude of the ripple size. Generally, the central wavelength peak showed an acceptable level of spectral modulation, especially taking into account that the material is a laser gain material designed for low threshold current operation. In such gain media it is difficult to supress the lasing, especially if straight waveguides are used.

On the other hand, the long wavelength peak experienced a rapid development in the ripple magnitude from no observable ripple to lasing. The location of this peak varies from one device to another, with the narrower device resulting in a longer wavelength peak. The long wavelength peak was observed in a range of wavelengths varied from

1009nm in the widest device up to 1015nm in the narrowest. The highest SMD levels recorded for the three devices were ~95%, 76.6%, and 57% for 5µm, 7µm, and 10µm wide stripes, respectively. Such SMD levels resulted from the fact that the window region is now totally transparent to the peak wavelength.

4.4.3 Length variation effect:

Since the width comparison of the 1mm active stripe devices showed that the 10µm wide device experienced the best performance, I decided to focus on this width with different cavity length. Two devices shorter than 1mm (0.5 and 0.75mm) and two longer (2, and 3mm) were tested in order to observe the effect of the length variation.

In the 500µm and 750µm devices the emission spectrum was broadened due to state filling (on the shorter wavelength side) and due to self-heating (on the long wavelength side) (as seen in Figure 4-7). The pumping level of the EL spectra plotted in Figure 4-7 for the 0.5 and the 0.75mm long devices was 4.4kA.cm^{-2} and 3.5kA.cm^{-2}, respectively. The main problem associated with the older batch of SLDs is the wavelength shift from the central wavelength towards the longer wavelength due to Joule heating. By increasing the pumping level the EL spectra showed ripples developing in the spectral areas outside the central emission range which subsequently become lasing peaks.

The wider active waveguide enabled broader emission spectra in the short cavity devices because of the high pumping level mentioned above. Keeping in mind that an imperfect AR-coating, which was a simple single SiN layer, was applied to the front facet could result in a higher reflectivity and correspondingly higher levels of feedback, together with strong feedback at wavelengths outside the bandwidth of the coating. The 0.5mm long SLDs exhibited SMD development at short wavelengths even more than the longer wavelength. It is worth mentioning that the developed SMD is still outside

the absorption bands as revealed in Figure 4-8 when the PC spectrum is plotted on the same figure.

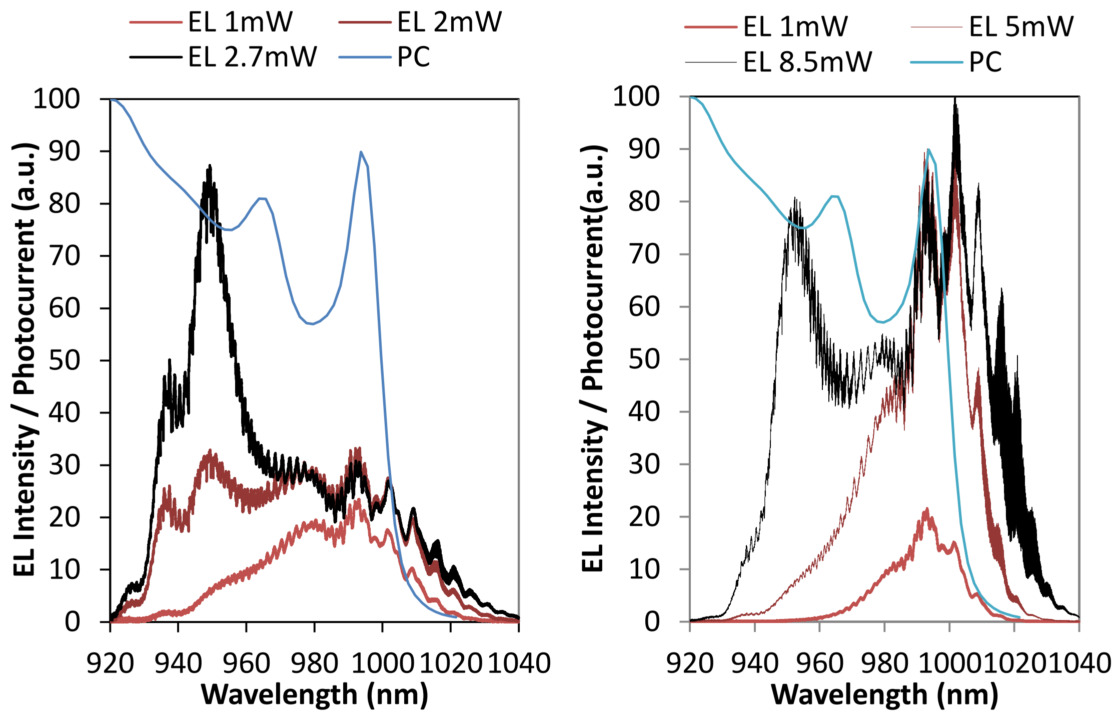

Figure 4-8: The EL spectra of a normal-to-facet SLDs one has $500\times10\mu m^2$ (left) and other has $750\times10\ \mu m^2$ dimensions at different pumping level. Both devices exhibited peak developments on both sides of the central wavelength (990nm), the short-wavelength peak developed because of the state filling, and the long-wavelength peak developed because of the Joule's heating effect.

Taking into account that the window will be less absorptive to both the shorter wavelength and the longer wavelength compared to the original emission/absorption wavelength, the development of SMD will be much easier than that in the central wavelength.

On the other hand, devices with longer active stripes required higher current (not current density) to achieve similar pumping levels in the older batch, this caused local heating underneath the bonding points and the heating caused a red shift in the central wavelength. Although it was not sufficient to cause the central emission wavelength to shift outside the absorption region, the longer wavelength portion of the spectrum faced a lower absorption (almost transparent at some point) window. As a result, enough long

wavelength energy was coupled back to the active stripe where it could be amplified. With further increase of current, a lasing peak develops to the long wavelength side of the spectrum. Figure 4-9 shows another comparison between the PC spectra and the lasing region that appeared in the EL spectra of the devices with 2 and 3mm active stripes and 1mm window.

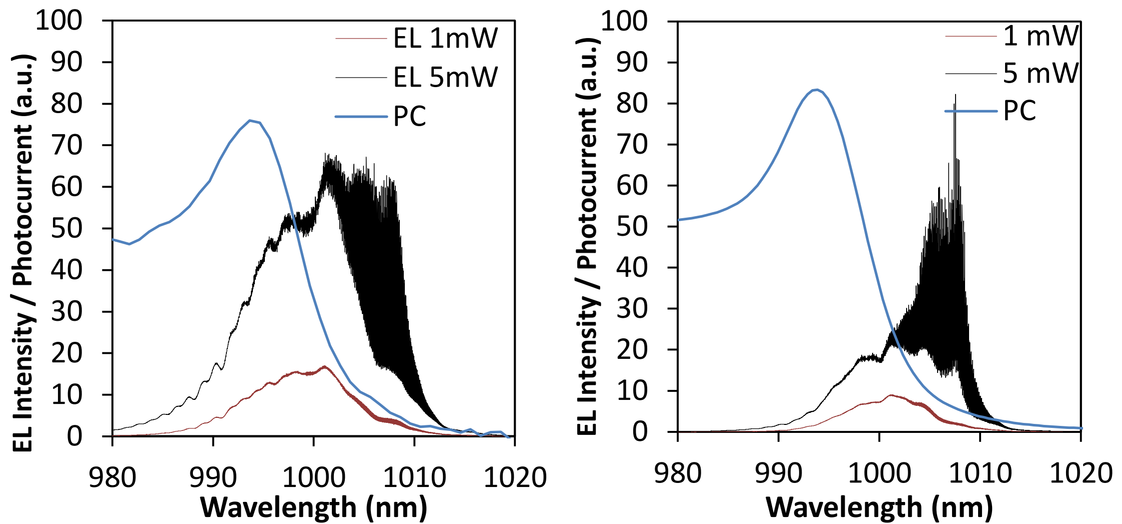

Figure 4-9: The EL spectra of two devices 2mm (left) and 3mm (right) both has 10µm wide stripes at different pumping levels showing the peak on the long wavelength side and outside the absorption peak which is defined by the photocurrent shown in the blue line on both graphs.

The lasing at longer wavelengths in devices longer than 1mm demonstrated here may have revealed a limit for the normal-to-facet SLDs in terms of possible active lengths that could be used in their design.

4.4.4 Stripe width effect in > 1mm devices:

The problems exhibited in the longer devices questioned my conclusions drawn from chapter three, which was "the device with larger active area should perform better". The set of devices tested for 2 and 3mm long devices operated somehow in the opposite manner in which the narrower devices (i.e. the ones that had 5 and 7µm) started to lase at marginally higher current. Yet, a device of a comparable active length performed the best in the last batch. This leads us to examination of the major difference between the two batches. In the old batch, the stripe widths were to 3 and 4µm while in the new

batch the stripes are widened to 5, 7, and 10µm. The fact that the effective real index step between the active stripe area and the window area is only 0.002-0.003 raised a question about the divergence angle of the beam spread in the unguided window region.

The divergence angle of the beam spread from the stripe/window interface was investigated by simulating the structure grown and processed (as shown in chapter two) by the commercial software FIMMPROP supplied by PhotonDesign Ltd. This software simulate the propagation and distribution of light in the semiconductor structure focussing on the effect of the refractive index of the layers included in the structure on the device operation. Two structures were simulated representing the active and the window regions and the two sections were aligned (by the software) successively to simulate a light beam propagated from the active stripe part to the window part. This software does not simulate the device gain or the resultant output power. The active part was 100µm long and had three widths (5, 7, and 10µm) and the window portion was extended to 1000µm to emulate the tested devices window section in this chapter. Figure 4-10 plots the output of the simulation performed for 5µm wide stripe active as an example of the other devices, on a colour scale from Dark Blue where the intensity is at minimum up to White to represent the maximum intensity.

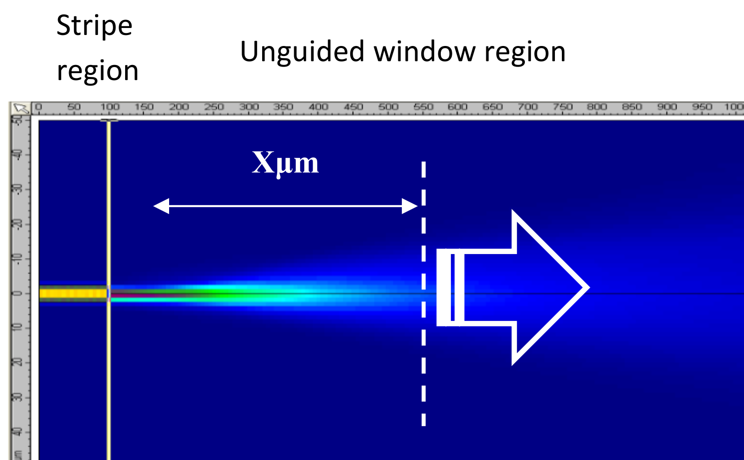

Figure 4-10: The simulation outcomes as shown in the FIMMPROP output screen, the figure is a plane view of the device describes how the optical mode propagates in the window unguided region.

For each stripe width, 2D slices were taken across the beam propagated in the window region at Xμm from the interface. The full width half maximum (FWHM) of the propagated beam is recorded as shown in Figure 4-11, the beam width was increased from 5, 7, and 10μm for the three devices at the interface to 54.4, 43.3, and 34.1μm, at 800μm for the devices 5, 7, and 10μm, respectively. Comparing the FWHM at each point to the first one can yield the divergence angle of the beam with respect to each width and their average. The angle can be found from the arctan of the difference between the propagated length (x) and the expansion added (y)

$$\emptyset = \arctan\left(\frac{x_1 - x}{y_1 - y}\right) \quad \text{…. (4-1)}$$

where x_1 is 100μm and y_1 is the related beam width.

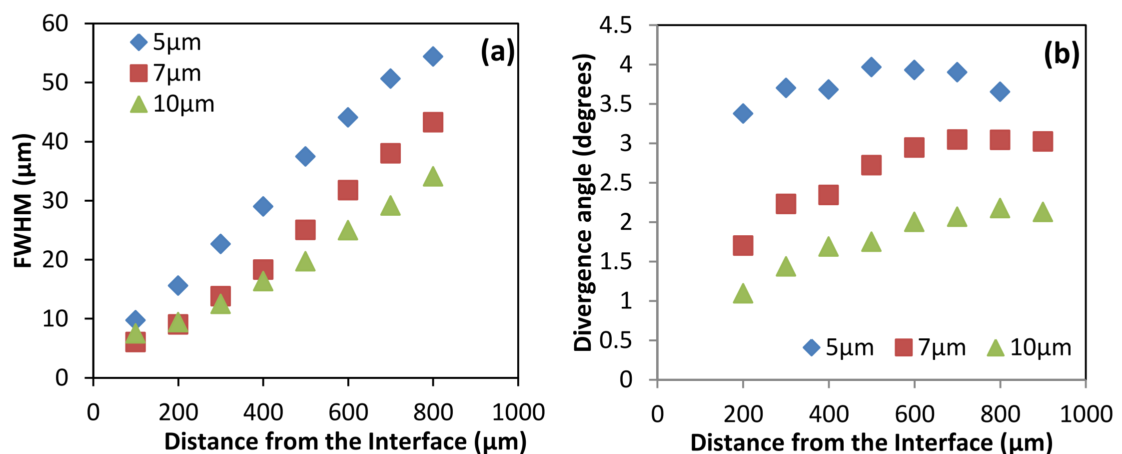

Figure 4-11: The full width half maximum (FWHM) of the propagated beam intensity shown in (a) which reflects the beam divergence angle in (b).

The divergence angle measurement of the three stripe widths shows that the 10μm wide stripe resulted in the narrowest divergence angle (the maximum it reached was only 2°), while the 5μm offered at least 3.5° divergence angle, this value is expected to be higher in narrower stripe SLDs. This resulted from the fact that the index step is very small (0.002-0.003) which provides a very small divergence. The difference between the devices all comes to the stripe widths. This is very similar to the effect of the slit separation in Young's slit experiment. In the tilted stripe batch this effect was not

noticed because the device was tilted and most of the propagated mode is already deflected to the cladding layers due to the axis misalignment.

The effect of the stripe width in the normal-to-facet SLD is explained schematically using Figure 4-12. Examining Figure 4-12 reveals that the probability to couple the reflected light from the rear facet is increased in the 10µm stripe due to the small divergence of the light beam at the interface. This increased the difficulty to suppress lasing in the new batch.

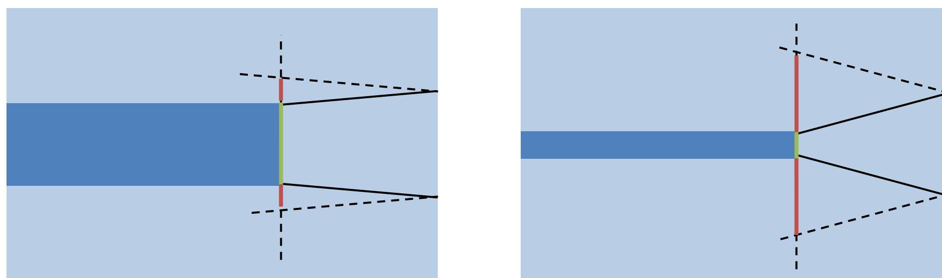

Figure 4-12: A Comparison between two devices having 1 mm window one with active of 3µm and other with 10µm stripe. The green line is the portion of the reflected beam coupled back in the active and the red one is the portion that is dissipated.

Depending on the optical power emitted from the active stripe to the unpumped area and the absorption in the window region, the effect of the stripe width was determined. The problem that appeared in this batch can be solved quickly by 1) increasing the window length to increase the beam spreading, and 2) decrease the rear facet reflectivity by depositing AR-coating on it.

4.5 Heat Effect Reduction:

Following the argument presented in chapter three, minimization of the self-heating can result in better performance as the emission central wavelength will not shift in the same manner as observed in the CW characteristics described here. For this reason, devices with 0.75 and 2mm active stripe length were tested using the low resolution setup to investigate the device performance.

4.5.1 Shorter Than 1mm Device

Recalling the performance of devices with active stripes < 1mm, the EL spectra showed development of two peaks in addition to the original peak at 990nm. The reasons for these peaks were state filling and Joule heating for the short and long peaks, respectively. To verify that, devices with 0.75mm long stripes and different stripe widths were tested under pulsed current injection with 10µsec pulse width and 1% duty cycle using the low resolution setup. Figure 4-13 shows the EL spectra measured for the three devices at different pumping levels.

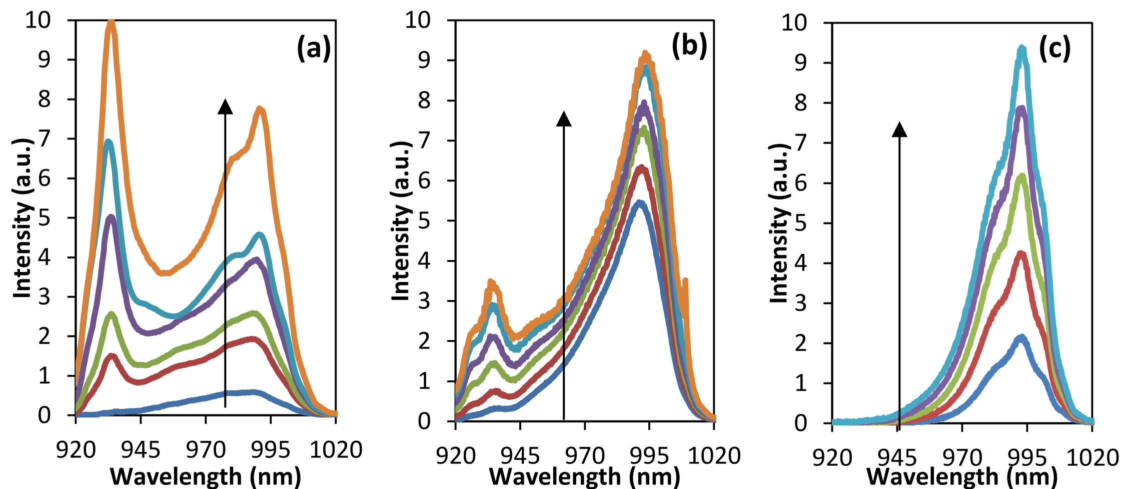

Figure 4-13: The low resolution EL recorded for devices with 0.75mm long stripe and varied stripe widths, the stripe widths in the figure shown were 5µm in (a), 7µm in (b), and finally 10µm in(c). In the three sub-figures the arrow shows the direction of increasing the pumping current.

The recorded spectra verified the spectral broadening due to state filling in the short devices while no peak was detected by this resolution at the long wavelength side (>1000nm). I expect that this is due to prevention of Joule heating when the device was operated in the pulsed mode. Examining Figure 4-13 can reveal that the short wavelength peak appeared due to state filling as the peak developed very obviously in the narrower device to the level that made it higher than the original peak. This development decreased when we move from the 5µm wide stripe to moderate development in the 7µm, and in the 10µm wide device the peak did not develop at all as can be seen in the related figure.

4.5.2 Longer Than 1mm Device

The CW measurement carried out previously for the 2mm stripe SLD showed peak development on the longer wavelength side only. The reason for this was attributed to the red-shift of the central wavelength. The same SLD was tested again under pulsed conditions similar to that of the 0.75mm mentioned above. Figure 4-14 shows low resolution EL spectra at three pumping levels.

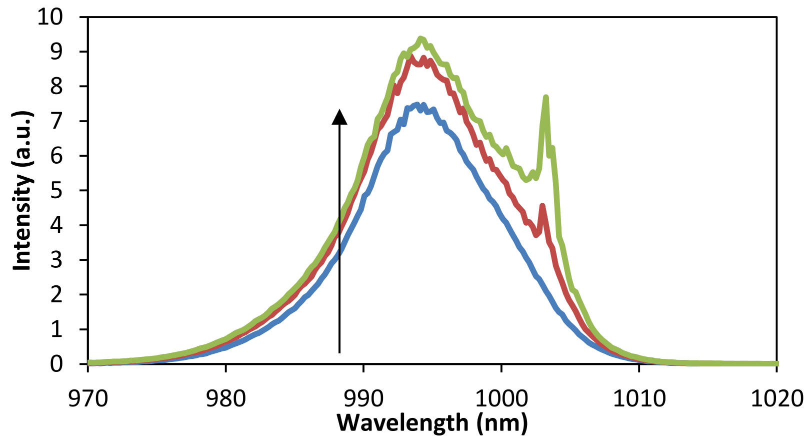

Figure 4-14: The low resolution EL of a device that has dimensions of 2mm × 10µm. The device experienced lasing at the right hand side of the spectrum at power ~7mW. This level is a bit higher than the CW operated.

Although lasing still takes place at around 7mW output power, it is increased by ~2-3mW from the previous level in the CW operation. Lasing in these devices with such low power and low current density can be explained by as the pumping level increases the spontaneous emission rate increases, as in Suhara's book analysis [3]. This increase is usually accompanied by increase in the width of the EL spectrum of the device. Because the device now has an active stripe of 2mm, enough gain will be added to the transparent portion of the spectrum (in the range >1000) and more forced transitions will take place which causes the emission of the device to move from the amplified spontaneous emission to the amplified stimulated emission. This might be considered as the modal limit for such devices, this limit can be changed from one device to another according to many factors described in chapters 3 and 4.

4.6 Summary and Conclusions:

In chapter four I tested the grown structure in a normal-to-facet optical waveguide configuration. This configuration has two main advantages, first the output beam profile has been maintained to elliptical shape rather than the crescent shape that resulted from tilting the facets. This should increase the device coupling efficiency to standard single mode optical fibre couplers and connectors. Second is the decrease in the production cost by minimization of the use of semiconductor material real estate, especially for long cavity devices.

The first trial was to test a 2mm long active with 2mm rear window device epi-side down. The device was coated with anti-reflective coating on the front facet to decrease the carrier depletion by the reflected light at the cleaved facet. Output power recorded was 6.5mW before lasing took place at 1010nm (20nm away from the device central wavelength).

Another batch of devices was prepared from the same planner and different overgrowth run (same material used in all re-growths). The difference between the older batch and this one is the designated stripe widths, in this one 5, 7, and 10µm wide stripes can be fabricated. Devices with various active lengths were cleaved and all with 1mm window length. The devices were reported in CW and pulsed operations.

For this batch specifically, the device showed 3 different behaviours. The first one is the one identical to the devices/batch reported in chapter three, this length was tested in three stripe widths 5, 7, and 10µm and as expected the best performance was for the 10µm where power up to 20mW was recorded with spectral modulation depth of <10%, while the 5µm device started to lase at the long wavelength side at ~14mW. In these three devices two peaks were noticed, the original one (the one resulted from the room temperature operation of the quantum well) and a long wavelength are. The latter is

very likely to be caused by Joule heating at the junction. The spectral modulation depth was tracked at both peaks. Spectral modulation at the original peak achieved maximum values of~16% for 5μm, 10%for 7μm, and less than 4% for the 10μm wide stripes. Yet, all the devices lased at long wavelength (20-25nm away from the designated central wavelength). The power at which the devices started to lase varied according to the device width, the lasing output powers were 14, 22, and 30mW for the devices with 5, 7, and 10μm stripe widths, respectively.

To thoroughly investigate the device limits, two shorter and two longer devices were measured. The performance was also in contrast in the two groups of devices. The shorter ones exhibited short wavelength peak development and at higher currents another peak appears at the long wavelengths due to heating. The lasing at long wavelength observed in the longer devices occurred due to two reasons, the first one is the localized heating since the injected current was high. The second reason is accumulated gain in these wavelengths when the current is increased, this gain could overcome the excess losses provided by the window which is mainly due to the beam divergence in the case of long wavelengths.

Another reason expected for lasing especially in the long stripe devices is the low divergence angle at the interface since the index step is as low as 0.002-0.003. This angle didn't play a great roll in the tilted stripe SLDs batch since the waveguide was tilted already. On the other hand, the straight devices always experienced lasing at some point even with actives of 3μm wide (which provide larger divergence angle than the one provided by 5-10μm).

4.7 Future Work

1- Testing the configuration with an active that is designed for superluminescence operation rather than a laser active.

2- Design the same structure with a different upper cladding and/or different current blocking layer to increase the index step between them, this can increase the divergence angle and eventually decrease the percentage of the reflected light coupled back into the active stripe.

3- Design a different interface edge that increases the divergence angle of the incident light at the interface using the same material. Interfaces having a see-saw, sinusoidal, or spherical shapes can do the job.

4.8 References

[1] W. T. Tsang, R. A. Logan, and J. A. Ditzenberger, "Multilongitudinal Mode Operation in Angled Stripe Buried Heterostructure Lasers," *Journal of Applied Physics*, vol. 54, no. 2, p. 1137, 1983.

[2] W. Drexler and J. G. Fujimoto, *Optical Coherence Tomography: Technology and Applications*, 1st ed. Berlin: Germany, 2008.

[3] T. Suhara, *Semiconductor Laser Fundamentals*. New York, USA: CRC Press, 2004.

Chapter Five: Self-Aligned Stripe Semiconductor Optical Amplifier.

5.1 Introduction:

So far I described the GaAs-based Self-aligned Stripe as SLDs with one windowed facet in tilted (chapter 3) and normal-to-facet (chapter 4) configurations. In this chapter we explored the potential for SASs actives with two windowed facets as semiconductor optical amplifiers (SOAs). A brief literature review is presented reviewing the state-of-the-art in SOAs and the requirements that need to be met. At the end of the chapter I presented a self-aligned stripe SOA operating at ~995nm and discussed the SOA characterization results.

5.2 SOA Background

Semiconductor Optical Amplifiers (SOA) are key devices used in wide variety of applications since their presentation by Crowe and Craig Jr. from IBM in 1964 [1]. Applications like optical communications [2] and [3], OCT [4], high power lasers [5], optical signal processing [6]and optical logic[7], wavelength conversion [8]and other applications are all covered by SOAs.

Since optical communications and optical fibre applications were the main field of interest for a very long time, the main bandwidths that SOA were developed in were 1550 [2], 1300 [3], [4], and 850 [9]. As the erbium doped fibre amplifier EDFA technology grew bigger and the presentation of the optical coherence tomography the need for amplifier to enhance these devices performance increased. The 980nm amplifiers and 1050nm amplifiers were presented by implementing InGaAs strained quantum wells in the GaAs/AlGaAs material systems [5]. Emissions at 1550 and 1300nm were usually achieved by implementing InGaAsP/InP material systems, while the 850n was achieved by the GaAs actives. Recently, reports on 1550nm band using

different material systems such as AlGaInAs [10] and GaInNAsSb[11] in order to enhance the SOA performance (e.g. noise reduction, temperature performance enhancement) in the 1550nm. The 1300nm band also reported with diluted nitride (GaInNAs) [12].

As most of the semiconductor devices privileged over their counterparts, SOA size and volume production cost are considered their main advantages. Integratability with other semiconductor components as lasers, LEDs, or SLDs is opening a new field of applications especially when the coupling losses are minimized when the SOA is integrated monolithically.

5.2.1 Operation principle:

The simplest description for the SOA is that the input light signal stimulates the free injected carriers to recombine at the wavelength it propagates at. Figure 5-1 explains the operation schematically.

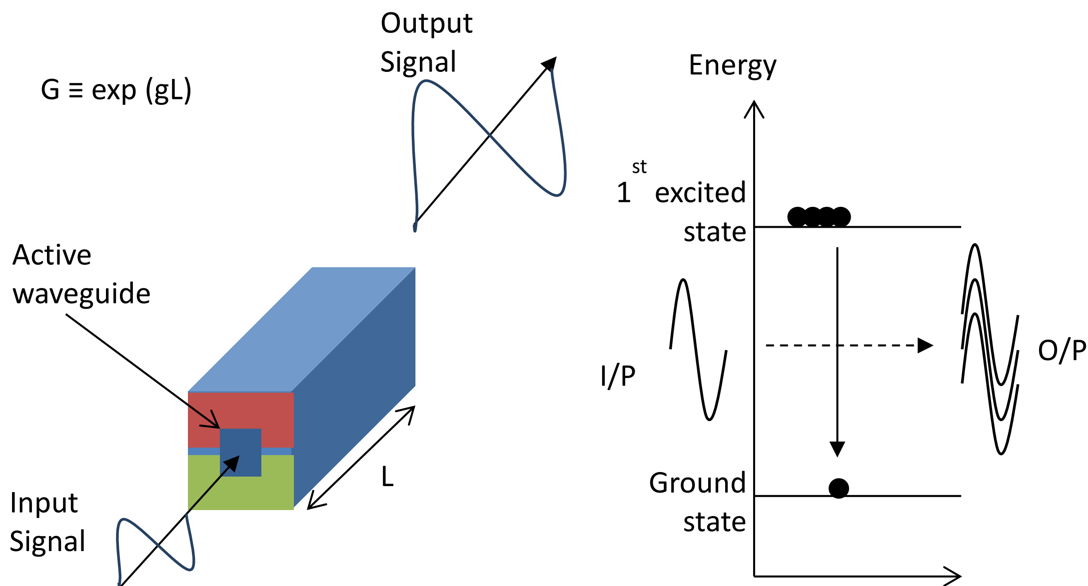

Figure 5-1:The simplest schematic diagram of the SOA showing a buried waveguide within a p-i-n junction (shaded red-blue-green) in which the input signal with intensity I_{in} enters the active waveguide and get amplified to the I_{out} output signal. The SOA gain is the ratio of I_{out} to I_{in}. The device gain is not similar to the material gain g provided by the device studied earlier yet it is not so irrelevant where ($G \equiv gL$). The right Figure 5-on the other hand is the two-level energy system showing that the amplification of the I/P signal to O/P is due to the transition of the excited carriers from the upper level to the lower level. Maintaining the population of the excited carriers defines the devices performance.

When a light signal (coded or not) with a specific wavelength (λ) enters the SOA waveguide, it excites the free carriers. If energy E, is provided, (where E=$\frac{h\,c}{\lambda}$, h = plank constant, c= light speed in free space, and λ= the propagated light wavelength) the free carriers will overcome the bandgap and recombine. This results in accumulation of photons that has the same properties of the input ones and sensed as increase in the output power if the same power meter is used to measure the input and the output powers. This increase is a basic property of any SOA and is called the small signal gain G, where [13]

$$G = 10\ \log\frac{P_{out}}{P_{in}} \qquad \text{...... (5-1)}$$

The gain relates directly to the ability of the device to produce spontaneous emission or amplified spontaneous emission which is the spontaneous emission rate R_{spont}. As the pumping current increases the gain at specific input power increases as we can see in all gain measurement done by developers [9], [14]–[18]. What happens when the input power increases, is the thing that governs the modal limit of the device. The increase in the photon density (more optical power) of the input signal results in an increase in the free carrier recombination according to the R_{spont} of the device, this increase will reach a point that the free carrier population cannot maintain this rate so this rate will decrease and eventually reduce the gain provided.

5.2.2 The four parameters:

As mentioned above, each device has limits that is govern by the geometrical and epitaxial structure or the material used. Mukai and Yamamoto suggested 4 figures of merit to evaluate the device performance [16]. They named these parameters to be: 1) Gain, 2) Bandwidth, 3) Saturation Power, and 4) Noise Figure.

Gain is described as shown in the equation above, by including the coupling losses that can take place the gain is considered as the small signal gain. The recent

applications of SOAs include a coupling to single or multimode fibre to perform. When the coupling losses are not considered in the gain measurement they usually refer it to fibre-to-fibre gain. The difference between the two gain types can be large especially if the fibre coupling is not optimized and the fibre-to-fibre gain will not reflect the actual amplification ability of the SOA. Common values of the device gain

As in any semiconductor optical device, the operation is limited to a specific band governed by the available energy levels within the epitaxial structure in order to do the transitions. By fixing the input power and the pumping level of the SOA, the gain will vary along the spectral range of the device. The wavelength values at which the gain reaches -3dB of the maximum gain are considered as the bandwidth limits of the device. Generally, the operating bandwidths of the devices are between 30 and 100nm for MQW active devices [19], [20]. The recent reports of SOAs increased this limit to 100nm and more [21] by using either QD actives [22], [23]or variable widths and compositions QWs [24].

For a specific pumping level and spontaneous emission rate, the input power results in specific output power according to the gain. As the input power increases the spontaneous emission increases. Since the increase in the spontaneous emission results from an increase in the carrier recombination, extra free carriers need to be replaced. As long as the free carrier level is fixed the gain level will be the same. Once the density of the free carrier does not meet the requirements to maintain the spontaneous emission rate, the gain will decrease. When the gain is dropped 3dB below the maximum gain, this value is denoted by saturation gain and the related output power is called the saturation output power. Common value of saturation power is 10-15dBm in quantum well devices, increases in the quantum dots devices up to >20since more transitions states are available.

The noise in the SOAs is the amount of unwanted spontaneous emission added to the output signal. The signal to noise ratio SNR can be found for the input and the output signals as shown in Figure 5-2 c. The ratio of SNR at the input and output of the device is denoted as the noise Figure of the device. Figure 5-2 shows general figures of the SOA devices with the four performance parameters highlighted on it.

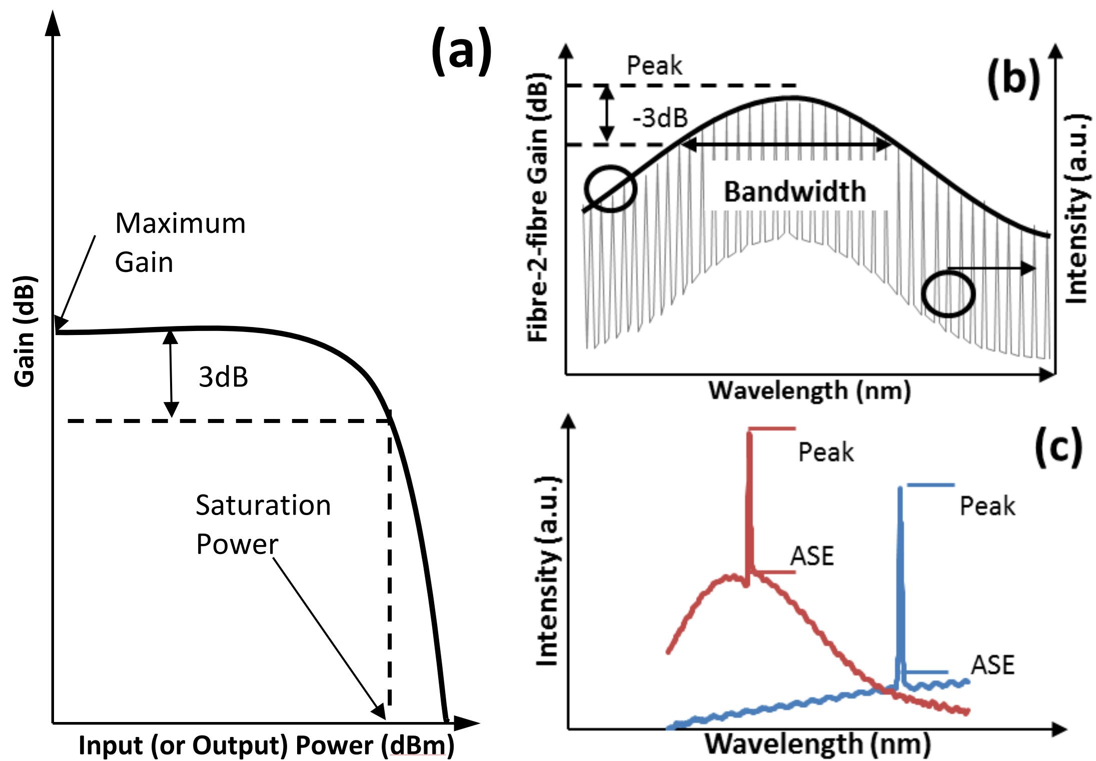

Figure 5-2: The four parameters described above are shown in this Figure 5-(a) is the small-signal-gain as a function of the input or the output power (most commonly the output) shows the maximum gain and the saturation power which is the power at which the gain decreases by 3dB w.r.t the peak gain. (b) is the fibre-to-fibre gain black line combined with the lasing peak movement along the wavelength, the bandwidth is also shown in this sub-figure. Finally (c) is examples of an input signal (blue line) and the amplified output signal (red line) from where we can extract the noise figure, the comparison between peak and valley values can show the SNR for each signal and the ratio of SNRs of the input to output declares the noise figure.

5.2.3 Structures used

Reviewing the four parameters evaluating any SOA, we can notice that it all governed with the spontaneous emission generated. It is true that the gain clamps when the device turns from spontaneous to stimulated emission, yet, the gain clamp usually occurs for the central wavelength (in the cleave/cleave device) and all the spontaneous emission will be suppressed. In the case of SOA it is required to increase the pumping

current as high as possible to provide more and extra free carriers; this will result in even higher gain or higher saturation power or both. So, as in the case of SLD it is required to suppress the lasing of the device to move the emission in the amplified spontaneous emission region. This is done by reducing the facet reflectivity to minimum. The methods used are very similar to the one used for SLDs.

The first method used was the AR-coated when Craig Jr. and Crowe presented the first laser amplifier [1]. Again, this is done by depositing dielectric layers with $\lambda/4$ thickness. The main problem in this technique is that reduction of reflectivity less than 10^{-4} requires 1) multilayer coating, and 2) layer thickness control <20nm scale [25]. Adding to that, the since the reflectivity is wavelength dependent, the reflectivity of the facet will vary across the wavelength range even with the perfect coating. Yet, this method is still very active nowadays when combined with the other two methods.

The second method used was the tilted facet, tilting the facet by itself can result in effective facet reflectivity down to 10^{-3} and it is widely used with the buried waveguides SOA. This method as mentioned in 3.1 is considered the easiest to fabricate SOAs, it is wavelength independent, although the divergence angle depends on the refractive index of the material at the operating wavelength. Semiconductor optical amplifiers were fabricated usually tilted 5-8° with respect to normal-to-facet axis. Increasing the tilt angle does not result into continuous decrease in the facet reflectivity. As reported by Gerard Alphonse [26] R_{eff} has a cosine shape function with peak value (maximum reflectivity) decreases exponentially as the tilt angle increases.

The last method used to suppress facet reflectivity is the buried facet (transparent window facet). This is done by terminating the waveguide before the cleaved facet. Although this has its advantages such as easy of fabrication and wavelength independency, yet, there is a major drawback in this configuration regarding the concept

used to achieve the low reflectivity. This method depends on mode divergence when the light propagates in the unpumped region. In the case of SLD all was required is to increase the amount of decoupled light, so the device with longer window had better performance. In the amplifier case we cannot keep increasing the window lengths since this will result in more divergence of the propagated mode and eventually coupling efficiency reduction. For that reason usually the window devices are combined with AR coating on both facets. Figure 5-3 shows the three configurations of SOAs as reported by Stubkjaer *et.al.* [27].

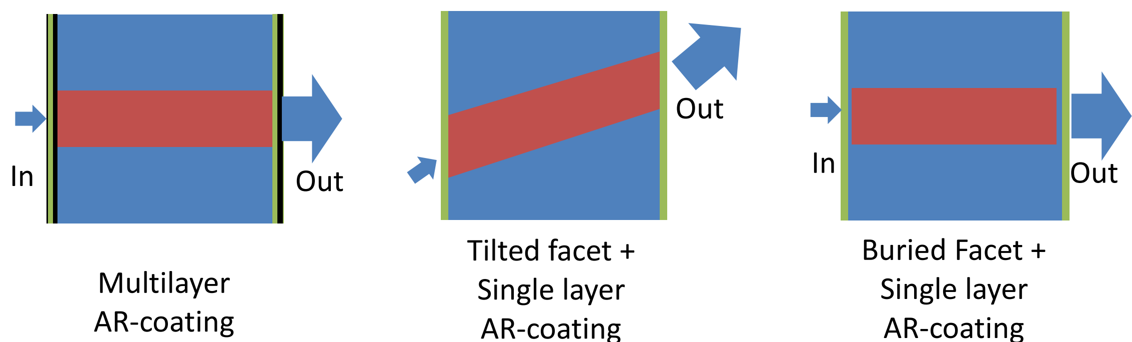

Figure 5-3: The three configurations used to decrease the facet reflectivity for SOAs as reported by Stubkjaer et.al. [27]

5.3 Sample Preparation:

SOA were prepared from the same material as the SLDs in chapters 3 and 4. So this SOA has a central wavelength at ~990nm. A typical configuration of SOA is the window structure, in which the active waveguide is terminated before reaching the device facets [28]. Usually this method is also combined with AR-coating provides an effective reflectivity down to 1E-5. This type of structure can be realized in GaAs process, but with waveguide terminated prior to both facets. Au/Zn/Au top contact layer was deposited on the entire stripe followed by the required electrical isolation by trenches and SiN deposition, finished by bond pads deposition in windows opened in the SiN over the stripes and lapping to reduce the device thickness to ~120µm before deposition of InGe/Au as back contact layer, the process is exactly the same as the one

detailed in chapter 2 (read section 2.2.2 for full process description). The final tested SOA included 4µ wide × 5000µm long active SAS and a 100µm long window at each facet. A schematic cross-section through and along the stripe is shown in figures 4a and 4b, respectively. Also a plan view highlighting tilting angle is shown in Figure 5-4c. According to the effective reflectivity measurement done in chapter 3 (see Figure 5-8 in section 3.5.4), 100µm window can provide ~0.1 effective reflectivity in addition to the reduction in reflectivity provided by the tilted waveguide geometry it is expected to achieve 10^{-5} – 10^{-4} effective reflectivity can be achieved. The device is mounted on a gold coated c-mount epi-side up, the windows at each end of the device were hung over the mount by ~20µm on either sides for more alignment freedom of the input and output fibres during the measurements

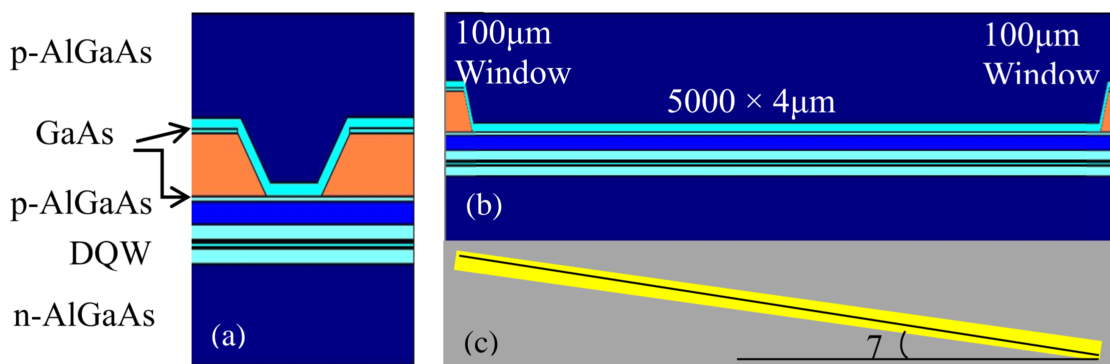

Figure 5-4: A schematic diagram showing the device epitaxial structure taken across (a) and along (b) the buried stripe, also the top view (c) showing the waveguide tilt with respect to the normal to facet axis.

5.4 SOA Characterization:

The experimental setup used to characterise the SOA is described in section 2.3.6. The Tunable laser used is Thorlabs TKL1050 as an external cavity tunable laser with a central wavelength at 1050nm and a 60nm scanning range and 8mW typical output power (16mW maximum). Although the range is shifted ~20nm from central wavelength of the SOA, by increasing the tunable laser pumping current to 120mA, peak intensity up to -10dBm can be obtained at wavelength in the range 990-1020nm,

this spectral range covers the longer wavelength part of the SOA spectrum, a slight drop in this intensity occurs when the wavelength is shorter than 993nm. Figure 5-2 shows the typical performance of the tunable laser kit as provided by Thorlabs Ltd. [29]. This -10dBm output power is found to be enough to characterize the SOA under test especially that the side mode suppression ratio (SMSR) can be maintained to 30dB over the whole spectral range. The spectral range to be tested as will be seen in later section is 990nm – 1020nm.

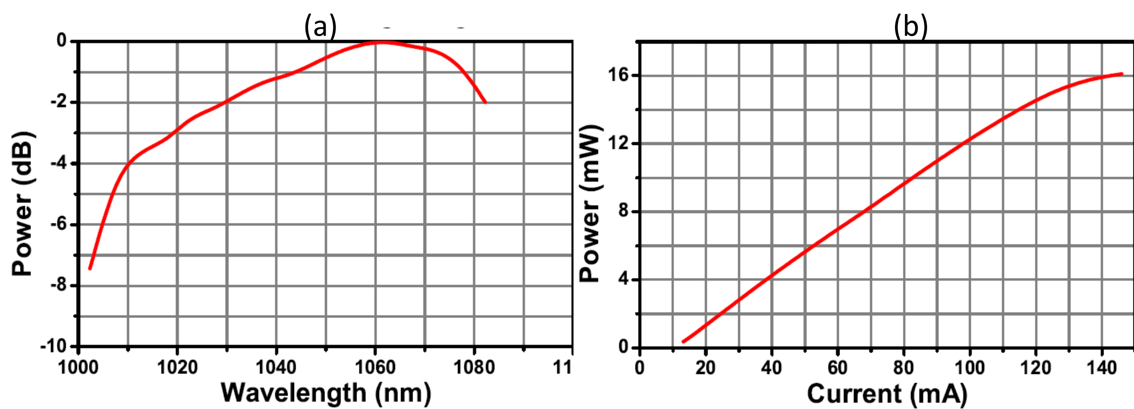

Figure 5-5: The basic characterisation of the TLK-L1050M tunable laser module as confirmed by Thorlabs [29]. *(a) The typical tuning range of the laser that shows the power at wavelength shorter than 1000nm can drop to -10dB or less. (b) On the other hand shows the LI curve at room temperature of the fibre coupled tunable laser. The typical power collected is 8mW as the user's manual detailed.*

5.4.1 Initial Screening

The SOA was operated first as an SLD to confirm the no lasing could be observed over an appropriate range of power/pumping current. Figure 5-(6a) shows the ASE spectra of the device at 130, 200, 300 and 360mA pumping currents (equivalent to output powers from the device facet 0.18, 3.8, 10.7 and 14.8mW). While the spectra were recorded using the low resolution EL setup, the LI curve shown in Figure 5-(6b) is measured by the light-current characteristic apparatus. Both experimental setups are described in chapter 2 (2.3.1, 2.3.2). The data demonstrates that the device didn't lase and suggests that the bandwidth can be around 7nm around the central wavelength. This

narrow bandwidth was a result of using an active layer with two quantum wells designed originally for low threshold laser operation.

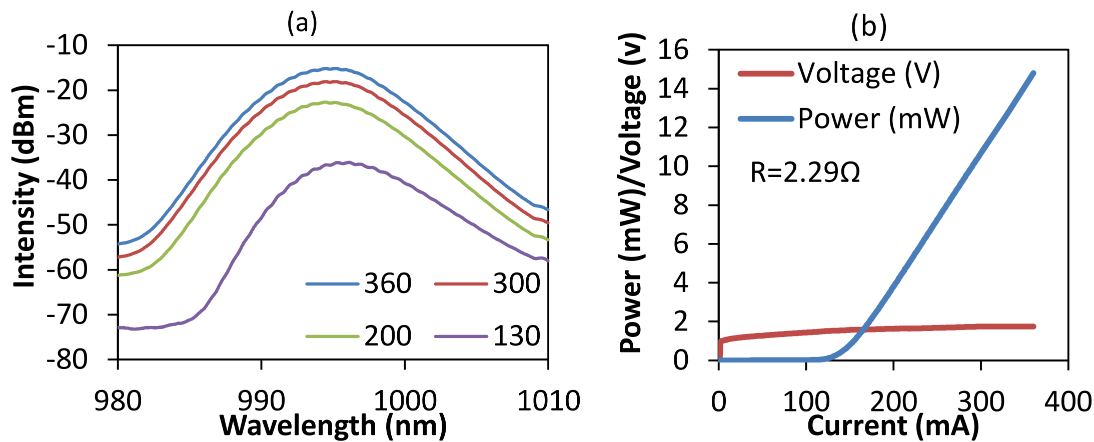

Figure 5-6: The ASE emission showing the non-lasing case (a) and the LI and VI curves of the tested device, the blue line is the light collected directly from the front facet of the device and the red line represents the voltage measured at each current value. The device resistance is found to be 2.29Ω.

5.5 Results

The four main parameters that are used in the evaluation of any SOA device performance as introduced by Mukai *et.al.* in 1981 [16] are the amplification bandwidth, device gain, saturation output power, and the noise figure. The bandwidth of the device is the range of wavelengths that the device shows amplification above -3dB drop from the peak gain, this value is usually marginally wider than the ASE bandwidth of the device since the device still provide ASE at these points which can be advantageous in signal amplification. While the gain describes the amount of amplification provided by the SOA to the original signal, the saturation output power is the power at which the gain at specific conditions decreases by 3dB from the maximum gain. Finally the noise figure is the ratio of the input to output signal- to-noise ratios. The noise in the SOA is the excess ASE in the input or the amplified signals. The four parameters were measured and the data collected is shown in the following.

5.5.1 Amplification bandwidth

In order to determine the SOA bandwidth, the input laser peak was swept to measure the fibre to fibre gain of the device at different wavelengths. I extracted the fibre-to-fibre gain without taking into account the coupling losses of the system, therefore a gain lower than the maximum capability of the chip is expected to result. Higher gain is also expected if a professionally coupled fibre is associated in the design. As shown in the EL curve in Figure 5-6a, the ASE spectrum covers the range ~985-1010nm. Figures 5-7a and 5-7b plot the swept laser peak from 990nm to 1020nm wavelength at the input and output ends of the SOA, respectively. The pumping current of the tunable laser was set at 120mA while the current applied to the SOA was fixed at 400mA. While the tunable laser was operated at 20°C the SOA was left without a temperature control. The reason for this was partially to naturally push the central wavelength of the SOA to longer wavelength by Joule heating. The peak wavelength was successfully red-shifted from 990nm to 993nm, however, but this also caused the optical power of the device to drop by a certain amount, but this reduction was not measured. Unfortunately, the wavelength range of the tunable laser does not extend to cover wavelengths shorter than 990nm. The tunable laser peak power also drops to below -50dBm at wavelengths shorter than 990nm.

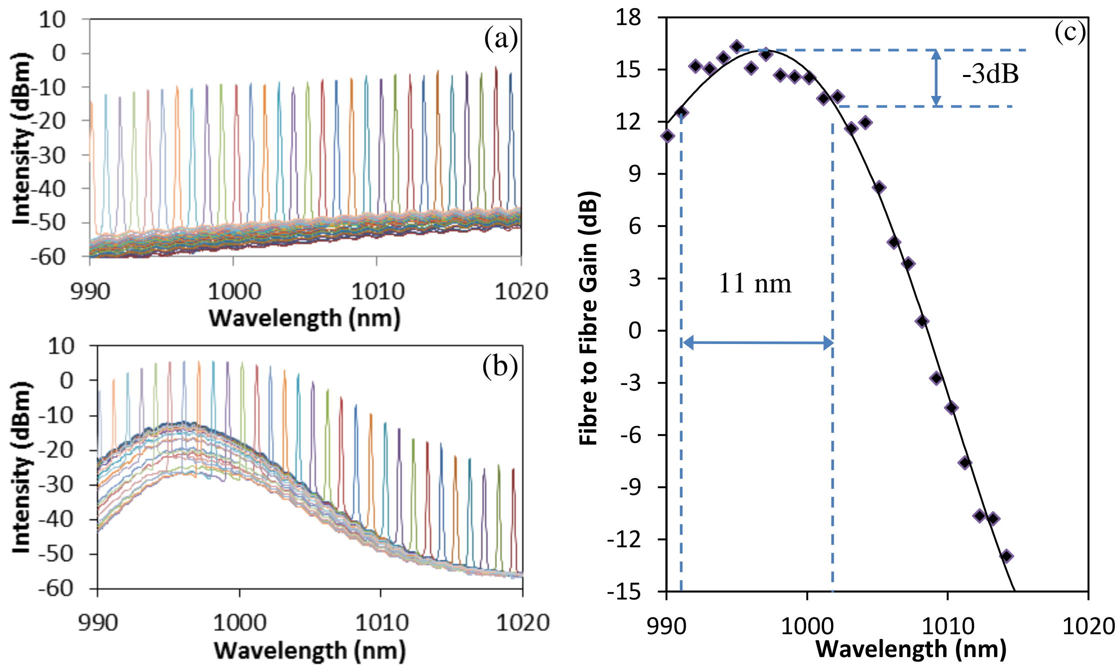

Figure 5-7: The injected signal wavelength sweep and the fibre to fibre gain of the tested SOA. (a) is the sweep input signal, (b) the amplified signal swept along 990-1020nm, and (c) the fibre-to-fibre gain is shown in which the output is compared to the input signal.

Figure 5-7c shows the measured fibre-to-fibre gain along the spectral range. The maximum fibre-to-fibre gain is measured to be 15.5dB at ~995nm. The amplification bandwidth of the device is measured (as mentioned in section 5.2.2) at -3dB from the maximum measured gain, in this case the -3dB cut-off gain points are the ones at which the gain is ~12.5dB. According to the measured data shown in Figure 5-7c, the cut-off points are 991nm and 1002nm. The bandwidth of this SOA under these conditions is ~11nm. This narrower bandwidth compared to the common amplifier bandwidths [21] resulted from the fact that the active layer is designed as a laser active targeting narrow bandwidth and high gain rather than broadband and a gain distributed over a wide spectrum. This active is comprised of two identical quantum wells layers and no effort was made to chirp the emission in any way.

5.5.2 Small signal gain and saturation output power

The small signal gain, or chip gain, describes the amount of amplification within the SOA chip, and therefore all fibre coupling losses should be taken into account. In

measuring chip gain, the wavelength of the tunable laser is fixed to a specific wavelength and the input power is varied. The wavelength of the tunable laser is fixed at 997nm. This wavelength was selected in order that the input peak would be applied at a wavelength within the 3dB band of the SOA, whilst also ensuring that the peak intensity of the tunable laser is ≥-10dBm.

The coupling losses result from the imperfect alignment and other optical properties of both the waveguide and the traveling light such as the insertion angle of the fibre, the divergence angle of the propagated beam, and the losses due to the reflection from the fibre facet. Although all the optical fibres used to transmit the light in this apparatus are lensed fibres, they are AR-coated for 1300nm operation. For that reason, the reflectivity from the fibre is expected to be higher than usual, which will increase the coupling losses especially at the output facet of the SOA. Also, because the fibres are not welded in place in a fixed package, , misalignment is highly possible at both facets.

Recalling the figure describing the SOA characterisation kit shown in chapter 2 (Figure 2-12 section 2.3.6), the points at which potential losses can occur are highlighted in Figure 5-8, in red squares and circles. The points in the red circles are coupling losses resulting from fixed connections in which the losses are already considered in the next step or neglected. These points are (starting from the tunable laser) the tunable laser injection into the attenuator, from the attenuator into the polarizer, from the polarizer into the input fibre, and from the output fibre into the optical spectrum analyser.

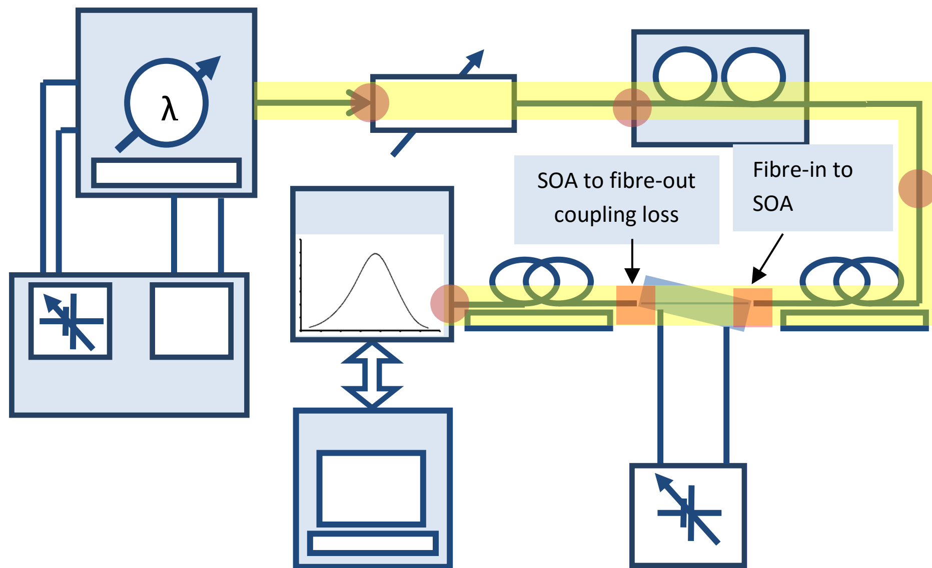

Figure 5-8: The experimental setup used to characterise the buried waveguide structure as an SOA device highlighting the coupling points where losses can occur.

On the other hand, the connection points highlighted in red squares shown in Figure 5-8 are actually the ones that provide the greatest coupling losses and have to be considered in the small signal gain measurement. Estimation of coupling losses can be done by holding a comparison between the free-space power at a specific input current and the power measured from the fibre output end. This comparison was held for both the input and output facets of the SOA.

After continuous alignment of each fibre using the xyz-stage, the position that results in maximum power recorded by the power head is fixed. The maximum output powers are recorded and compared to the power measured in Figure 5-6b in the initial screening. Table 1 below summarizes the power measurements performed for selected currents at both input and output facet.

Table 1: The output power collected from the facets (input and output) and their associated efficiency as they are compared to the power from the output facet as shown in Figure 5-5b.

Pumping Current (mA)	Facet Power (mW)	$P_{fibre-out}$ (mW)	Efficiency (%)	$P_{fibre-in}$ (mW)	Efficiency (%)
130	0.184039	0.053541	29.09191	0.048417	26.308
165	1.559925	0.488257	31.3	0.414645	26.5811
200	3.800125	1.100136	28.95	0.979714	25.7811
225	5.515161	1.627524	29.51	1.421257	25.77
250	7.247383	2.170885	29.95405	1.877547	25.90655
280	9.312739	3.004738	32.26481	2.428865	26.0811
300	10.67355	3.366491	31.5405	2.764354	25.8991
330	12.7	3.9751	31.3	3.2996	25.9811
360	14.8	4.52	30.54054	3.86	26.08108

The measurement done for the 360mA pumping current is shown also in Figure 5-9 below. Considering that the power delivered to the front facet is 100µW (-10dBm) as measured in the OSA, only 26% of this power is coupled to active waveguide at the SOA input facet. This amount is amplified by the amount G and emitted from the output facet of the SOA. Only 31% of this light is coupled to the output fibre and delivered to the OSA. These two values need to be taken into account when measuring the gain at 360mA to estimate the chip-gain accurately.

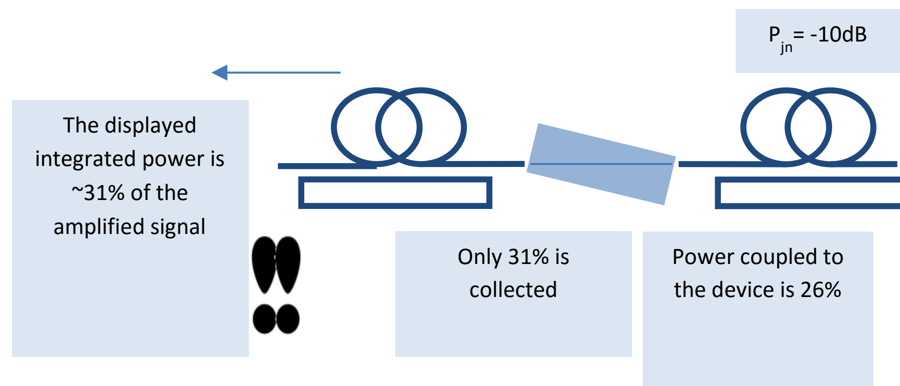

Figure 5-9: Tracing the light signal from the tunable laser to the spectrum analyser showing the coupling losses in numbers.

Another point to be considered in the gain measurement is the difference in the polarizations of the injected signal and the SOA. This polarization changes in the edge emitting devices from run to run. In case the two signals are out of phase, the amplified signal is minimized and maximized if they are in phase. For that reason a manual polarizer was inserted to obtain the maximum output. The polarizer used is a FPC24 manual fibre polarization controller supplied by Thorlabs. When the light propagates through a circular optical fibre, its polarization can be changed by changing the rotation diameter. The rotation diameter alteration is done by changing the paddle location which will cause strain in the crystal structure and eventually cause the polarization of the propagated light to alter.

The small signal gain graph contains two pieces of information. The first one is the maximum gain provided by the chip in the case of perfect coupling (coupling efficiency =100%), and the second one is the saturation power which is the power at which the optical gain starts to fall lower than 3dB from the maximum gain. In order to produce this gain, variable input power is required and so an attenuator is placed prior to the polarizer. The lasing peak (the input power) was varied from -10dBm to -45dBm as appeared on the OSA. By repetition, it was found that input power less than -45dBm could not be detected on the output facet because of the background ASE emitted from the SOA.

By comparing the coupled input and output signals, the small signal gain of the device can be calculated. Figure 5-10 shows the measured small signal gain as a function of the output power at λ=997nm. The maximum gain achieved when the SOA is pumped with 1.8kA.cm^{-2} was 33.5dB. The saturation gain defined as G_{max}-3dB was 30.5dB and the saturation output power (P_{out} at G_{sat} was found to be 7.75dBm. Typically

published values for the maximum gain (G_{max}) of a double (or multiple) quantum well active SOA are 15-25dB.

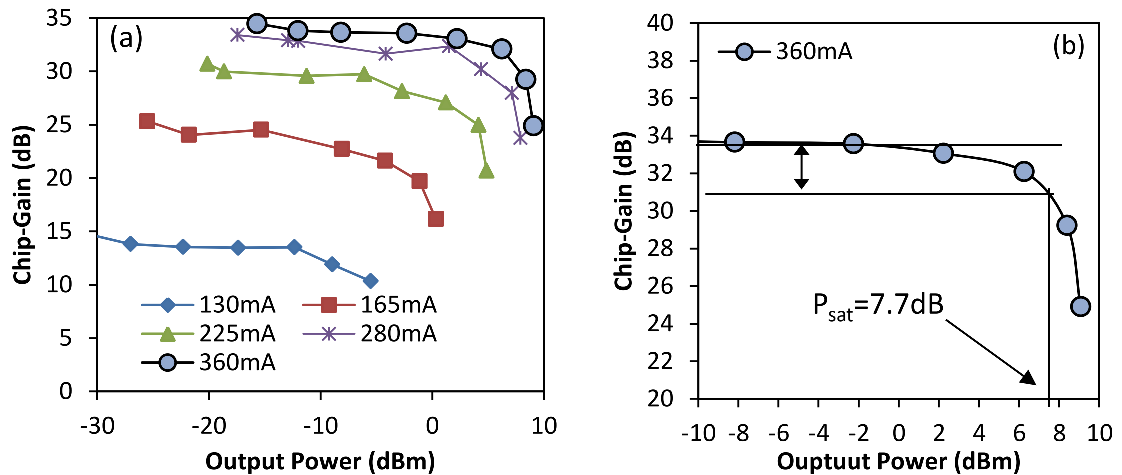

Figure 5-10: The small-signal gain of the developed SOA at different pumping currents with a zoomed-in version showing the saturation gain and the saturation output power.

The larger gain exhibited in our device is a result of using an active that was designed to distribute most of the gain to a very small wavelength range rather than smearing the gain over a wider range to achieve broadband operation. Yet, using this method to achieve high gain exposes a penalty of low saturation output power compared to the common values (usually for quantum well system is higher than 10dBm) [20], [30]–[32].

5.5.3 Noise figure

The last parameter to explore is the noise Figure 5-(NF), which is a quantified value for the degradation in the signal-to-noise ratio (SNR) in the amplified signal due to the added amplified spontaneous emission. Figure 5-11 shows examples of the input and the output signals. If we examine Figure 5-11, we can notice the difference between the two signals. In most of the SOA applications, the signals are transmitted as laser pulses (stimulated emission pulses). Examining Figure 5-11 again reveals that most of the input signal is actually a stimulated emission signal. For this reason the SNR of the input signal is very high. On the other hand, the output signal contains two main

emissions. The first one is the amplified signal which is the stimulated emission. The other one is the amplified spontaneous emission that was the main reason for the amplification. Although in the Figure 5-shown the difference looks like very high (~25dB in the picture shown), eventually making the SNR too high. The SNR drops significantly in the case of low input (output) powers. For that reason the noise Figure 5-of the SOA should be quantified.

Extracting the noise Figure 5-requires calculation of input and output signal-to-noise ratios (SNR) such that [33]

$$SNR = 10log\left(\frac{I_{stimulated\ emission}}{I_{spontaneous\ emission}}\right) \qquad \text{……. (5-2)}$$

where $I_{stimulated\ emission}$ and $I_{spontaneous\ emission}$ are the intensities of the notated emissions in linear scale. The noise Figure 5-is measured by comparing the input to output SNR, where

$$F_{dB} = 10\ \log\left(\frac{SNR_{IN,linear}}{SNR_{OUT,linear}}\right) \qquad \text{…… (5-3)}$$

Taking into account that $SNR_{IN,linear}$ ($SNR_{OUT,linear}$) is the linear signal to noise ratio for the input (output) signals.

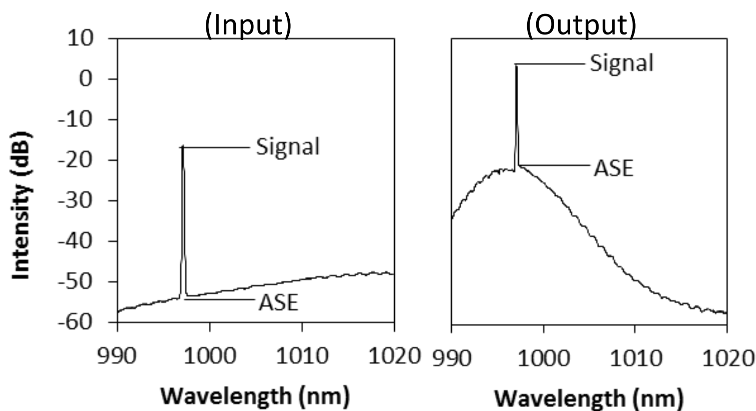

Figure 5-11: The input (left) and output (right) with the signal and the background highlighted.

The determination of the noise Figure 5-started with measuring the EL spectra of the input and output signals in the spectral range 990-1020nm in a step of 1nm. The peaks of the signals and the associated ASE value are plotted as a function of wavelength in Figure 5-12a for the two signals. We can notice that in spite of the fact that the SMSR of the tunable laser is maintained to >30dBm, the peak intensity of the tunable laser started to drop below -10dBm (100μW). The amplified signal, on the other hand, had two regions regarding the SMSR, the first one was for wavelengths longer than 995nm and the other region was at shorter wavelength. The reason of that is probably the decrease in the injected signal and eventually further decrease of the output signal peak compared to the ASE noise. The SNRs of the two signals are plotted in Figure 5-12b shown below. As expected the SNR of the input signal was more stable and consistent along the spectral range compared to the one of the output signal. The SNR of the input signal can be braced within a range of 7dB (40-47dB) while the SNR of the output signal started with only 20dB at 990nm and risen up to 35 or more at 1010nm before it drops again following that to 30dB. Finally the noise Figure 5-of the device along the mentioned wavelength range is determined at each point. The minimum value recorded was 5.9dB at 1003nm.

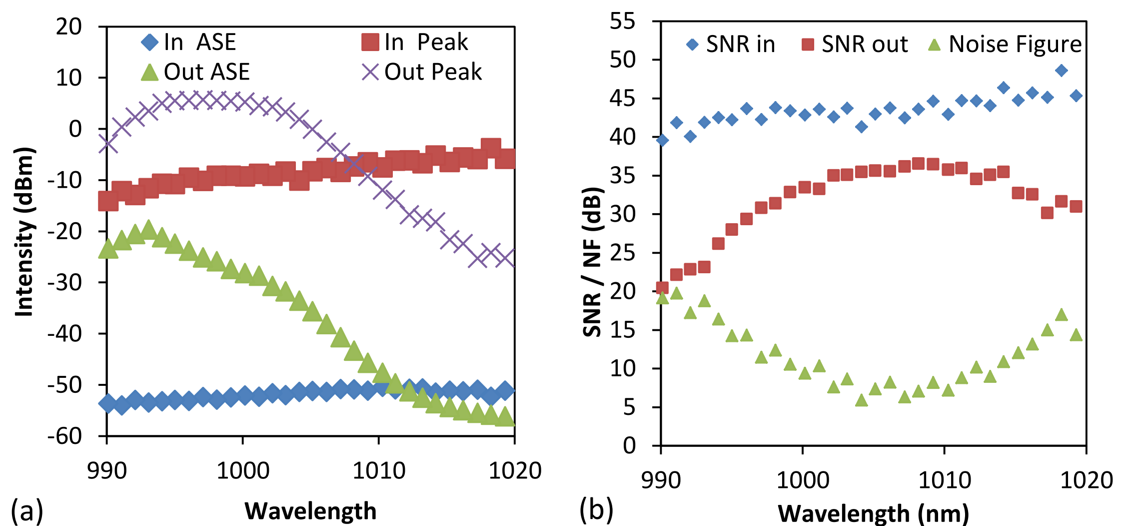

Figure 5-12: The noise Figure 5-of the device by comparing the signal to noise ratio of the input and the output.

Although this value is still in the typical NF range published which is reported by many to be (5-12dB) [13], [28], [33]. Yet, the problem appeared in the shorter wavelength (closer to the central wavelength of the device), the noise Figure 5-in that range is very high. The reason of that is expected to be the incompatibility of the tunable laser for specifically this SOA at this wavelength range. This incompatibility resulted in decrease in the SNR_{out} while the SNR_{in} was the same along all the range since the SMSR is maintained in the tunable laser (the input) signal unlike the amplified signal.

5.6 Discussion.

Device characterisation returned various outcomes regarding the SOA performance, the device features were strongly dependence on the active layer used in the device (the 2 identical quantum wells). Although such active enabled high gain operation compared with most of the similar devices published, the device operated in a narrow bandwidth, lower than expected saturation power, and a noise Figure 5-that had a problem on the shorter wavelength range. The reason of the narrow bandwidth came from the fact that the active layer was designated for low threshold current laser devices in which the transitions are very limited in the spectral range.

The saturation output power appears because of the carrier depletion which results in a reduction in the stimulated emission rate [13] Figure13 below shows two cases one when the rate of carrier replacement is close to or exceed the recombination rate which maintain the stimulated emission rate and another case where the carriers are depleted.

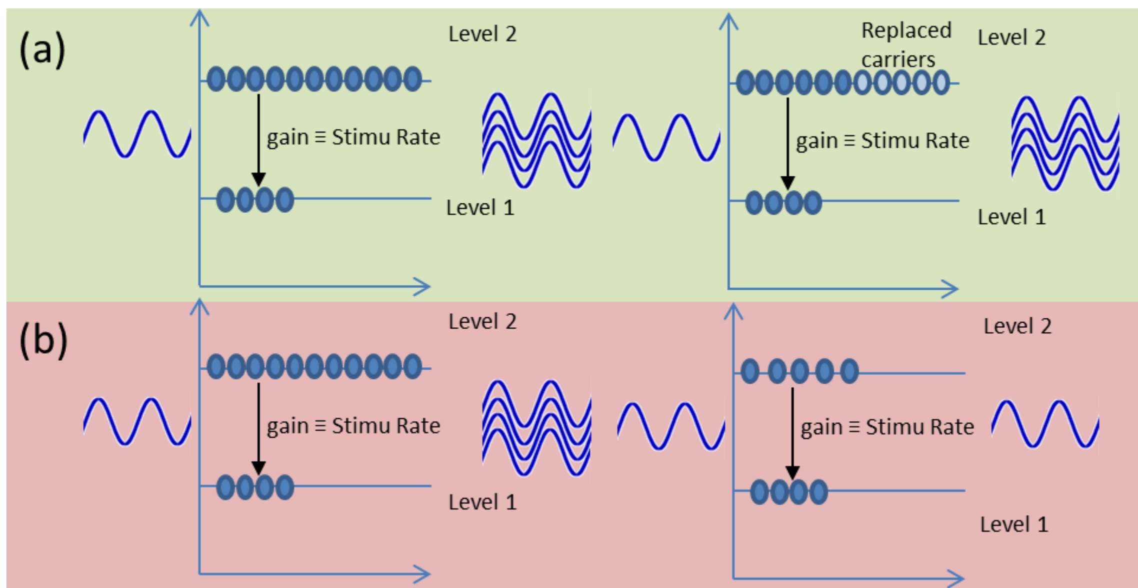

Figure 5-13: A simplified 2-level-system showing the difference at non-saturated (a) and saturated (b) cases. Where in (a) the pumping enable the replacement of the carriers used in amplification which maintain the population inversion while in (b) the carriers depleted in the amplification are not replaced so the population inversion was destroyed.

So as a starting point, increasing the carriers density can increase the Saturation output power, this can be noticed in Figure 5-14 below where the gain as a function of output power at 300 and 360mA. Although the gain was very close, the saturation output power was increased from 6dB at 300mA to 7.75dBm in the case of 360mA, this supports the whole argument.

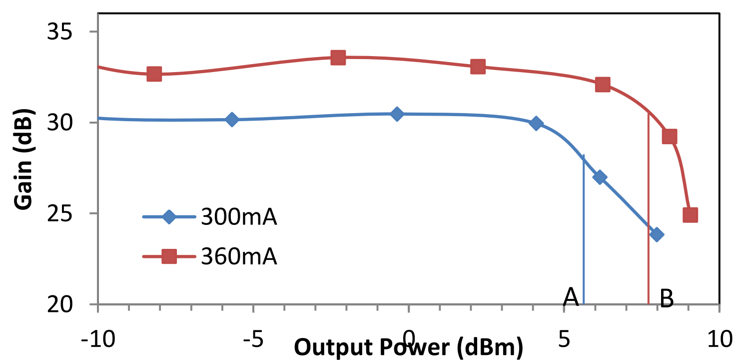

Figure 5-14: The gain as a function of output power at 300mA (blue line and markers) and 360mA (red line and markers) pumping currents. The maximum gains are the two pumping levels are 30 and 33.5dB for 300 and 360mA, respectively. The saturation output powers are ~5.7dBm for the lower pumping level and 7.75dBm for the higher one. This supports the theory of increased saturation power at higher pumping level at gain level close to the maximum.

Nevertheless, Carney *et.al.* [34]stressed that it is not the amount of carriers you pump in that governs the saturation power alone but also the carrier distribution along the active layer, this recommend additional current spread control technique such as segmented contact SOA . [34] [Carney *et.al.* optics express and their older paper]. In their paper they proved that pumping the output part of the device heavier than other parts as the gain goes higher can extend the saturation power to higher level even when the pumped current density over the whole active remained the same [34].

Carney *et.al.* also discussed the effect of current distribution profile along the active stripe on the noise Figure 5-of the device. We first have to put in mind that because the noise Figure 5-is directly proportional to the population inversion factor n_{sp} which is defined as [34]

$$n_{sp} = \frac{\gamma}{\gamma - \alpha} \qquad \text{……. (5-4)}$$

where γ and α are the stimulated emission and the absorption rates, respectively, the minimum noise Figure 5-to be achieved for ideal SOA is 3dB where the noise Figure 5-(nf) is twice the population inversion factors [34]–[36]. The increase in the pumping current should result in a decrease in the measured noise Figure 5-of the same device at different current levels as stated again by Carney *et.al.* [34]. This can noticed in Figure 5-15 where the noise Figure 5-of the device at varied current level is recorded. A decrease from 8 to 5.8dB was found at the same spectral point.

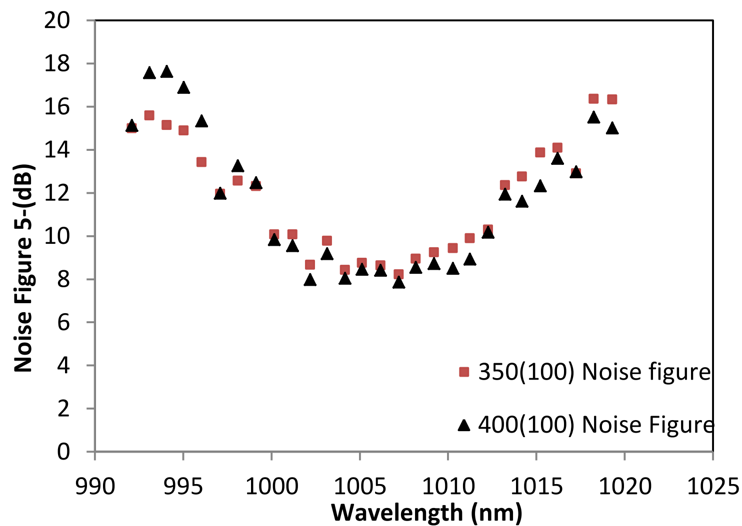

Figure 5-15: The noise Figure 5-of the tested SOA at 100mA tunable laser pumping current and two different level of pumping at 350 and 400mA for the SOA.

The increase in the noise Figure 5-shown in Figure 5-(13b) is primarily caused by the decrease in the tunable laser intensity causing more domination of the amplified spontaneous emission, this eventually decreases the SNR of the output signal and raises noise Figure 5-of the device since the SNR of the input signal is maintained to 40dB or more. This can be justified by examining Figure 5-16 below where the output signal is plotted for -8 and -15dBm under the same conditions.

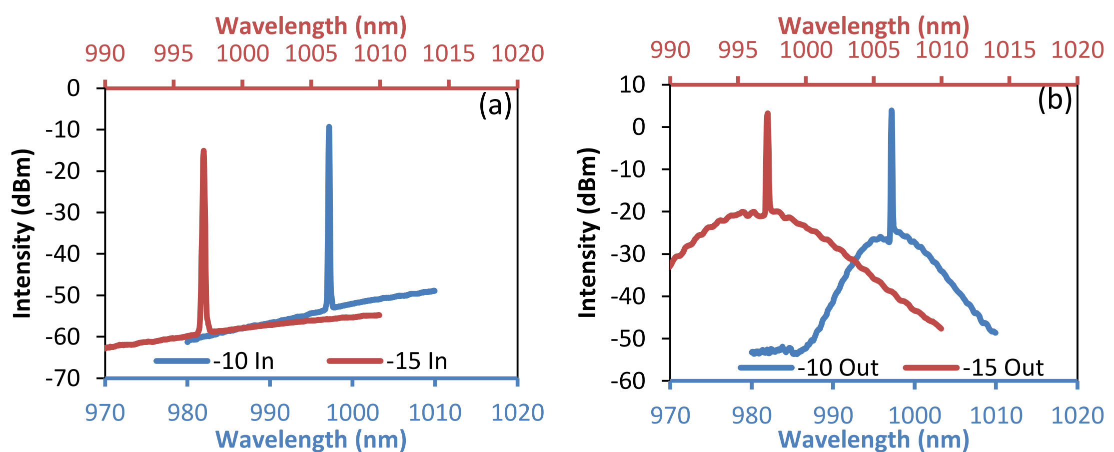

Figure 5-16: The input (left) and output (right) signals at -10 and -15dBm measured under the same conditions, the peaks in the two graphs are at identical wavelengths 997nm. They are only shifted by the axes for clarity. The difference between the ASE levels in the output signals is obvious in the right hand side figure. The ASE emission increased from -26 to -20dBm in the output signal which caused the SNR_{out} reduction and noise Figure 5-increase.

We can notice the increase in the noise emission when comparing it to the amplified peak. The ASE emission peak was increased from -26dbm to -20dbm in the -8 and -15dBm, respectively. From the equation above that relates the population inversion to the absorption, it can be expected that the small 100µm window at the output facet specifically contributed in this increase in the noise figure, yet, further investigation is required to prove or disprove the effect of the window.

5.6 Summary and Conclusions:

Chapter five discusses the use of the processed material detailed in chapter 2 in a semiconductor optical amplifier (SOA) configuration. This configuration has a 100µm window at each end. Due to the mask limitation only 5mm long actives could be produced.

In this chapter, the free space power and the device EL spectrum were tested to identify the device spectral range and use the power as a reference level to measure the coupling losses later. The amplifier was characterised using the SOA characterization setup briefly detailed in chapter two.

The four basic parameters that evaluate the SOA performance were measured for this amplifier, these four parameters are: the amplifier bandwidth, small signal gain, saturation power, and the signal to noise figure. The four parameters were affected directly by the active layer features. The first parameter to that has a direct relation is the amplification bandwidth of the device which was 11nm. This is expected for a device that has an ASE bandwidth of only 6.2nm.

In order to measure the device gain more accurately, the coupling losses of the system were estimated. After estimation of the coupling losses the small-signal-gain was found to be 33.5dB which is larger than most of the double quantum well devices. This high gain came with a penalty of low saturation power of only 7.7dBm the reason

of that is the low pumping level applied to the device, increasing the pumping level (the current density) will result in higher saturation power. Finally, the signal to noise ratio was measured for the input and output signals to determine the noise Figure 5-(NF) if the device. The noise Figure 5-is estimated to be 5.8dB at its minimum value. The minimum value for this parameter is 3dB in the ideal amplifier that is not modified for parametric amplification.

5.7 Future Work:

1. The device tested was only a confirmation that window type SOA is available with the presented window. Validation of good operation has to be done with more geometrical varieties for both the active stripe and the rear window sections.
2. Due to the equipment and the proposed cavity length (5000µm) I was incapable of measuring the device ripple since it requires a spectrum analyser with resolution < 0.1nm. It is recommended to measure the gain ripple at the output spectra of the device using the proper equipment.
3. Active layer designed for semiconductor optical amplifiers is recommended to be implemented in such a window structure SOA in order to investigate more thoroughly.
4. The implementation of broader active can enhance the device performance in terms of bandwidth, saturation output power, and noise figure.

5.8 References

[1] J. W. Crowe and R. M. Craig, "SMALL-SIGNAL AMPLIFICATION IN GaAs LASERS," *Applied Physics Letters*, vol. 4, no. 3, p. 57, 1964.

[2] M. J. O'Mahony, "Semiconductor laser optical amplifiers for use in future fiber systems," *Journal Lightwave Technology*, vol. 6, no. 4, pp. 531–544, 1988.

[3] E. Dietrich, B. Enning, G. Grosskopf, L. Kuller, R. Ludwig, R. Molt, E. Patzak, and H. G. Weber, "Semiconductor-Laser Optical Amplifiers for Multichannel Coherent Optical-Transmission," *Journal of Lightwave Technology*, vol. 7, no. 12, pp. 1941–1955, 1989.

[4] Y. X. Mao, C. Flueraru, S. D. Chang, D. P. Popescu, and M. G. Sowa, “High-Quality Tissue Imaging Using a Catheter-Based Swept-Source Optical Coherence Tomography Systems With an Integrated Semiconductor Optical Amplifier,” *Ieee Transactions on Instrumentation and Measurements*, vol. 60, no. 10, pp. 3376–3383, 2011.

[5] K. Sakai, N. Shimada, K. Shibata, Y. Hanamaki, and A. D. Structure, “High-Power 1.06μm Near-Diffraction-Limited Planar Tapered Amplifier Injected With Seed Light Through a Fiber Biconical Microlens”, Journal of *Lightwave Technology*, vol. 26, no. 6, pp. 710–719, 2008.

[6] G. Contestabile, “All optical processing in QD-SOAs,” *Optical Fiber Communication Conference*, p. W4F.6, 2014.

[7] P. Li, D. Huang, and X. Zhang, “SOA-Based Ultrafast Multifunctional All-Optical Logic Gates With PolSK Modulated Signals,” *IEEE Journal of Quantum Electronics*, vol. 45, no. 12, pp. 1542–1550, 2009.

[8] T. Simoyama, H. Kuwatsuka, B. E. Little, M. Matsuda, Y. Kotaki, and H. Ishikawa, “High-efficiency wavelength conversion using FWM in an SOA integrated DFB laser,” *IEEE Photonics Technology Letters*, vol. 12, no. 1, pp. 31–33, 2000.

[9] C. Tombling, T. Saito, Y. Suzuki, and H. Tanaka, “Experimental Gain and Saturation Performance of GaAs/AlGaAs SCH Quantum Well Travelling Wave Optical Amplifier,” *Electronics Letters*, vol. 27, no. 15, 1991.

[10] P. M. Stolarz, V. Pusino, J. Akbar, L. Hou, A. C. Coleman, J. H. Marsh, A. E. Kelly, and M. Sorel, “High-Power and Low-Noise Mode-Locking Operation of Al-Quaternary Laser Diodes,” *IEEE Journal of Selected Topics in Quantum Electronics*, vol. 21, no. 6, 2015.

[11] G. Giannoulis, V. M. Korpijärvi, N. Iliadis, J. Mäkelä, J. Viheriälä, D. Apostolopoulos, and M. Guina, “Dilute Nitride SOAs for HighSpeed Data Processing in Variable Temperature Conditions,” in *Optical Fiber Communication Conference*, 2015, vol. 6, pp. 6–8.

[12] J. Hashimoto, K. Koyama, T. Katsuyama, Y. Iguchi, T. Yamada, S. Takagishi, M. Ito, and A. Ishida, “1.3 µm Traveling-Wave GaInNAs Semiconductor Optical Amplifier,” *Japanese Journal of Applied Physics*, vol. 43, no. 6A, pp. 3419–3423, 2004.

[13] H. Ghafouri-Shiraz, *Principles of Semiconductor Laser Diodes and Amplifiers: Analysis and Transmission Line Laser Modelling*. London: Imperial College Press, 2004.

[14] M. Anagnosti, C. Caillaud, G. Glastre, J.-F. Paret, D. Lanteri, and M. Achouche, “High performance monolithically integrated SOA-UTC photoreceiver for 100Gbit/s applications,” *26th International Conference on Indium Phosphide and Related Material*, no. 2, pp. 1–2, 2014.

[15] K. Magari, S. Kondo, H. Yakasha, Y. Noguchi, To. Kataoka, and O. Mikami, “A High Gain GRIN-SCH MQB Optical Semiconductor Laser Amplifier,” *IEEE Photonics Technology Letters*, vol. 2, no. 11, pp. 792–793, 1990.

[16] T. Mukai and Y. Yamamoto, “Gain, frequency bandwidth, and saturation output

power of AlGaAs DH laser amplifiers," *IEEE Journal of Quantum Electronics*, vol. 17, no. 6, pp. 1028–1034, 1981.

[17] G. Sherlock, C. P. Seltzer, D. J. Elton, S. D. Perrin, M. J. Robertson, and D. M. Cooper, "1.3um MQW Semiconductor Optical Amplifiers with High Gain and Output Power," *Electronics Letters*, vol. 27, no. 2, pp. 165–166, 1991.

[18] P. Brosson, B. Fernier, and J. Benoit, "Design and Realisation of High-Gain 1.5µm Semiconductor TW Optical Amplifiers," *Elecronics Letters*, vol. 23, no. 6, pp. 254–256, 1987.

[19] T. Ito, N. Yoshimoto, K. Magari, and H. Sugiura, "Wide-Band Polarization-Independent Tensile-Strained InGaAs MQW-SOA Gate," *IEEE Photonics Technology Letters*, vol. 10, no. 5, pp. 1997–1999, 1998.

[20] K. Morito and S. Tanaka, "Record high saturation power (+22dBm) and low noise Figure (5.7dB) polarisation insensitive SOA module," *IEEE Photonics Technology Letters*, vol. 17, no. 6, pp. 1298–1300, 2005.

[21] H. Kim, J. Lim, J. Ha, and W. Jang, "Broadband Wavelength Swept Source Combining a quantum Dot and a Quantum Well SOA in The Wavelength Range of 1153–1366 nm," *Electronics Letters*, vol. 49, no. 19, pp. 1205–1206, 2013.

[22] H. Schemeckebier, B. Lingnau, S. Koenig, K. Ludge, C. Meuer, A. Zeghuzi, D. Arsenijevic, M. Stubenrauch, R. Bonk, C. Koos, C. Schubert, T. Pfeiffer, and D. Dimberg, "Ultra-Broadband Bidirectional Dual-Band Quantum-Dot Semiconductor Optical Amplifier," in *Optical Fiber Communication Conference*, 2015.

[23] G. Contestabile, "Ultra-broadband, highly efficient coherent wavelength conversion in quantum dot SOA," *2013 IEEE Photonics Conference IPC 2013*, vol. 25, no. 9, pp. 525–526, 2013.

[24] F.-S. Choa, "Growth and Processing Techniques for Fabricating Ultra Broadband High-Power Low-Cross-Talk Semiconductor Optical Amplifiers," in *Laser and Electro-optics society meeting 2006, LEOS 06 Conference Proceedings, the 19th annual meeting of IEEE*, 2006, vol. 3, pp. 322–323.

[25] G. A. Alphonse, J. C. Connolly, N. A. Dinkel, S. L. Palfrey, and D. B. Gilbert, "Low spectral modulation highpower output from a new AlGaAs superluminescent diode / optical amplifier structure," *Applied Physics Letters*, vol. 55, no. 22, pp. 2289–2291, 1989.

[26] G. A. Alphonse and M. Toda, "Mode coupling in angled facet semiconductor optical amplifiers and superluminescent diodes," *Journal of Lightwave Technology*, vol. 10, no. 2, pp. 215–219, 1992.

[27] K. E. Stubkjaer, B. Mikkelsen, T. Durhuus, N. Storkfelt, C. Joergensen, K. Jepsen, T. Nielsen, and U. Gliese, "Recent Advances in Semiconductor Optical Amplifiers and Their Applications," in *Fourth International Conference of Indium Phosphide and Related Materials*, 1992.

[28] M. J. Connelly, *Semiconductor Optical Amplifiers*. Springer Science & Business Media, 2007.

[29] Thorlabs, "User's Manual for Tunable Laser Kit," *TLK-1050*, vol. Ely, Campb, p. 49, 2014.

[30] L. F. Tiemeijer, P. J. A. Thijs, T. Van Dongen, J. J. M. Binsma, E. J. Jansen, S. Walczyk, G. N. Van Den Hoven, and E. C. M. Pennings, "Independent MQW Optical Amplifier," IEEE Photonics Techonlogy Letters, vol. 8, no. 9, pp. 1142–1144, 1996.

[31] F. Koch, S. A. E. Lewis, S. V Chernikov, and J. R. Taylor, "Broadband Raman gain characterisation in various optical fibres," *Electronics Lett*ers, vol. 37, no. 24, pp. 1437–1439, 2001.

[32] K. Morito, M. Ekawa, T. Watanabe, and Y. Kotaki, "High output power polarisation insensitive semionductor optical amplifier," IEEE *Journal of Lightwave Technology*, vol. 21, no. 1, pp. 176–181, 2003.

[33] N. K. Dutta and Q. Wang, *Semiconductor Optical Amplifier*, First Edit. Singapore City-State, Singapore: World Scientific Publishing Co. Pte. Ltd., 2006.

[34] K. Carney, R. Lennox, R. Maldonado-Basilio, S. Philippe, F. Surre, L. Bradley, and P. Landais, "Method to improve the noise Figure and saturation power in multi-contact semiconductor optical amplifiers: simulation and experiment.," *Optics Express*, vol. 21, no. 6, pp. 7180–95, Mar. 2013.

[35] C. M. Caves, "Quantum limits on noise in linear amplifiers," *Physics Review D*, vol. 26, no. 8, pp. 1817–1839, Oct. 1982.

[36] E. Desurvire, "On the physical origin of the 3-dB noise Figure limit in laser and parametric optical amplifiers," *Optical Fiber Technology*, vol. 5, pp. 40–61, 1999.

Chapter Six: Index-Guided buried waveguide in the visible range in the GaAs-Based material system

6.1 Introduction

The self-aligned stripe, SAS, investigated in chapters 3, 4, and 5 focussed on the emission at 980nm. Such a scheme is applicable for wavelengths longer than the GaAs bandgap (λ=850nm) and all the way up to 1300nm and beyond (bearing in mind that the GaAs-based devices can extend up to 1600nm). For wavelengths <800nm where the GaAs used in SAS design becomes absorptive, an alternative strategy is required for buried waveguide. The extreme wavelength in GaAs is the case of red emission ~620nm which will be investigated in this chapter.

In this chapter a buried waveguide laser based on a different method of light confinement, Anti-Resonance Reflecting Optical Waveguide (ARROW), is investigated, since appropriate low index cladding for conventional waveguides cannot be formed. The difference between the buried heterostructure and the ARROW is that the buried heterostructure uses the total internal reflection as a mean of confinement while the ARROW depends on the reflections taking place when an incident light propagates from low to high index mediums. The phenomenon is similar to reflections in mirrors or at a water surface where light is reflected to the air (n=1) from the higher index. The use of ARROW scheme is better suited to the material available in the AlGaInP/GaInP/GaAs region.

The chapter starts with a chronological history to the development of red laser, including a study into the main problems associated with realization of high performance. Two methods used to overcome these problems, namely the multiquantum

barrier MQB and the ARROW, are reviewed briefly. Results of this study are fed into simulation used to design a red laser based on the MQB and ARROW principles. Following the simulation, experimental implementation of the simulated design discussed and results presented.

Unfortunately the experimental implementation was not a successful attempt due to technical problem and material shortage. Methods used to grow high Al-containing layers and processing them afterward are not matured to this point in our labs, this resulted delay in these two steps and eventually prevented another enhanced attempt after the one presented in this chapter.

6.2 Red Laser Background

The first semiconductor laser operating at red wavelengths (~640nm) which was presented by Nathan *et.al.* in 1962 [1]. Yet, the development of such wavelength had to wait for a while until the technique developed from only GaAs active layer to $Al_xGa_{1-x}As$ actives appeared with high Al-compositions and then to the AlGaInP/GaInP material systems in order to achieve larger bandwidth.

The development of the red emitting semiconductor laser can be described by three different stages of development. Initially, the wavelength coverage was extended from the faded red (~720nm) [2] down to the very bright red ~630nm [3] in order to replace the HeNe laser at 633nm. The output power was then extended to a level where applications such as ranging and levelling could be addressed. The output power and the single wavelength operation was improved from multiple milliwatts in the early examples up to 2.1W from a single device [4]. The third stage was to improve the beam quality. Beam divergence is important in high-brightness applications such as THz generation and photodynamic therapy where the output power needs to be contained

within a small diameter spot. Also, with burgeoning applications in telecoms and DVD storage, the device reliability was required for long lifetime operation in the 1990s.

The first heterostructure red laser was presented by Kressel *et.al.* [2] in 1968, where a structure that could emit at 845nm and 728nm depending on the operating current where the longer wavelength lased first. Presenting a laser device that operate in the red region with no proper optoelectronic confinement was a challenge that was overcome by Kressel and Nelson who implemented a confinement layer to present a structure in the GaAs/AlGaAs material that can emit in the red region of the spectrum [5] [6].

As with development of other wavelengths, all of the presented structures aimed for low threshold current and high quantum efficiencies. The best way to achieve this is through carrier confinement. An early structure applying current blocking layers was presented by Itoh *et.al.* in 1975 [7]. The stripe geometry in Itoh's structure overcame the problems associated with alternative methods used to form the stripes, such as the isolated stripe (using dielectric) or bombardment stripe. In the dielectric defined stripes the main problem was the poorer heat dissipation resulting from the poor thermal properties of the device. The bombardment stripe suffered high absorption in addition to the accurate and complex post bombardment/implantation annealing required. The proposed structure which was called the heteroisolation stripe laser (HIS) in which an n-doped layer was deposited at the top of the structure and after etching down to define the stripe a contact layer topped the structure. This modification enabled the structure to operate via pulsed operation at 668nm and CW operation at 762nm with a rather high current density (1.1×10^{-5} $A.cm^{-2}$) [7]. At this time, the operating wavelength was still longer than the obvious red region in the CW and it was operated at ambient temperature lower than the room temperature. The first who reported such operation was Kressel and Hawrylo in 1976 when they presented a laser device that emitted at

740nm at room temperature [8]. By decreasing the active width from 100µm to only 13µm by defining a stripe using SiO_2, successful CW operation was reported at room temperature of 13µm wide and 500µm long device [8].

By the implementation of the new growth techniques (MOVPE, MBE and MOCVD growth methods) in the late 1970s /early 1980s, devices with active regions comprising InGaP quantum wells started to appear. In such devices, strained quantum well regions were utilized to reduce the threshold current. Examples include those by Geels *et.al.* [9] using $In_{0.4}Ga_{0.6}P$ and Shirma *et.al.* [10] using $In_{0.62}Ga_{0.38}P$ to realize wavelengths shorter than 650nm, or $In_{0.5}Ga_{0.5}P$ lattice matched to the GaAs-substrate. The GaInP quantum wells are usually accompanied by $(Al_xGa_{1-x})_{0.5}In_{0.5}P$ optical guiding layers in which the aluminium composition, x, was $(0.7 \leq x \leq 0.5)$. Only few devices were reported with Al composition < 0.5, such as the one reported by Smowton and Blood [11] in which they compared 3 different guiding layers with three different Al compositions 0.5, 0.4, and 0.3 and confirming that the lowest composition provided the highest confinement factors among the three values. Some researchers included AlInP cladding layers [12], however, varying the Al-composition in AlInP can change the bandgap of the structure from direct to indirect, resulting in extra non-radiative recombination [11].

Higher output power was realize from an array of devices as the one demonstrated by Geels *et.al.* [13] and single diode like the devices presented by Tukiainen *et.al.* [4]. Geels array provided output power up to 90W from a 1cm bar of lasers [13] while Tukiainen’s laser 2.24W [4]. Improved crystal quality led to increased lifetime of the operated devices from 1000h, as the one presented by Fuji *et.al.* (tested at 5mW output power at 60°C) [14] up to 10000h at 30mW output power at 60°C as shown by Shirma *et.al.*[10].

The limiting factor presenting realization of a buried heterostructure in the red material system apart from the oxidation problem was the high diffusion of the zinc dopants in the p-doped layers. Oshini *et.al.* [15] used magnesium as a replacement for zinc. However, they faced the problem of the so called reactor memory, which they overcame by turning the doping source ON and OFF during the growth. By applying this to the layer just above the active layer, a successful buried ridge device with current blocking layer structure was presented. Alternatively, using carbon as a dopant rather than magnesium as in the devices presented by Kaspari *et.al.* [16], and Sumpf [17], prevented the occurrence of diffusion whilst also solving the problem of reactor memory.

In the last decade efforts have been concentrated on enhancing the optical beam produced by using a flared waveguide integrated with a straight one, such as the one presented by Kaspari *et.al.* [16] and Sumpf *et.al.*[18]. The straight waveguide is used to generate the initial amplified stimulated emission and the flared part is used to amplify this emission. The vertical farfield generally decreases for the devices include a flared section in the front window. The other method used to decrease the output beam divergence was the farfield reduction layer (FRL) which was suggested by Qiu *et.al.* [3]. This helped to enhance the output beam and also decreased the threshold current, since the layer is formed from a higher refractive index which increases the optical confinement.

6.3 Problems in Red material

Unlike the IR spectral range the structures which operated in the red range of the spectrum exhibited two main problems. The first one is the shallow energy step as the bandgap difference for the layers used usually in the structure. The second problem is

the high refractive index of the Al-free material; this problem appears when a buried structure is required with an anti-oxidation protection layer.

6.3.1 Problems in Total Internal Reflection

The main problem associated with realization of buried heterostructures in the visible range of GaAs-based material systems is the method used to provide optical confinement to the optical mode. Higher refractive index material is required for the optical confinement layer (which also can be used as a current blocking layer for electrical confinement). The material system used to grow most red emitting lasers is InGaP/AlGaInP on a GaAs substrate. To obtain a higher refractive index, higher Al-composition layers are required.

In spite of the fact that some authors presented buried structures with high Al-composition layers, the presented structures required complicated processing method or in-situ masking and etching, otherwise the etched surfaces suffer oxidation due to the presence of the aluminium in them.

6.3.2 ARROW structure

The problems associated with processing waveguides based on the total internal reflection as the method to confine the optical mode led the way to develop different configurations for optical waveguides. One configuration that can be used for optical guidance is the anti-resonant reflecting waveguide. In this waveguide the reflection occurs when the light beam hit the interface between the low refractive index medium and the high refractive index medium while propagating from low to high refractive index.

Early efforts toward realization of such waveguides were led by Duguay *et.al.* [19] when they presented an Anti-Resonant Reflection Optical Waveguide (ARROW) in the SiO2-Si material system. The structure comprised a stack of polycrystalline silicon

layer sandwiched between two SiO_2 layers deposited on a silicon substrate. The refractive index of polycrystalline silicon is much larger than that of SiO_2 for the wavelength tested (a He-Ne laser 632.8nm). The confinement was achieved successfully in the vertical direction (the growth direction) with low losses per unit length as the insertion losses for different waveguide lengths were measured [19]. In their structure two main reflections took place, the first one was at the SiO_2-air interface at which the optical mode experienced total internal reflection back to the SiO_2 layer. On the other side of the layer (Poly Si-SiO_2) anti-resonant reflection occurs with different incident angles. The other anti-resonant reflection is at the lower SiO_2 Si substrate, as shown in Figure 6-1. The reflectivity achieved by this configuration was around 99.96%. Duguay *et.al.* presented a set of empirical formulas to help select the anti-resonant layer and the lower SiO_2 layer [19].

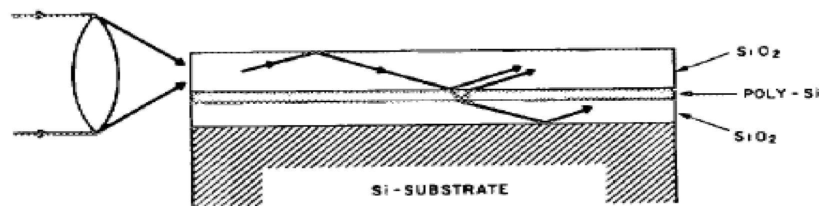

Figure 6-1: The ARROW structure in the Si system reproduced from Duguay et.al. [19]

The main difference between the waveguides that depend on total internal reflection and the ones using the anti-resonant reflection is in the wavelength spectrum that can be covered in a specific structure. In the first type of waveguides the critical angle limits the wavelengths that can undergo total internal reflections, while in the ARROW one the wavelengths that can be confined are the ones that can meet the condition of anti-resonance in the Fabry-Pérot cavities, which is related to N/2λ (N is a natural multiple).

The ARROW structure can be used to confine the optical mode not only in the vertical but in the lateral direction and with various optical material systems. Based on the analysis made on the poly-Si/SiO_2 system, Duguay *et.al.* [20] transferred the

technology to the InP-based material, realizing a passive waveguide of InGaAsP/InP with losses per unit length equal to 4dB.cm^{-1}.

The success of preparing ARROW vertical waveguides (in the growth direction) led to increased interests in their use. A pair of papers discussed the coherent arrays utilizing the ARROW waveguides to couple the emission from multiple devices [20] [21]. This paved the way the way to present the first active ARROWs (laser devices with ARROW cavities as the main waveguides)[23]–[25]. These structures were grown in the GaAs/$Al_xGa_{1-x}As$ system where the Al-composition, x, defined the refractive index step between the core and the high and low index reflecting layers. Of particular note here is that the wavelength which the device design was based on is the lateral wavelengths rather than emission wavelength. These wavelengths are defined by Mawst *et.al.* in their papers [21], [22] as:

$$\lambda_x = \frac{2\pi}{\sqrt{n_x^2 k_0^2 - \beta^2}} \qquad \text{...... eq. (6-1)}$$

where x=1 for the high index reflecting layer and x=2 for the low index core or reflecting layers, k_o is the free space propagating constant $\frac{2\pi}{\lambda_o}$ where λ_0 here is the original emission wavelength. Finally, β is the propagating constant which related the propagated wavelength (or wavenumber) to the effective refractive index of the waveguide such that ($\beta = k.n_{eff}$).

In order to achieve anti-resonance in a Fabry-Pérot cavity the length of the cavity (the width of the layers in here) should be an odd integer of quarter of the lateral wavelength calculated in (6-1) (λ/4), while the resonance widths should be a multiple of half the wavelength. So, in general the core width has to be $\frac{n\lambda_0}{2}$ depending whether and the reflecting layer thickness is $\frac{m\lambda_{1(2)}}{2}$ (n = natural number and m= odd natural number).

The index profile of the simple structure containing a core and two reflecting layers on each side is shown in Figure 6-2.

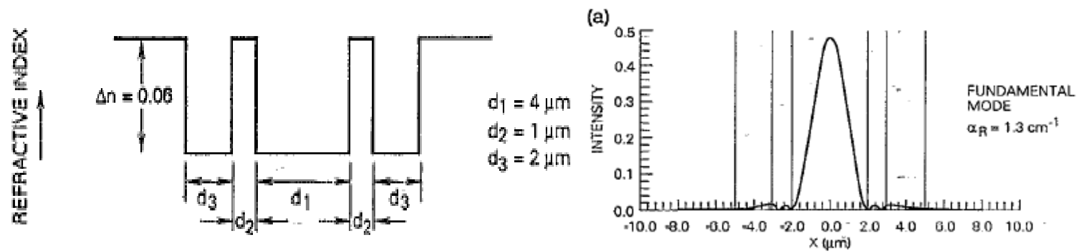

Figure 6-2: The refractive index profile (left) and the simulated intensity distribution (right) of the lateral ARROW waveguide presented by Mawst et.al. [23]

The active single core ARROW developed by Mawst *et.al.* emitted up to 500mW from a 1mm long cavity with AR/HR facet coating for the front/rear facets. The farfield pattern showed a beam divergence of 9°. The summary of the device performance is shown in Figure 6-3. On the other hand the operating wavelength was 980nm.

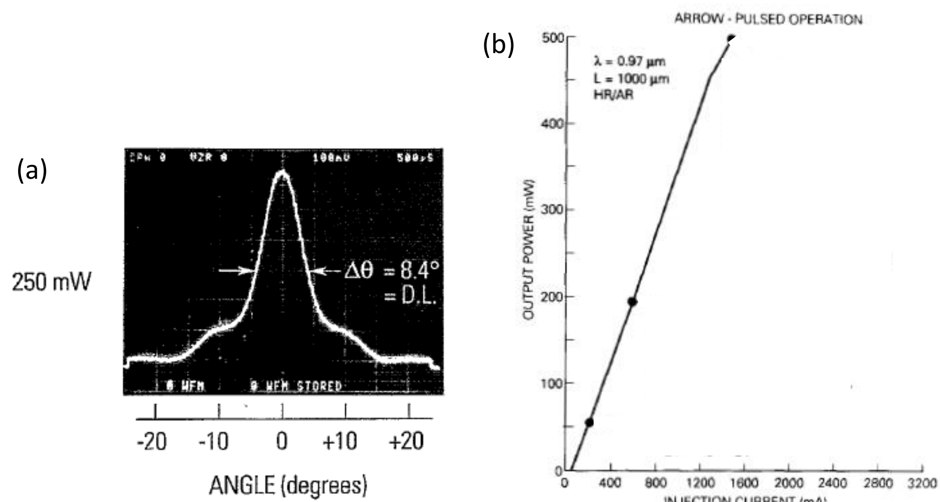

Figure 6-3: The farfield pattern of the single core ARROW structure presented by Mawst et.al. originally in [23] *and developed in* [24]*and* [25] *to emit 500mW as shown in the LI characteristics shown in (b).*

The development of the ARROW structure was continued by Mawst *et.al.* when they developed a Master Oscillator Power Amplifier (MOPA) comprising 3 cores operating at 980nm. This device benefitted from the fabrication flexibility of the ARROW and

intermodal discrimination in the ROW structures [26]. Integration of this MOPA design with an ARROW laser produced light of up to 1W operating at 980nm [26].

Modification to the main ARROW structure by using a single material and a single reflecting layer has been shown to decrease the error margin. Mawst *et.al.* presented this modification theoretically in [27] and applied it experimentally in [28] in an Al-free material system. Later, they presented a single mode DFB laser with ARROW structure in [29]and [30] in 1998, and then they compared the ARROW and Simplified ARROW (S-ARROW) laser structures operating in a fundamental spatial mode up to 2W from a single core cavity device [31].

6.3.3 The shallow bandgap step in $(Al_xGa_{x-1})_yIn_{y-1}P$ material system and the multiquantum barrier MQB.

Figure 6-4 shows the bandgap as a function of lattice constant for the AlGaInP material system. Examining this figure can determine the energy step between the core and the cladding, or the quantum wells and the barriers. A number of reports used AlInP as a cladding material. AlInP has the advantage of being lattice matched to Gas. However, use of AlInP will add in the fabrication process as a result of oxidation that can ultimately affect the device performance. Furthermore, with continuous operation and self-heating even this bulk barrier is not sufficient to stop carriers thermalizing out of the well, limiting CW operation.

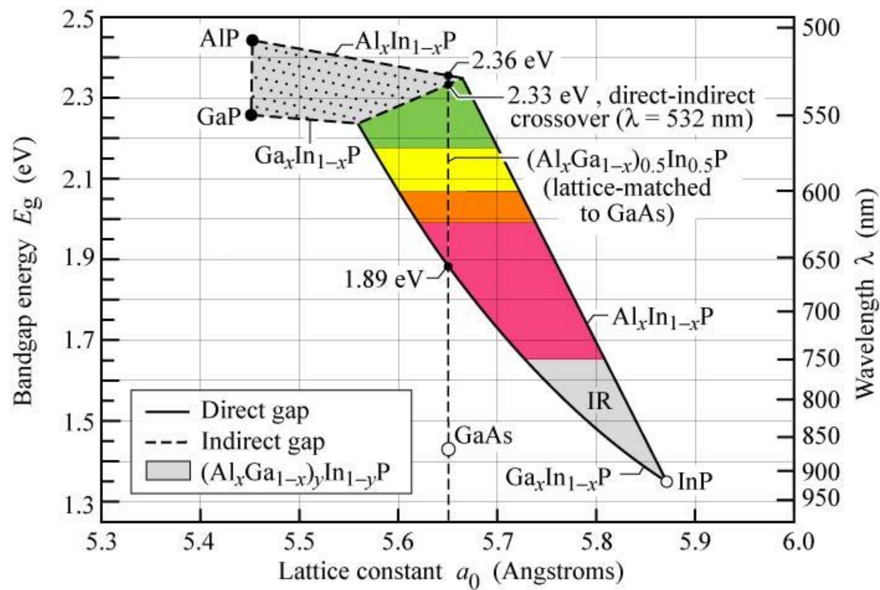

Figure 6-4: The band gap as a function of lattice constant for the (AlGa)InP "shaded" and the related material systems. Taken from [32]

Multiquantum Barriers (MQB) have been suggested by Iga *et.al.* [33] as an addition to the cladding layers. MQB helps to increase the electron reflectivity at the barriers and therefore increasing the thermal operational limit of the device by preventing carrier escape. The MQB section comprises a superlattice of high and low refractive index materials. The thicknesses of wells and barriers in the superlattice, and the number of repetitions determine the reflectivity of the electron or the virtual added potential to the barrier. Based on the classical form of the electron reflection of the barrier the electron is simply reflected back as long as the barrier has potential higher than the core (active), in the quantum form of the reflection both transmission and reflection of the incident electron take place with certain probabilities. From the quantum form increasing the number of barriers lead to increase in the reflectivity and this reflectivity can be expected using the classical form. Iga *et.al.* solved first order Schroidenger equation to estimate the resultant increase in the potential barrier when an MQB superlattice of GaAs/AlAs (or InGaAs/InP) is added to the GaAs (or InP) based device which was shown in Figure 6-5.

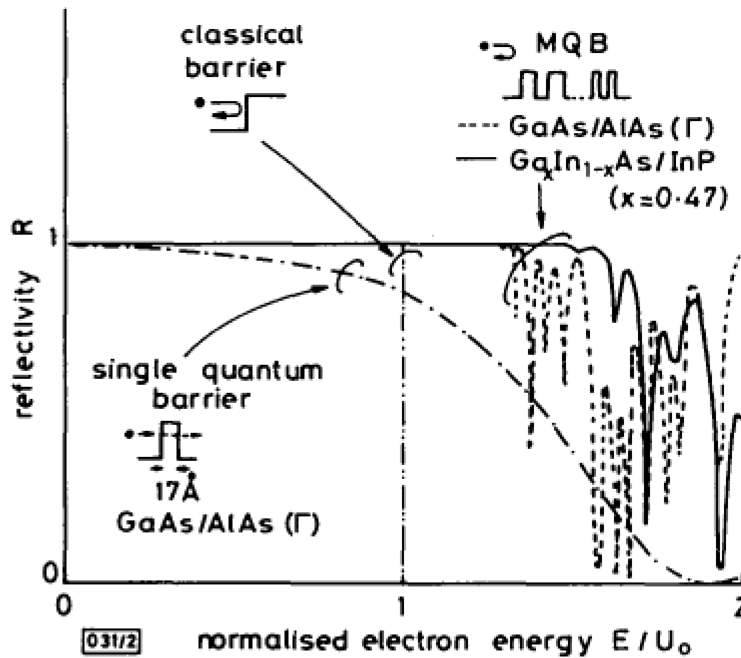

Figure 6-5: Simulation of Electron reflectivity as presented by Iga et.al. [34] *for bulk, single barrier, and the multiquantum barrier cases. Two material systems are presented GaAs/AlAs (dotted line) and GaInAs/InP (solid line).*

Following the work presented in the GaAs/AlAs superlattice, Takagi *et.al.* presented the MQB in the $(Al_xGa_{1-x})_{0.5}In_{0.5}P$ material system to enhance performance of the red lasers [35]. Following the same technique and procedure used by Iga *et.al.* above, Takagi *et.al.* calculated the barrier potential through variation of well thickness, barrier thickness, separation from the active (or first barrier thickness), and number of pairs included in the superlattice. Fine tuning of these parameters was calculated to increase the potential barrier to more than twice the original [35].

Later examples of devices incorporating MQBs in their structure showed enhancement in current blocking (electron reflection) in red and increased the characteristic temperature of the operating devices. Examples in the red emitting devices in the ranges (615-670nm) like [36]–[44], at 980nm in [45], 1.3µm [46]–[48] and 1.55µm [49], [50]. Other experimental examples of successful implementation of the MQB are the electron blocking layers in the n-i-n structure [51], electron filter like in [52]. Exceptionally high characteristic temperature was achieved in the

GaAs/AlGaAs system implementing a InGaAs/AlGaAs MQB with shorter periods where characteristic temperatures above 300K and lasing observation at temperatures as high as 238°C [53]. More recently, application of the MQB to GaN based high brightness LEDs operating at short wavelength [54] showed higher efficiency and improved thermal properties.

6.4 The Proposed Red ARROW Laser:

A buried heterojunction laser that operates at 650nm was designed as a first step towards transferring GaAs-based regrowth technology down to the visible range. The proposed design is built using GaAs lattice-matched $(Al_xGa_{1-x})_{0.49}In_{0.51}P$ with $(0<x<0.8)$ according to the required refractive index. Two design stages were required in order to achieve the final design. The first stage was to prepare the optimized active layer structure that could achieve low threshold current CW operation. The second stage was to design the index-guided optical waveguide. Based on the literature survey done, a single-core standard anti-resonant reflecting optical waveguide (ARROW) was selected in AlGaInP structure, while the guiding layer included a multiquantum barrier (MQB) for leakage current reduction. This structure is illustrated in Figure 6-6.

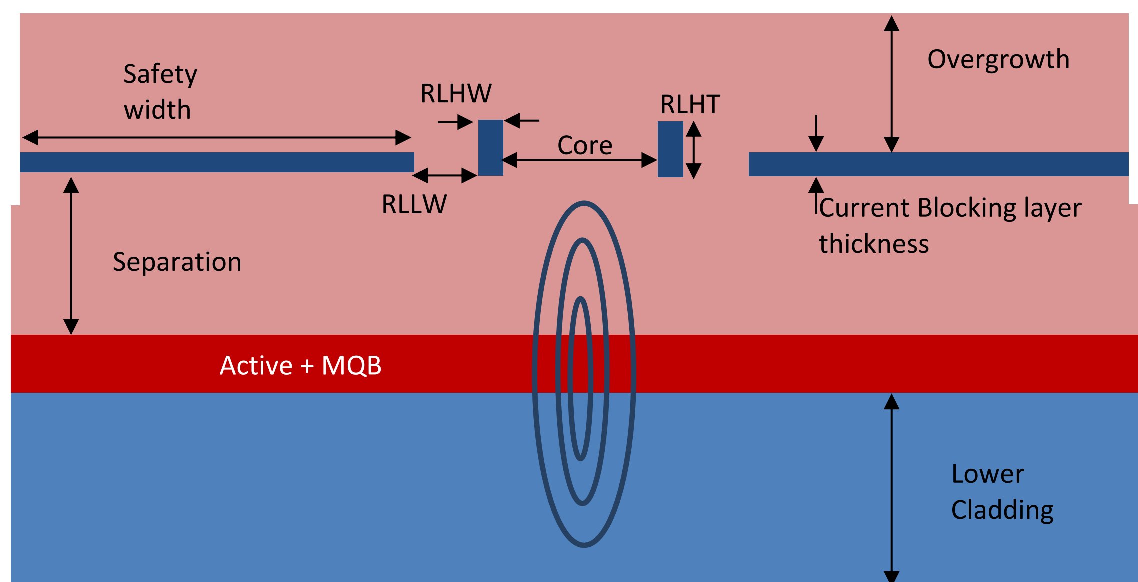

Figure 6-6: The proposed ARROW structure with general dimensions which have to be set in the final design.

Figure 6-6 shows the main parameters that have to be designed for a successful buried structure. The required beam size is preferred to be less than 10µm for both single mode operation and better fibre coupling. The ARROW structure has two reflecting layers with low and high refractive index, thickness and width of the high refractive index should be selected to meet the requirements, the thickness is noted as reflecting layer high index thickness (RLHT) and the width is reflecting layer high index width (RLHW). The second reflecting layer which has lower refractive index requires only selection of the width of the layer as its thickness will be the overgrowth applied later on; the width of this layer is noted by reflecting layer low index width (RLLW). The separation between the active layers and the current blocking layer is another parameter that should be tuned so that the latter will not cause the optical mode to be displaced to the higher refractive index layer. A trade off took place between the current blocking layer thickness and the separation from the active layer.

The commercial simulation software Fimmwave is used to simulate the waveguide structure where the related parameters are selected by changing only one of parameters at a time systematically.

6.4.1 The multiquantum barrier active design:

An active structure supplied by IQE PLC operating at 650nm was used as a starting point to design a multiquantum barrier active region. The IQE structure included a triple quantum well sandwiched by a guiding layer of GaInP/(Al_xGa_{1-x})InP material system lattice matched to GaAs where x=0.5. The cladding material was ($Al_xGa_{1-x}InP$) in which x=0.7, the cladding layer was meant to provide enough optical confinement using the refractive index step between the cladding and the guiding/barrier layers. Figure 6-7 shows the structure and the refractive index profile of the system developed by IQE.

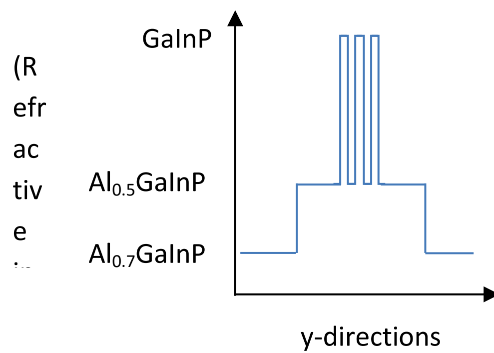

Figure 6-7: Index profile of the triple quantum well laser structure developed by IQW.

A multiquantum barrier superlattice was integrated into this original structure in addition to two extra wells to increase the gain of the structure. Simulation of the original and modified structures was performed using LaserMod commercial software supplied by RSOFT. This software enables the user to simulate a photonic semiconductor structure under conditions ranging from the ideal condition (no self-heating or carrier induced losses) to the general conditions where losses resulted from a range of causes. The structure assumes ideal contacts so the series resistance of the contacts are set to zero. The software optionally takes into account the lattice constant variation between the simulated layers, where the strain induced bandgap alteration and other properties can be considered. The light-current curve can be simulated using LaserMod and it was used a means to compare simulated structures with identical physical dimensions and differing only by their active regions. The dimensions used in the simulations were a 50 µm width and 500µm length (broad area lasers).

The starting point was simulation of the original triple well IQE material and comparing it to five quantum well structure. The reason of using the quantum well was primarily to increase effective refractive index of the active layer to benefit from it later in the waveguide design. Increasing the number of quantum wells helped increase the effective refractive index but the penalty paid was an increase in the threshold current in spite of the fact that the modal and material gains of the two structures are comparable,

as shown in Figure 6-8. Figure 6-8 shows the simulated LI curves of the IQE 3QW (a) and the 5QW (b) and the modal gain of the two structures in (c) and (d), respectively. This increase came from the increase in the number of wells which required an increase in the carriers' population.

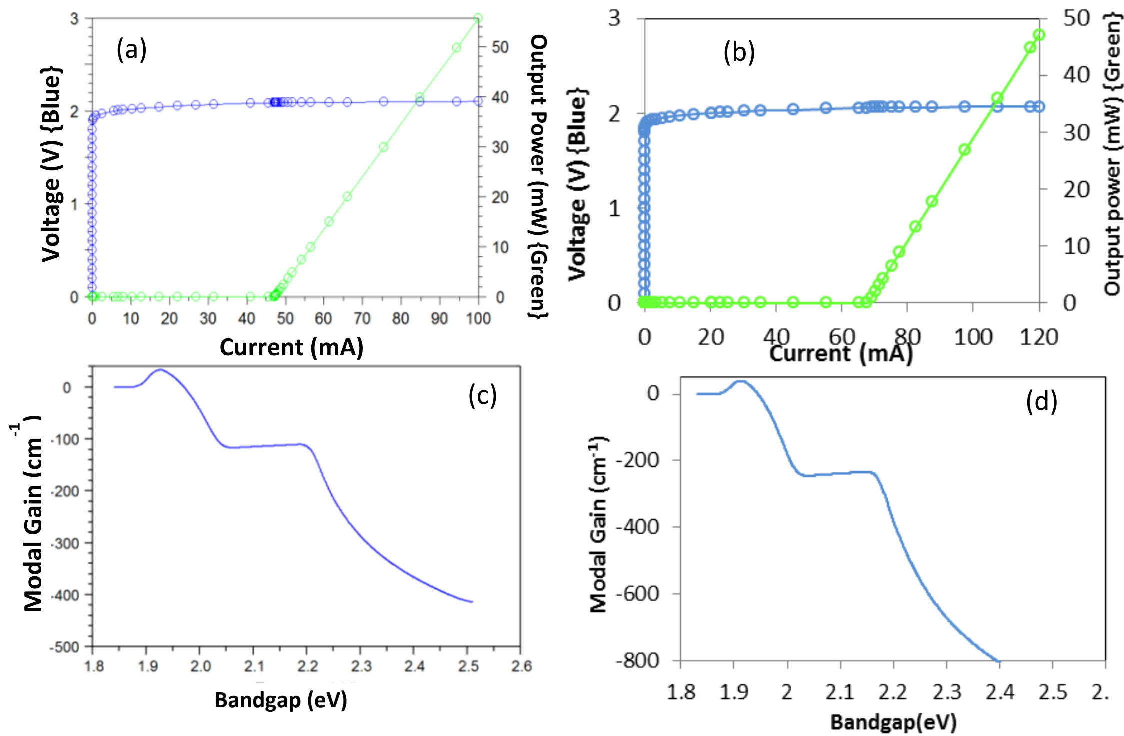

Figure 6-8: A comparison between the LIV curves (a) and (b), and the modal gain (c) and (d), for devices with 3 and 5 QWs, respectively.

Changing the reference point now from three quantum wells system to five quantum wells without MQB layer, the MQB layer is integrated in the attempt to decrease the threshold current of the structure. The MQB section was based on the one presented by Smowton and Blood [44], the MQB section presented by them included eleven periods of 4.3nm thick $Ga_{0.5}In_{0.5}P$ wells and 10 periods of 4.5nm thick $Al_{0.5}In_{0.5}P$ barriers. Since the structure used $(Al_{0.7}Ga_{0.3})InP$ as a cladding layer, the cladding barrier layers in the MQB superlattice was selected to be $(Al_{0.7}Ga_{0.3})InP$ instead of $Al_{0.5}In_{0.5}P$ to decrease the relative complexity of the growth process, in term of decreasing the number of calibrations needed. Six periods of Well/Barrier was simulated and three parameters were varied one at a time to achieve the best combination. The three variable parameters

were the combination of QW/QB width, the separation between the active and the MQB superlattice, and finally the number of QW/QB pairs.

First the width of both QW and QB was changed to 1/2, 1.5/2.5, 2/1, 2/2, 2/3, 3/3, and 3/4nm QW/QB. Just by integrating the reference structure with the MQB caused the threshold current to be reduced at least 10mA. This confirmed the effect of the multiquantum barrier superlattice on the electron confinement, where the electrons are reflected back from the superlattice with almost zero probability of the electron being transmitted through the supperlattice as Iga *et.al.* suggested [33]. Figure 6-9 shows a summary of threshold currents from the simulated LI curves. The threshold current was decreased from 67mA in the structure with no MQB to 55-57mA for all structures except the width combinations 1/2 and 1.5/2.5 in which less than 55mA threshold current was achieved. The minimum threshold current ever estimated was for the 1.5/2.5nm QW/QB thickness combination. During the alteration of the wells and barriers widths the whole MQB region was placed at 30 nm separation from the active medium on the p-cladding side of the device.

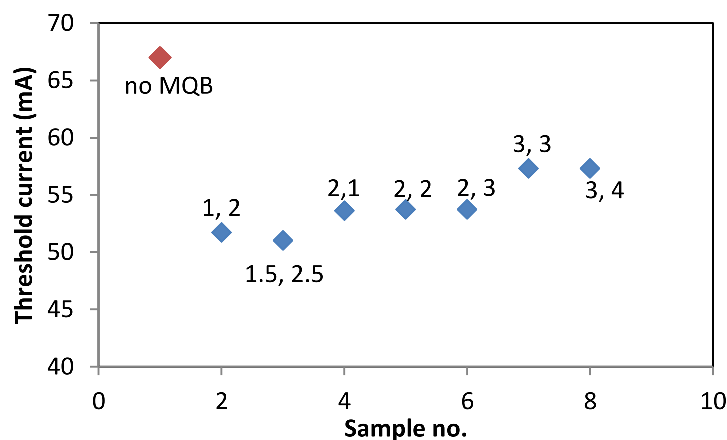

Figure 6-9: A summary of the threshold currents simulated for different widths of Wells and Barriers in the MQB section. The numbers in brackets over the figure marks are the widths for (well, barrier).

After determining the thicknesses that can provide the lowest threshold current, the widths were set to 1.5/2.5nm and the separation between the active and the MQB was

altered to determine whether or not the separation affects the threshold current. The separation ranged from 26-36nm. Figure 6-10 summarized the development of the threshold current as a function of the separation of the two regions. Comparing the 26nm separation case with the largest separation of 38nm only marginal change can be recorded between the 26 and the 38nm separations, for that reason the separation was set to 35nm separation in my design.

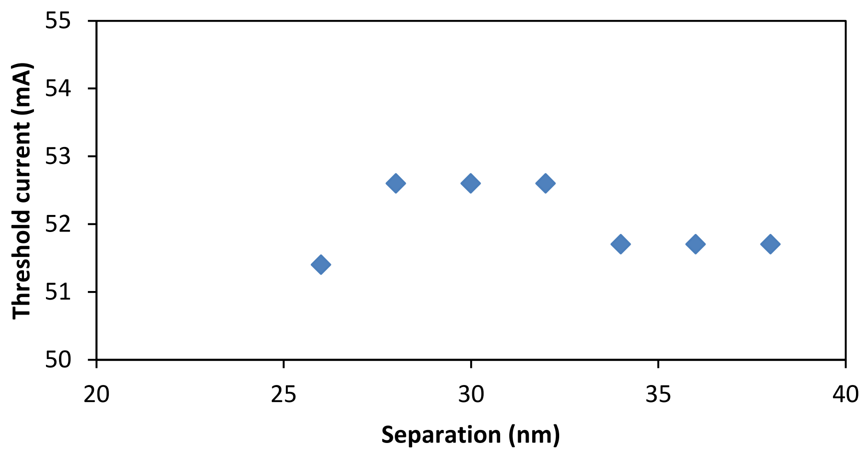

Figure 6-10: A summary of the effect of the separation between the active and the MQB section on the threshold current.

The last parameter to be changed was the number of periods in the MQB. Fixing the QW/QB widths to 1.5/2.5nm and the separation to 35nm, the number of periods in the MQB was set as 4 and 8, with the simulation plotted in Figure 6-11 showing no change in the LI characteristics between 4, 6, and 8 periods.

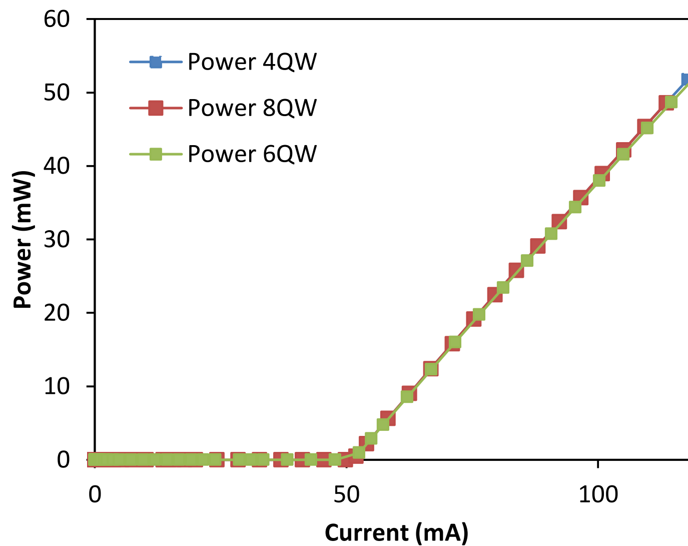

Figure 6-11: LI curves of MQB containing structure with 4, 6, and 8 QWs. The figure shows identical behaviours of the three devices suggesting that the number of wells does not affect the superlattice electron reflectivity.

Based on these simulations, the final active layer design is chosen to include, five GaInP quantum wells each of 5nm thickness with 7nm barriers of $(Al_{0.5}Ga_{0.5})InP$, a 35nm separation of the $(Al_{0.7}Ga_{0.3})InP$, 6 periods in the MQB with 2nm GaInP wells and 3nm $(Al_{0.7}Ga_{0.3})InP$ barriers. The n- and p- cladding was selected to be $(Al_{0.7}Ga_{0.3})InP$. All the layers selected for growth were lattice matched to GaAs to avoid any strain. The wavelength targeted was ~650nm which can be achieved with strain-free active design.

6.4.2 Anti-Resonance Reflecting Optical Waveguide Design:

Based on the analysis presented by Mawst *et.al.* [23]–[31], the optical waveguide of the red device was designed. First, the refractive index of the AlGaInP material system is calculated for a range of bandgaps (wavelengths) in order to select the most appropriate combination for the structure [55]. The primary goal was to select a combination of layers that would enable processing of the material without exposure of aluminium containing layers to the atmosphere as achieved in the 990nm self-aligned stripe devices discussed in chapters 2-5. For this reason, it is important to learn the refractive index dependence on the possible compositions of layers that can be accessed.

Figure 6-12 shows the calculated refractive index of the (AlxGa1-x)InP from x=0 to x=1. The calculated refractive index did not take into account the effect of the doping on the refractive index.

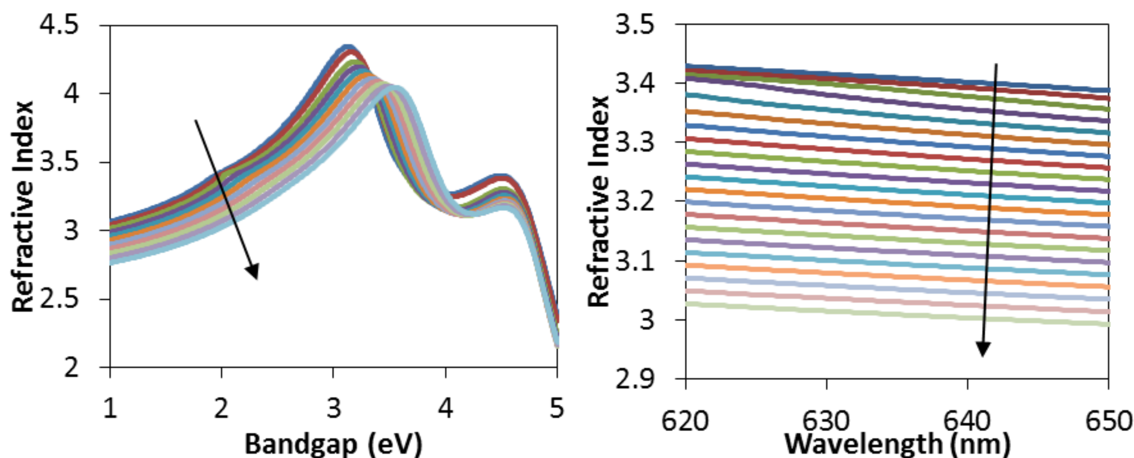

Figure 6-12: The calculated refractive index of (AlxGa1-x)InP lattice matched to GaAs substrate for different bandgap (i.e. Wavelengths), the general values are shown in (a) while (b) shows a zoomed in one to the range of the red light wavelengths. The arrows shown represent the increase of the Al-composition (x) from 0 to 1.

The option was to use a GaP/InGaP/GaP combination equivalent to the GaAs/InGaP/GaAs current blocking layer combination used in the 990nm structure discussed in chapters 3-5, where the GaAs layers acted as an etch stoppers as well as protection for the Al-containing layers during the fabrication process. Due to the large difference in the lattice constant between GaP and GaAs, a very thin layer of GaP can be grown before dislocations starts to take place. This layer thickness is estimated to be <5nm which is not enough to work as etch stopper, for that reason a strained $Ga_{0.65}In_{0.35}P$ layer is suggested since a selective etching is available between the strained and unstrained GaInP. The GaInP layer here was meant to be used as etch stopper as well as a protective layer for the high Al-containing layers below it.

However, upon investigation of the optical mode shown in the Fimmwave simulation shown in Figure 6-13, it was found that the high index for the GaInP layer which dislocates the optical mode from the active MQW region to be guided within the current blocking layer. This problem could not be overcome even with layer thickness as low as

70nm. The problem with such thin layers is that they could not provide sufficient current blocking based on the doping levels commonly known in the GaInP/AlGaInP material. For most of the visible lasers structure found in the literature the common doping levels is 10^{18}-10^{19} cm^{-3}, with this levels of carriers population the depletion region is usually ~80nm. Considering that the structure is n-p-n, this means that two depletion region should be taken into account. Which means the thickness of the layer should be > 160nm.

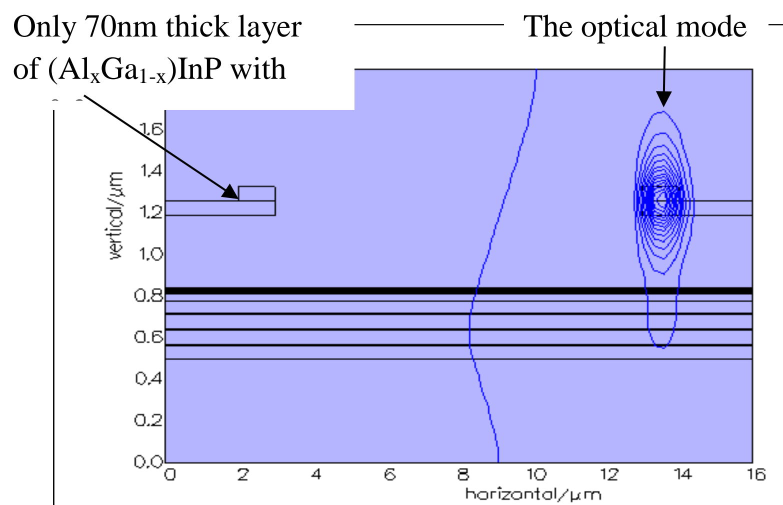

Figure 6-13: The simulated near field of a structure that has a current blocking layer of only 70nm, yet, the optical mode is still dislocated to the low Al-composition layer rather than the active MQW layer.

A solution could be to replace the GaInP high index layer with a layer that has a small concentration of aluminium to change the GaInP to $(Al_xGa_{1-x})_{1-y}In_yP$ with (0<x<0.4). For GaAs lattice matched AlGaInP y should be around 0.5 as the lattice constant figure shows in Figure 6-4. From the simulated refractive index values shown in Figure 6-12 and considering that the lasing wavelength is simulated to be 649nm as estimated by the LaserMod software, the lateral wavelength in the low refractive index material, λ_o, was calculated by the formula given in [22]

$$\lambda_x = \frac{2\pi}{\sqrt{n_x^2 k^2 - \beta^2}} \qquad \text{....... eq. (6-1)}$$

where x=0 for low refractive index material (core and outer reflecting layer) and x=1 for high refractive index material, n_x is the refractive index of the related material. According to the calculated refractive indices, the lateral wavelength in the cladding layers λ_o (0.7 aluminium composition in the AlGaInP) was 1.262×10^{-6}m, for an aluminium composition between 0 and 0.4, the lateral wavelength λ_1 was found to be (6.8×10^{-7} to 1.05×10^{-6} m).

The need for a specific thickness to form the current blocking layer imposed limitation on using AlGaInP with aluminium composition lower than 0.3 as the simulation shows dislocation of the optical mode from the active as the current blocking layer absorbs the light generated in the intrinsic region as shown in Figure 6-13 above. For this reason, the Al-composition > 20% is required so that the effective refractive index of the active region (including the wells and the $(Al_{0.5}Ga_{0.5})InP$ guiding layer) is kept higher than that of the current blocking layer. By calculating the depletion region for the pn-junctions to the sides of the current blocking layer based on the common carrier populations in both n- and p- sides, it is found that the depletion length of the two sides combined are ~160nm. Based on this estimation, a current blocking layer thickness of at least 200nm is needed to allow error margins.

By simulation trials using Fimmwave over a range of Al-compositions, it was found that $(Al_{0.3}Ga_{0.7})_{0.5}In_{0.5}P$ has the lowest value of Al-mole that does not cause dislocation to the optical mode.

The widths of the features of the ARROW structure are governed by the lateral wavelengths of the low and high refractive index material combination used. These lateral wavelengths are governed by the refractive index of the material used and the propagating wavelength as shown in equation 1 above.

The principle of the vertical ARROW presented by Koch *et.al.* [19] and the lateral one presented by Mawst *et.al.* [21]–[31] stated that the core width should be half of the lateral wavelength of the propagating light, $\frac{\lambda_x}{2}$, and the reflecting layers width should be one quarter of the lateral wavelength of the propagating light, $\frac{\lambda_x}{4}$. Three regions will be used in the device as shown in Figure 6-6, the core which should be resonant to the fundamental mode and this condition can be met by setting the width of the core to natural multiples of $\frac{\lambda_o}{2}$, and the high and low refractive index reflecting layers which should be anti-resonant to the lateral wavelengths, to achieve that the widths of the high and low indices layers should be odd natural multiples of $\frac{\lambda_1}{4}$ and $\frac{\lambda_o}{4}$, respectively. Figure 6-14 shows the three sections with the related dimensions. Since the core is selected to be $(Al_{0.7}Ga_{0.3})_{0.5}In_{0.5}P$, the related lateral wavelength, λ_o, was found to be 1.262µm. On the other hand the current blocking layer material is selected to be $(Al_{0.3}Ga_{0.7})_{0.5}In_{0.5}P$ and according to this the lateral wavelength of the high refractive index is found to be 0.7284µm. Based on these values the widths of the related layers were selected.

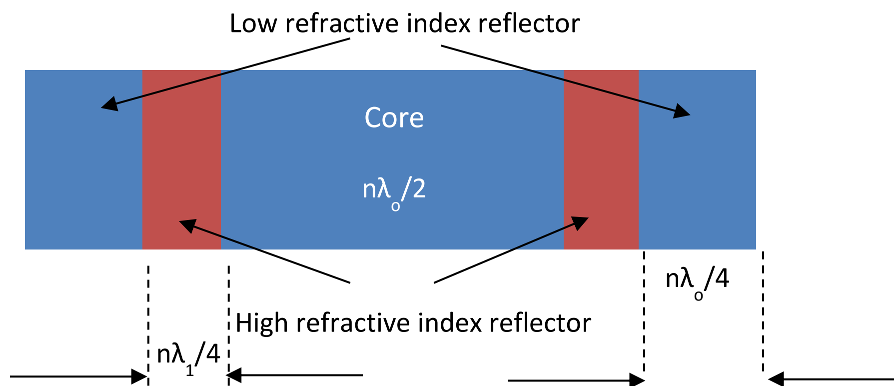

Figure 6-14: A schematic diagram showing the three main regions in ARROW structure.

The core width was selected to be 3µm, this value is very close to $5 \times \frac{\lambda_o}{2}$ (3.1541) which satisfy the condition put by Koch *et.al.* and Mawst *et.al.* The reflecting layers on the other hand was selected based on quarter lateral wavelengths value to be 1 for the

high refractive index reflecting layer, and 1.5 for the low refractive index reflecting layer. These two values are 5 times quarter the lateral wavelength in both high and low index cases. Table 1 shows a summary of the odd multiples of the two wavelengths.

Table 1: λ1 (high index material lateral wavelength) and λo (low index material lateral wavelength calculations. Highlighted the quarter wavelength (yellow) and the widths used in the design (red).

λ1	7.28399E-07	λo	1.26162E-06
Multiple n	Width $(n\times\lambda_1/4)$	Multiple n	Width $(n\times\lambda_o/4)$
1	1.821×10^{-7}	1	3.15406×10^{-7}
3	5.46299×10^{-7}	3	9.46218×10^{-7}
5	9.10499×10^{-7}	5	1.57703×10^{-6}
7	1.2747×10^{-7}	7	2.20784×10^{-6}

Figure 6-15 shows a schematic diagram of my final design I suggested for the ARROW laser that emits at around 650nm wavelength. The 1.5µm thicknesses of the lower cladding and the overgrowth are fixed to $(Al_{0.7}Ga_{0.3})_{0.5}In_{0.5}P$. The 800nm separation between the active and the ARROW layer is included in order to prevent dislocation of the optical mode from the active region.

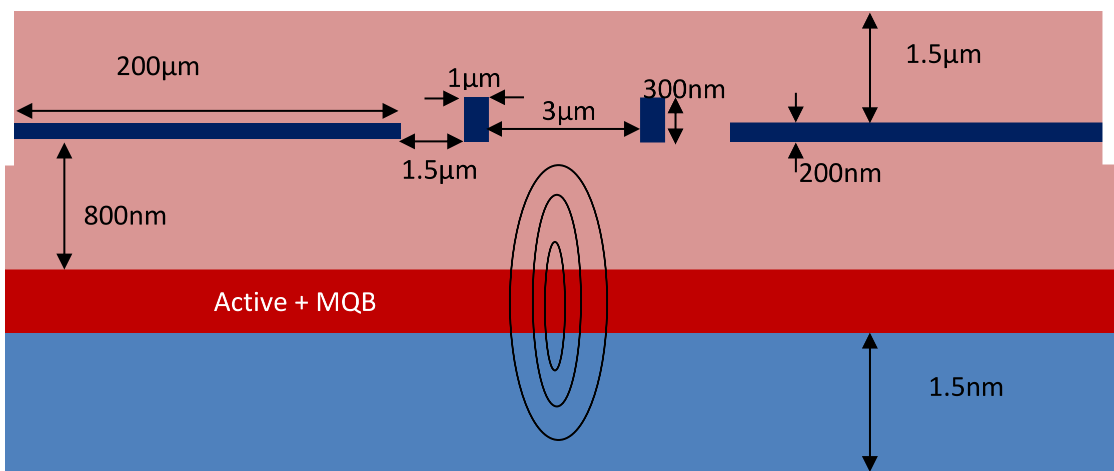

Figure 6-15: Illustration of the final ARROW structure from the simulation outcomes. This schematic diagram is not drawn to scale.

The colour coding in Figure 6-15 is made according to the material for simpler reading where the light blue is an n-doped $(Al_{0.7}Ga_{0.3})InP$ lower cladding layer, the red layer is an un-doped Active MQW and MQB layer as discussed earlier, The pink areas are p-doped $(Al_{0.7}Ga_{0.3})InP$, and the dark blue layer is n-doped $(Al_{0.3}Ga_{0.7})InP$. The black ellipses in the centre represent the optical mode confined by the ARROW structure which was simulated by the FIMMWAVE. The confined mode is shown in the simulation result in Figure 6-16.

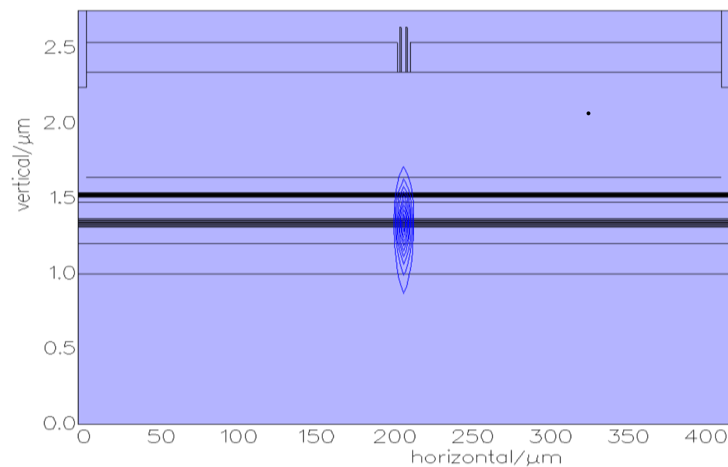

Figure 6-16: The simulated near field pattern of the ARROW laser as simulated by FIMMWAVE

6.5 Experimental Implementation of the Simulated Device.

In order to justify the simulations done in the previous sections, structures are grown and characterized. A broad area lasers without MQB was grown first as reference device performance. The second growth was a MQB broad area lasers to address the efficiency of including the MQB in the structure. The last structure grown was the ARROW structure which included a two-step growth intersected by patterning.

6.5.1 The full clad structure:

The structure was grown on an n-doped GaAs-substrate with crystal orientation 100 tilted 10degrees toward 111. Table 2 summarize the epitaxial structure of the full clad laser with and without the MQBs section. Both of the structures had the same cladding

layers which was $(Al_{0.7}Ga_{0.3})_{y-1}In_yP$ cladding lattice-matched to GaAs where the In-composition was set to 0.51. Two higher refractive materials were used in the active part $(Al_{0.5}Ga_{0.5})_{0.49}In_{0.5}P$ for barrier or guiding layers and GaInP for quantum well.

Table 2: The epitaxial structure of the full clad lasers used to investigate the MQB impact on the device performance.

Layer	Material composition	Thickness	Doping type and carrier concentration
Lower Cladding Layer	$(Al_{0.7}Ga_{0.3})_{0.49}In_{0.51}P$	1µm	n-type $10^{18}cm^{-3}$
Lower guiding layer	$(Al_{0.5}Ga_{0.5})_{0.49}In_{0.51}P$	80nm	Undopped
Active layer	GaInP QW/ $(Al_{0.5}Ga_{0.5})_{0.49}In_{0.51}P$ QB		Undopped
Upper Guiding layer	$(Al_{0.5}Ga_{0.5})_{0.49}In_{0.51}P$	80nm	Undopped
Lower Cladding Layer	$(Al_{0.7}Ga_{0.3})_{0.49}In_{0.51}P$	1µm	p-type $10^{18}cm^{-3}$
1st Contact layer	GaInP	50	P-type $2\times10^{18}cm^{-3}$
2nd contact layer	GaAs	200nm	P-type $2\times10^{19}cm^{-3}$

The two devices differ in their active layers. The reference structure included the 5 quantum wells only and these wells are separated by $(Al_{0.5}Ga_{0.5})_{0.49}In_{0.51}P$ barriers. The other structure prepared to investigate the MQB effect on the device performance. This structure included 35nm of $(Al_{0.7}Ga_{0.3})_{0.49}In_{0.51}P$ between the quantum wells stack and the MQB superlattice, this section was added on the p-side of the structure. The MQB comprises six periods of 2nm GaInP well and 3nm $(Al_{0.5}Ga_{0.5})_{0.49}In_{0.51}P$ barrier. Figure 6-17 shows a simplified schematic of the grown structure and its index profile. A reference wafer was also grown in which the separation and the MQB were not included leaving a 5QW guided active layer sandwiched between $(Al_{0.7}Ga_{0.3})_{0.49}In_{0.51}P$ cladding layers.

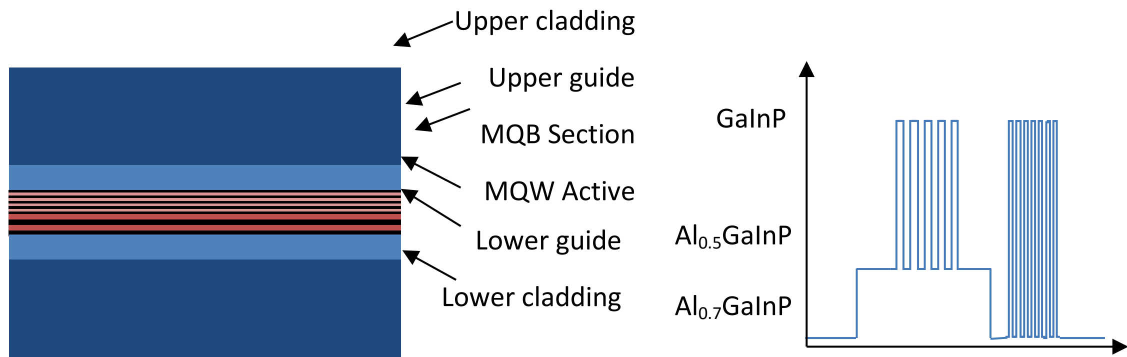

Figure 6-17: epitaxial structure (left) and refractive index profile (right) of the grown MQB containing wafer.

These two wafers were processed into broad area (50µm wide) lasers for basic characterization. To prepare such devices, the p-contact was formed by depositing an alloy of Au/Zn/Au with thicknesses of (5/10/200)nm which was annealed at 360°C for 3sec to create the p-contacts. In order to electrically isolate adjacent devices trenches were etched using 1:1:1 HBr:$C_2H_4O_2$:$K_2Cr_2O_7$ (diluted with DI water 50:50 ratio) etchant to a depth of ~1µm. Before deposition of back (n-type) contacts the wafers were thinned down to ~150µm. For the back contacts, an InGe/Au alloy was deposited with thicknesses 20/250nm followed by annealing at 340°C. The wafer was cleaved into 300µm and 500µm long devices. 300µm was at the limit of what was possible to cleave which is typically 2-3 times the substrate thickness.

6.5.2 The ARROW buried structure.

To realize the buried structure designed above, two growths are required. The first growth should include the layers up to the protecting layer above the $(Al_{0.3}Ga_{0.7})_{0.49}In_{0.51}P$ ARROW forming layer. The original intention was to sandwich the n-doped $(Al_{0.3}Ga_{0.7})_{0.49}In_{0.51}P$ current blocking layer was sandwiched by two GaP protection layers. Because GaP has a large lattice mismatch with GaAs, growing GaP layer > 4-5nm will cause unwanted strains in the structure. For this reason strained GaInP with a thickness less than 15nm was used instead. This thickness is sufficient for it to be used as an etch stop layer whilst not causing sever material strain that. 10nm of

undopped $Ga_{0.7}In_{0.3}P$ was grown below and above the 300nm of n-$(Al_{0.3}Ga_{0.7})_{0.49}In_{0.51}P$ current blocking layer and the doping level was set to 10^{18} cm^{-2} in this layer.

To form the optical waveguide, the wafer was patterned using standard photolithography. Two mask patterns were used to achieve the final processed structure shown in Figure 6-15 in section 6.4. The first stage defined the core and the reflecting layers laterally. The high index reflecting layers was left un-etched while the lower index reflector and the core were etched down to the strained GaInP lower layer by SiCl4 and Ar using the inductive coupled plasma (ICP) dry etching. The second mask was used to cover the ARROW part of the layer and etch the surroundings by 100nm. The second etching was also done by SiCl4 and Ar utilizing ICP and relied on multiple trials to achieve the proper time for 100nm etching.

To complete the ARROW lasers structure the patterned wafer should be overgrown with 1µm thick p-$(Al_{0.7}Ga_{0.3})_{0.49}In_{0.51}P$, 50nm GaInP and the p^{+}-GaAs contact layers.

The second etch step was designed to terminate within the $(Al_{0.3}Ga_{0.7})_{0.49}In_{0.51}P$ layer. Typically, one would not wish to overgrow upon Al-containing layers. However, incorporating low composition AlGaInP is necessary in design of appropriate refractive index structure for the ARROW. Furthermore, it was not believed that the affinity of oxygen to such a low Al-composition would be sufficiently low that good quality growth could be achieved.

6.6 Device Characterization

6.6.1 The LI characteristics of the reference laser structure:

Devices were tested under pulsed conditions with small pulse widths used in order to reduce the effect of self-heating. The set-up used is the same LI setup described in

section 2.3.1 but with a pulsed current source rather than a continuous one. First the reference full clad grown structures were cleaved into 300 and 500µm long devices.

Presentation of room temperature LI curves are shown in Figure 6-18, for 300µm lasers, with the pulse width varied between 100nsec and 500ns while the pulse width was fixed to 1% of the pulse period.

When the pulse width is increased from 100nsec to 500nsec, the threshold current dropped significantly from >500mA down to 200mA. The reason for such difference can be the high internal losses of this red structure. The minimum threshold current and the maximum slope efficiency were found to be for 300nsec pulse width and 30µsec pulse duration. Figure 6-17 shows the effect of the pulse width variation on the threshold current and the slop efficiency. The measurement shows that the device has a strong temperature dependency where the threshold current is almost fixed for 300-500nsec while the slop efficiency decreases by increasing the pulse width.

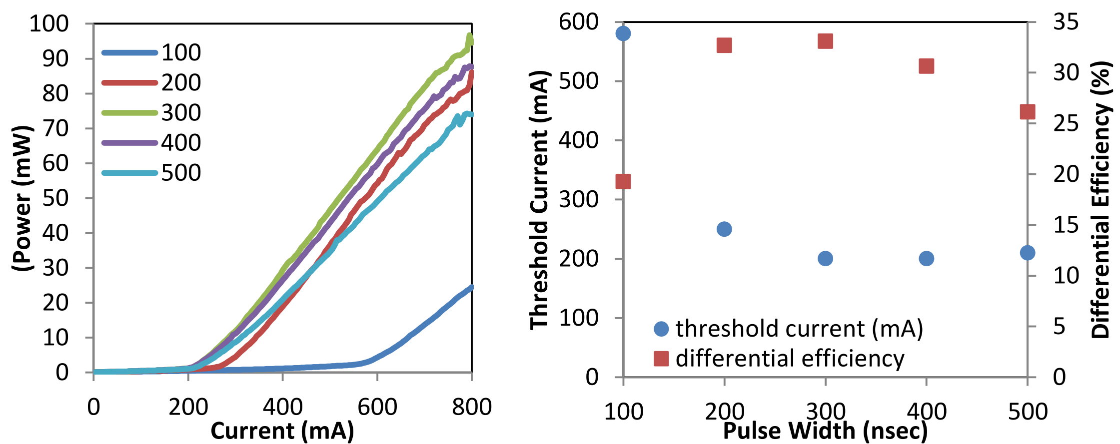

Figure 6-18: LI characteristics comparison of various pulse widths (left) and the differential efficiency and threshold current comparison as a function of pulse width for a 300µm device.

500µm long lasers were found to operate with improved characteristics. The threshold current reduced from 200mA (1.33kA.cm^{-2}) down to 135mA (540A.cm-2) under the same condition as the 300µm long device. The reason for this is the increased

active length which results in a reduction in mirror losses. Figure 6-19 shows the LI curve of the 500µm long broad area laser (a) and both the threshold current and the slope efficiency as a function of pulse widths. The same self-heating problem can be observed in the 500µm long devices, which also exhibited a large variation in the slope efficiency and an increase in the threshold current.

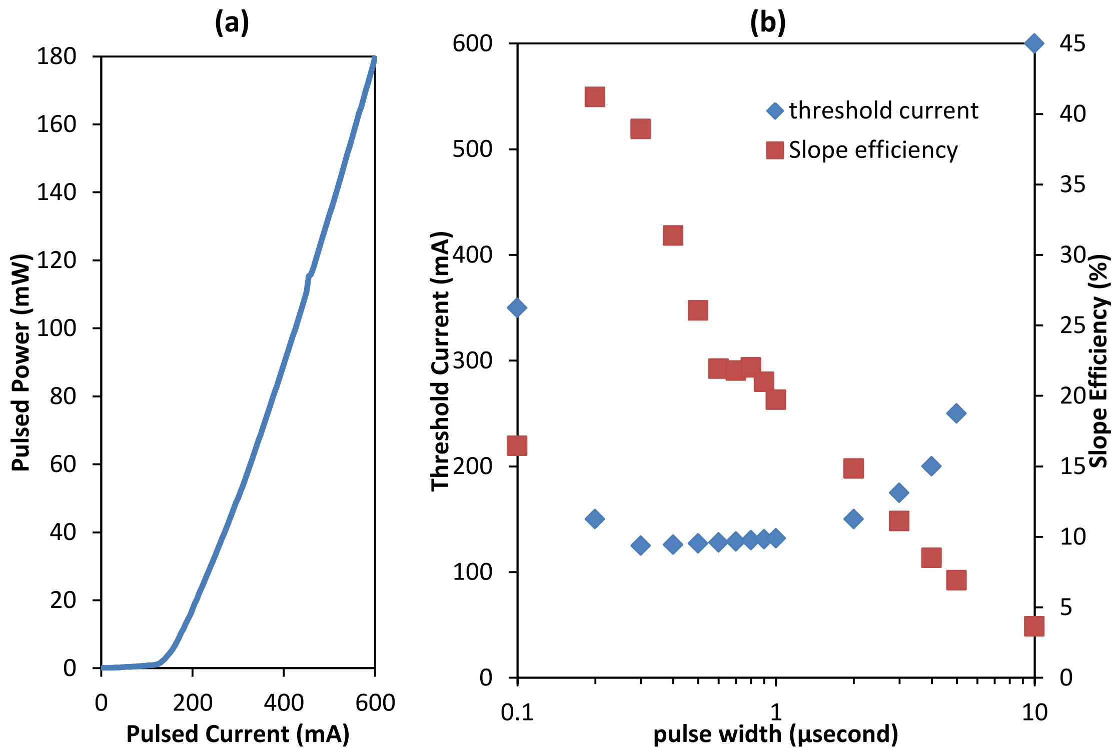

Figure 6-19: LI curve of the 500µm device from the reference wafer at 300nsec pulse width and 30µsec pulse duration (left) and a comparison of the threshold current and the slope efficiency for various pulse widths (right).

The threshold current of the 500µm reference device in pulsed shows a high increase in the threshold current required for the same device simulated via LaserMod software where the simulated device had a threshold current of ~70mA while the measured data showed a threshold current almost doubled, this can be caused by the high series resistance of the processed device. This fact is confirmed by examining the threshold current shift when the pulse width is increased more than 1µsec in Figure 6-19b.

The low resolution EL spectra was measured for the 500µm long devices beyond the threshold current point between 400-800mA (1.6-3.2kA.cm^{-2}) at room temperature, the EL measurement is plotted in Figure 6-20a. The central wavelength shows a shift of roughly 16nm from the central wavelength of the unprocessed material PL spectrum (not shown) by applying pulsed pumping only, this means that the junction temperature is risen by 160°C for a device that operate at 300nsec pulse width and 30µsec pulse duration if 0.1nm/°C is assumed for GaAs based devices. Such an increase in the junction temperature, even when applying such a short pulse, is indicative of self-heating.

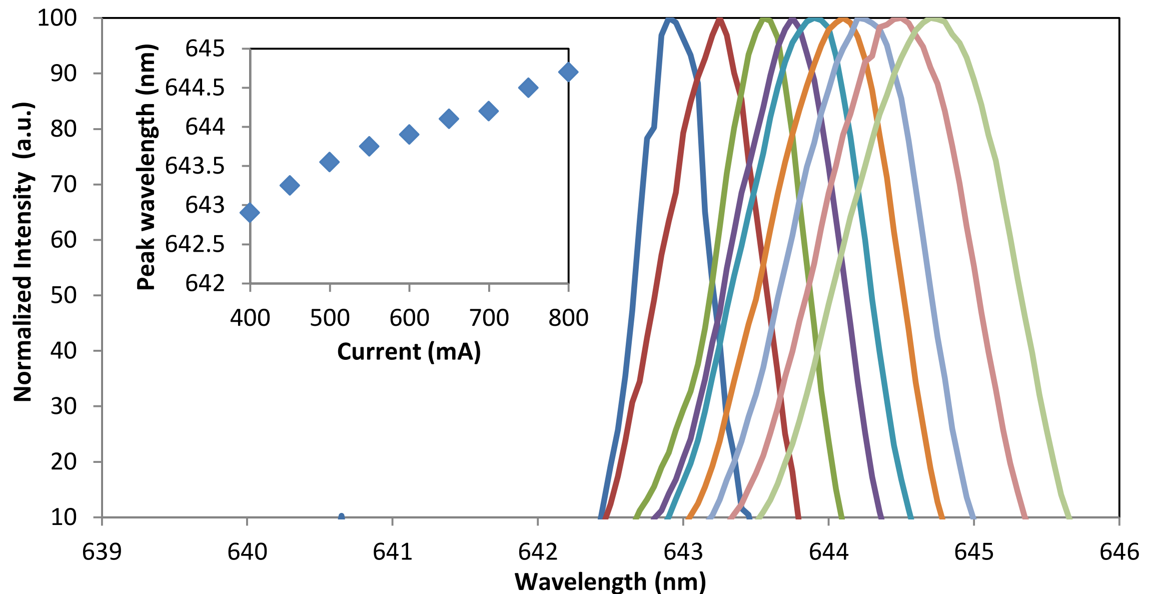

Figure 6-20: EL spectra of 500µm long device from 400 to 800mA (main figure) and the peak wavelengths as a function of increasing current (inset figure).

6.6.2 MQB laser characterisation:

400µm long MQB lasers were tested under the same conditions as the reference lasers above. The results are shown in Figure 6-21 below which plots the pulsed LI curves of such device at room temperature (a) and the threshold current and slope efficiency as a function of pulse width in (b). Unfortunately the MQB samples did not show the same behaviour as the reference ones but instead exhibited a 3× increase of threshold current density compared with the reference lasers.

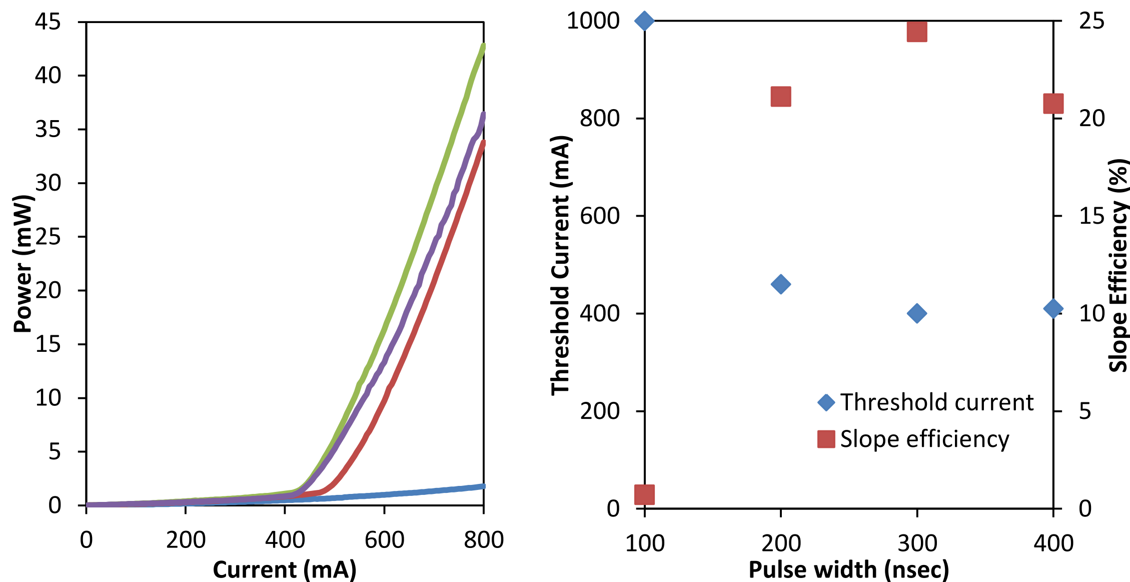

Figure 6-21: LI curves comparison for a 400μm long device from the MQB containing wafer (left) and the comparison of the threshold current and slope efficiency for different pulse widths (right).

A possible reason for this increase could be the added non-radiative recombinations in the MQB section where the simulation of this structure shows an increased carrier population around that area (in spite of the decrease of the threshold current). This is in addition to the self-heating problem which was evident even in the reference structure.

6.6.3 Arrow structure observations:

Although the original incorporation of GaInP in the current blocking layer design was as a protective layer to protect the rich Al-composition layers from exposure to oxygen during processing, the high index of GaInP for wavelengths as short as 645nm meant that it could not be used in this way. Instead the device was designed to have an opto-electronic confinement layer with 15% aluminium $(Al_{0.3}Ga_{0.7})_{0.5}In_{0.5}P$ in it, it was accused that the affinity to oxygen of this compound would be very small and that oxidation of this layer would be negligible with rapid transportation of the patterned wafer into MOVPE reactor for overgrowth, in addition to performing an in-situ anneal to remove any oxides from the surface prior to overgrowth. The surface would also have benefited from an HF wash prior to loading, to remove any surface oxides.

However, even with 9min anneal at 690°C under H_2 overpressure, good quality overgrowth was not possible. The surface and the patterned features can be seen in Figure 6-22 which shows optical microscopic images of (a) InGaP surface, (b) ARROW patterned surface without annealing and (c) ARROW patterned with annealing at 690°C. Improvement was made on the surface quality by increasing the temperature but more attempts needed.

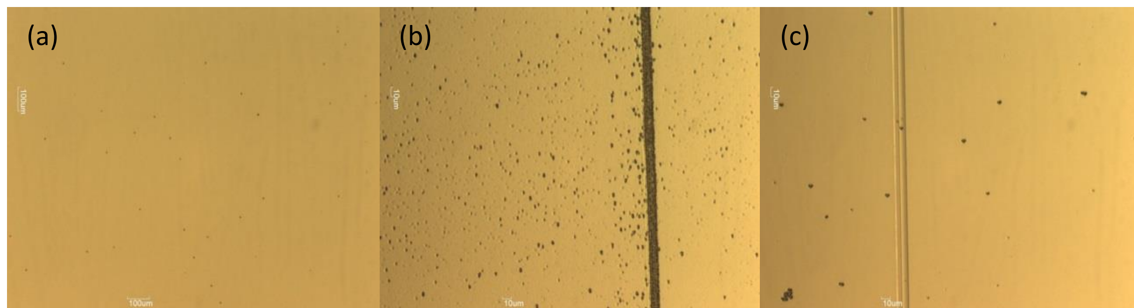

Figure 6-22: Microscopic images of three surfaces, (a) GaInP layer only which is considered as a reference, (b) an ARROW patterned surface with no annealing prior to overgrowth, while (c) is an ARROW overgrown material with annealing. The enhancement is obvious between (b) and (c) yet more work is needed to enhance it to the level of Al-free overgrowth quality.

6.7 Future Work

1. The growth and processing methods are not mature enough in the University of Sheffield in this range of the spectrum, further development in the processing method and MOVPE growth technique used in this thesis and possibly MBE. Techniques that can overcome the problem of extra heating resulted in the devices presented in this chapter would open a new field of work for developers in this field in The University of Sheffield.
2. Specifically for the MQB lasers, more rigorous simulation of MQB structures should be performed and experimentally verified to achieve the expected performance (decrease in the threshold current and increase in characteristic temperature). Different well/barrier width, different material combinations, and different separations can be explored. Another design that can be tested is to have an MQB

section with variable widths of quantum wells and barriers within the same structure as shown in Figure 6-23a and also various material compositions of the wells and the barriers as in 1b.

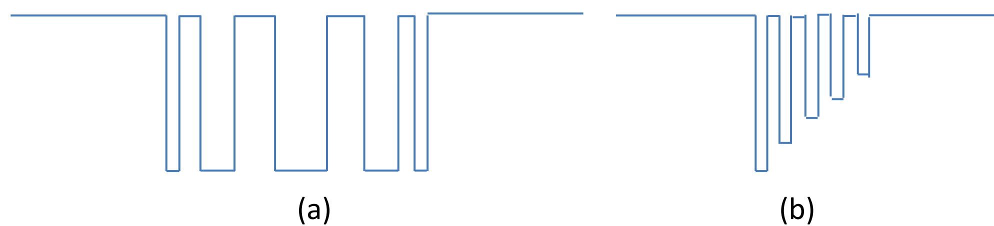

Figure 6-23: Proposed variable wells/barriers widths (a) and different well compositions (b). Variation of either of the two parameters can randomize the energy sub-bands and decrease the probability of electron tunnelling.

3. The ARROW structure can be developed in three ways. The first is to continue to develop a process for realization of the design in section 6.5. Another way would be to investigate different material combinations in different geometries in order to allow use of GaInP as the current blocking layer rather than AlGaInP, to completely avoid the need to regrow over Al-containing material. The third direction is to use the anti-resonance waveguide in both lateral and the vertical directions, by combining the concept of Mawst *et.al.* [23]–[31] of the lateral mode devices and the concept presented by Koch *et.al.* [20] of the vertical anti-resonant waveguide in the InP material system and apply it in the GaInP/AlGaInP system. The two dimensioned ARROW structure would serve to produce diode lasers with low divergence angle since the confinement method is not based on total internal reflection. The main challenge to face the developer is to grow enough material to planarize the patterned area of the wafer. This can be done by selective or masked growth process. This selective growth method is similar to the selective QD growth method developed by Ozaki et.al. [56]. Figure 6-24 can summarize the idea in simplified schematic diagram of the structure cross-section.

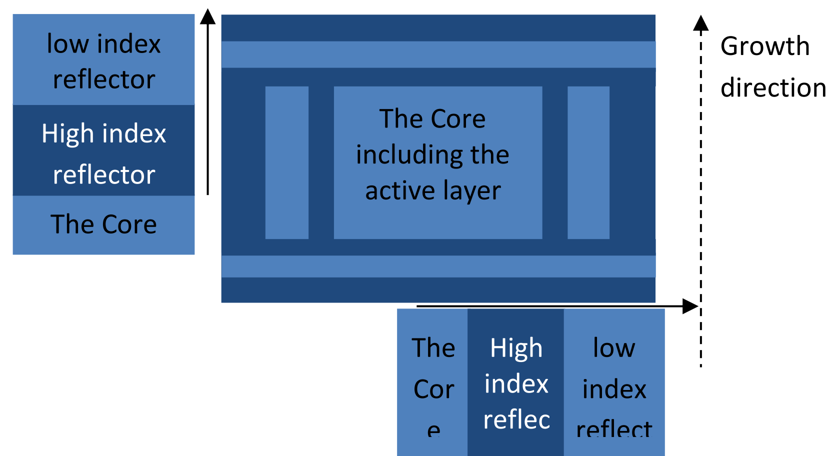

Figure 6-24: The suggested structure in which anti-resonance reflecting waveguide is applied in both vertical and lateral directions.

6.8 References

[1] M. I. Nathan, W. P. Dumke, G. Burns, F. H. Dill, and G. Lasher, "Stimulated Emission of Radiation from GaAs pn-Junctions," *Applied Physics Letters*, vol. 1, no. 3, pp. 62–64, 1962.

[2] H. Kressel and F. Z. Hawrylo, "Stimulated Emission at 300°K and Simultaneous Lasing at Two Wavelengths Epitaxial $Al_xGa_{1-x}As$ Injection Lasers," *Proceedings of IEEE*, p. 8600, 1968.

[3] O. P. Kowalski, S. McDougall, B. Schmidt, and J. H. Marsh, "High-Performance Visible Semiconductor Lasers Operating at 630 nm," *IEEE Photonics Journal*, vol. 2, no. 4, pp. 563–570, 2010.

[4] A. T. Tukiainen, L. J. Toikkanen, I. A. T. Hirvonen, and M. Pessa, "High-Power 2.1W CW-Operation of 650nm Laser Diodes Grown by Solid-Source Molecular Beam Epitaxy," *Conference on Lasers and Electro-optics CLEO 2003*, vol. 2, pp. San Jose:CA: USA, 6–8 June 2003.

[5] H. Nelson, H. Kressel, "Improved Red and Infrared Light Emitting $Al_xGa_{1-x}As$ Laser Diodes Using The Close-Confinement Structure," *Applied Physics Letters*, vol. 15, no. 1, p. 7, 1969.

[6] H. Kressel, H. Lockwood, and H. Nelson, "Low-Threshold AlxGa1-xAs Visible and IR-Light-Emitting Diode Lasers," *IEEE Journal of Quantum Electronics*, vol. QE-6, no. 6, pp. 278–284, 1970.

[7] K. Itoh, M. Inoue, and I. Teramoto, "New Heteroisolation Stripe-Geometry Visible-Light-Emitting Lasers," *IEEE Journal of Quantum Electronics*, vol. QW-11, no. 7, pp. 421–426, 1975.

[8] H. Kressel and F. Z. Hawrylo, "Red-Light-Emitting Laser Diodes Operating CW at Room Temperature," *Applied Physics Letters*, vol. 28, no. 10, p. 598, 1976.

[9] R. S. Geels, D. F. Welch, D. R. Scifres, D. P. Bour, D. W. Treat, and R. D. Bringans, "High Power, Low Threshold Singlemode 630nm Laser Diodes," *Electronics Letters*, vol. 28, no. 19, pp. 1810–1811, 1987.

[10] A. Shima, H. Watanabe, H. Tada, S. Arimoto, T. Kamizato, K. Kadoiwa, E.

Omura, and M. Otsubo, “10000h, 30-50mW CW Operation of 670nm-690nm Visible Laser Diodes,” *Electronics Letters*, vol. 30, no. 16, pp. 1293–1294, 1994.

[11] P. M. Smowton and P. Blood, “GaInP-(AlyGal-y)InP 670 nm Quantum-Well Lasers for High-Temperature Operation,” *IEEE Journal of Quantum Electronics*, vol. 31, no. 12, pp. 2159–2164, 1995.

[12] H. Murata, Y. Terui, M. Saitoh, Y. Satoh, and R. Terasaki, “Low Threshold Current Density of 620nm Band MQW-SCH AlGaInP Semiconductor Lasers with Mg-Doped AlInP Cladding Layer,” *Electronics Letters*, vol. 27, no. 17, pp. 15–17, 1991.

[13] R. S. Geels, M. Sakamoto, D. F. Welch, R. O. Way, and S. Jose, “90 W CW Red Laser Diode Bar,” *Laser Electro-optics Society Meeting 1994, LEOS 94 Conference Proceedings, IEEE*, vol. 1, 1994.

[14] H. Fujii, H. Yoshii, K. Endo, T. Kishi, H. Makita, J. Okuda, and H. Yamada, “Low-Threshold-Current 670nm Multi-Quantum-Well Laser Diodes,” *Laser and Electro-optics Society Meeting 1994, LEOS 94 conference Proceedings, IEEE*, 1994, vol. 1.

[15] T. Onishi, K. Inoue, K. Onozawa, T. Takayama, and M. Yuri, “High-Power and High-Temperature Operation of Mg-Doped AlGaInP-Based Red Laser Diodes,” *IEEE Journal of Quantum Electronics*, vol. 40, no. 12, pp. 1634–1638, 2004.

[16] C. Kaspari, G. Blume, D. Feise, K. Paschke, G. Erbert, and M. Weyers, “Optimisation of 660 nm High-Power Tapered Diode Lasers,” *Optoelectronics IET*, vol. 5, no. 3, pp. 121–127, 2011.

[17] B. Sumpf, M. Zorn, R. Staske, J. Fricke, P. Ressel, G. Erbert, M. Weyers, and G. Tränkle, “5W Reliable Operation Over 2000 H of 5mm-Wide 650nm AlGaInP-Gainp-Algaas Laser Bars With Asymmetric Cladding Layers,” *IEEE Photonics Technology Letters*, vol. 18, no. 18, pp. 1955–1957, 2006.

[18] B. Sumpf, P. Adamiec, M. Zorn, H. Wenzel, and G. Erbert, “Nearly diffraction-limited tapered lasers at 675 nm with 1-W output power and conversion efficiencies above 30%,” *IEEE Photonics Technology Letters*, vol. 23, no. 4, pp. 266–268, 2011.

[19] M. Duguay, Y. Kokubun, T. Koch, and L. Pfeiffer, “Antiresonant reflecting optical waveguides in SiO-Si multilayer structures,” *Applied Physics Letters*, vol. 49, no. 1, pp. 13–15, 1986.

[20] T. L. Koch, U. Koren, G. D. Boyd, P. J. Corvini, and M. A. Duguay, “Antiresonant Reflecting Optical Waveguides for III-V Integrated Optics,” *Electronics Letters*, vol. 23, no. 5, pp. 244–245, 1987.

[21] D. Botez, L. J. Mawst, G. L. Peterson, and T. J. Roth, “Phase-locked arrays of antiguides: Modal content and discrimination,” *IEEE Journal of Quantum Electronics*, vol. 26, no. 3, pp. 482–495, 1990.

[22] D. Botez, L. J. Mawst, and G. Peterson, “Resonant Leaky-Wave Coupling in Linear Arrays of Antiguides,” *Electronics Letters*, vol. 24, no. 21, pp. 1328–1330, 1988.

[23] L. J. Mawst, D. Botez, C. Zmudzinski, and C. Tu, “Antiresonant reflecting optical waveguide-type, single-mode diode lasers,” *Applied Physics Letters*, vol. 61, no. 5, p. 503, 1992.

[24] L. J. Mawst, D. Botez, C. Zmudzinski, and C. Tu, “0.3W CW Singla-Spatial-Mode Operation From Large-Core ARROW-Type Diode Lasers,” *Electronics Letters*, vol. 28, no. 19, pp. 1793–1795, 1992.

[25] L. J. Mawst, D. Botez, C. Zmudzinski, and C. Tu, “Design optimization of ARROW-type diode lasers,” *IEEE Photonics Technology Letters*, vol. 4, no. 11, pp. 1204–1206, 1992.

[26] C. Zmudzinski, D. Botez, L. J. Mawst, a. Bhattacharya, M. Nesnidal, and R. F. Nabiev, “Three-core ARROW-type diode laser: novel high-power, single-mode device, and effective master oscillator for flared antiguided MOPA’s,” *IEEE Journal of Selected Topics in Quantum Electronics*, vol. 1, no. 2, pp. 129–137, 1995.

[27] I. V Goltser, L. J. Mawst, and D. Botez, “Single-cladding antiresonant reflecting optical waveguide-type diode laser.,” *Optics Letters*, vol. 20, no. 21, p. 2219, 1995.

[28] A. Bhattacharya, L. J. Mawst, M. Nesnidal, J. Lopez, and D. Botez, “0.4W CW Diffraction Limited Beam Al-Free 0.98um Wavelength Three Core ARROW-Type Diode Laser,” *Electronics Letters*, vol. 32, no. 7, pp. 657–658, 1996.

[29] L. J. Mawst, H. Yang, M. Nesnidal, a. Al-Muhanna, D. Botez, T. a. Vang, F. D. Alvarez, and R. Johnson, “High-power, single-mode, Al-free InGaAs(P)/InGaP/GaAs distributed feedback diode lasers,” *Journal of Crystal Growth*, vol. 195, no. 1–4, pp. 609–616, 1998.

[30] H. Yang, M. Nesnidal, A. Al-Muhanna, L. J. Mawst, D. Botez, T. A. Vang, F. D. Alvarez, and R. Johnson, “High-Power Single-Mode Simplified Antiresonant Reflecting Optical Waveguide (S-ARROW) Distributed Feedback Semiconductor Lasers,” *IEEE Photonics Technology Letters*, vol. 10, no. 8, pp. 1079–1081, 1998.

[31] A. P. Napartovich, N. N. Elkin, V. N. Troshchieva, D. V. Vysotsky, L. J. Mawst, and D. Botez, “Comprehensive analysis of mode competition in high-power CW-operating diode lasers of the antiresonant reflecting optical waveguide (ARROW) type,” *IEEE Journal of Selected Topics in Quantum Electronics*, vol. 17, no. 6, pp. 1735–1744, 2011.

[32] E. F. Schubert, *Light-Emitting Diodes*, Second. Cambridge, UK: Cambridge University Press, 2006.

[33] K. Iga, H. Uenohara, and F. Koyama, “Electron Reflectance of Multiquantum Barrier (MQB),” *Electronics Letters*, vol. 22, no. 19, pp. 21–23, 1986.

[34] K. I. H. Uenohara, F. Koyama, “AlGaAs/GaAs Multiquantum-Well MQW surface emitting laser,” *Electronics Letters*, vol. 25, no. 12, pp. 770–771, 1989.

[35] T. Takagi, F. Koyama, and K. Iga, “Potential Barrier Height Analysis of AlGaInP Multi-Quantum Barrier (MQB),” *Japanese Journal of Applied physics*, vol. 29, no. Part 2, No. 11, pp. L1977–L1980, 1990.

[36] G. H. J. Rennie, M. Watanabe, M. Okajima, "High Temperature (90'C) CW Operation of 646nm InGaAlP Laser Containing Multiquantum Barrier," *Electronics Letters*, vol. 28, no. 2, pp. 150–151, 1992.

[37] K. Kadoiwa, T. Motoda, T. Nishimura, S. Arimoto, H. Watanabe, T. Kamizato, K. Mizuguchi, and T. Murotani, "Multiple Quantum Barrier Structures and Their Application to High Power Visible Laser Diodes with Strained InGaP Active Layers Grown by MOCVD," *Journal of Crystal Growth*, vol. 124, pp. 757–762, 1992.

[38] M.Shono, S.Honda, T.Ikegami, Y.Bessyo, R.Hiroyama, H. Kase, K.Yodoshi, T.Yamguchi, and T.Niina, "High-Power Operation of 630nm-Band Tensile Strained Multiquantum-Well AlGaInP Laser Diodes With a Multiquantum Barrier," *Electronics Letters*, vol. 29, no. 11, pp. 1010–1011, 1993.

[39] S. Arimoto, M. Yasuda, a. Shima, K. Kadoiwa, T. Kamizato, H. Watanabe, E. Omura, M. Aiga, M. Ikeda, and S. Mitsui, "150 mW fundamental-transverse-mode operation of 670 nm window laser diode," *IEEE Journal of Quantum Electronics*, vol. 29, no. 6, pp. 1874–1879, 1993.

[40] T.Tanaka, H. Yanagisawa, M.Takimoto, and S.Minagawa, "Tensile-Strained AlGaInP Singl-Quantum Well LDs Emitting at 615nm," *Electronics Letters*, vol. 29, no. 21, pp. 1864–1866, 1993.

[41] M. Watanabe, K. Tani, K. Takahashi, K. Sasaki, H. Nakatsu, M. Hosoda, S. Mastui, O. Yamamoto, and S. Yamamoto, "Fundamental-Transverse-Mode High-Power AlGaInP Laser Diode with Windows Grown on Facets," *IEEE Journal of Selected Topics in Quantum Electronics*, vol. 1, no. 2, pp. 728–733, 1995.

[42] T. G. Algainp, Q. W. Lasers, L. Toikkanen, A. Tukiainen, M. Dumitrescu, V. Rimpiläinen, S. Ikonen, and V. Erojärvi, "Suppression of TE Polarization by a Multiquantum-Barrier Structure in Sub-630-nm," *IEEE Photonics Technology Letters*, vol. 17, no. 12, pp. 2517–1519, 2005.

[43] J. M. Kim, C. Y. Park, Y. T. Lee, and J. D. Song, "Optical characterization of digital alloy In[sub 0.49]Ga[sub 0.51]P/In[sub 0.49](Ga[sub 0.6]Al[sub 0.4])[sub 0.51]P multi-quantum-wells grown by molecular beam epitaxy," *Journal of Applied Physics*, vol. 100, no. 9, p. 093503, 2006.

[44] K. S. Teng, M. Brown, A. Kestle, P. Smowton, P. Blood, P. Pinches, P. A. Mawby, and S. P. Wilks, "An Investigation of Multi-Quantum Barriers for Band Offset Engineering in AlGaInP/GaInP Lasers," *Applied Surface Science*, vol. 190, pp. 284–287, 2002.

[45] M. Usami, Y. Matushima, and Y. Takahashi, "Extremely high characteristic temperature To of 0.98um InGaAs/InGaP Strained Quantum Well Lasers with GaAs/InGaP Superlattice Optical Confinement Layer," *Electronics Letters*, vol. 31, no. 3, pp. 192–193, 1995.

[46] M. Irikawa, Y. Sasaki, M. Iwase, and K. Iga, "Strained-Layer Multi-Quantum Barriers for Reducing Hot Electron Leakage in Long- Wavelength Semiconductor Lasers," *Japanese Journal of Applied Physics*, vol. 31, no. Part 2 No. 9B, pp. 1351–1354, 1992.

[47] T. Fukushima, A. Kasukawa, M. Iwase, T. Namegaya, and S. Mituyoshi, “GaInAsP / InP Multiple Quantum Well Lasers for High-speed Parallel Data Transmission Systems,” *IEEE Journal of Quantum Electronics*, vol. 29, no. 6, pp. 1536–1543, 1993.

[48] P. A. Postigo, D. Golmayo, H. Gómez, D. Rodríguez, and M. L. Dotor, “Improvement of the Temperature Characteristic of 1.3 µm GaInAsP Laser Diodes with GaInAsP/InP Short-Period Superlattice Barriers,” *Japanese Journal of Applied Physics*, vol. 41, no. Part 2, No. 5B, pp. L565–L567, 2002.

[49] T. Fukushima, H. Shimizu, K. Nishikata, Y. Hirayama, and M. Irikawa, “Carrier confinement by multiple quantum barriers in 1.55 µm strained GaInAs/AlGaInAs quantum well lasers,” *Applied Physics Letters*, vol. 66, no. 16, p. 2025, 1995.

[50] N. Ohnoki, G. Okazaki, F. Koyama, and K. Iga, “Record High Characteristic Temperature (To=122K) of 1.55um strain-compensated AlGaInAs/AlGaInAs MQW lasers with AlAs/AlInAs Multiquantum Barrier,” *Electronics Letters*, vol. 35, no. I, pp. 51–52, 1999.

[51] K. I. T. Takagi, F. Koyama, “Electron Wave Reflection by Multiquantum Barrier,” *Japanese Journal of Applied Physics*, vol. 31, no. Part 1 No.2A, pp. 197–200, 1992.

[52] C. Sirtori, F. Capasso, J. Faist, D. L. Sivco, S. N. G. Chu, and A. Y. Cho, “Quantum wells with localized states at energies above the barrier height: A Fabry-Pérot electron filter,” *Applied Physics Letters*, vol. 61, no. 1992, pp. 898–900, 1992.

[53] F. Schäfer, B. Mayer, J. P. Reithmaier, and A. Forchel, “High-temperature properties of GaInAs/AlGaAs lasers with imprived carrier confinement by short-period supperlattice quantum well barriers,” *Applied Physics Letters*, vol. 73, no. 20, pp. 2863–2865, 1998.

[54] Y. Huang, P. Li, Z. Yang, Y. Hao, and X. Wang, “High efficiency and enhanced ESD properties of UV LEDs by inserting p-GaN/p-AlGaN superlattice,” *Science China Physics, Mechanics, and Astronomy*, vol. 57, no. 5, pp. 887–891, 2014.

[55] H. Tanaka, Y. Kawamura, and H. Asahi, “Refractive indices of $(In_{0.49}Ga_{0.51})_{x-1}Al_xP$,” *Journal Applied Physics*, vol. 59, no. 3, pp. 985–986, 1986.

[56] N. Ozaki, T. Yasuda, S. Ohkouchi, E. Watanabe, N. Ikeda, Y. Sugimoto, and R. A. Hogg, “Near-Infrared Superluminescent Diode Using Stacked Self-Assembled Inas Quantum Dots With Controlled Emission Wavelengths,” *Japanese Journal of Applied Physics*, vol. 53, no. 04EG10, pp. 1–4, 2014.

Chapter 7: Summaries and Conclusion

In this chapter I briefly summarize the outcomes of the chapters 2-6 and conclude the work done during the period of study.

7.1 Summaries:

The summary for each chapter are listed in the following sub-sections for each chapter.

7.1.1 Chapter two summary:

In this chapter two main subjects were highlighted, the first one was the measurement setups used in this thesis to characterize the devices and the material used in this study. While there was no novel thing presented in term of the characterisations setups, the chapter highlighted the structure used to achieve the presented devices.

1. Double quantum well active layer was implemented in this structure which resulted in a narrow bandwidth structure as shown by the photoluminescence measurement performed.
2. The modal gain of the devices used in here is expected to be 75-90 cm^{-1} as the length dependant measurement showed.
3. The photocurrent measurement held for the structure suggested that quantum well absorption peak will be 990, 960 and 915nm.
4. On the other hand, the peaks appeared in the wavelength range shorter than 850 is expected to be related to the GaAs material used as separate confinement layer and quantum barrier. The

7.1.2 Chapter three conclusions:

In this chapter tilted SAS superluminescent diodes (SLDs) fabricated from the wafer discussed earlier in chapter two were presented. The methods to achieve

superluminescence from laser are briefly introduced followed by a thorough study of the introduced window structure is given in the early sections of the chapters.

1. The intact active layer enabled realization of window-like natural absorber at the rear end of the device rather than just a transparent window. This absorber in addition to the propagated mode spreading suppressed the feedback to the active stripe efficiently.
2. With this effective suppression, the window like structure could achieve reflectivity as low as 8×10^{-13} from a facet that had 2.25mm window.
3. According to the measured facet effective reflectivity, simulation was held to estimate the behaviour of the devices with identical window part and three active parts with identical length and three different widths. The trend obtained from the simulation suggests that the wider active perform better.
4. Tilted cavity SLDs were fabricated from the material described in chapter 2 in two configurations epi-side up and epi-side down. The epi-side up presented a very good start to characterize the presented SLDs where 3mm active stripe device offered >40mW ASE with 17% spectral modulation depth.
5. The trend shown in the simulation was confirmed from such devices. The reason of this higher than expected SMD was the fact that the central emission wavelength red-shifted with respect to the absorption peak due to Joule's heating. This caused the rear absorbing window to turn into a transparent window.
6. To improve the heat sinking of the device in order to decrease the red-shift, the devices were mounted epi-side down. This configuration actually enhanced the performance of the device where output power of 30mW was collected from 3mm long active device with only 5.5% SMD.

7. The enhancement appeared obviously when a 1.7mm active device emitted 32mW output power with 20% while the epi-side up counterpart showed the SMD at half the output power level.
8. The effect of the heat was confirmed by running the device in pulsed operation in which 38mW was collected from the 1.7mm device with only 1-2% (ideal case) SMD.
9. Another configuration was tested by heating up the window region to red-shift the absorption peak to the emission peak. Although the conditions of this experiment wasn't ideal but promising drop in SMD from 16%-10% was recorded from applying 5W of thermal power to the window region.

7.1.3 Chapter four conclusions:

In chapter four I tested the grown structure in a normal-to-facet optical waveguide configuration. This configuration benefited in two main aspects, first the output beam profile is maintained to elliptical shape rather than the crescent shape that resulted from tilting the facets, this should increase the device coupling efficiency to standard couplers and connectors, and second is the decrease in the production cost by minimization of the semiconductor material losses especially for long cavity devices. The first benefit was reflected to the coupling efficiency of the devices.

1. The farfield measurement showed output beam enhancement by changing the beam shape from crescent back to elliptical shape. This will increase the coupling efficiency of such devices.
2. The first trial was to test a 2mm long active with 2mm rear window device epi-side down. The device was coated with anti-reflective coating on the front facet to decrease the carrier depletion by the reflected light at the cleaved facet. Output power recorded was 6.5mW before lasing took place at 1010nm (20nm away from the device central wavelength).

3. Wider SLDs were fabricated from new batch with stripe widths 5, 7, and 10µm in order to investigate the effect of device geometry on these devices. The effective reflectivity of 1mm long window section was able to maintain laser suppression in all of the devices but other limitations appeared to affect the performance of such devices.
4. The behaviour of devices with 1mm stripe and 1mm window was identical to the devices/batch reported in chapter three. The spectral modulation depth of 10µm wide stripe device for 20mW was <10%.
5. In the shorter than 1mm devices the state filling caused the device to lase at shorter wavelength, while in the longer than 1mm devices Joule's heating caused the devices to lase at longer wavelengths.
6. The lasing always occurs in the normal-to-facet devices because of the stripe alignment normal to the cleaved facet. Bearing in mind that the step index is only 0.002-0.003 between the active and window sections, this will result in a small divergence angle of the propagated beam. In the case of emission outside the absorption band of the window (where the window is transparent of such wavelengths), there is always reflected optical intensity that is coupled in the active stripe and amplified.

7.1.4 Chapter five conclusions:

Chapter five discusses the use of the processed material detailed in chapter 2 in a semiconductor optical amplifier (SOA) configuration. This configuration has a 100µm window at each end. Due to the mask limitation only 5mm long active was available.

1. The lasing suppression was successful in these devices in the pumping range measured as the initial screening showed.
2. The four parameters investigated by Mukai and Mamamoto were measured for the presented devices to evaluate its performance.

3. The device had 11nm bandwidth, 33.5dB small signal gain, 7.7dBm saturation output power, and 5.8dB noise figure.
4. The reason of the narrow bandwidth is the material used as the original bandwidth measured by free space was 6.2nm.
5. The high gain (33.5dB) resulted from the active layer properties where identical two quantum wells were used as an active layer.
6. The low saturation power occurred mainly due to the low pumping currents, this low pumping levels caused the carriers to be depleted in the case of high stimulated emission rate.
7. The increase in the noise figure in the wavelengths shorter than 997nm resulted from the drop in the input signal intensity to lower than -10dBm. This caused SNR_{out} to decrease and resulted in higher noise figure.

7.1.5 Chapter six summary:

Although this chapter did not show a successful realization of ARROW laser operating in the visible range of GaAs-based material due to the technical difficulties, some conclusions can be drawn from the simulation work done.

1. The simulations done for the active structure showed an obvious improvement of the device performance sensed as a decrease in the threshold current of the device.
2. Buried structures are available by implementing a higher refractive index layer to work as an optical and electrical confinement layer.

7.2 Conclusion:

In this thesis I mainly presented broadband devices which implemented a window-like facet to suppress the optical feedback. Although this rear section was tested with an active medium that was designed originally for low threshold current laser devices, feedback suppression was observed to a very high pumping level. This high level of feedback suppression enabled presentation of windowed-facet devices in three different configurations, tilted SLDs, normal to facet SLDs, and SOAs. These devices operated at 990nm wavelength. The active chosen was designed originally for low threshold laser. The reasons behind selecting this active were first: a well-known active with enough gain was needed in order to test the window (since the effect of such type of window was not very well understood) and second: such active enabled testing the window to its maximum limit.

The effective reflectivity of the windowed facet was measured to a record low effective reflectivity $< 10^{-14}$ for an unpumped region of 2.25mm long. This value resulted from a combination of mode spreading and absorption in the unpumped region. Both of them can be engineered to achieve even better results by increasing the active medium absorption and increase the mode spreading by increasing the effective refractive index step between the pumped and unpumped sections although it might increase the reflection at the interface. Since the rear section has an absorption peak at the emission peak of the active part, this method is inherently broadband and there is no need for further processing to tailor the absorption band to the emission spectrum.

In spite of such a low effective reflectivity, spectral modulation still appears in the EL spectra of the tilted SLDs, the reason of that is most probably because of the high gain generated in the active stripe which the rear section could not totally overcome. The magnitude of such spectral modulation was dependent upon the device dimensions in which the longest cavities gave the best output (lowest spectral modulation depth at

highest power). The best performance under CW operation was attained from a device with 3mm long and 3μm wide active stripe and integrated with 2mm long window section mounted epi-side down. The output power was 30mW with only 5% spectral modulation depth. These values were enhanced to 38mW and 1-2% spectral modulation depth when the same device is tested under pulsed conditions. The reason of this difference between the pulsed and CW operation modes is related to the difference in the heat dissipation mechanisms in the two cases.

The effective reflectivity of the device was found to be active-junction-temperature dependent such that the uncontrolled shift in the emission wavelength, due to heating, causes the absorption in the rear section to be non-resonant with the emission from the active section, and decreases the effective reflectivity of the rear facet which eventually causes the spectral modulation depth to increase. Minimizing the emission wavelength shift or tailoring absorption band will improve the device performance. The active medium used exposed the limits of such window devices, it is expected for the device to operate much better in case broadband active medium is used.

The same structure was implemented in a normal-to-facet configuration in order to maintain the elliptical shape of the output beam and reduce the gross cost of the device by saving the excess semiconductor material wasted in the tilted SLDs configuration. The implementation was successful under specific dimensions. Devices performance can be improved by engineering the beam divergence at the active/window sections interface which depends mainly on the waveguide widths and the refractive index, also the shape of the interface may increase the beam divergence. The experiments done proved that the implementation of the windowed facet and high performance are expected with the suitable broadband active medium.

Two windowed facets were used in the same device to test the structure as an SOA. The effective reflectivity resulted from the unpumped window and tilting the active waveguide was enough to suppress the lasing over a suitable range of pumping power. Implementing such an active enabled high gain operation as high as 31dB with pumping level less than 2kA.cm^{-2}. However, the use of such active resulted in a penalty which was the narrow bandwidth and the low saturation output power. The noise figure of the amplifier was measured to be around 5-7dB which is within the common values of the linear SOAs.

The last chapter of the thesis included an attempt to extend the concept explored in chapters 2-5 to the edge of the GaAs-based operating wavelength. Red emitting devices implementing AlGaInP active layer was designed. The red devices had two main problems toward the index guided buried laser, these two problems can be summarized by the shallow bandgap and the high refractive index for the material that does not contain Al in it. Two solutions were suggested by the literature for the two problems, the first one was solved by integrating a multiquantum barriers (MQB) layer close to the quantum wells in order to reflect the electrons back and virtually increase the gap. The second problem was solved by implementing a buried structure that uses anti-resonance reflection instead of the total internal reflection to form an optical waveguide. The structure is called Anti-Resonance Reflecting Optical Waveguide (ARROW).

A structure included five quantum wells, a MQB layer, and an ARROW waveguide was simulated with successful operation. The simulated devices showed an improved performance of the devices compared to a reference device included only 5 quantum wells. Unfortunately the experimental implementation of the devices did not show coherent performance compared to the simulation. The self-heating was very high in the broad area lasers tested with the MQB which demand more investigation toward better

heat sinking. The overgrowth, on the other hand, was the main problem faced the experimental attempt to form the ARROW structures. It showed high contamination due to Al exposure in the etched layer which resulted in poor quality overgrowth. More attempts are needed to try different configurations of ARROW structures.